

Sheffield Hallam University

Creep crack initiation and growth in 2.25% chromium - 1% molybdenum alloy steel

COLLINGTON, Rachel A.

Available from the Sheffield Hallam University Research Archive (SHURA) at:

<http://shura.shu.ac.uk/3172/>

A Sheffield Hallam University thesis

This thesis is protected by copyright which belongs to the author.

The content must not be changed in any way or sold commercially in any format or medium without the formal permission of the author.

When referring to this work, full bibliographic details including the author, title, awarding institution and date of the thesis must be given.

Please visit <http://shura.shu.ac.uk/3172/> and <http://shura.shu.ac.uk/information.html> for further details about copyright and re-use permissions.

CITY CAMPUS, POND STREET,
SHEFFIELD, S1 1WB.

101 657 651 X



REFERENCE

ProQuest Number: 10694376

All rights reserved

INFORMATION TO ALL USERS

The quality of this reproduction is dependent upon the quality of the copy submitted.

In the unlikely event that the author did not send a complete manuscript and there are missing pages, these will be noted. Also, if material had to be removed, a note will indicate the deletion.



ProQuest 10694376

Published by ProQuest LLC (2017). Copyright of the Dissertation is held by the Author.

All rights reserved.

This work is protected against unauthorized copying under Title 17, United States Code
Microform Edition © ProQuest LLC.

ProQuest LLC.
789 East Eisenhower Parkway
P.O. Box 1346
Ann Arbor, MI 48106 – 1346

**CREEP CRACK INITIATION AND GROWTH IN
2.25% CHROMIUM - 1% MOLYBDENUM ALLOY
STEEL**

Rachel A. Collington

A thesis submitted in partial fulfilment of the requirements
of Sheffield Hallam University for the degree of Doctor of
Philosophy

April 2001

Collaborating Establishment: Alstom Energy, UK, Ltd.



Preface

This thesis is submitted in partial fulfilment of the requirements of Sheffield Hallam University for the degree of Doctor of Philosophy. It contains an account of research carried out, on a part-time basis, between May 1988 and December 2000 in the School of Engineering and Materials Research Institute at Sheffield Hallam University. Supervision of the project was by Dr J. Cawley and Dr R. Stratton of Sheffield Hallam University and Dr S. Holdsworth of Alstom Energy, UK, Ltd. Except where acknowledged and referenced, this work is, to the best of my knowledge, original and has been carried out independently. No part of this thesis has been, or is currently being, submitted for any degree or diploma at this, or any other, university.

Rachel A. Collington

March 2001

Acknowledgements

I wish to acknowledge Dr Jess Cawley for his continuing support and supervision of this project and for not giving up on me during the difficult times.

I would like to thank Dr Rod Stratton and Dr Stuart Holdsworth for their advice and guidance, particularly in the early stages of this project.

For his encouragement and guidance during the arduous writing up stage I would like to express my sincere gratitude to Dr Robin Acheson.

Many thanks go to all my colleagues in both the School of Engineering and The Materials Research Institute who have provided help and given their support throughout.

And last, but definitely not least, I would like to acknowledge the love and support given to me by my partner Lawrence and my children Elliot and Amelia. This is for you!

Abstract

2.25%Cr-1%Mo Steel has been utilised extensively for the manufacture of power plant components.

This study has highlighted the implication of the presence of pre-existing defects in such components and, in particular, the influence of the microstructure on the creep deformation response ahead of a defect during the crack initiation, or incubation, period.

The investigation was conducted by carrying out creep tests on compact tension specimens in three microstructural variations of the alloy and, subsequently, using optical, scanning and transmission electron microscopy techniques to evaluate the creep damage in the “defect” tip region up to a point where ~1mm of crack extension was detected.

Details of two image analysis routines devised specifically for this project have been presented and their suitability for purpose discussed. The first of these routines allowed the distribution and density of creep voids occurring ahead of the simulated defect to be quantified using back scattered electron imaging in the scanning electron microscope. The second allowed carbides, extracted from the alloy, to be classified in the STEM on the basis of their key element ratios.

The microstructural constraint imposed by the material ahead of the defect tip was shown to critically affect the crack initiation and growth process; the order of constraint observed being that of 100% bainite > mixed ferrite / bainite > mixed ferrite / pearlite.

A correlation between the carbide type, distribution and shape and the creep deformation and crack initiation process has been discussed and the implications of this to remanent life assessment suggested. Evolution of $M_{23}C_6$ grain boundary carbides to the equilibrium carbide, M_6C , and the affect of the grain boundary sliding on the shape of the M_6C , were proposed to be the most important microstructural phenomena contributing to the crack initiation process.

A detailed review of published literature relating to the topic studied and recommendations for further work have also been included in this thesis.

Contents

	Page
Preface	ii
Acknowledgements	iii
Abstract	iv
Contents	v
Nomenclature and Abbreviations	ix
Chapter 1.0 Introduction	1
Chapter 2.0 Literature Review	8
2.1 Introduction	
2.2 The Chromium – Molybdenum Creep Resisting Steels	9
2.2.1 The Transformation Structure	10
2.2.2 The Carbide Structure	13
2.3 Creep Deformation	19
2.3.1 Creep Deformation Mechanisms and Maps	21
2.3.2 Creep Deformation of Chromium – Molybdenum, Steels	25
2.4 Creep Fracture	30
2.4.1 Creep Fracture Mechanisms	31
2.4.2 Creep Cavity Initiation and Growth	33
2.4.3 Creep in the Presence of a Pre-existing Defect	41
2.5 Creep Failure Prediction and Remanent Life Assessment	47
2.5.1 Creep Life Assessment of Initially 'Defect Free' Structures	47
2.5.2 Creep Life Assessment of Structures Containing Pre-existing Defects	52
2.5.3 Microstructural Investigation Techniques for Creep Life Prediction Methods	59
Chapter 3.0 Experimental Procedures	61
3.1 Introduction	62
3.2 Raw Materials	65

Contents cont.

3.3 Heat Treatment	67
3.3.1 Production of 100% Bainite CT Creep Test Specimens	67
3.3.2 Bainite Tempering Investigation	68
3.4 Mechanical Testing	69
3.4.1 Hardness Tests	69
3.4.2 Tensile Tests	70
3.4.3 Creep Deformation Tests	70
3.4.3 (a) Creep Rig Design	70
3.4.3 (b) Creep Test Specimens and Loading Regime	73
3.4.3 (c) Crack Opening Displacement Measurement	75
3.5 Optical Microscopy Techniques	77
3.5.1 Specimen Preparation and Microstructural Examination	77
3.5.2 Grain Size Determination	77
3.5.3 Determination of the Volume Fraction of Transformation Products	78
3.6 Electron Microscopy Techniques	79
3.6.1 Scanning Electron Microscopy	79
3.6.1(a) SEM Specimen Preparation	80
3.6.1(b) General SEM Examination	81
3.6.1(c) Creep Damage Quantification using SEM Image Analysis	81
3.6.2 Transmission and Scanning Transmission Electron Microscopy	84
3.6.2(a) Preparation of Carbon Extraction Replicas	85
3.6.2(b) Preparation of Thin Foils	86
3.6.2(c) Microstructural Examination in the TEM	87
3.6.2(d) Carbide Characterisation by Image Analysis in the STEM	88
Chapter 4.0 Experimental Results	92
4.1 Introduction	93
4.2 Characterisation of the Starting Materials	93

Contents cont.		
4.2.1	Mechanical Properties	94
4.2.2	Optical Microscopy	95
4.2.3	Scanning Electron Microscopy	96
4.2.4	Transmission Electron Microscopy	98
4.3	The Tempering Behaviour of Fully Bainitic 2.25%Cr-1%Mo Alloy Steel	110
4.3.1	Hardness Test Results	111
4.3.2	Microstructural Changes During Tempering	113
4.3.2(a)	Examination by Scanning Electron Microscopy	113
4.3.2(b)	Examination by Scanning Transmission Electron Microscopy	114
4.4	Creep Testing and Deformation Assessment	129
4.4.1	Crack Opening Displacement Measurement	129
4.4.2	Creep Damage Assessment in the Scanning Electron Microscope	135
4.4.2(a)	100% Bainite Specimens	135
4.4.2(b)	Mixed Pro-eutectoid Ferrite / Bainite Specimens	147
4.4.2(c)	Mixed Pro-eutectoid Ferrite / Pearlite Specimens	159
4.4.3	Correlation and Summary Of The Creep Test Investigation Data	168
4.4.4	Carbide Analysis of Creep Tested Materials in the TEM	174
4.4.4(a)	Carbide Analysis of the 100% Bainite Specimens	174
4.4.4(b)	Carbide Analysis of the Mixed Ferrite / Bainite Specimens	176
Chapter 5.0	Discussion	187
5.1	Starting Structures and Basic Mechanical Properties of 2.25%Cr-1%Mo	188
5.1.1	Transformation Structures	188
5.1.2	Carbide Structure	190
5.1.3	Basic Mechanical Properties	194
5.2	Tempering Characteristics And The Carbide Evolution Process In 2.25%Cr-1%Mo Steel.	195
5.3	Creep Deformation in the Presence of a Pre-existing Defect	200

Contents cont.		
5.3.1	Creep Damage Response	200
5.3.2	The Affect of Microstructural Variables on the Creep Crack Initiation and Growth Process	207
5.3.3	The Contribution of Grain Boundary Carbides to the Creep Crack Initiation Process	213
5.4	Contribution to Life Assessment Strategy	216
5.4.1	The Effect of Notch Tip Constraint and Life-Time Prediction	216
5.4.2	The Mechanisms of Creep Deformation Occurring Ahead of a Pre-existing Defect and Life-Time Prediction	219
5.4.3	Carbide Evolution and Life-Time Prediction	220
5.5	Experimental Considerations and Suggestions for Further Work	221
Chapter 6.0	Conclusions	223
References		228
Appendices		242
Appendix 1	Creep Data For The Derivation Of σ_{ref} .	243
Appendix 2	EDX Spot Analysis For The Determination Of Carbide Classification Schemes	245
Appendix 3	Elemental Factors Determined for Use in the STEM Image Analysis Routine	247
Appendix 4	Published Paper	248
Index		256
	Index to Table Nos.	257
	Index to Figure Nos.	259
	Index to Plate Nos.	263

Nomenclature and Abbreviations

a	Crack length
\dot{a}	Crack growth rate
A_{c1}	The eutectoid reaction temperature on cooling
A_{c3}	The austenite – ferrite transformation temperature on cooling
b	Burgers vector
B	Specimen thickness
BCC	Body-centred cubic
B_n	Net specimen thickness
C	Constant in the Larson-Miller equation
C_∞	Solute concentration in a solvent when a particle has an infinite radius of curvature
C^*	Creep crack parameter
CCT	Continuous cooling transformation
CDM's	Continuum damage mechanics
COD	Crack opening displacement
CT	Compact tension
CTOD	Crack tip opening displacement
d	Grain diameter as measured by the mean linear intercept method
D	Damage parameter
D_0	Material constant in equation for determining creep crack growth rate
E	Young's modulus
EDXA	Energy dispersive X-ray analysis
f_0	Reaction force of a precipitate against dislocation movement during creep
FCC	Face-centred cubic
G	Elastic strain energy release rate
H	Hardening parameter
J	J-contour integral
K	Linear elastic stress intensity factor
K_{nom}	Nominal value of stress intensity
LEFM	Linear elastic fracture mechanics
LMP	Larson-Miller parameter
LPD	Load point displacement
m	General yield ratio
M	Metal atoms in alloy carbides
MTDATA	Metallurgical and thermodynamic data
n	Creep stress exponent
n.a.	Not applicable
n.d.	Not determined

p	Diameter of a particle subjected to a stress concentration imparted by grain boundary sliding
P'	Applied load
Q	Activation energy
r	Mean particle radius
r'	Radius of the damage zone
R	Gas constant
SEM	Scanning electron microscope
STEM	Scanning transmission electron microscope
t	Time
t_f	Time to failure
t_g	Time to grow a creep crack
t_i	Time to initiate a creep crack
t_r	Time to rupture
t_x	Time at stress σ_x and temperature T_x
t_{xf}	Failure time at stress σ_x and temperature T_x
T_x	Temperature at the x^{th} fraction of creep life
T	Temperature
TEM	Transmission electron microscope
T_m	Homologous temperature
V_m	Molar volume of a dispersed phase
W	Specimen width
x_c	Crack initiation criterion
Y	Specimen compliance function
α	Ferrite
$\dot{\Delta}$	Specimen load point displacement
ε	Epsilon carbide
$\dot{\varepsilon}_0$	Strain rate in uniaxial creep
ε_{f0}	Creep ductility in uniaxial tension
ε_f^*	Local rupture strain
$\dot{\varepsilon}_s$	Secondary creep rate
ε_x	Strain at stress σ_x and time t_f
ε_{xf}	Failure strain at stress σ_x and t_{xf}
ϕ	Material constant in equation for determining creep crack growth rate
γ	Austenite
σ_0	Stress in uniaxial creep
σ_p	Average stress on a particle due to grain boundary sliding
σ_{ref}	Reference stress

σ_x	Stress at the x^{th} fraction of creep life
σ_y	Yield strength
\sum_x	Sum of the creep life fractions
τ	Shear stress
ν	Poisson's ratio

The use of steam power for the generation of electrical power has been utilised in Europe since the late 1800's and since its introduction there has been a continuing drive to improve the efficiency of the process. The 'efficiency' of the thermodynamic process of coal fired power describes how much of the energy fed into the cycle is converted into electrical energy. The greater the output of electrical energy for a given amount of energy input, the higher the efficiency.

It is well understood, by an examination of the Carnot cycle^[1], that the efficiency of a steam turbine is proportional to temperature and pressure and that relatively small increases in these bring a considerable efficiency benefit. If, therefore, the energy input is kept constant the output can be increased by selecting elevated pressures and temperatures for the water-steam cycle^[2], for example a temperature rise from 560°C – 600°C can provide a relative efficiency increase of 2^[3].

Figure 1.1 shows the trend for higher steam conditions utilised between 1988 and the present.

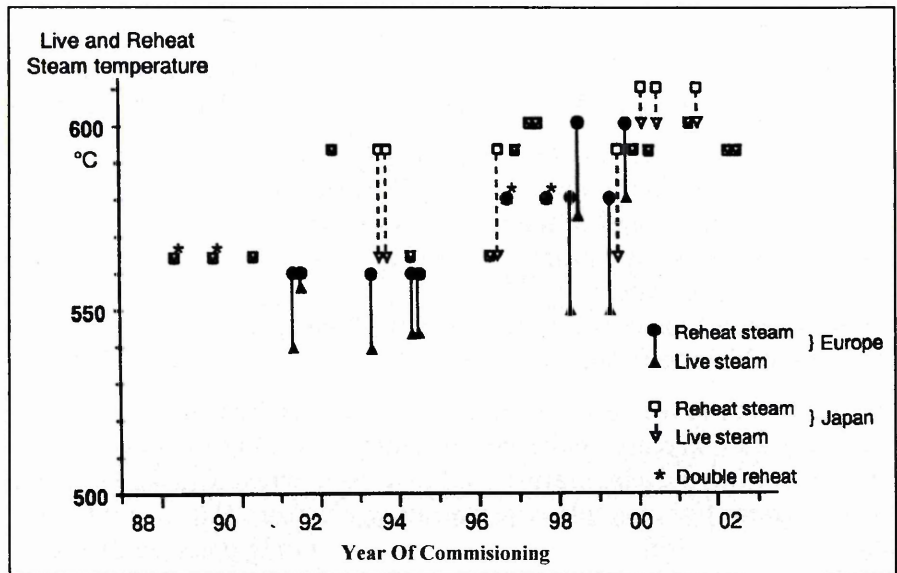


Figure 1.1: Trend to higher steam conditions for steam power plant – after Scarlin^[3]

To enable power plant to operate at improved efficiencies there has been, since the process began, a requirement for materials with improved resistance to the high temperature deformation process of creep. The development of these creep resistant alloys is based on fundamental theories of creep deformation and fracture which are well understood and have been extensively reported ^{[4] - [6]}.

Methods for predicting the lifetime of components destined for operation in high temperature environments have traditionally been based on the steady state period of creep deformation determined by testing specimens subjected to uniaxial loading conditions. It became evident, however, that there was also a need for studies to be carried out to predict the behaviour of material in non-uniaxial situations, for example material ahead of pre-existing defects in large castings or in welds. Research in this area has since been reported by many authors ^{[7] - [14]} with the prediction of material behaviour ahead of defects being predominantly based on fracture mechanics theory and on crack propagation rates.

One of the alloys that has been used extensively for high temperature power plant components in the last five decades is 2.25%Cr-1% Mo steel. 2.25%Cr-1%Mo steel confers good creep strength and corrosion resistance up to service temperatures of $\sim 565^{\circ}\text{C}$ ^[15] and although the current materials requirements for new plant have superseded that of the relatively low alloy Cr-Mo steels there are still a substantial number of components of this type in operation necessitating means of remanent life prediction.

The long term creep resistance of 2.25%Cr-1%Mo steel is afforded by a combination of interaction solid solution hardening and precipitation hardening effects ^[16] the combination of which is dependent upon the initial alloy heat treatment and in service conditions. Over a period of time, at elevated temperatures in excess of $\sim 400^{\circ}\text{C}$, the microstructure of 2.25%Cr-1%Mo steel, and in particular the carbide morphology, has been shown to age ^[17]. This microstructural ageing process has a direct effect on the creep strength of the

steel and, consequently, any design codes or remaining lifetime prediction models must take into consideration this continuously varying factor.

Many attempts have been made to predict the lifetime of a component containing defects using mathematical models based on fracture mechanics theory^[14] and, as a result, standards based on the use of the C* parameter and critical COD have now been established^[18]. Although lifetime prediction models were initially based on crack propagation times alone it has become clear that a significant proportion of component life may also be accounted for by an incubation period prior to crack initiation and that this should also be included^{[11][18]}. Consequently the most recent life assessment models are based on the equation :

$$t_i + t_g = t_f \quad \text{-Equation 1.1}^{[11]}$$

Where :

t_i = time to initiate a creep crack

t_g = time to grow the creep crack to rupture of the remaining ligament

t_f = component lifetime

To estimate the period of crack initiation, or incubation, accurately it is necessary to understand the various contributory factors that may affect it and the most critical of these is the material microstructure.

During the incubation period, it has been established that, a creep damage zone develops ahead of the pre-existing defect and that there is a redistribution of the stress intensity at the defect tip. The structural degradation that occurs in this period is dependent upon the operating stress and temperature regime and includes changes in chemistry, size, distribution and spacing of second phase particles and nucleation and growth of cavities and cracks.

The gradual accumulation of damage ahead of the defect leads to strain in the component and this can be monitored in terms of crack opening displacement,

(COD). Critical CODs may then be defined for a given crack initiation criterion, ^[19], where crack initiation may be defined as the formation of the first creep cavity occurring ahead of the crack tip or the formation of an engineering sized crack, 0.5mm to 1mm long.

There is a fundamental requirement to understand the physical mechanisms of crack initiation from its earliest stages and the role of the ageing microstructure on this process. To this end, establishing a crack initiation criterion of 1mm, this research project intended to correlate information regarding COD data and corresponding microstructural evidence from various structures of 2.25%Cr-1%Mo alloy steel.

In large cast components microstructural variations occur due to differences in cooling rate from the core of the castings to the surface and thin sections. The core material in large castings of normalised and tempered 2.25%Cr-1%Mo steel is typically mixed pro-eutectoid ferrite and pearlite and/or bainite and the surface material, and that in central regions of thin sections, are fully bainitic. As each of these microstructures imparts a unique resistance to the creep deformation mechanisms occurring in the alloy, components possessing these structures exhibit a range of crack opening displacement rates and creep crack initiation times. Consequently, there is a need to establish the influence of the microstructure on these parameters so that they may be accounted for in life-time and remanent life-time prediction models.

The main aims of this study then were to:

- i) establish a relationship between critical crack opening displacement and damage accumulation in three microstructures of 2.25%Cr-1%Mo steel with a view to improving creep life prediction models and
- ii) to make a contribution to knowledge by proposing a mechanism for the creep cavitation and coalescence process occurring in a material ahead of a pre-existing defect.

To achieve the aims of this study a detailed review of the relevant literature was carried out as detailed in chapter 2.

The creep deformation response of material ahead of a pre-existing defect was studied by creep testing compact tension specimens, in three microstructures of 2.25%Cr-1%Mo steel, and performing physical measurement techniques to establish their critical COD values. An extensive microstructural investigation was carried out to quantify the amount of creep damage occurring in the specimens and to establish the mechanisms by which that damage occurred. The various experimental procedures for the techniques established and used in this study are detailed in chapter 3 and are summarised below in Figure 1.2. The experimental results derived are presented and described in detail in chapter 4 and discussed in context with the current knowledge in chapter 5. Finally, chapter 6 defines the major conclusions from the investigation and highlights the contribution to knowledge.

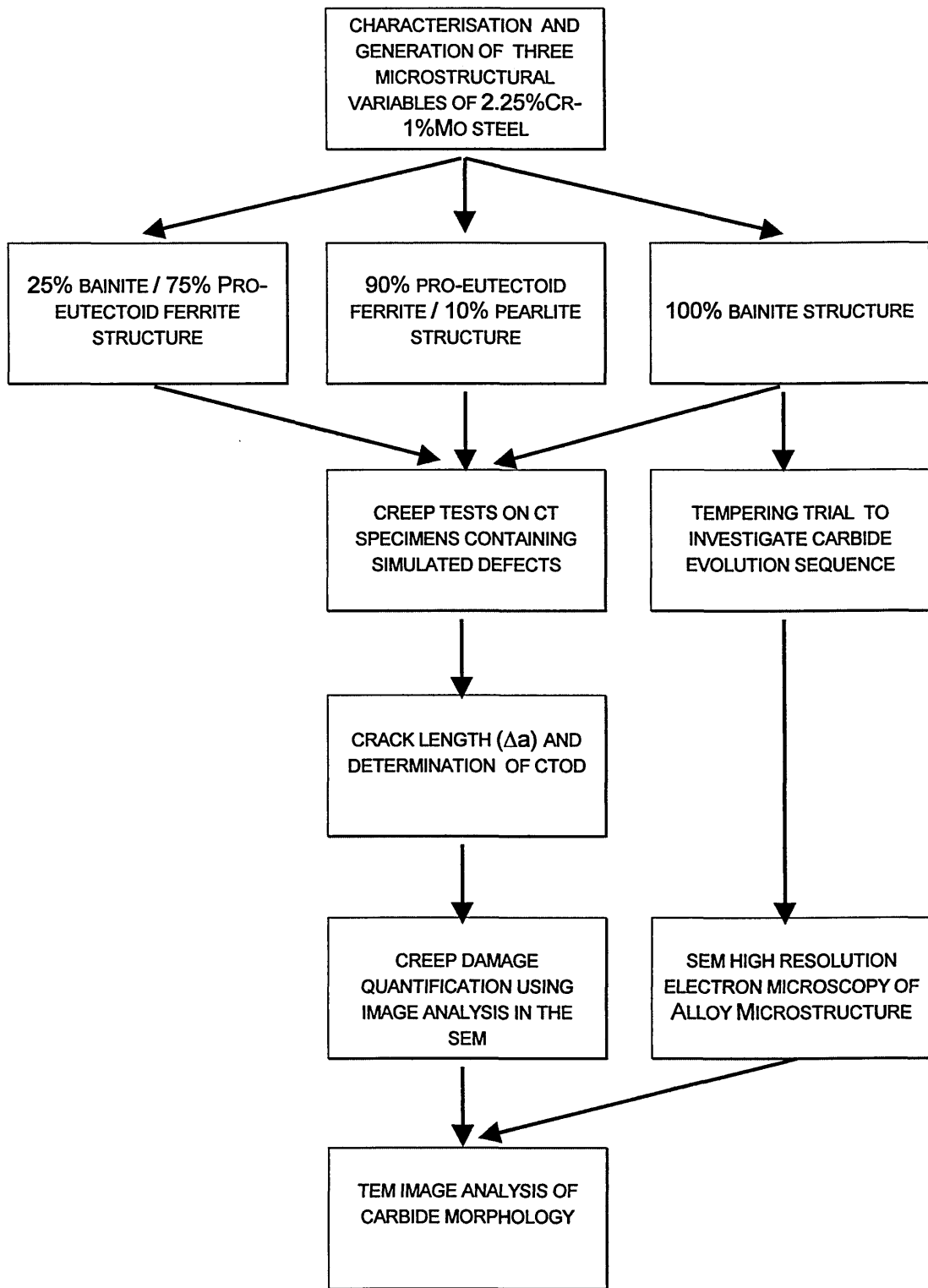


Figure 1.2: Flow diagram summarising the experimental process.

2.1 Introduction

The ideal material for components destined for power plant applications requires a combination of both high creep strength and creep ductility to resist deformation and fracture at high operating temperatures and stress levels. To develop new materials for such applications, and to predict the remaining lifetime of those already in service, it is necessary to fully understand the mechanisms of creep deformation and fracture and to appreciate the effect of these on the inherent and operational variables: composition, microstructure, temperature, stress, stress state, strain rate. These variables are not, of course, mutually exclusive but affect each other leading to complex inter-relations which are difficult to interpret. However, due to the vast amount of research that has been conducted in the last 50 years in this area, methods of predicting the behaviour of components over long periods at elevated temperatures are now in operation and are, on the whole, being utilised successfully. The aim of this section is to review the existing knowledge regarding creep deformation and fracture in chromium - molybdenum power plant steels, and specifically 2.25%Cr-1%Mo steel, with a view to providing a basis to interpret and place the data derived in this study into context. This section necessarily begins with a consideration of the microstructure of chromium – molybdenum steels and their stability at high temperature and finishes with a review of creep remanent life assessment techniques.

2.2 The Chromium – Molybdenum Creep Resisting Steels

The chromium - molybdenum, (Cr-Mo), series of steels are used widely in the power and process industries because they offer high strength at ambient and elevated temperatures combined with adequate toughness ^[20]. The properties of the steels are a direct consequence of the material microstructure which in turn is controlled by a relatively simple heat treatment process. Microstructure and mechanical properties can, therefore, be optimised for a particular

application by controlling the heat treatment parameters; austenitising temperature, cooling rate and tempering temperature and duration.

2.2.1 The Transformation Structure

The chromium – molybdenum steels belong to a group commonly referred to as ferritic creep resisting steels; the term ferritic being derived from the fact that on cooling from austenite, (γ), the microstructure consists of one, or a combination, of three essentially body centred cubic structures, namely ferrite, bainite or martensite. For a given chemical composition the transformation product that results is dependent upon the cooling rate from the austenitising temperature.

The grain size of the transformed structure can be considered as a direct function of the austenitising temperature but is regarded, generally, as only having a small influence on the long term creep resistance of the alloys ^[21]. Cane and Fidler ^[22], however, showed that the grain size effect on creep properties varies from steel to steel and reported a greater dependency of creep properties on grain-size for a fully bainitic tempered 2.25%Cr-1%Mo steel than for a tempered martensitic 9%Cr-1%Mo steel. The fracture ductility of Cr-Mo steels, in particular, is considered to be adversely affected by a large grain size and consequently the austenitising temperature used for these steels does not rise significantly above the Ac_3 ^[20].

In commercial applications, Cr-Mo steels are put into service in a microstructurally meta-stable condition. The structure that exists is a result of both continuous cooling from above the Ac_3 , to give the initial transformation product, and any subsequent stress relief / tempering treatment to develop the fine precipitate structure. The transformation product is dependent on not only the alloy composition and cooling environment but also on the section size, as indicated by reference to the continuous cooling diagrams for typical Cr - Mo steels as shown in Figure 2.1. In this figure the transformation structure can be seen to vary from ferrite and pearlite in slow cooled material, (thick sections), to

bainitic or even martensitic structures in rapidly cooled material, (thin sections). In the alloys containing higher chromium contents the transformation time required to produce ferrite, pearlite and bainite is significantly retarded and austenite decomposes directly to martensite. The likelihood of partitioning of elements and their effect on the kinetics of the austenite to ferrite transformation is well documented [23] and the mechanisms of diffusion controlled and diffusionless transformation to ferrite / bainite and martensite respectively have been comprehensively reviewed [24]. Both of the aforementioned papers drew attention to the effect on the creep resistance of the Cr - Mo alloys of the non-equilibrium existence of elements in either precipitate form or in solid solution in the as cooled structure and the move to equilibrium during further exposure to elevated temperatures.

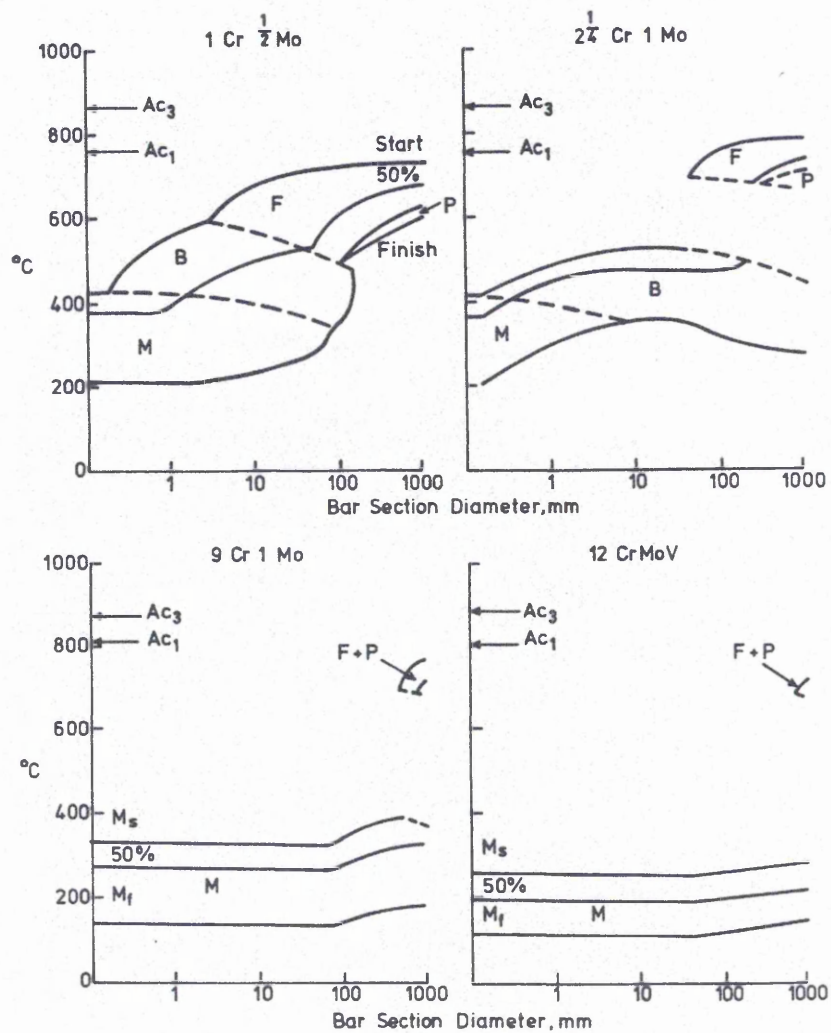


Figure 2.1: Continuous cooling diagrams for some Cr-Mo Steels – after Orr [20].

The remainder of this section will concentrate on the development of the microstructure, for elevated temperature service, of Cr-Mo steels in the annealed or normalised conditions.

During slow cooling through the $Ac_3 - Ac_1$ region, Figure 2.1, transformation to ferrite occurs progressively, enriching the remaining austenite in carbon. Eventually any remaining austenite transforms to pearlite ^[23] in which the carbon precipitates as cementite, (Fe_3C). In the case where strong carbide formers are present in the alloy, the cementite may be replaced by alloy carbides ^[25]. Up to 20% of iron atoms in cementite can be replaced by chromium, 10% by vanadium and only 4% by molybdenum without affecting the crystal structure of the carbide. The pearlite interlamellar spacing, detailed morphology and tendency to spheroidise may, however, be more significantly affected.

When cooling of the alloy is sufficiently rapid to avoid the pearlite transformation curve, but not sufficient to produce diffusionless transformation to martensite, the remaining structure will consist of a mixture of ferrite and bainite or may even be fully bainitic. In the austenite to bainite reaction, the austenite may transform to bainite in two ways ^[26],

- i) to upper bainite where cementite forms between the bainitic ferrite laths only, or
- ii) to lower bainite where the cementite additionally forms within the platelets of ferrite.

During the displacive transformation to bainite ^[26] there is no diffusion of substitutional iron atoms across the transformation interface. The excess carbon trapped in the bainitic ferrite is removed by a combination of diffusion into the residual austenite and by precipitation of carbides between the ferrite plates.

In the situation where pro-eutectoid ferrite forms prior to the transformation to bainite, the enhanced concentration of carbon in the remaining austenite, due to its rejection from the ferrite, leads to an increased density of cementite

particles in the bainite phase when compared to that in fully bainitic structure [24].

In all cases, the carbides in the as cooled condition do not exist in their equilibrium state and subsequent heat treatment and service at elevated temperatures leads to a change in their composition and morphology that consequently affects their long term creep properties. This process will be reviewed in the following section.

2.2.2 The Carbide Structure

In developing alloys for service at elevated temperatures the aim is to produce a material which not only withstands the initial service conditions but is capable of withstanding the service conditions throughout the whole of the expected design life, ~20 years for power plant components. The coarsening and evolution of carbides is of great importance in terms of the long term creep resistance of alloys and is controlled by the process of Ostwald ripening. Ostwald ripening involves the growth of large particles at the expense of small particles, which are taken into solution. It is controlled by the transfer of vacancies through the ferrite lattice to the growing particle and by the diffusion of the solute through the matrix. An increase in temperature brings about an increase in the diffusion rate, so that Ostwald ripening occurs more rapidly at high temperatures.

According to Nutting [27] it is possible to describe the particle coarsening process by the following rate equation:

$$r_t^3 - r_0^3 = \frac{K.V_m.C_\infty t}{RT} \quad \text{-Equation 2.1}$$

Where:

r_t = mean particle size after time t

r_0 = mean particle size at the start of the observations

K = constant related to the rate controlling diffusing species

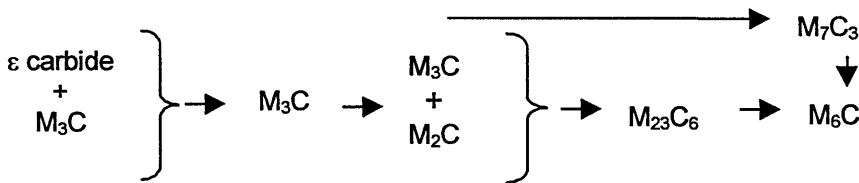
V_m = molar volume of the dispersed phase

C_{∞} = solute concentration in the solvent when the particle has an infinite radius of curvature
 t = time
 R = gas constant
 T = temperature in Kelvin

For optimum performance low alloy Cr-Mo steels usually enter service in either the normalised and tempered or annealed condition [28], thus the evolution process in terms of carbide ripening is already under way. Such steels are in an active metastable condition and further carbide precipitation, accompanied by changes in composition and coarsening, occurs throughout high temperature exposure.

In the normalised condition the microstructure is predominantly bainitic with varying amounts of pro-eutectoid ferrite, dependent upon component section size. The tempering temperature and duration used are selected to optimise the steels properties for a particular application, the knowledge to do so being drawn from works by authors such as Baker and Nutting, [17]. Baker and Nutting determined the sequence of carbide precipitation events which occurred upon tempering a normalised 2.25%Cr-1%Mo steel at temperatures ranging from 400°C to 750°C and times up to 1000 hours, as summarised below in Figure 2.2.

In bainite –



and in ferrite –

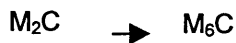


Figure 2.2: Carbide evolution sequence for 2.25%Cr-1%Mo steel, where M indicates a mixture of metal atoms- after Baker and Nutting [17].

In the annealed condition the microstructural constituents are basically the same as for the normalised and tempered material but due to the slower cooling rate there is now a significant amount of pro-eutectoid ferrite present and some pearlite.

The nature of the carbides in low alloy creep resisting steels has been extensively investigated ^{[17] [28] [27]} and those most likely to be encountered in 2.25%Cr -1%Mo steel are summarised below in, Table 2.1.

Carbide Type	Crystal Structure	Composition (metal- atom ratios)	Description and Location
ϵ Carbide	Hexagonal	Fe rich. Cr /Mn - high solubility Mo - low solubility	In the bainite between the ferrite laths. Metastable precursor to M_3C
M_3C	Orthorhombic structure of cementite, Fe_3C	Fe rich. Cr - high solubility (0.2) Mn - high solubility Mo - low solubility (0.04)	Replaces ϵ carbide on ageing. Predominantly Fe_3C .
M_7C_3	Pseudo hexagonal structure of Cr_7C_3	Chromium rich. Fe - high solubility (up to 0.6) Mn - high solubility Mo - low solubility (up to 0.055)	Stick like precipitate, bainite side of α /bainite grain boundaries. Nucleates in vicinity of Fe_3C .
$M_{23}C_6$	FCC structure	Cr rich. Fe - high solubility (up to 0.4) Mn - high solubility Mo - high solubility can replace Cr .	Precipitates in bainite at the expense of Mo_2C and Fe_3C . Not observed in immediate vicinity of Cr_7C_3 therefore considered to be based on Fe and Mo predominantly.
M_2C	Hexagonal	Mo rich Cr - high solubility (up to at least 0.3) Fe - solubility upto 0.2	Fine matrix precipitate - stable up to long times in α . May also form fringe like precipitates at α side of α /bainite grain boundaries .
M_6C	Complex cubic	Ternary carbide of Fe and Mo from $Fe_4Mo_2C \rightarrow Fe_3Mo_3C$ Cr - solubility up to 0.3	Equilibrium carbide. Forms from Mo_2C in α and eventually from M_7C_3 and $M_{23}C_6$ in bainite.

Table 2.1: Nature of carbides in normalised 2.25%Cr-1%Mo steel ^{[17] [28] [27]}.

The carbides in the bainite structure of 2.25%Cr-1%Mo steel precipitate from a matrix saturated in carbon, chromium and molybdenum on tempering. The M_2C in the pro-eutectoid ferrite, however, precipitates directly on cooling from above the Ac_3 by a process known as interphase precipitation^[23].

M_6C has been shown by many workers^{[17] [29] [30]} to be the equilibrium carbide in 2.25%Cr -1%Mo steel. More recent studies^[31], however, suggested that in silicon containing steels, 0.61% in the alloy studied, M_6C precipitates at earlier times than in the steels studied by Baker and Nutting^[17] which contained only 0.18% Si, and the equilibrium carbide is $M_{23}C_6$. In the same study, manganese was shown to have a similar effect. Decreasing the carbon content of the alloy has been shown,^{[30] [32]} to accelerate the precipitation sequence described in Figure 2.2. This has commercial implications when Cr-Mo steels are welded to mild steels as carbon migration will affect weld properties,^[33].

Detailed studies of the enrichment of carbides in chromium during the ageing of 2.25%Cr-1%Mo steel has been carried out by Thomson and Bhadeshia^{[24] [34] [35]}. These studies indicated that small cementite particles become enriched in chromium more quickly than larger ones and that the enrichment rate of cementite in bainite is slower in mixed ferrite / bainite structures than in those which are fully bainitic. MTDATA^[36], a computerised databank that allows the computation of chemical equilibrium as a function of composition and conditions, was used in conjunction with energy dispersive X-ray analysis (EDXA) to investigate the chromium levels of M_7C_3 and $M_{23}C_6$ in equilibrium with ferrite. It was concluded that the amount of chromium each carbide can support increases with decreasing tempering temperature. The concentration of chromium in M_7C_3 tempered at 565°C, however, was found to increase with time at temperature and the mass percent at extended times exceeded that predicted from the equilibrium constant obtained from MTDATA. This anomaly was considered to be due to the fact that some of the molybdenum predicted to be in the M_7C_3 , was actually in another carbide, M_2C , which was not accounted for in the analysis. Tempering at 750°C for 48hours allowed the $M_{23}C_6$ and M_7C_3 to mature and subsequently the equilibrium compositions of these carbides were determined by energy dispersive X-ray analysis, (EDXA), as described in Table 2.2 :

Carbide Type	Element Mass %			
	Cr	Mn	Mo	Fe
$M_{23}C_6$	31	2	9	58
M_7C_3	51	2.5	7	39.5

Table 2.2: Equilibrium compositions of $M_{23}C_6$ and M_7C_3 carbide - after Thomson [24].

Data derived from MTDATA was used in conjunction with a model developed by Robson and Bhadeshia [37] to predict precipitation sequences in power plant steels. Figure 2.3 shows the outcome of their prediction for 2.25%Cr-1%Mo steel at 600°C.

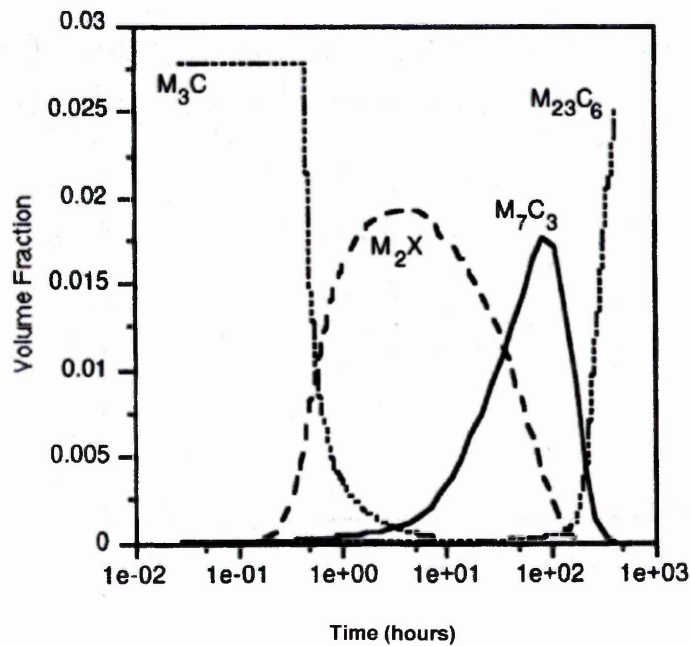


Figure 2.3: Predicted evolution of precipitate volume fractions at 600°C in 2.25%Cr-1%Mo steel -after Robson and Bhadeshia [37].

The microstructural changes occurring in 1%Cr-0.5%Mo steel have been investigated by Varin and Haftek [38] and compared with the ageing studies on 2.25%Cr-1%Mo steel by Baker and Nutting [17] and those of Abdel-Latif et al [39]. Discrepancies between the times for the formation of the equilibrium carbide, M_6C , to form in the ferrite were attributed to the lower chromium and molybdenum content of the 1%Cr-0.5%Mo steel. In the study carried out by

Abdel-Latif et al ^[39] the transformation structure of the annealed 2.25%Cr-1%Mo steel was undefined but appeared from representative microstructures to consist of a mixture of pro-eutectoid ferrite, pearlite and possibly some bainite. The authors did not attempt to attribute specific carbides to their location in the microstructure but considered only the general trend for a change from predominantly $M_{23}C_6$ type carbides in the structure at relatively short service times to a mixture of $M_{23}C_6$ and M_6C at greatly extended times. It was noted that the chromium rich carbide, M_7C_3 , was not detected in this study and that the carbide evolutionary process was, hence, described as:



In the study by Varin and Haftek ^[38] M_7C_3 carbides were detected in the pearlite after 1.22×10^5 hours having precipitated at the expense of Fe_3C . In the ferrite grains it was suggested that M_2C gave way to $M_{23}C_6$, which is in contradiction to that described by Baker and Nutting ^[17] for precipitation in ferrite where $M_2C \rightarrow M_6C$. This variation may be due to the difference in the partitioning of elements between the ferrite / pearlite phases in the former study compared to that between the ferrite / bainite phases in the latter or simply due to the difficulty in uniquely identifying the carbides by the techniques used. M_6C , the equilibrium carbide was found in this study only at extended times at the ferrite grain boundaries.

Most of the studies outlined above have only considered the effect of time and temperature on the carbide evolution process, but in fact it has been shown that the action of an applied creep stress plays a role. Gope et al ^[15] carried out microstructural studies on gauge and shoulder sections of long term creep tested specimens in normalised and tempered, fully bainitic, 2.25%Cr-1%Mo steel. It was found that the applied stress had the effect of accelerating the dissolution of M_2C in the structure, promoting the precipitation of the equilibrium carbide M_6C and aiding the recovery and recrystallization of the ferrite matrix. In both the case of the stressed and unstressed regions the M_2C particles were observed to grow in length initially with time at temperature and then decrease just prior to the precipitation of M_6C .

In reviewing the foregoing work it was clear that many anomalies existed in the precipitation sequences defined for the low alloy Cr-Mo steels and, to summarise, these can be attributed to:

- i) Variations in the starting microstructures studied; annealed structures of ferrite/ pearlite ^{[38][39]}, normalised structures of ferrite / bainite ^[17] or 100% bainite ^{[15][17]}.
- ii) Compositional variations; comparing alloys containing different carbon, chromium and molybdenum mass percents.
- iii) Uncertainty in the methods used for identifying the precipitate types; X-ray diffraction, energy dispersive X-ray analysis, carbide morphology and electron diffraction.

If estimations of component remaining life are to incorporate changing material microstructural maturity it is obvious that the carbide evolution process must be uniquely understood for a particular composition, initial microstructure and phase constitution and that the techniques used for this identification of the carbides involved must be reproducible and consistent.

2.3 Creep Deformation

The creep behaviour of metals and alloys are commonly portrayed in terms of the well known 'creep curve' exhibiting the classical three stage deformation process ^{[6][40]}. Conventionally the design lifetime of a metallic component has been based upon the secondary creep rate portion of the creep curve, where the deformation rate is governed by the combined action of strain hardening and thermally activated recovery of the dislocation structure ^[6]. Equation 2.2 describes the generally accepted inverse relationship between secondary creep rate of metals and alloys, $\dot{\epsilon}_s$ and their rupture time, t_r ^[41]. Both parameters vary similarly as a power function of the applied stress ^[42] and Arrhenius function of temperature.

$$\frac{1}{t_r} \propto \dot{\epsilon} \propto \sigma^n \exp(-Q/RT) \quad \text{-Equation 2.2}$$

Where:

n = stress exponent (varies with creep mechanism acting)

Q = activation energy

R = gas constant (8.315J/mol.K)

To correlate the vast bank of data for creep tests derived from specific materials under various conditions, several empirical formulae have been derived which describe the dependence of the rupture time on stress and on temperature^{[41] [43] [44]}. One of the most commonly used of these is the Larson – Miller parameter^[44], (LMP), which proposes the following relationship between time, stress and temperature:

$$\text{LMP} = T (C + \log t_r) / 1000 \quad \text{-Equation 2.3}$$

Where:

T = absolute temperature in Kelvin

C = constant generally accepted to have a value of 20

t_r = time to rupture

The practical application of this parameter is to allow long time rupture to be predicted from short term test as described by Dieter^[45].

Lifetime predictions based on such relationships and data extrapolated from relatively short term tests can lead to misinterpretation due to microstructural changes which occur with time. Hence, to prevent under-estimation, lifetime predictions are often conservative estimates incorporating generous safety factors to cover deficiencies in knowledge. Detailed knowledge about a particular material and how it's creep behaviour is affected by changes in composition, stress state, temperature and microstructure provides the basis for more accurate prediction of component lifetime and consequently prevents unnecessary, and expensive, premature removal of components from service. The techniques developed for the estimation of remanent life will be reviewed further in section 2.4.

2.3.1 Creep Deformation Mechanisms and Maps

Creep is known to involve a number of diffusion rate controlled processes. The process of atom movement by diffusion, leading to creep deformation, is in turn governed by the temperature and stress regime in which the material operates and can be conveniently summarised for a specific material, by a deformation mechanism map as first proposed by Frost and Ashby^[5]. Figure 2.4 shows a schematic representation of a map for the general case.

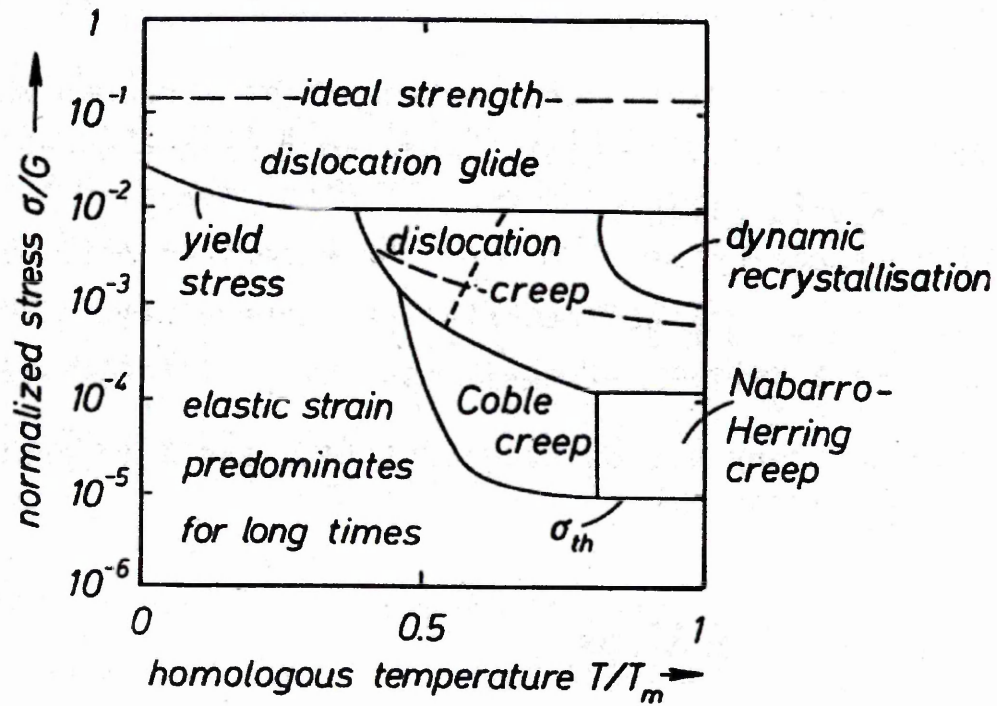


Figure 2.4: Typical deformation map – plot of normalised stress against homologous temperature - after Reidel^[40].

At low temperatures and high stresses plastic deformation occurs mainly by dislocation glide. At high temperatures, however, above $0.3T_m$ creep deformation occurs at much lower stresses than those associated with dislocation glide by the processes of either dislocation creep or diffusion creep^[5]. As indicated in Figure 2.4 diffusion creep may operate in two ways by either

diffusion of atoms through the bulk of the grain, Nabarro – Herring creep, or by diffusion predominantly along grain boundaries, Coble creep.

The stress required to deform a crystalline material plastically is that needed to move dislocations within it's structure. Dislocation movement is resisted by:

- i) the intrinsic lattice resistance, (Peierls force), and
- ii) the obstructing effect of obstacles, for example, dissolved solute atoms, precipitates or other dislocations.

Diffusion of atoms can unlock dislocations from obstacles and the diffusion of these unlocked dislocations under an applied stress leads to dislocation creep, also known as power law creep.

In this process the glide force, τb , per unit length is balanced by the reaction force, f_0 , from the precipitate and unless the dislocation intercepts the precipitate in mid-plane there is a force, $\tau b \tan \theta$, that attempts to deflect the dislocation out of the slip plane, as illustrated in Figure 2.5. Edge dislocations cannot move out of the slip plane by glide upwards by shearing of atom planes, however, they can climb perpendicular to the slip plane if atoms at the bottom of the extra half plane are able to diffuse away, as shown in Figure 2.6. Thus the dislocations appear to climb until they overcome the obstacle to glide.

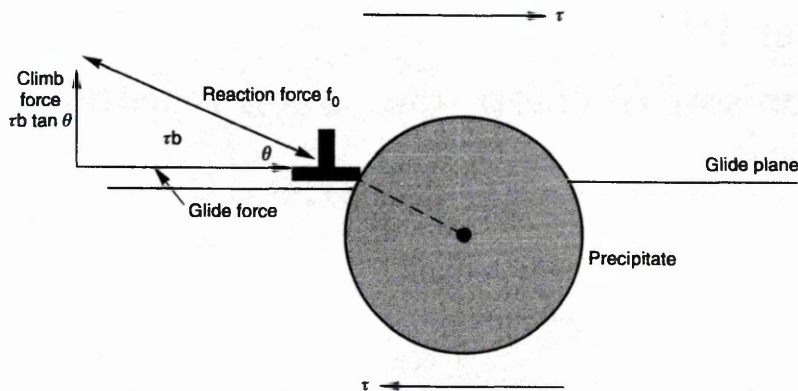


Figure 2.5: The climb force on a dislocation - after Ashby and Jones [46]. Where: τ =shear stress and b =Burgers vector.

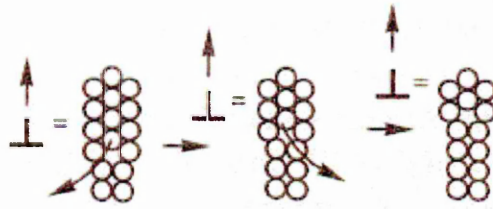


Figure 2.6: Diffusion of atoms leading to dislocation climb - after Ashby and Jones ^[46].

As indicated in Figure 2.4 the region of dislocation creep can be further divided into sub-zones behaviour dependent on the temperature and stress operating. The approximately horizontal broken line separates the low-stress regime, where grain boundary sliding contributes markedly to the total strain ^{[47] [48] [49]}, from the high stress regime, where the grain boundaries behave as if they were rigid. Various mechanisms for grain boundary sliding have been proposed ^{[50] [51] [52] [53]} and summarised by Pickering ^[6] to involve:

- i) Sliding along the grain interface, in which there may be ledge type obstacles, with accommodation being provided by diffusion of atoms and vacancies.
- ii) Sliding in regions adjacent to the boundaries by dislocation climb and glide resulting in the sub-grain formation adjacent to the boundary.
- iii) Sliding by the motion of grain boundary dislocations and grain boundary migration.

In each case, grain boundary sliding may be accommodated by the development of local cavities, the formation of which will be reviewed in section 2.4.2.

The vertical dashed line in the low stress regime of dislocation creep in Figure 2.4 separates the zones where low temperature, vacancy diffusion along dislocation lines, known as core diffusion, and illustrated in Figure 2.7, dominates over that where diffusion is mainly through the lattice.

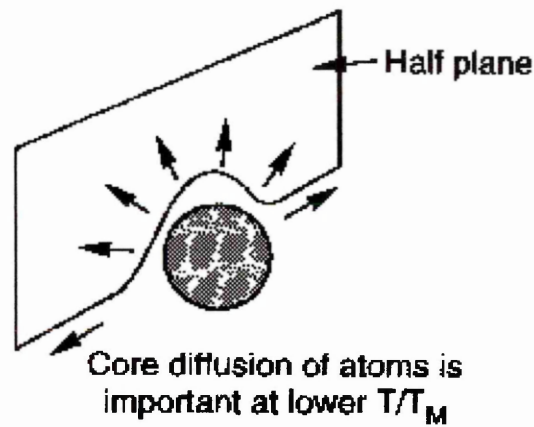


Figure 2.7: Diffusion along dislocation lines, core diffusion, at low T/T_M – after Ashby and Jones ^[46].

As the externally applied stress decreases the rate of dislocation creep falls quickly but creep does not stop. At high T/T_M ratio, diffusion may occur from one set of grain faces to another and dislocations are not involved. This process is known as the Nabarro-Herring mechanism ^[54], as shown schematically in Figure 2.8 .

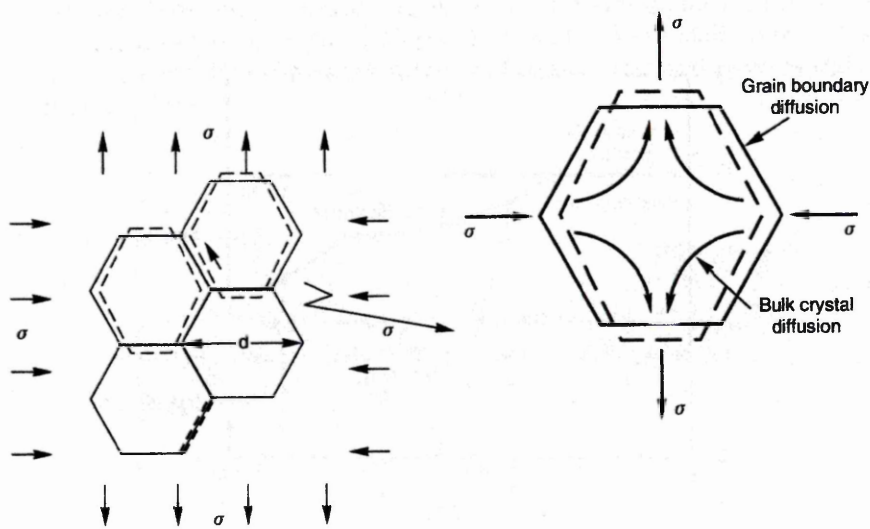


Figure 2.8: The process of creep deformation by diffusion at high T/T_M –after Ashby and Jones ^[46].

The rate of creep by this process is proportional to the diffusion coefficient, D , and to the stress, σ , which provides the driving force for diffusion. Creep rate in this regime varies inversely with (grain-size)², that is $1/d^2$. Effectively as the grain size increases the atoms have to diffuse further and thus the rate of creep deformation diminishes.

At lower values of T/T_m , bulk diffusion becomes more difficult and the mechanism which predominates is that of Coble creep ^[4]. In this case, atoms diffuse along grain boundaries rather than through the grains and grain boundary sliding takes place in order that holes do not open up between grains.

The accuracy of creep deformation maps derived for specific alloys are, as Ashby ^[55] points out, “only as good as the constitutive equations used to construct them”, but, they do provide an excellent qualitative basis on which to choose material for a particular application, to predict operative mechanisms and to select appropriate strengthening mechanisms ^[6].

2.3.2 Creep Deformation of Chromium-Molybdenum Steels

It is generally recognised ^{[20] [56]} that all creep resistant alloys depend primarily on finely dispersed particles for their strength and that inter-particle spacing is an important factor controlling the movement of dislocations. In ferrite areas the dominant carbide to form in molybdenum steels is Mo_2C , whereas, in chromium steels it is M_7C_3 and in vanadium steels V_4C_3 . A fine dispersion of these carbides gives rise to secondary hardening peaks during tempering and initially high creep resistance. The reduction in creep strength with time at elevated temperatures is widely considered to be due to microstructural degradation associated with the coarsening of these precipitates and it is this which is responsible for the initiation of tertiary creep in low alloy steels. Consequently it was recognised that there is a relationship between the critical particle spacing and the onset of rapid creep deformation ^[57] and this has been

extended to creep life prediction from microstructural assessment ^{[56] [58] [59] [60]}. Eventually, with time at temperature the material microstructure matures to its equilibrium state, as outlined in section 2.2.2, and the carbides resulting will be stable. In creep deformation terms this usually occurs towards the end of the component life as the equilibrium structure offers little resistance to the mechanisms of deformation and failure.

It has been shown by Abe and Yagi ^{[61] [62]} that although the initial microstructural differences between the chromium – molybdenum steels of various compositions imparts significant differences in creep rupture strength over extended periods, corresponding to Larson Miller Parameter $>19 \times 10^3$, the properties converge, as illustrated in Figure 2.9. The fundamental creep strength is an inherent property of the Cr-Mo steels at long times and is referred to as “inherent creep strength” ^[62]. The inherent creep strength is dependent on the chemical composition of the ferrite matrix and not on the initial microstructure as a whole.

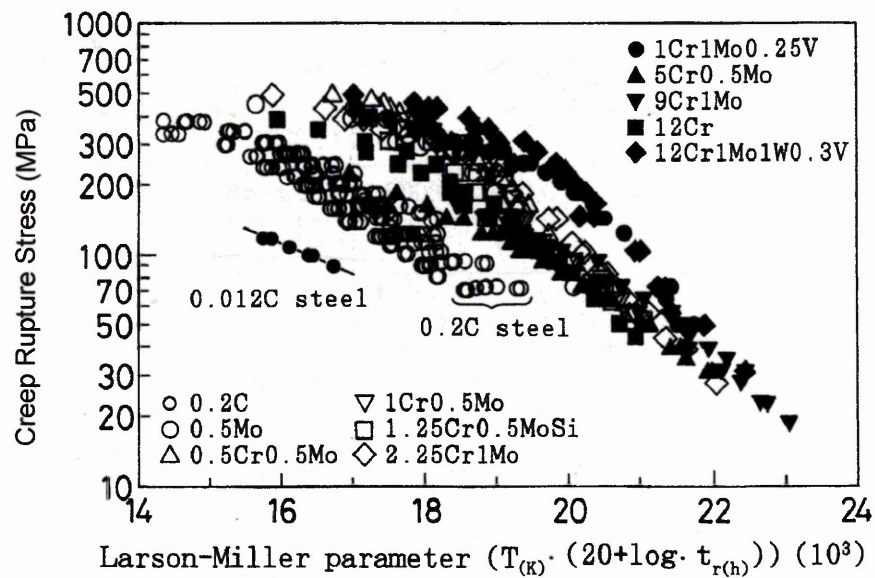


Figure 2.9: Creep rupture strength of carbon steels and Cr-Mo steels - after Abe and Yagi ^[62].

The optimum combination of transformation and precipitate structure for creep resistance in 2.25%Cr-1%Mo steel has been discussed by many authors ^[17] ^[29] ^[22]. It is generally accepted that creep strength is conferred by the presence of fine M_2C precipitates in both ferrite and bainite phases, the M_2C causing precipitation hardening due to interactions with moving dislocations. The growth and dissolution of M_2C is much more rapid in bainite than in ferrite and in the former is followed by recovery and recrystallization of the matrix. Consequently, although bainite is beneficial for short term low temperature strength, this advantage is lost after longer term service or service at high temperatures ^[29].

In addition to precipitation strengthening, solid solution strengthening also plays an important role in the creep deformation behaviour of 2.25%Cr-1%Mo alloy. Solid solution strengthening involves the inhibition of movement of dislocations decorated by atmospheres of carbon and molybdenum atom clusters ^[16] ^[64] ^[65].

Kleuh ^[16] showed that creep curves for 2.25% Cr-1%Mo alloy may differ from the classical three stage curve due to a combination of precipitation and solid solution strengthening mechanisms being operative, Figure 2.10. At intermediate stresses non classical curves, exhibiting 2 steady state stages, were observed. It was considered that the first steady state stage was controlled by interaction solid solution strengthening and that the second steady state stage was controlled by precipitation strengthening. In the low stress regime classical curves were produced and deformation was considered to be being controlled by dislocation movement only. At high stresses, classical curves occurred once more, this time due to the combined effect of deformation controlled by both solid solution and precipitation strengthening.

The effect of stress regime on the creep behaviour of 2.25%Cr-1%Mo steel has also been studied by Yamauchi et al ^[66], who assessed the relevance of the Larson-Miller Parameter constant, commonly taken to be 20, on creep life prediction times. From extrapolation of long term data from short term tests it

was concluded that in the low stress regime, $< 60\text{MPa}$, the LMP constant should be 15.6 and in the high stress regime, $>60\text{MPa}$, 18.8. It was proposed that the difference in the constant for the two stress regimes was due to the different mechanisms controlling the deformation processes and that in the high stress regime deformation was controlled by Orowan bowing between particles and in the lower stress regime by dislocation climb or grain boundary sliding, Figure 2.11 .

Creep deformation mechanisms operating in various stress regimes for 2.25%Cr-1%Mo alloy have also been proposed by Maruyama et al ^[67]; their study being portrayed in the form of a deformation map, Figure 2.12, in the manner of Frost and Ashby ^[5]. The range of conditions depicted in Figure 2.12 were considered to reflect those typical of the service conditions for a 2.25%Cr-1%Mo steel component in operation in a power plant .

Maruyama et al ^[67] suggested that below the athermal yield stress, σ_A , creep deformation took place by dislocation creep after initial elastic deformation upon loading. In this regime the dislocation creep rate is controlled by lattice diffusion and the main obstacle to dislocation motion is by fine precipitates in the microstructure. Creep by the process of bulk diffusion did not appear to be a contributing mechanism under the conditions used to obtain the test data from which this map was derived.

Above σ_A , it was proposed that athermal plastic deformation (dislocation glide) took place during loading and then creep deformation occurred by the same dislocation creep mechanism as at lower stress level. However, in this high stress regime the main obstacle to dislocation movement changes to dislocation substructure. Dislocation creep controlled by core diffusion, (low temperature power law creep), was not observed in this study.

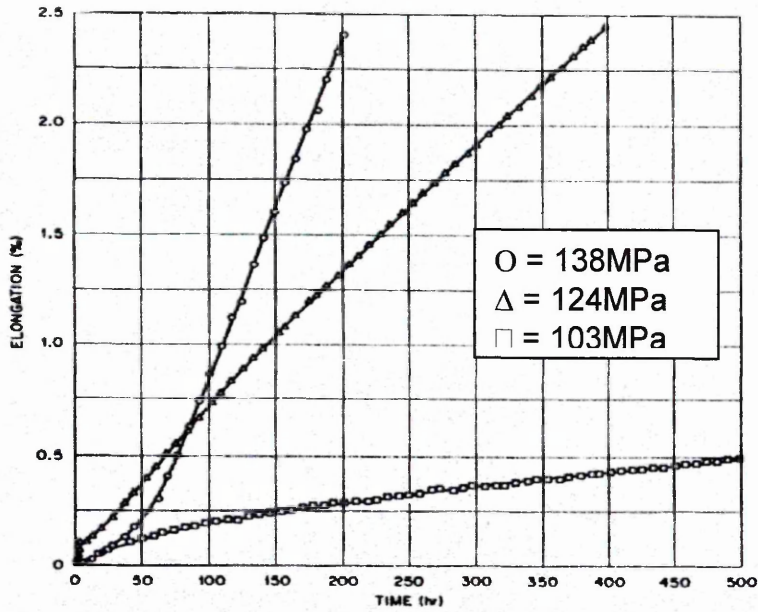


Figure 2.10: Creep curves for various stress regimes at 565°C - after Kleuh ^[16]

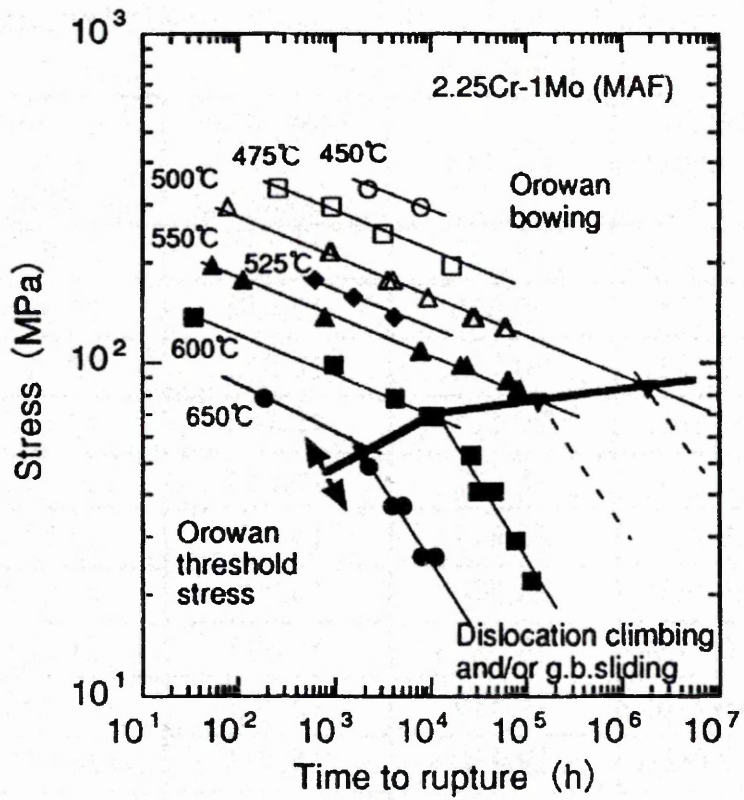


Figure 2.11: Creep rupture mechanism diagram for 2.25%Cr-1%Mo steel - after Yamauchi et al ^[66].

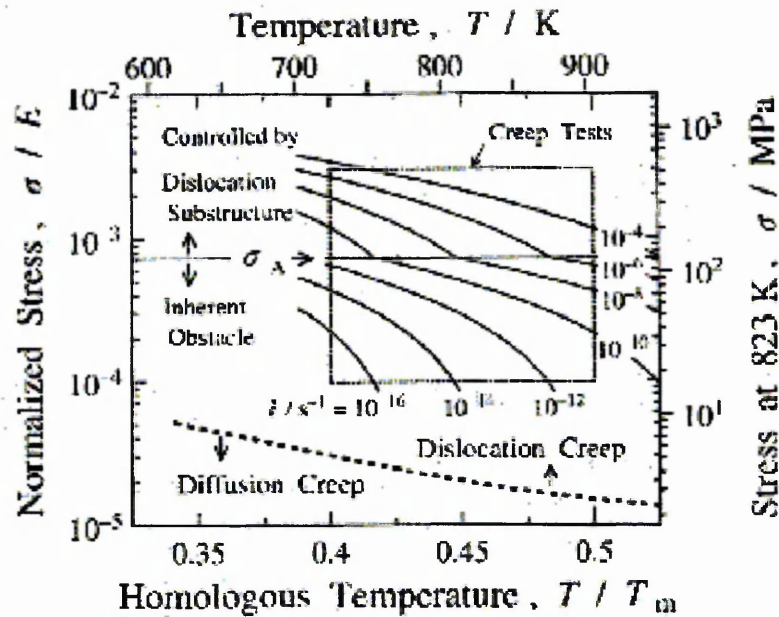


Figure 2.12: Proposed creep deformation mechanism map of 2.25%Cr-1%Mo steel – after Maruyama et al ^[67].

2.4 Creep Fracture

In the latter stages of the creep process, the so called tertiary stage, the stressed material undergoes a period of rapid deformation followed by failure. With materials exhibiting low rupture ductility, the advent of tertiary creep can be quite abrupt, the acceleration in the creep rate occurring over a very short period of time immediately prior to fracture.

Many mechanisms have been postulated to explain tertiary creep behaviour. These have been reviewed by Pickering ^[6] and also by Ashby and Dyson ^[68] and are summarised as follows:

- i) necking leading to an increase in stress by decreasing the load bearing area

- ii) the development of grain boundary cracking and cavitation of sufficient intensity to affect the deformation rate, or which can decrease the load bearing area and thus increase the stress
- iii) microstructural changes such as precipitate particle coarsening, recovery, recrystallization and grain growth
- iv) environmental changes
- v) increase in specimen volume due to cracking which makes a contribution to strain.

In terms of industrial significance, the creep ductility of a material is deemed to be of paramount importance as it reflects the ability of the material to resist cavitation and cracking during the period of rapid strain.

The following section aims to review the most industrially significant mechanisms proposed for creep fracture and, in particular, examines the mechanisms for the process of cavity nucleation and growth. The phenomena of notch sensitivity will also be covered with reference to creep damage mechanisms in the presence of a pre-existing defect.

2.4.1 Creep Fracture Mechanisms

Crystalline solids can fracture by one or more of several mechanisms which can be displayed simplistically on a fracture mechanism map ^{[69] [70]}, analogous to the deformation maps discussed in section 2.2.1. A schematic of such a diagram is shown in Figure 2.13 .

The location of the boundaries between the different mechanism fields depends on the material, its heat treatment, the chemical environment and any

additional stress components. Actual fracture mechanisms maps for iron and various steels have been constructed by Fields et al ^[71].

In the stress and temperature regimes experienced by Cr-Mo steel components in power plant applications, failure is most likely to occur by the process of intergranular creep fracture, with ductile transgranular failure being of much lesser significance.

Transgranular creep fracture occurs by a mechanism not unlike that of normal ductile fracture at low temperature, in that voids nucleate and grow and eventually coalesce to give fracture ^[6]. Nucleation occurs at non-metallic inclusions or other second phase particles, with the void nucleation mechanism depending on the nature of the particle / matrix interface and its degree of coherency and surface energy. Sulphides, for example, usually decohere whilst carbides may either decohere or crack. As most engineering components fail by transgranular ductile failure at room temperature, extensive literature describing this mechanism is available and has been reviewed by Goods and Brown ^[72] and Knott ^[73].

At lower stresses and elevated temperatures, hole growth by plastic straining or creep flow becomes so slow that fracture by grain boundary cavitation intervenes, the strain to fracture is then relatively low and fracture is intergranular ^[40].

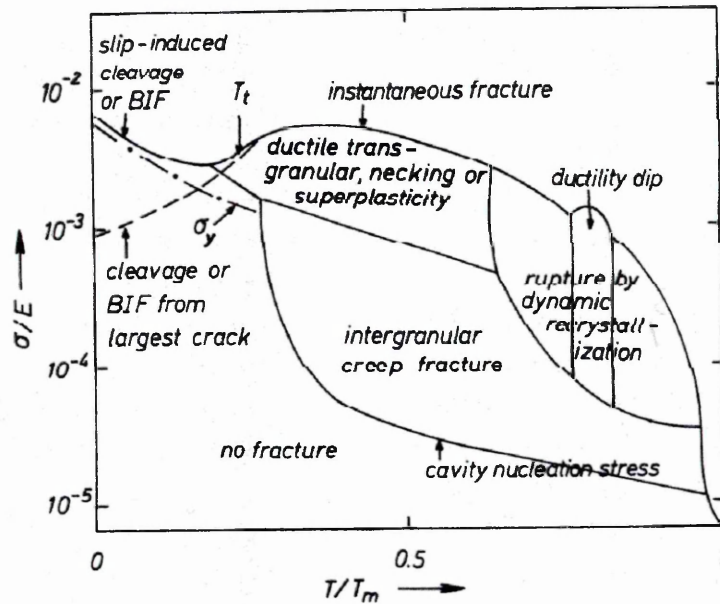


Figure 2.13: Fracture map – after Reidel [40].

2.3.2 Creep Cavity Initiation And Growth

Many of the steels operating in power plant applications develop creep cavities under their normal conditions of service, eventually leading to failure. There is, therefore, a need to understand the mechanisms by which the cavities form and grow with a view to improving future generations of power plant steels for increased creep resistance.

Voids in polycrystalline materials nucleate by either wedge type cracking at grain boundary triple points or by more diffuse cavitation at grain boundaries.

The mechanisms of grain boundary cavity nucleation and growth have been reviewed by Pickering [6] and more comprehensively covered by Reidel [40].

Wedge cracks of the type shown in Figure 2.14 occur due to grain boundary sliding, building up stress concentrations at triple points and initiating cracks on boundaries normal to the applied stress axis. These types of cracks are found predominantly in samples tested at high stresses or in coarse grained material where grain boundary segregation of impurities decreases the surface energy.

The more widespread type of cavity formation involves the development of “spherical cap” or lenticular voids, mainly on grain boundaries which have a high grain boundary sliding component. The main mechanisms which have been proposed to explain their formation are illustrated in Figure 2.15.

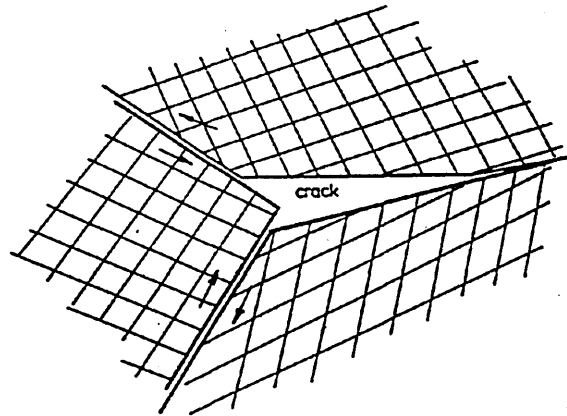


Figure 2.14: Wedge cracking at grain boundary triple point due to sliding – after Lagnebourg [74].

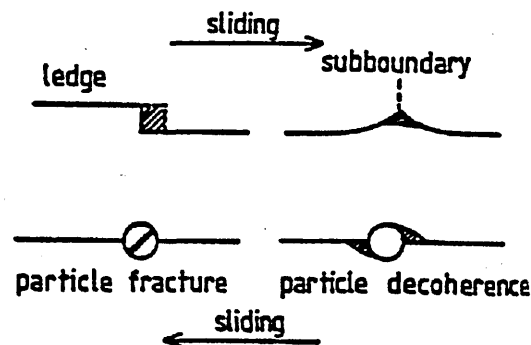


Figure 2.15: Various mechanisms for grain boundary cavity nucleation due to grain boundary sliding – after Evans and Wilshire [50].

In commercial alloys the most common sites for cavity nucleation are second phase grain boundary particles. Numerous investigations have shown that in low alloy steels, cavities are often associated with carbide particles [75] [76]. Although such particles at the boundaries in creep resisting steels are initially beneficial, that is they transmit the shear stresses which the grain boundaries would otherwise not be able to support, eventually stress concentrations may build up at the particle / matrix interface leading to cavity initiation. Once initiated the cavities grow and coalesce forming microcracks, which subsequently, upon reaching a critical size, lead to failure of the remaining ligament.

The role of particles in creating stress concentrations on sliding grain boundaries has been analysed by Reidel [40] and reviewed by Perry [77]. Sliding of grain boundaries, is believed to occur in bursts, causing stress concentrations to be set up at irregularities in the boundaries. These local stresses cause boundary separation to occur and cavities initiate if the process of atom / vacancy diffusion is insufficient to prevent it. Two general mechanisms for the nucleation of cavities have been cited [77]:

- i) Steps or ledges in grain boundaries have been supposed to result from the intersection of slip bands with grain boundaries.
- ii) Local break down of adhesion associated with precipitates or impurities.

In both cases local plastic strain is a pre-requisite. Evidence for both the mechanisms proposed has been observed during metallographic examination of creep tested material and it is believed that one or other may dominate at any particular instance.

Figure 2.16 summarises Reidel's [40] analysis of the stress concentrations which occur in the steady state after elastic stress concentrations have been relaxed; σ_p is the average stress focused on a particle by grain boundary sliding or by inhibited Coble creep and p and λ_p are the particle diameter and spacing respectively.

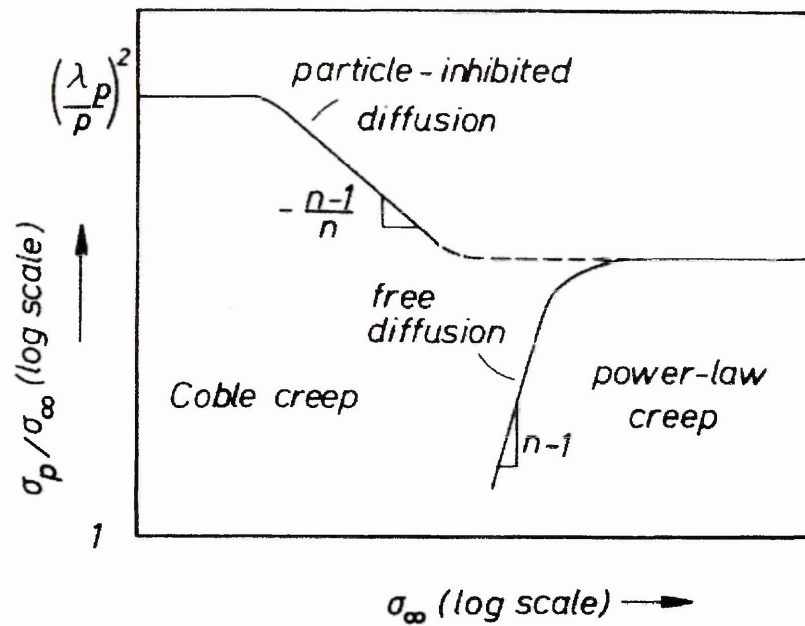


Figure 2.16: Stress concentration factor, σ_p/σ_∞ at particles versus applied stress – after Reidel ^[40].

Cavity nucleation has been shown to occur over a substantial fraction of creep life and as such may be used in some materials to estimate remaining life ^[78].

Once voids have been nucleated, they will continue to grow as creep deformation proceeds. It has been demonstrated that whilst clearly continued grain boundary sliding can result in the progressive growth of both wedge and the rounded type of cavities, another more important growth mechanism is that due to vacancy diffusion to the cavities ^{[79] [80]}. Whereas grain boundary sliding would tend to give cavities which are elongated along the boundaries, growth by vacancy diffusion gives the more rounded cavities frequently observed. Additionally, vacancy diffusion would be expected to give more pronounced cavities on boundaries normal to the stress axis, whereas with grain boundary sliding they would be more apparent on boundaries at 45° to the stress axis. In a study by Tipler et al ^[81] on void formation in chromium – molybdenum steels, it was reported that although the lines of cavities were frequently normal to the applied stress, few of the voids were so oriented. This suggests that the dominant mechanism for void nucleation may differ from that for void growth.

Hancock ^[86] has proposed an alternative growth mechanism which occurs in situations where stresses are high and plastic dislocation creep is sufficiently rapid that, in the limiting case, the transport of matter along the grain boundary can be neglected. This is illustrated below in Figure 2.18. Co-operative diffusion of atoms and vacancies in the vicinity of the void wall tend to make the void increase in volume and decrease in radius. If surface diffusion is rapid, local matter transport along the void surface always serves to retain the quasi-equilibrium spherical cap shape so that in this case the net effect is to increase void radius.

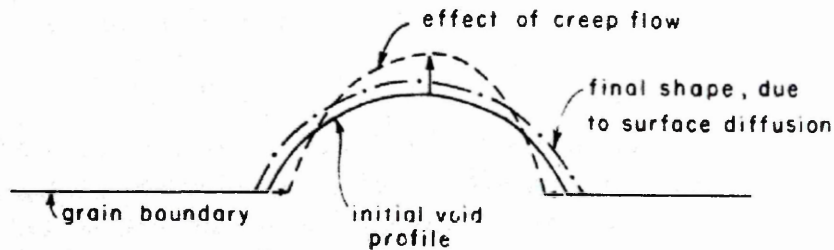


Figure 2.18: Schematic illustration of cavity growth by the combination of plastic creep flow and rapid surface diffusion – after Hancock ^[86].

If both the above processes of creep flow and grain boundary diffusion are operative at the same time, as discussed in detail by Needleman and Rice ^[87], active cavity growth rates can be many times greater than would be the case if either mechanism acted in isolation and the path length over which matter must diffuse is effectively shorter. In turn this means that less stress is required for growth to occur. Conversely, for a given stress level, the growth rate will be more rapid when local stress accommodation of the diffused matter is possible by creep ^[87].

Figure 2.19 shows rupture life-times of 2.25%Cr-1%Mo steel, as measured by Cane ^[88], compared to estimated rupture lifetimes based on models proposed for constrained and unconstrained cavity growth involving either instantaneous or continuous nucleation derived from Reidel ^[40]. The study showed that the

constrained model with continuous nucleation gave the most accurate prediction for time to failure for 2.25%Cr-1%Mo steel.

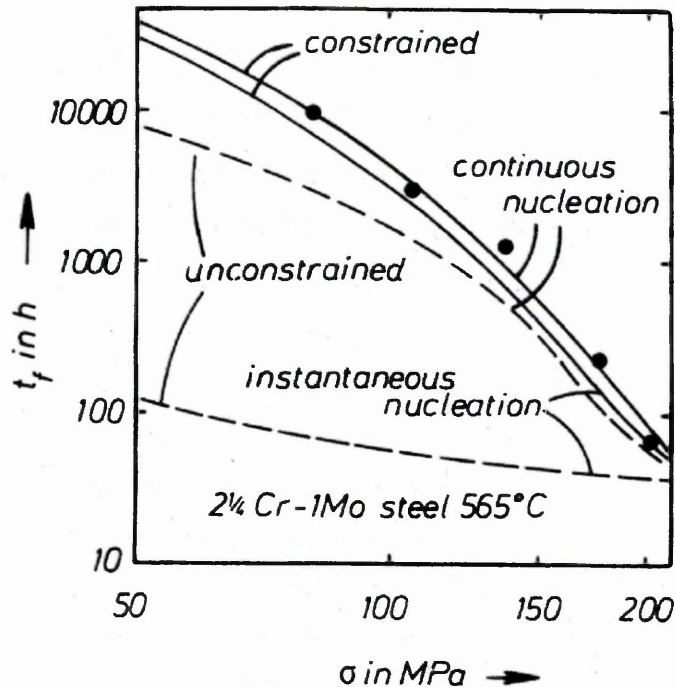


Figure 2.19: Comparison of creep curves from uniaxial creep data for 2.25%Cr-1%Mo steel compared with predictions for constrained and unconstrained cavity nucleation –after Reidel ^[40].

As the mechanisms of creep deformation and failure are affected by both the transformation products and precipitate structure of steels it is essential when discussing creep deformation that the condition of the material is accurately described. An example of this effect was apparent in a study by Cane ^[89] on the effect of transformation structure on creep rupture behaviour of 2.25%Cr-1%Mo steel. In this study an increase in the ferrite / bainite ratio in tempered coarse grained 2.25%Cr-1%Mo alloy was found to modify the rupture properties by improving ductility, increasing rupture life up to intermediate ferrite contents and causing a subsequent decrease thereafter. Additionally the final fracture mode was observed to change from brittle intergranular to ductile transgranular failure. These effects were considered to be due largely to a

reduction in susceptibility to cavitation damage caused by the progressive elimination of prior austenite grain boundaries with increase in ferrite content. Minimum creep rate, $\dot{\epsilon}$, was shown to be relatively independent of transformation structure at intermediate and high bainite contents but increased markedly at low bainite contents.

At high bainite contents, cavitation damage was considered to have made a significant contribution to the overall creep rate, while at intermediate bainite contents, the respective age hardening and softening in the ferritic and bainitic constituents lead to a corresponding structural insensitivity to creep rate. At low bainite contents, however, coarse precipitation occurring during transformation resulted in a consequent loss in super-saturation and, therefore, any ferrite strengthening potential.

In summary, fracture of power plant steels operating at temperatures of 0.3-0.4 times the melting temperature under creep conditions is governed predominantly by intergranular cracking. The underlying physical mechanisms are nucleation and subsequent growth of microscopic cavities on the boundaries of the grains. When sufficient cavities have reached a critical size, they will coalesce to form a microcrack along a grain boundary. Subsequent linking-up of microcracks leads to the growth of macroscopic cracks and eventually failure of the component remaining ligament. Cavity growth occurs mostly by grain boundary and surface diffusion, other important mechanisms being creep of the grain material and grain boundary sliding. All of these have different time scales and different dependencies on stress state, and it is the competition between them that controls damage evolution and the final lifetime of the component ^[90].

2.4.3 Creep in the Presence of a Pre-Existing Defect

Prior to the 1970's, the majority of work carried out to estimate the design life of a component in a creep environment was determined from data extrapolated from uniaxial creep tests. It soon became apparent, however, after the occurrence of a few premature failures in electricity power plants, that uniaxial data did not give an accurate estimation of design life if the component contained a pre-existing defect. Consequently many researchers have since carried out investigations relating to this phenomena ^[14]. The most recent studies include not only a means of estimating and appreciating failure due to crack growth, but also consider the period of initiation, or incubation, prior to crack extension ^{[9] [11]} and these will be reviewed in more detail in section 2.5.2. To accurately predict the safe operating life of a component, which may include a period of damage tolerance, many factors have to be taken into consideration and these can be broadly categorised into two areas:

- i) The continuum-mechanics deformation fields around the crack tip, characterized in terms of stress intensity factor, K_I , ^[91], the J-contour integral ^[92], and creep fracture mechanics parameter, C^* ^{[93] [95]}.
- iii) The micro-mechanisms occurring at the crack tip, such as stress relaxation, microstructural evolution and cavity formation.

The aim of this section is to review the studies which have been carried out on creep crack initiation and growth from pre-existing defects with a view to understanding how the state of stress at the defect tip affects the microstructure and, hence, the creep crack initiation and growth mechanisms in this region.

When a body is loaded under creep conditions in the presence of a pre-existing defect, there may be a period of time before that defect begins to grow, the so-called initiation time. During this period a creep process zone develops at the defect tip, the size and rate of development of which is governed predominantly by the elastic-plastic characteristics of the material ^[94]. The

damage zone that develops, undergoes microstructural changes due to the influence of the operative creep mechanisms, as described in section 2.3.1, and the effect of the triaxial state of stress at the defect tip. Hence, creep brittleness rather than creep strength of a service component is often the vital factor in failure by creep or thermal fatigue ^[95] under such conditions.

Relaxation of stress by heat treatment, due to atom / vacancy diffusion, represents displacement – controlled situations where stress can decrease as local creep strain accumulates. The probability of crack initiation and growth depends on the magnitude of the displacement relative to the properties of the local microstructure. Ductile crack growth occurs with a large displacement and is accompanied by widespread microstructural damage, whereas brittle cracking is accompanied by small displacements and little damage visible away from the main crack. It therefore follows that, the greater the notch opening / creep crack length ratio the more ductile the situation ^[96].

The factors affecting the mode of crack growth and failure has been described schematically by Gooch and King ^[95], as shown in Figure 2.20.

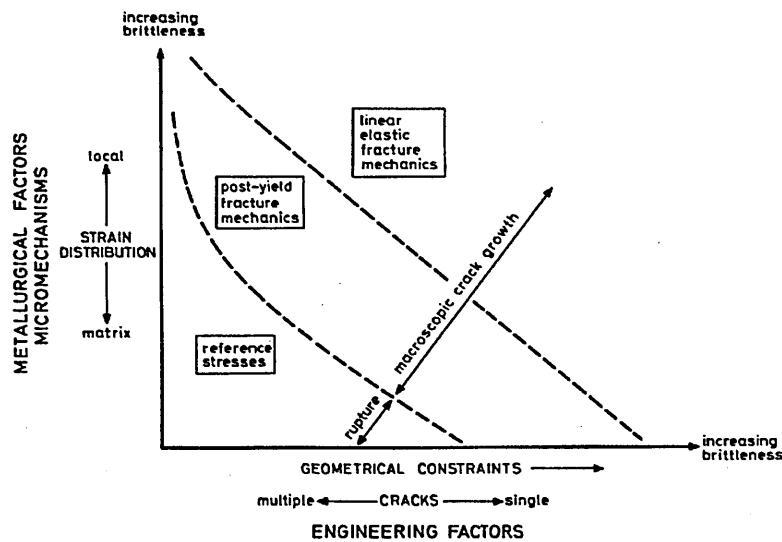


Figure 2.20: The factors that affect ductile-brittle creep behaviour - after Gooch and King ^[95].

The three regions of this diagram can be described as follows:

- i) The top right hand corner of the diagram portrays the creep brittle situation, where crack growth rates are commonly described by the use of *linear elastic fracture mechanics* (LEFM) ^[97] in the form :

$$\frac{da}{dt} = AK^n \quad \text{-Equation 2.4}$$

Where,

K = the linear elastic stress intensity factor

a = crack length,

t = time and

A and n = constants

The LEFM approach assumes that stress relaxation is slow in relation to crack growth rate and, hence, the stress and the displacement distribution are represented by K to a reasonable degree of accuracy.

- ii) The bottom left hand corner of the diagram represents the case where *reference stress*, σ_{ref} , can be used to assess the lifetime of a component by comparison with uniaxial creep rupture tests ^[98]. This approach assumes that stress relaxation by creep at the crack tip is rapid compared with crack growth in the same region and, hence, there is negligible stress concentration remaining ahead of the crack.
- iii) The intermediate region, represents all other cases where crack growth rates need to be calculated from time dependent fracture mechanics methods using C*, J or COD (crack opening displacement) parameters. These methods, the so called *post-yield fracture mechanics* methods ^[95] involve complex calculations to account for microstructural changes taking place with time.

The geometrical factors which affect the situation at the notch tip of the pre-existing defect have been defined by Haigh ^[99] by the equation:

$$\frac{K_{nom}}{\sigma_{ref} \sqrt{W}} = mY \quad \text{-Equation 2.5}$$

Where:

K_{nom} = nominal value of stress intensity

σ_{ref} = reference stress (equivalent stress level in a uniaxial test which causes failure in the same time)

W = specimen width

m = general yield ratio = $\left(\frac{\text{load to yield a cracked specimen}}{\text{load to yield an uncracked specimen}} \right)^{[100]}$

Y = compliance function = $\frac{KBW^{1/2}}{P'}$

and

B = specimen thickness

P' = applied load

Typical values of $\frac{K_{nom}}{\sigma_{ref} \sqrt{W}}$, shown for common specimen geometry's and plotted as a function of a/w (crack length / specimen width) in Figure 2.21, indicate that compact tension (CT) specimens exhibit the most brittle situation at the notch tip.

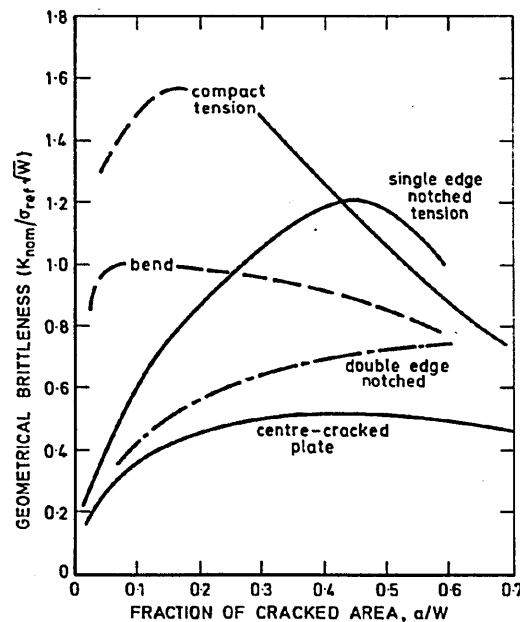


Figure 2.21: The effect of specimen geometry on brittleness in plane strain –after Gooch and King ^[95].

Materials operating in power plant predominantly fall into the intermediate regime of Figure 2.20, where the ductile microstructure allows the initially high crack tip stress to relax at the same time as the integrity of the structure is reduced. Haigh [7] has shown that in the situation where constraint is high, such as in the case of CT specimens, and the material is ductile then the C^* characterising parameter is valid and the reference stress can be re-written as shown in equation 2.6 for the plane stress situation:

$$\sigma_{ref} = \left(\frac{P}{m \cdot B \cdot W} \right) \quad \text{-Equation 2.6}$$

For the plane strain situation the equation is adapted to give equation 2.7:

$$\sigma_{ref} = \left(\frac{P}{m_{PL\epsilon} \cdot B_n \cdot W} \right) \quad \text{-Equation 2.7}$$

Where:

B_n = net specimen thickness

$m_{PL\epsilon} = -(1+1.702a/w) + (2.702+4.599(a/w)^2)^{1/2}$ [19]

Whether plane stress or plane strain conditions are operative at the crack tip will depend upon the degree of constraint; this constraint, in turn, will be dependent upon the test piece dimensions, notch geometry and creep deformation which accompanies fracture. The effect of specimen geometry on defect tip constraint has been studied by many authors and some of the factors observed are outlined below.

- i) Constraint increases with increased specimen thickness [94]
- ii) Constraint increases with the presence of side grooves [101]
- iii) Constraint increases as depth of side grooves increase [101]
- iv) Constraint varies with specimen geometry and is greatest for CT specimens [102] [103].
- v) Constraint varies with notch geometry and is higher for sharp notches than blunt notches [14].

In general, the greater the degree of constraint at the notch tip the more creep brittle the situation.

The microstructure can also have a powerful effect on creep brittleness / constraint as demonstrated by Gooch and King ^[95] who showed that an increase in the prior austenite grain-size of bainite increased the tendency to brittleness of a Cr-Mo-V steel as did an increase in the bainite content of a mixed ferrite / bainite structure.

The effect of triaxiality, defined as the ratio of the average of the radial, axial and tangential stresses to the Von Mises stress ^[104], on the deformation process of coupled creep and grain boundary diffusion was shown in a study by Sham and Needleman ^[105]. They reported that an increase in triaxiality from 0.33 – 4.0 resulted in an increase in the flow of matter from the cavity to the grain boundary but did not significantly alter the effective diffusion path lengths. This hypothesis was later discussed and developed by Van Der Giessen et al ^[106] who found that for higher triaxialities, >4.0, and in the presence of large voids, the diffusion path essentially vanishes since dislocation creep completely dominates. In a complex study by Maille ^[107] on the effect of multiaxiality on the creep deformation of 1%Cr-1%Mo steel, it was found that increasing the multiaxiality quotient resulted in a decrease in rupture strain and an increase in the severity of creep damage.

A recent study conducted by Frères and El-Magd ^[104] showed the influence of a multi-axial stress state on the behaviour of inter-crystalline creep microcracks. Tests carried out on circumferentially notched creep specimens showed that deep, sharp notches enhanced multiaxiality and stresses in the tangential and radial directions, leading to notch constraint and reduced cavitation density. Shallow, sharp notches enhanced the stress in the axial direction. A similar effect was noted by Molinie ^[108] who not only showed that cavity density decreased with increased triaxiality but also that the maximum damage occurred in the location of the principal stress axis.

2.5 Creep Failure Prediction and Remanent Life Assessment

The purpose of obtaining creep rupture data is to assess a particular material for service at elevated temperatures. The design code for components is usually based upon uniaxial creep rupture data and defines a maximum allowable stress which can exist in the structure for the required life at the operating temperature. Design codes give a conservative estimate of useful life and the actual life may not be expended in service, therefore, it is economically advantageous to be able to assess components in service and, where possible, extend their life. In service component assessment also avoids costly plant shutdown time due to unexpected failures.

A review of life assessment methods by Cane and Williams^[88] details two main approaches to this problem. The first method is based upon data taken during the operation of plant, for example temperature and pressure measurements and the second method is based upon periodic examination during plant shut-down, for example by crack detection, microstructural examination and strain analysis. For the purpose of the review, damage was considered to have occurred if the material life had been reduced by service. Damage characterisation was by assessment of the presence, size and distribution of cavities or second phase particles, the local softening of the material caused by exposure, or any other effect which reduced life under subsequent creep loading.

Additionally, life assessment techniques must be able to account for the situation where components are put into service containing pre-existing defects, such as in large castings, and in the main this is addressed by fracture mechanics concepts.

2.5.1 Creep Life Assessment of Initially 'Defect Free' Structures

Traditionally most creep rupture data for design purposes is obtained from uniaxial stress rupture tests which are carried out at higher stresses or

temperatures than those used in service. Long term rupture behaviour is then predicted by extrapolation of the short term data of test stress against a time temperature parameter, as described previously in section 2.3 .

Parametric equations have also been used in conjunction with life fraction rules in attempts to predict the creep behaviour of materials under variable stresses and temperatures ^[88].

The original life fraction rule put forward in 1952 by Robinson ^[109] suggested that for any series of stress and temperature conditions the life fractions could be linearly summed with failure occurring at unity.

$$\sum_x \frac{t_x}{t_{xf}} = 1 \quad \text{-Equation 2.8 ^[88]}$$

Where

t_x = time at stress σ_x and temperature T_x

t_{xf} = failure time at σ_x, T_x

This model assumed that material behaviour was independent of history, which was soon shown to be incorrect ^[110] when smaller specimens machined from a failed uniaxial creep specimen were found to have a reduced life on re-testing. Many variations of the rules have since been refined to account for the effects of material variability, multiaxial stresses and environmental effects and these have been rationalised by Grounes ^[111]. The most successful improvement to the life fraction time rules incorporates strain fractions ^[112].

$$\sum_x \frac{\epsilon_x}{\epsilon_{xf}} = 1 \quad \text{-Equation 2.9 ^[88]}$$

Where

ϵ_x = strain at stress σ_x and time t_x

ϵ_{xf} = failure strain at stress σ_x and t_{xf}

These methods are used in conjunction with creep models which simulate time dependent strain accumulation of materials under load at temperature and models have been developed to characterise the growth of creep cavities, wedge cracks and the formation of macroscopic cracks to ultimate failure. Such strain based methods require disciplined monitoring and ensuring that the measurements taken are representative of the component as a whole is difficult. Microstructural examination can provide useful supporting information and studies have been carried out to correlate creep strain with quantitative microstructural damage.

Creep strain data generated under accelerated test conditions can provide residual life estimates if a model can be developed relating creep strain, ϵ , or strain rate, $\dot{\epsilon}$, to creep life, t_r . To determine remaining lifetime by microstructural examination predictive models are required that relate the relevant damage feature to the life fraction.

The important mechanisms of microstructural damage that must be considered for such a model, and their relationship to strain rate, have been reviewed and defined quantitatively by Dyson and McLean ^[113]. The so-called, physically based 'continuum damage mechanics' (CDM's) equations, as defined in Table 2.3, are all related to strain rate as a function of applied stress, σ , temperature, T , hardening parameter, H and a damage parameter, D .

The use of advanced computer systems allows the various contributions to creep deformation, in the form of CDM parameters, to be assessed both individually and concurrently resulting in a very powerful tool for life assessment. Of particular relevance to the current study is the use of data based on the microstructural aspects of cavity nucleation and growth together with the carbide evolution process.

Several methods have been used to quantify creep damage by the process of cavitation. These methods include the use of parameters, such as A_1 , A_2 and A^* ^[114], that quantify the number of cavitating grain boundaries on, or in the vicinity of, a reference line, and those due to observations based on a visual classification scheme, such as that derived by Neubauer and Wedel ^[115]. In a

study by Sandstrom ^[116] the creep damage classes of Neubauer and Wedel were related to a measure of physical damage in order to allow a direct estimation of remaining life and a suggested time scale for the next plant inspection.

The observation of the changing microstructure in power plant steels has often been proposed as a useful mechanism for estimating the remaining life of a component ^{[117] [118] [119] [120]}. In particular the composition of the evolving carbides has been used to predict the onset of failure by tertiary creep. An example of such a study is that of Sugita ^[120] who found that in the heat affected zone of a 2.25%Cr-1%Mo steel sample, creep voids formed when the equilibrium carbide M_6C was present in volume fractions >60%.

Pioneering work by Bhadeshia et al ^{[34] [37] [121] [122]} has shown that the microstructural evolution process in power plant steels can be predicted using a computer programme called MTDATA ^[36], as mentioned previously in section 2.2.2, from a knowledge of chemical composition and relevant transformation kinetic equations. Knowing the time to reach a particular microstructural maturity, allows components to be assessed by periodic microstructural assessment for suitability for extended service. For example an accurate means of determining data by the predictions of Bhadeshia et al could negate the need for long term creep rupture testing as used in the studies on Cr-Mo steels by Dobrzanski and Hernas ^[103]. In this latter study the influence of phase constitution and damage process was linked to residual life time, as described in Figure 2.22 and Table 2.4.

CREEP DAMAGE CATEGORY	DAMAGE MECHANISM	DAMAGE PARAMETER D	DAMAGE RATE \dot{D}	STRAIN RATE $\dot{\epsilon}$
Strain-Induced	Cavity Nucleation Control; Growth Constrained	$D_n = \frac{\pi d^3 N}{4} = \omega$	$\dot{\omega} = \frac{k_s}{\epsilon_s} \dot{\epsilon}$	$\dot{\epsilon} = \dot{\epsilon}_0 \sinh \left[\frac{\sigma(1-H)}{\sigma_0(1-\omega)} \right]$
	Cavity Growth Controlled by Creep-Constrain	$D_c = \frac{\pi d^3 N}{4} = \omega$ $D_c = \left(\frac{r}{l} \right)^2$	$\dot{\omega} = 0$ $\dot{D}_c = \frac{d}{2lD_0} \dot{\epsilon}$	$\dot{\epsilon} = \dot{\epsilon}_0 \sinh \left[\frac{\sigma(1-H)}{\sigma_0(1-\omega)} \right]$
	Dynamic Subgrain Coarsening	$D_g = 1 - \left(\frac{r_{sub}}{r_g} \right)$	$\dot{D}_g = (1 - D_g) \frac{\dot{\gamma}}{r_g}$?
Thermally-Induced	Multiplication of Mobile Dislocations	$D_d = 1 - \frac{\rho_i}{\rho}$	$\dot{D}_d = C(1 - D_d)^2 \dot{\epsilon}$	$\dot{\epsilon} = \frac{\epsilon_0}{(1 - D_d)} \sinh \left[\frac{\sigma(1-H)}{\sigma_0} \right]$
	Particle-Coarsening	$D_p = 1 - \frac{\rho_i}{\rho}$	$\dot{D}_p = \frac{K_p}{j}(1 - D_p)^4$	$\dot{\epsilon} = \dot{\epsilon}_0 \sinh \left[\frac{\sigma(1-H)}{\sigma_0(1-D_p)} \right]$
Environmentally-Induced	Depletion of solid-solution elements	$D_s = \beta \phi_p$	$\dot{D}_s = K_s D_s^{1/2} (1 - D_s)$	$\dot{\epsilon} = \frac{\dot{\epsilon}_0}{(1 - \beta D_s)} \sinh \left[\frac{\sigma(1-H)}{\sigma_0} \right]$
	Fracture of Surface Corrosion Product	$D_{cor} = \frac{2x}{R}$	$\dot{D}_{cor} = \frac{1}{R} \left(\frac{K_{cor}}{e^{x/R}} \right)^{1/2}$	$\dot{\epsilon} = \dot{\epsilon}_0 \sinh \left[\frac{\sigma(1-H)}{\sigma_0(1-D_{cor})} \right]$
	Internal Oxidation	$D_{ox} = \frac{2x}{R}$	$\dot{D}_{ox} = \frac{K_{ox}}{R^2 D_{ox}}$	$\dot{\epsilon} = \dot{\epsilon}_0 \sinh \left[\frac{\sigma(1-H)}{\sigma_0(1-D_{ox})} \right]$

Table 2.3: Creep damage categories, mechanisms and incorporation into continuum damage mechanics equations – after Dyson and McLean [113].

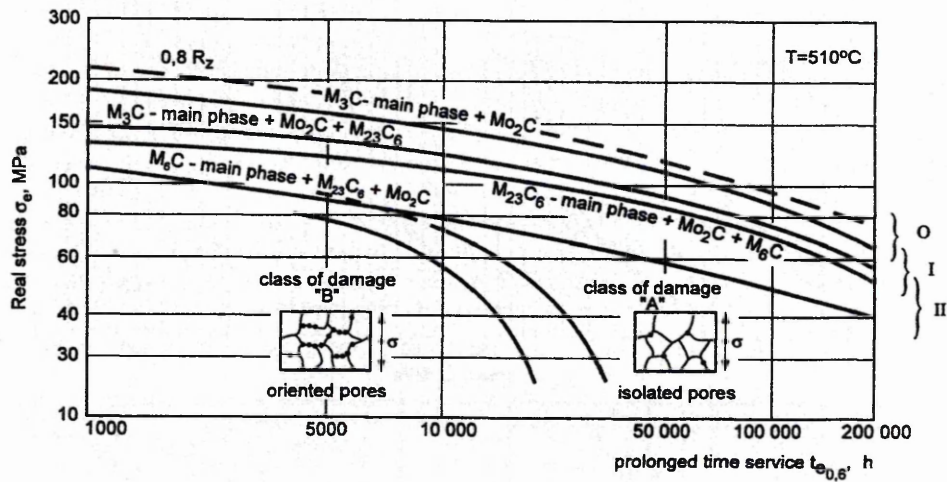


Figure 2.22: Influence of phase constitution and damage process on safe residual lifetime of 1Cr-0.5Mo steel - after Dobrzanski and Hernas [103].

Pearlite/Bainite decomposition	Precipitation processes	Processes of damage	The main class of microstructure	Exhausted creep life fraction t/t_c
0	0	0	0	0.1
I			1	0.2
I	a		2	0.3
I	a	A	3	0.4
II	b	B	4	0.5
II	b	C	5	0.6
II	b	D	6	0.7
II	b		7	0.8
II	b			0.9
II	b			1.0

Table 2.4: Classification of damage process and exhausted creep life - after Dobrzanski and Hernas ^[103].

2.5.2 Creep Life Assessment Of Structures Containing Pre-existing Defects

If a component has been put into service containing a pre-existing defect, as described in section 2.4.3, then it is likely that failure will occur before that anticipated by the routine examination of microstructure or even strain. To ensure safe operation, therefore, it is necessary to detect any pre-existing defects and assess the likelihood of them growing to an unacceptable size. Effective procedures for defect assessment and remanent life prediction of power plant components have been developed in recent years ^{[10] [18] [94] [123]} based on fracture mechanics concepts and an understanding of material creep ductility.

It has been recognised that when a component containing a defect is loaded in creep, there will be a period of stress redistribution at the defect tip prior to crack growth and that this process could occupy a considerable period of the component lifetime, that is, there will be a period of crack incubation ^{[124] - [126]}. The life of a structure operating under creep conditions, therefore, may be regarded as comprising two components ^[11] as reflected in equation 2.10:

$$t_f = t_i + t_g \quad \text{-Equation 2.10}$$

Where:

t_i = time to initiate a crack

t_g = time to grow the crack to failure

Immediately after loading, in the absence of plastic deformation, the stress distribution ahead of the crack tip will be defined by the elastic stress intensity factor, K . With time creep will cause stress redistribution until a steady state condition is reached which can be described by the fracture mechanics parameter, C^* . The creep strain rate, $\dot{\epsilon}$, and rupture life, t_r , properties of a material can be expressed in terms of stress, σ as :

$$\dot{\epsilon} = \dot{\epsilon}_0 \left(\frac{\sigma}{\sigma_0} \right)^n \quad \text{-Equation 2.11}$$

and

$$t_r = \frac{\epsilon_{f0}}{\dot{\epsilon}_0} \left(\frac{\sigma_0}{\sigma} \right)^\nu \quad \text{-Equation 2.12}$$

Where

$\dot{\epsilon}_0$ = strain rate in uniaxial creep

ϵ_{f0} = uniaxial creep failure strain at a stress of σ

n = creep exponent

ν = Poisson's ratio

The time taken for this stress distribution to be complete, t_T , is given by ^[40]:

$$t_T = \frac{G}{(n+1)C^*} \quad \text{-Equation 2.13}$$

Where

G = the elastic strain energy release rate.

C^* = steady state crack tip parameter.

According to Webster et al ^[10], this time is usually a small fraction of the component lifetime and it is found that creep crack growth rate, \dot{a} , can be correlated satisfactorily in terms of C^* by the relationship:

$$\dot{a} = D_0 C^{*\phi} \quad \text{-Equation 2.14}$$

Where, D_0 and ϕ are material constants which can be determined by equations 2.15 and 2.16 respectively:

$$D_0 = \left(\frac{n+1}{n+1-\nu} \right) \frac{\dot{\epsilon}_0}{\epsilon_{f0}} \left(\frac{1}{I_n \sigma_0 \dot{\epsilon}_0} \right)^{\frac{\nu}{n+1}} r_c^{\frac{n+1-\nu}{n+1}} \quad \text{-Equation 2.15}$$

and

$$\phi = \frac{\nu}{n+1} \quad \text{-Equation 2.16}$$

Several broadly compatible models relating creep crack growth to C^* have been postulated ^{[94] [127] [128] [129]}. When C^* has been shown to predict the stress situation ahead of a crack tip the following general equation can be used to relate crack growth rate to C^* :

$$\dot{a} \propto C^{*\phi} \quad \text{-Equation 2.17}$$

Where

\dot{a} = crack growth rate

ϕ = fraction close to unity

Nikbin et al ^[94] derived an equation of this form for a ductile 2.25%Cr-1%Mo steel CT specimen at 538°C as follows:

$$\dot{a} = \frac{3 C^{*0.85}}{\epsilon^* f} \quad \text{-Equation 2.18}$$

Where

ε_f^* = creep ductility at the crack tip as a fraction

(for plane stress $\varepsilon_f^* = \varepsilon_{10}$ and for plane strain $\varepsilon_f^* = \varepsilon_{10}/50$ where ε_{10} is the uniaxial creep ductility).

A subsequent study by Wang and Wu ^[101] based on the $\dot{a}-C^*$ relationship of Nikbin et al, showed that the relationship is temperature dependent for 2.25%Cr-1%Mo steel as indicated below:

$$\dot{a} = \frac{4C^{*0.85}}{\varepsilon_f^*} \quad \text{at } 550^\circ\text{C} \quad \text{-Equation 2.19}$$

and

$$\dot{a} = \frac{4.93C^{*0.85}}{\varepsilon_f^*} \quad \text{at } 565^\circ\text{C} \quad \text{-Equation 2.20}$$

In this study the Kubo ^[130] form of the C^* equation was used for CT specimens where:

$$C^* = \frac{2n}{n+1} \cdot \frac{P'\dot{\Delta}}{B(W-a)} \quad \text{-Equation 2.21}$$

and

n = creep exponent

P' = applied load

$\dot{\Delta}$ = load point displacement

In a review of aspects relating to the initiation and early growth of creep cracks from pre-existing defects by Holdsworth ^[11] it was pointed out that equation 2.10 depends to a large extent on the increment of crack extension, Δa_i , adopted as the definition of crack initiation (x_c). For example, as shown in Figure 2.23, it was shown that the time to generate the critical displacement necessary to initiate a micro-crack, for example $x_{c[1\mu\text{m}]}$, was significantly less than the time to develop a macro crack, for example $x_{c[1\text{mm}]}$. The advantages and disadvantages of the crack initiation criteria adopted were discussed and overall it was considered that a macro-crack criterion of $>0.5\text{mm}$, had the most benefits.

If the minimum crack extension that can be resolved is Δa then the incubation period, t_i , is given by ^[126]:

$$t_i = \int_0^{\Delta a} \frac{dr'}{\dot{a}_i} \quad \text{- Equation 2.22}$$

Where

t_i = incubation period

r' = radius of damage zone

\dot{a}_i = crack growth rate

An upper bound t_i can be obtained by replacing \dot{a}_i in this equation with \dot{a}_0 and a lower bound by replacing it with the steady state crack growth rate ^[10] giving:

$$t_{iL} = \frac{\Delta a}{D_0 C^{*\phi}} \quad \text{- Equation 2.23}$$

Alternatively, when the approximate growth relation is used, equation 2.23, it becomes:

$$t_{iL} = \frac{\Delta a \varepsilon_f^*}{3C^{*0.85}} \quad \text{- Equation 2.24}$$

The critical crack tip opening displacement, δ_{ix} , is an important parameter for characterising the creep crack initiation resistance of a material. Conventionally, in the laboratory tests of CT specimens, it is only the crack opening displacement at the load line which is measured ^[131] and this does not always convey accurately the situation at the notch tip. An alternative method has been proposed by Holdsworth and Cunnane ^[19] that accurately assesses the actual notch tip displacement and is based on the displacement measurement of hardness indentations placed either side of the notch and pre-crack in the CT specimen as shown in Figure 2.24.

As reported by Holdsworth ^[132], deformation and crack development are strongly influenced by the creep ductility in the alloy. Crack initiation occurs in creep brittle materials on the attainment of a relatively low crack tip opening displacement, δ_{ix} , Figure 2.25a, whereas in creep ductile materials relatively large δ_{ix} values, Figure 2.25b, are required to initiate cracking with the onset of cracking occurring later in life.

Based on the above knowledge and relationships developed for crack initiation and growth, defect assessment procedures have now been developed ^{[10] [18]} and are in use to monitor in service operation of power plant components.

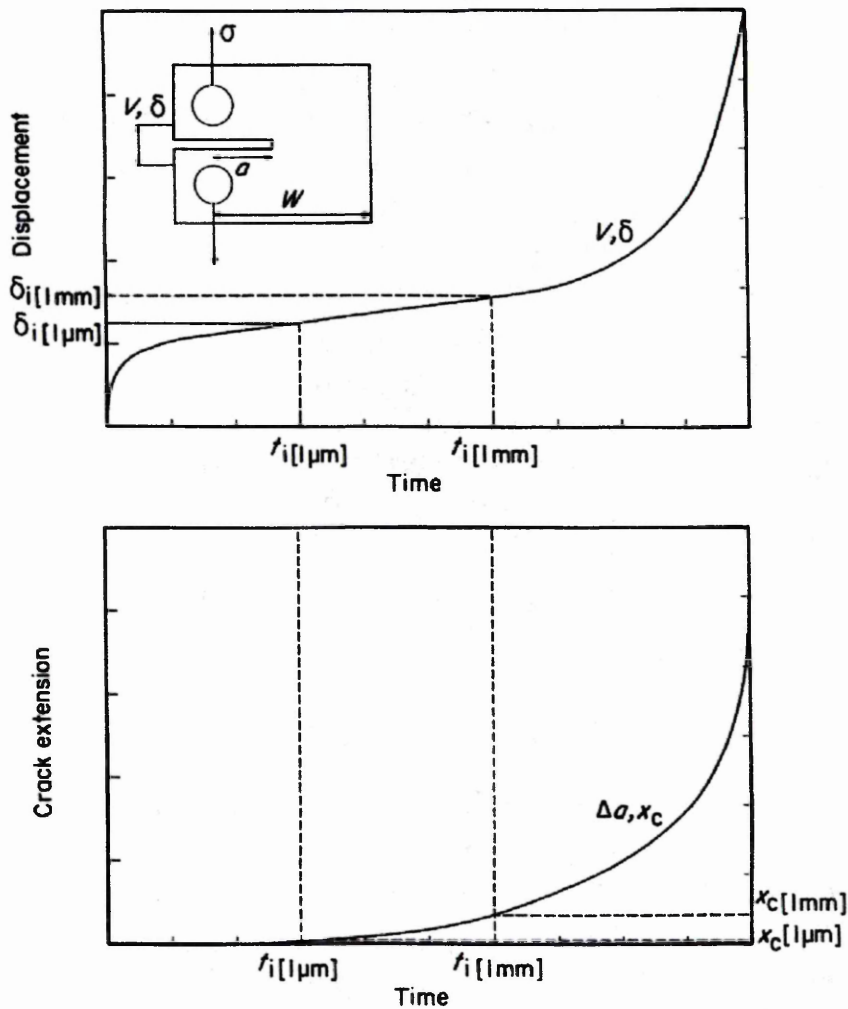


Figure 2.23: Variation of crack opening displacement and crack length in a fracture mechanics specimen indicating the importance of specifying crack initiation criteria – after Holdsworth ^[11].

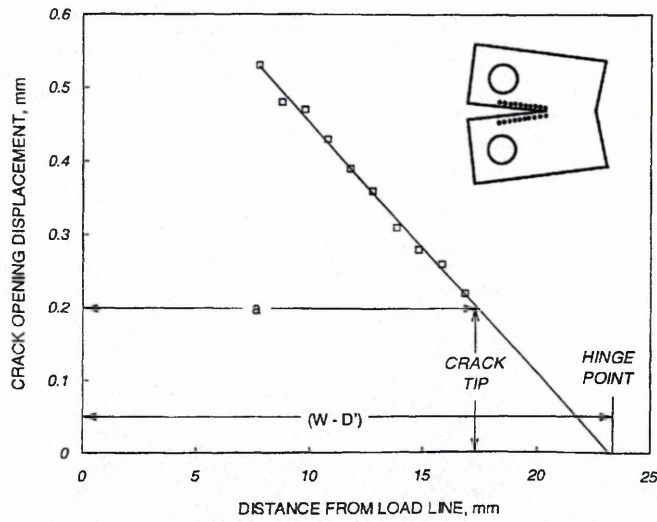


Figure 2.24: Derivation of δ_{ix} using hardness indentations – after Holdsworth [132]

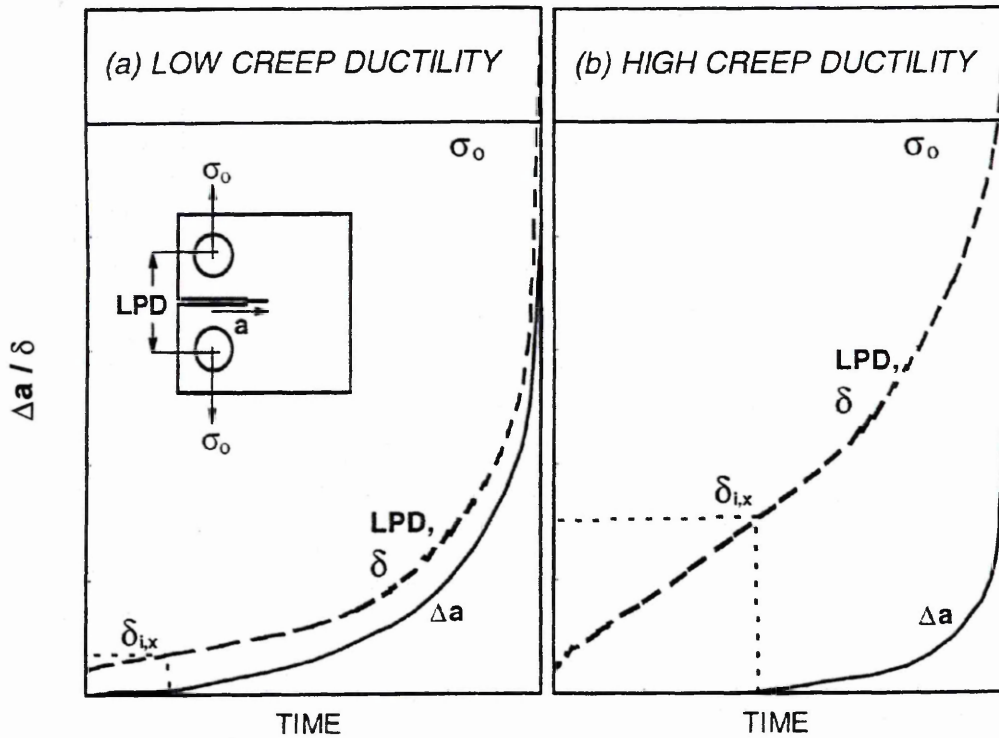


Figure 2.25 a & b: Influence of creep ductility on crack opening displacement and growth behaviour in a fracture mechanics test piece subject to steady load at high temperature, a) brittle 0.5%Cr-0.5%Mo-0.25%V HAZ, b) ductile 2.25%Cr-1%Mo weld metal – after Holdsworth [132].

2.5.3 Microstructural Investigation Techniques For Creep Life Prediction Methods

To ensure accuracy of information from quantitative microstructural analysis for remanent life assessment it is essential that the techniques used are standardised and reproducible. In particular this relates to methods based on damage parameters such as quantification of creep cavitation and microstructural maturity.

Cavitation damage may be assessed from laboratory and in service components by three main techniques:

- i) Direct replication ^[133]
- ii) Extraction replication ^[134]
- iii) Bulk sample examination

For each of the techniques the quality of preparation of the material surface is of paramount importance to ensure faithful results. In a study by Silveira and May ^[135], based on the Neubauer and Wedel ^[115] cavitation classification scheme, the sensitivity of the final classification to sample surface preparation was analysed. Prolonged polishing or repeated polish – etch cycles were shown to exaggerate the degree of creep cavitation by the pull out of matrix or precipitates at damage centres along grain boundaries. It was concluded that the extent of creep damage and hence the prediction of remaining life should not be based purely upon the quantitative measurements of cavities and micro-cracks observed but also on an appreciation of the distribution of the damage centres disclosed. A surface preparation procedure using a minimum of three final stage polish – etch cycles was proposed to define, unequivocally, the presence or absence of creep damage.

In a related study by Samuels et al ^[136] extended etching was found to widen cavities that had opened up at grain boundaries perpendicular to the applied stress in uniaxial creep specimens. It was noted, however, that etching did not in itself generate any new cavities.

As discussed in section 2.5.1 the evaluation of carbide morphology may be used to assess the fraction of lifetime remaining in a component operating in a creep environment. To avoid removal of bulk samples from components, necessitating costly weld repair, a technique for generating extraction replicas has been devised by Corti et al ^[134]. In a study by the same authors on extraction replicas taken from steam headers in 2.25%Cr-1%Mo steel, EDX analysis was used, in the mode of Titchmarsh ^[137] ^[138] and Li ^[139], to identify the morphological carbide types and relative Cr/Fe ratios. A linear correlation between the Cr/Fe ratio in M₂₃C₆ carbide and the cube root of exposure time was obtained for steam pipes service exposed at 540°C for up to 160,000 hours, that is:

$$\text{Cr/Fe} = 0.33362 + 0.01516t^{1/3} \text{ -Equation 2.25}$$

In the original work by Titchmarsh ^[137] it was emphasised that to uniquely identify carbide on the basis of EDX analysis, the carbides types must first be established, for the specific composition and heat treatment, by electron diffraction.

Chapter 3.0

Experimental Procedures

3.1 Introduction

2.25%Cr-1%Mo alloy steel is a microstructurally complex alloy, that is generally put into service in a meta-stable condition. At elevated temperatures, the carbides present evolve with time, and in so doing change the response of the alloy to the processes of creep. The inter-relationship between microstructure and creep behaviour is complex. In the presence of a pre-existing defect, the carbide ripening process and hence the creep response may, for example, be affected by the stress intensity developed at the defect tip. To improve the lifetime of a component by controlling its initial microstructure, or to predict the remanent life, it is therefore essential to fully understand the role of the carbides in the process of creep and the effect that carbide ripening has on this process during service.

The microstructure of 2.25%Cr-1%Mo alloy steel may vary according to the prior heat treatment to which it has been subjected. In large heat-treated components, the microstructure may also vary through the cross-section, due to the differential response to heating and cooling. In general, commercial alloys tend to exhibit three different types of microstructure, namely:

- i) mixed pro-eutectoid ferrite + pearlite
- ii) mixed pro-eutectoid ferrite + bainite and
- iii) a tempered, fully bainite structure.

The purpose of this investigation has been to obtain a detailed understanding of the effect of each of these microstructural profiles, and their subsequent evolution at elevated temperature, on the creep initiation process ahead of a defect, in samples of 2.25%Cr-1%Mo alloy steel. The experimental work progressed in three stages, as explained in outline below:

(a) Characterisation of the starting material:

The first requirement of the investigation was to obtain a full understanding of the microstructural profile of the as received starting material, prior to creep deformation.

Two commercial sources of 2.25%Cr-1%Mo steel alloy, with different thermo-mechanical histories were obtained for this work. These are described in detail in section 3.2. The microstructure of one consisted of a mixture of pro-eutectoid ferrite and pearlite, while that of the other contained pro-eutectoid ferrite and bainite, thus providing representative examples of microstructure (i) and (ii) above. Material with a 100% bainite structure was obtained by heat treatment of the as-received material and subsequently tempered to produce microstructural type (iii) - see section 3.3.

Samples of all three microstructural variables were subjected to microstructural analyses and investigation of their basic mechanical properties. These materials eventually provided the samples on which detailed studies of creep behaviour were carried out.

(b) The tempering characteristics of fully bainitic 2.25%Cr-1%Mo steel:

Exposure of the bainite phase to elevated temperatures results in a dispersion of carbides, which progressively coarsen and evolve with time. To facilitate a comparison with microstructural changes during subsequent creep tests, when there is the added complication of both external and localised internal stresses, a tempering trial on samples initially with the fully bainitic microstructure, was carried out.

The tempered samples were investigated using scanning electron and scanning transmission electron microscopy techniques - see section 3.6. A major part of this work involved the development of an image analysis procedure to aid the interpretation of the carbide evolution process. A thorough understanding of the complex processes involved in carbide precipitate development in this alloy, was thus obtained.

(c) Creep testing and investigation:

A mechanical testing rig, described in section 3.4, was designed and built to accommodate suitable test specimens, in order to generate samples of the steel exhibiting creep damage initiation features, ahead of a pre-existing

defect. The test rig design allowed a number of compact tension (CT) type specimens, each containing a fine spark machined notch, to be creep tested at the same time, under controlled test conditions. After pre-designated time intervals, a specimen was removed from test and the microstructure developing ahead of the notch, assessed for evidence of creep damage.

Scanning electron microscopy was used to assess the extent of creep damage in terms of void formation and flaw/crack extension. Crack extension was measured using a linear measuring device in the microscope and the area percentage of voids and void orientation, was determined with the aid of an image analysis routine, specially devised for the purpose of this project. These techniques are described in section 3.6.

To assess the affect of the pre-existing defect and subsequent crack propagation, on the carbide ripening and creep damage initiation mechanisms, an in depth analysis of the carbide morphology was necessary. A study of the carbide precipitates in the defect tip region was made possible by devising a technique for selectively extracting the carbides from the area of interest and analysing them in a transmission electron microscope using energy dispersive X-ray analysis as detailed in section 3.6.

3.2 Raw Materials

Samples of 2.25%Cr-1%Mo steel, exhibiting the three different microstructural profiles identified below, were required for the investigation:

- i) mixed pro-eutectoid ferrite + pearlite,
- ii) tempered mixed pro-eutectoid ferrite + bainite and,
- iii) tempered 100% bainite.

The raw material for this work was supplied by courtesy of the collaborating establishment Alstom Energy, UK. Ltd. The material came from two sources, namely:

- a) cast and heat treated round bar, and
- b) wrought and then heat treated steel pipe.

The composition of each is presented in Table 3.1.

The bulk of the material supplied came from source (a). This consisted of 87mm diameter x 465mm long round bars, extracted from trepanned out bolt holes in the flange of a high quality, cast and heat-treated, steam turbine generator casing. The heat treatment schedule to which it had been subjected is summarised in Table 3.2, producing a microstructure consisting of pro-eutectoid ferrite and tempered bainite. This, therefore, provided the source of all sample material with this microstructural profile. To avoid any end effects due to the casting / heat treatment processes, 50mm was discarded from the end of each of the trepanned bars supplied.

Source (b) provided a lesser amount of material, supplied in the form of micro-specimens extracted from creep tested compact tension, (CT), specimens. These had previously been machined from 74mm wall thickness x 419mm outside diameter, wrought and then heat-treated steam pipe. This material, during manufacture, had finally been subjected to a full annealing treatment at 960°C, followed by furnace cooling to room temperature. This produced a microstructure consisting of pro-eutectoid ferrite and pearlite and thus provided the source of all sample material with this microstructural profile.

Material Source	Element (mass %)						
	C	Si	Mn	P	S	Cr	Mo
(a) Casting	0.11	0.35	0.59	0.006	0.005	2.34	1.00
(b) Steam Pipe	0.13	0.29	0.54	0.026	0.028	2.31	0.96

Table 3.1: Composition of as-received material .

Material Source	Heat-treatment
(a) Casting	Normalised at 960°C and then air cooled + Temper for 12 hours at 705°C and then furnace cooled + Stress relieve at 700°C for 12 hours and furnace cooled.
(b) Steam Pipe	Annealed at 960°C and furnace cooled.

Table 3.2: Final commercial heat-treatment of as-received material.

3.3 Heat Treatment

Heat treatment procedures were necessary for two areas of investigation in the research programme:

- a) To produce material with a microstructure consisting of a 100% bainite from which creep test specimens could be machined and,
- b) To produce samples with a 100% bainite structure and subsequently study the affect of tempering temperature and time on the carbide evolution process.

In all cases, the heat-treatment procedures were carried out in a Carbolite muffle furnace, controlled by an in-situ chromel-alumel thermocouple and Eurotherm 808 temperature controller to a nominal accuracy of 0.25% x temperature of reading. The temperature distribution profile of the furnace chamber was established using a chromel-alumel type thermocouple, in conjunction with a cold junction corrected Fluke digital temperature recorder.

3.3.1 Production of 100% Bainite CT Creep Test Specimens

The cast and trepanned bar, from source (a) identified in section 3.2, was used as the starting material for manufacturing CT specimen blanks with dimensions of 48mm x 45mm x 19mm. In order to protect them against oxidation during heat treatment, all specimens were coated with Birkatec paint.

Consideration of the relevant continuous cooling transformation diagram, presented in Figure 3.1, for the CT blank dimensions, indicated the necessary cooling conditions, following austenitising, to achieve a 100% bainitic structure. Austenitisation was achieved by soaking each blank at 960°C for one hour, followed by air cooling to room temperature to produce a fully bainite structure. The blanks were subsequently tempered at 700 °C for 24hours, followed by air cooling to room temperature.

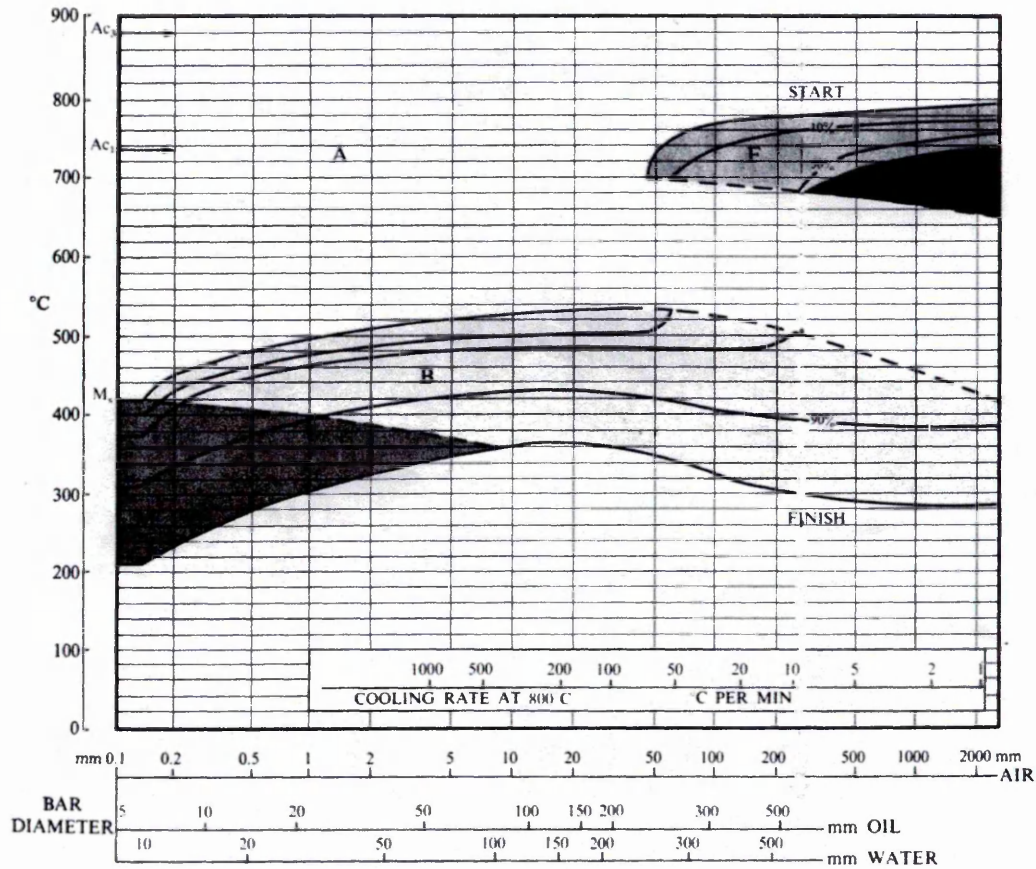


Figure 3.1: The continuous cooling transformation diagram for a 2.25%Cr-1.0%Mo steel – after M. Atkins ^[140].

3.3.2 Bainite Tempering Investigation

Specimens for the tempering studies were obtained from CT test piece blanks, following austenitising at 960°C for one hour and air cooling to room temperature. The fully bainite blanks were then cut into 29mm x 16mm x 19mm samples, illustrated in Figure 3.2, for the tempering investigation.

All samples were again coated in protective Birkatec paint. Tempering was carried out at temperatures of 650°C, 700°C and 750°C for periods of 0.5, 1.0, 5.0, 10, 25, 50 and 100 hours, followed by air-cooling to room temperature. In addition, two specimens were heat treated at 700°C for 1000 and 5000 hours.

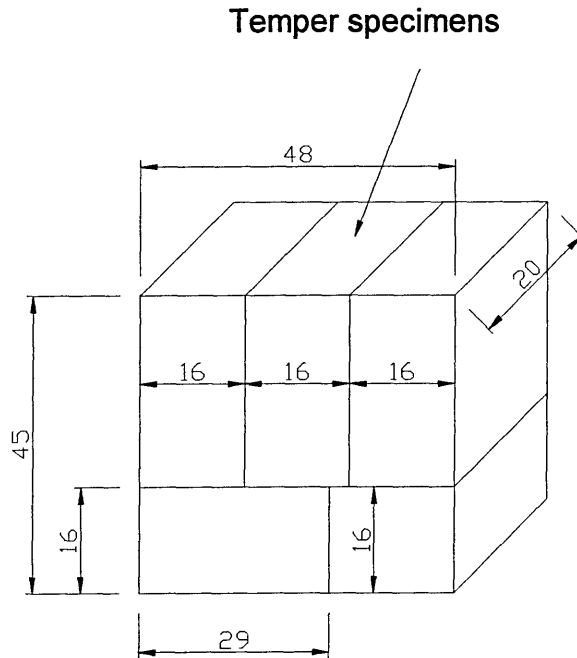


Figure 3.2: Plan for sectioning of bainite tempering samples from CT blank (48 x 45 x 20mm).

3.4 Mechanical Testing

3.4.1 Hardness Tests

Hardness measurements were made using a Vickers hardness testing machine. A pyramidal diamond indenter of angularity 136° , was employed with a 20kg applied load, on specimens previously prepared to a 600 SiC grit surface finish.

The hardness value was determined by measuring the diagonals of the indentation using a calibrated ocular micrometer scale and then converting the average of the two orthogonally opposite diagonals, using a conversion chart, to obtain a Vickers hardness number.

To ensure accuracy a Vickers certified hardness machine was used and a calibration test block was checked immediately prior to testing, in accordance with BS427 (1990).

3.4.2 Tensile Tests

To gain an appreciation of the general properties of the materials under consideration, tensile specimens, 10mm² in cross-sectional area, were machined and submitted to a NAMAS approved test house for the determination of their tensile properties at both room temperature and at 550°C. The properties determined were the Young's modulus, 0.2% proof stress, ultimate tensile strength and percentage elongation.

3.4.3 Creep Deformation Tests

The main purpose of this programme of work was to study the mechanism of creep initiation in the presence of a pre-existing defect, in the nominated microstructures of interest, and to correlate this information with critical crack tip opening displacement (CTOD) data.

To facilitate these aims, it was decided to subject a series of ¾ size CT specimens, each with a spark eroded notch <0.2mm in width, to a pre-determined creep load and test temperature of 550°C, and to interrupt the tests to microstructurally examine the crack tip region after various time intervals.

3.4.3.(a) Creep Test Rig Design

In order to reduce the experimental error, due to temperature fluctuations, and maximise the number of specimens available for examination, a test rig and

furnace were designed to accommodate four CT specimens in series to fit an existing ESH 50kN capacity creep testing machine.

A schematic diagram of the test rig designed for this project is shown in Figure 3.3.

The test rig incorporated a three zone split furnace of sufficient size to accommodate four ¾ size CT specimens. The furnace was supported on a wrought aluminium alloy frame. The key dimensions of the furnace were as follows:

Internal bore diameter = 90mm

Centre hot zone length = 350mm

Top and bottom heating zones = 100mm

The furnace was controlled by three Eurotherm 808 temperature controllers to a claimed accuracy of 0.25% x temperature of reading, i.e. $\pm 1.37^{\circ}\text{C}$ for a furnace setting of 550°C . In addition to the furnace control thermocouples, three external chromel-alumel, type k, thermocouples were also positioned inside the furnace tube to monitor the actual temperature of the specimens during the tests.

The specimens were linked together and to the loading bars of the creep machine by shackles, pins and bars heat treated and machined, specifically for this project, from the following nickel based Superalloys:

Loading Bars : Nimonic 80A - heat treated at 1080°C for 8 hours, air cooled, machined and then heat treated at 705°C for 16 hours and finally air cooled.

Loading Pins : Nimonic 115 - heat treated at 1190°C for 1.5 hours, air cooled, machined and then heat treated at 1100°C for 6 hours and finally air cooled.

Loading Shackles : PK 33 - heat treated at 1100°C for 2 hours, air cooled, machined and then heat treated at 850°C for 4 hours and finally air cooled.

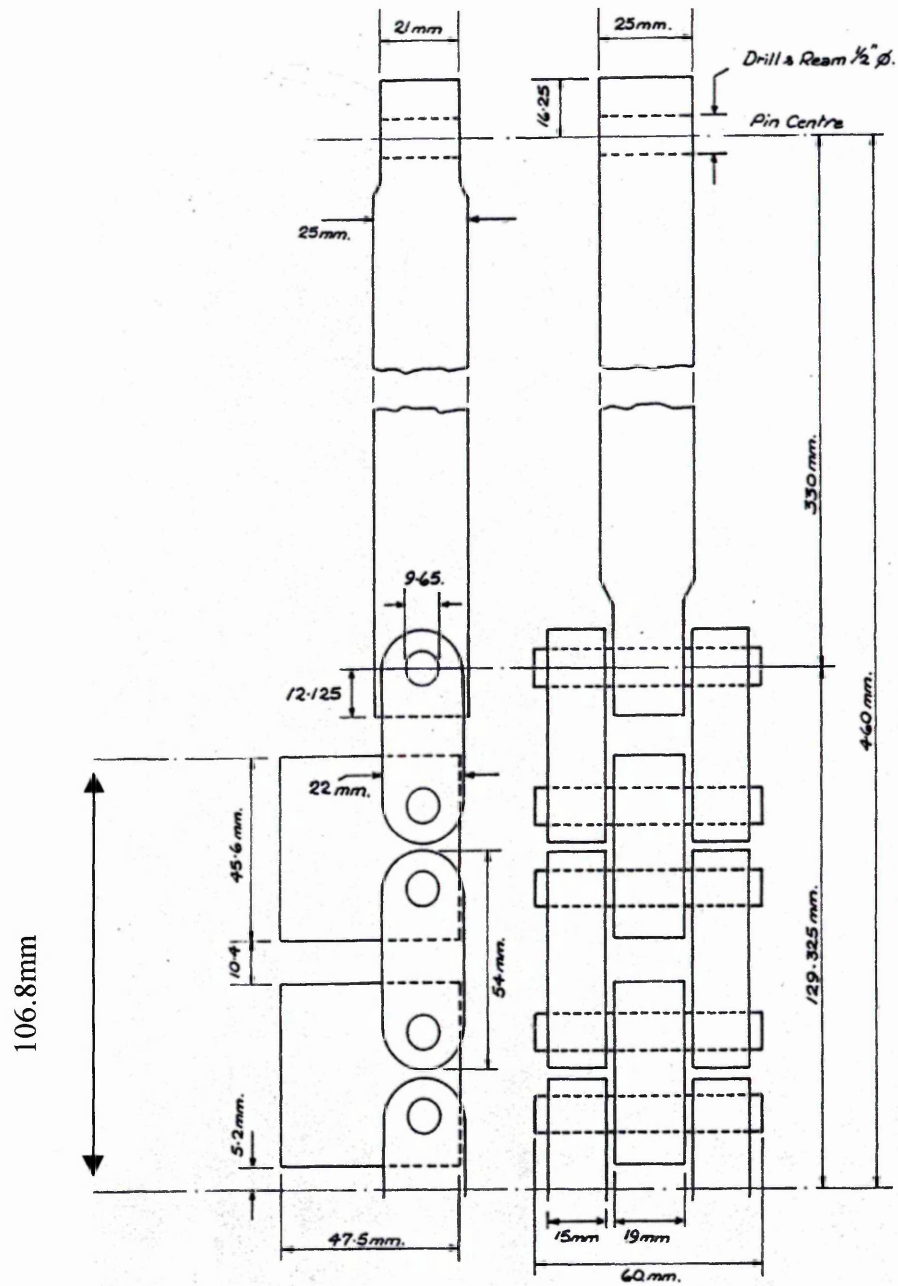
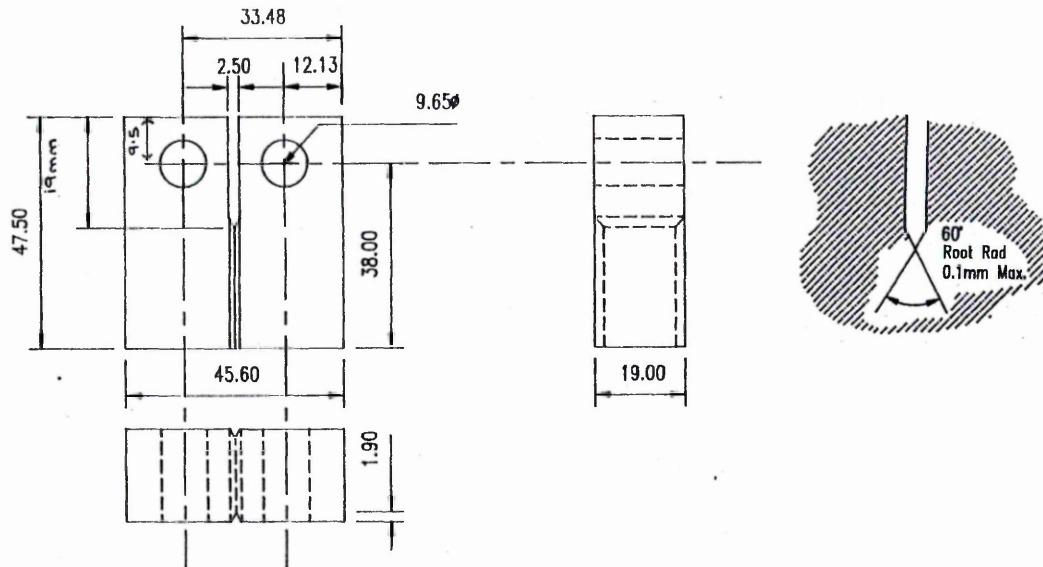


Figure 3.3: Creep test rig design.

3.4.3(b) Creep Test Specimens and Loading Regime.

Three quarter scale compact tension specimens were selected for the CTOD/creep testing programme. The specimens were machined to the dimensions given in BS5477:1977 and are depicted schematically in Figure 3.4.



Width, $W = 38\text{mm}$

Total thickness, $B = 19\text{mm}$

Depth of side grooves = 1.9mm on each side

Nominal thickness, $B_n = 15.2\text{mm}$

Effective crack length, $a = 11.4\text{mm}$

Figure 3.4: Schematic diagram of CT specimen and dimensions.

To simulate the presence of a defect in the specimen, the final 1.9mm of the effective crack length was machined by spark erosion, using a copper wire electrode 0.2mm in diameter.

The applied stress for the tests was based upon the plane strain reference stress criteria, σ_{ref} , as described in section 2.4.3 of the literature review, and applied to the CT specimens by the use of equation 3.1.

$$\sigma_{ref} = \frac{P}{m_{pl\epsilon} B_n W} \quad \text{- Equation 3.1}$$

Where

P = applied load

$m_{pl\epsilon}$ = yield ratio in plane strain

B_n = net specimen thickness after side grooving

W = specimen width

and,

$$m_{pl\epsilon} = - (1+1.702 a/W) + (2.702 + 4.599 (a/W)^2)^{1/2}$$

In the initial absence of any unidirectional creep testing data specific to the three microstructural profiles identified for 2.25%Cr-1%Mo steel in this project the loading conditions for the test specimens were initially based upon $\sigma_{pl\epsilon}$ values reported by The Creep of Steels Working Party Of Institution Of Mechanical Engineers^[141] for this alloy.

The ferrite / pearlite specimens, tested at Alstom Energy, UK. Ltd., were tested at a stress level of 85MPa, predicted to give failure in ~10,000 hours, whereas the stress values for the two bainite structures, tested in house, were selected to give failure in ~2,500 – 5,000 hours and give creep crack initiation, i.e. crack growth up to 1.0mm, in approximately 1,000hours. After an initial testing programme based on the above, and information gained from newly acquired uniaxial creep testing data obtained from the collaborating establishment, it soon became apparent that the loading regimes did not give an accurate assessment of time to rupture and, hence, time to initiate a creep crack. Subsequently a reference value based on newly acquired uniaxial creep data for the heat-treated as cast material, detailed in Appendix 1, was subsequently used to determine the test stress.

The uniaxial creep test specimens in the as cast and heat treated ferrite / bainite structure, tested at a stress of 110MPa, were found to fail in a rupture

time of 1589 hours. From literature on similar structures it had been shown by Holdsworth and Cunnane ^[19] and Ainsworth ^[9] that the time to initiate a crack in a notched specimen was approximately 0.3-0.4 of the uniaxial rupture time and, therefore, the CT test specimens in this study were subsequently tested at 110 MPa to give crack initiation in a predicted 500-700 hours. Although this prediction proved to be reasonably accurate for the ferrite / bainite structures it was not satisfactory for the bainite structure. The fully bainitic structure when tested at this stress was found to initiate a crack 1mm long after only 300 hours and consequently the stress was further reduced to 100MPa. The final test regime utilised is detailed in Table 3.3 below.

Microstructure	Estimated time to initiate a crack at 550°C (h)	Test stress / reference stress, σ_{plc} (MPa)	Test load – based on equation 3.1 (KN)	Load on creep machine (Lever ratio 25:1) (N)
Ferrite / Pearlite	~8000h	85	Tested at Alstom Energy	Tested at Alstom Energy
Ferrite / Bainite	~600	110	16.125	645
Bainite	~600	100	14.706	588

Table 3.3: Creep test loading conditions.

3.4.3(c) Crack Opening Displacement Measurement

Crack opening displacement, (COD), measurement by conventional electronic methods is difficult at elevated temperatures due to specimen oxidation effects, strain gauge degradation and electronic instability. The method utilised in this project was based upon that described in section 2.5.2 after Holdsworth and Cunnane ^[19] and involved monitoring of the crack opening displacement, dy , of Vickers hardness indentations made parallel to the specimen notch at a known distance, x , from the front face of the specimen, as illustrated in Figure 3.5a.

Prior to the commencement of a test, diamond indentations were made at intervals of 2.54mm (0.1"), to a distance of about 20.32mm (0.8") from the front face of the specimen, using a Vickers hardness testing machine, with the specimens clamped in a sliding vice arrangement with micrometer stage movement. The displacement values, dy , were accurately measured before and after the creep test using an optical microscope and calibrated ocular graticule. A graph of dy against x was subsequently plotted and the relative positions of the load point and notch tip points indicated on the charts, as illustrated in Figure 3.5(b). Values of crack tip opening displacement, (CTOD), could then be read directly from the graph. Extrapolating the displaced indentation lines to $dy = 0$ gives the point of rotation for the crack opening, or the "hinge point", which varies with test duration.

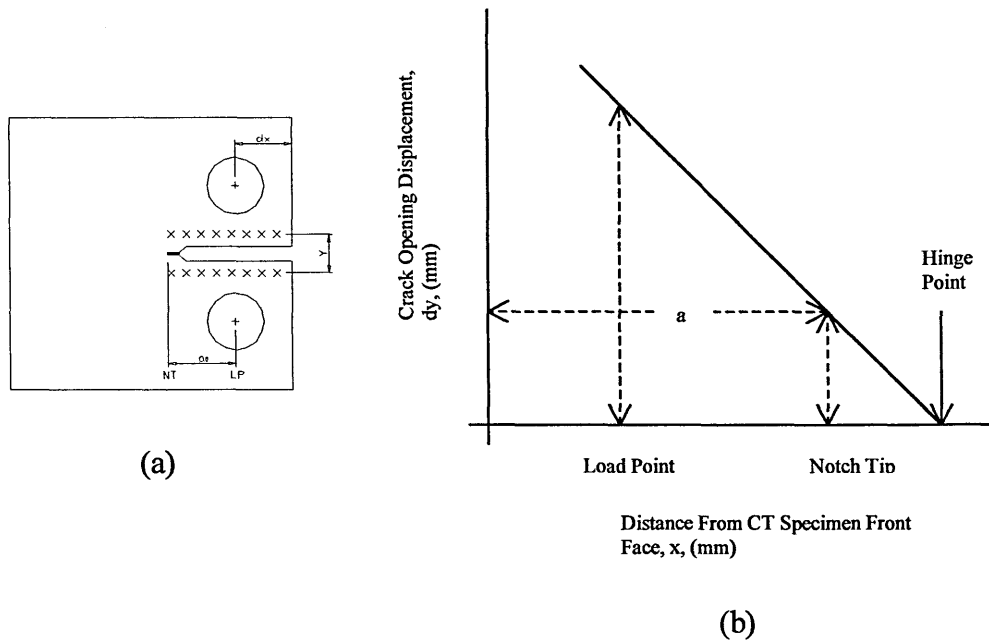


Figure 3.5: Crack opening displacement measurement.

- a) Schematic diagram of CT specimen notch and hardness indentations.**
- b) Schematic diagram of crack opening displacement against indentation position.**

3.5 Optical Microscopy Techniques

3.5.1 Specimen Preparation and Microstructural Examination

Microstructural examination of the material under investigation was carried out using both Zeiss and Vannox optical microscopes with 35mm camera attachments.

Examination was carried out on micro-specimens mounted in conducting bakelite, ground and polished to a 1 μ m diamond finish and subsequently etched in 2% nitric acid in methanol solution, (2 % Nital). Uniformly etched and stain free surfaces were achieved by using freshly polished specimens and by applying a layer of industrial methanol to the surface of the specimens immediately prior to immersion.

3.5.2 Grain Size Determination

The grain size of an alloy may have an effect on its creep resistance since it is known that:

- grain boundaries can act as easy pathways for the diffusion of elements at high temperatures, i.e. Coble creep
- grain boundaries may act as barriers to dislocation movement, and
- precipitates can pin grain boundaries and thus prevent grain deformation.

A knowledge of the grain-size of the starting material was, therefore, considered important to this study.

The average grain-size of the microstructures of interest was determined by the mean linear intercept (MLI) method, using a Vickers 55 projection microscope. This involved counting the number of grain boundaries, N, which crossed a line of known length, L, and thus:

$$\text{"MLI Grain Size"} = L/N \quad - \text{Equation 3.2}$$

The intercept line was provided by superimposing the microstructural image on a calibrated 1mm graticule, at the magnification chosen, prior to the counting procedure.

It is accepted that the true mean diameter of the grains in a sample is greater than the measured MLI, due to grain shape and improbability of measurement at the true grain diameter, ^[142]. The following generally accepted relationships have been established:

i) $D \approx 1.75 \text{ MLI}$, - Equation 3.3

where,

D = mean grain diameter taking into consideration improbability of measuring true grain diameter.

ii) $D_m \approx 1.86 \text{ MLI}$, - Equation 3.4

where,

D_m = mean grain diameter taking into consideration true grain shape.

In this study the mean grain diameter quoted was that in accordance with equation 3.3. For each specimen, ~300 intercepts were counted.

3.5.3 Determination of the Volume Fraction of Transformation Products

The volume fraction of micro-structural phases present in an alloy has a significant affect on its mechanical properties. The starting materials for this project were, therefore, assessed in terms of the volume fraction of their transformation products by 2-D manual point counting, using the technique as described by Pickering ^[142].

The procedure was carried out on a Vickers 55 projection microscope using a suitable magnification and point counting grid to ensure that no one phase region intercepted two consecutive grid points. For each sample determination ~3000 points were counted, i.e. ~20 fields per specimen.

3.6 Electron Microscopy Techniques

Electron microscopes allow small objects or features present in a material's microstructure to be magnified with a level of image resolution and depth of field which is far superior to that of the optical microscope.

The scanning electron microscope (SEM) is used for imaging surface morphological features, whereas, the transmission electron microscope (TEM) probes the internal structure of solids and gives access to both microstructural and ultra-structural details. In both techniques, high velocity electrons impinging on the material in a vacuum, produce X-ray spectra characteristic of the elements present. Energy dispersive X-ray (EDX) and wavelength dispersive X-ray (WDX) analysis of the spectra produced, thus provide a means of assessing the chemical composition of micro-structural features observed in electron microscopes.

In this project, both SEM and TEM techniques were employed, in conjunction with energy dispersive X-ray (EDX) analysis systems.

3.6.1 Scanning Electron Microscopy

Examination by SEM was primarily employed in this investigation to aid the identification of the microstructural phases present in the alloy, to study the evolution of carbide morphology with tempering time and temperature and to examine and quantify the creep damage in the tested compact tension specimens.

Scanning electron microscopy was carried out using both a JEOL 840A Scanning Electron Microprobe and a Philips XL 40 Scanning Electron Microscope. Both instruments were equipped with Oxford Instruments EDX analysis systems. The Philips XL 40 microscope was also equipped with

Oxford Instruments analysis software, Feature Scan, which was usefully employed in the quantification of creep damage.

3.6.1(a) SEM Specimen Preparation

Specimens of the as-received and heat-treated steel samples prepared for optical examination, were also suitable for examination by SEM. Apart from ensuring cleanness, no additional preparation was necessary.

To examine the microstructure and creep damage around the notch tip in tested CT specimens, a section as shown in Figure 3.6, was extracted using a Discotom cut-off machine and then mounted in conducting bakelite.

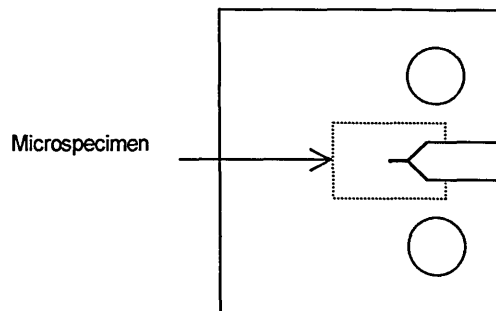


Figure 3.6: Micro-specimen extraction from notch tip region.

The mounted sections were ground and subsequently polished to a $1\mu\text{m}$ diamond paste finish and then etched for ~ 20 seconds by immersion in a solution of 2% nitric acid in methanol. To ensure that the surface was free from preparation damage, the latter two stages, i.e. the $1\mu\text{m}$ polish and etch, were repeated three times. Samples were stored in an air tight desiccator to prevent deterioration of the polished and etched surfaces.

To prevent charging of the oxide layer around the notch sample in the SEM, the prepared micro-specimens were coated with a thin layer of carbon using a carbon evaporation process. The coating was achieved by placing the specimens in an Edwards vacuum coating unit at a pressure $\sim 1 \times 10^{-5}$ bar,

beneath a pair of carbon electrodes through which a current passed, thus evaporating carbon onto the specimen surface.

To improve the electrical conductivity of the specimens in the SEM, and hence limit image noise, a thin trail of silver dag conducting paint was used to link the specimen surface to the conducting, aluminium, support stub.

3.6.1(b) General SEM Examination

General micro-structural examination of the starting materials, tempered bainite specimens and creep tested samples was carried out on an SEM using an accelerating voltage of 25keV.

Secondary electron imaging was used to resolve the fine microstructural details in samples of interest whereas back-scattered electron imaging was used to locate creep cavitation and measure crack extension in the tested specimens.

Micro-structural evidence was recorded using either a 35mm camera attachment or digital image capturing device.

3.6.1(c) Creep Damage Quantification using SEM Image Analysis

Microstructural examination and damage accumulation of the creep tested CT specimens was performed utilising a Philips XL 40 SEM and Oxford Instruments image analysis software. The micro-specimens prepared were examined using both back-scattered electron (BSE) and secondary electron (SE) imaging modes. BSE imaging allowed the creep voids and micro-cracks to be clearly delineated from the general micro-structural features for quantification purposes whilst SE imaging enabled the operator to determine whether the damage was present at inter or intra-granular sites.

The accuracy of the analytical process relied on imaging conditions remaining consistent between consecutive fields of view and between samples and, therefore, a systematic routine was devised to ensure reproducible image contrast and brightness and feature detection.

The following microscope conditions were maintained during the analytical procedure:

Working Distance:	15mm
Accelerating Voltage:	20Kev
Beam Current:	~85 μ A
Probe Size:	Spot size 6 (large)
Image Type:	Back scattered electron
Magnification:	x1000
Scan Rate:	200ms/line

As the stability of the beam current cannot be guaranteed over long periods of time, or from sample to sample, it was necessary to establish a datum for the contrast and brightness levels to ensure consistency. This was achieved by using the wave-form meter on the SEM control panel to ensure that the average contrast and brightness signal for the general microstructure was at a known position with respect to the “white” level and that the signal from the voids and micro-cracks fell into the “black” level, Figure 3.7 .

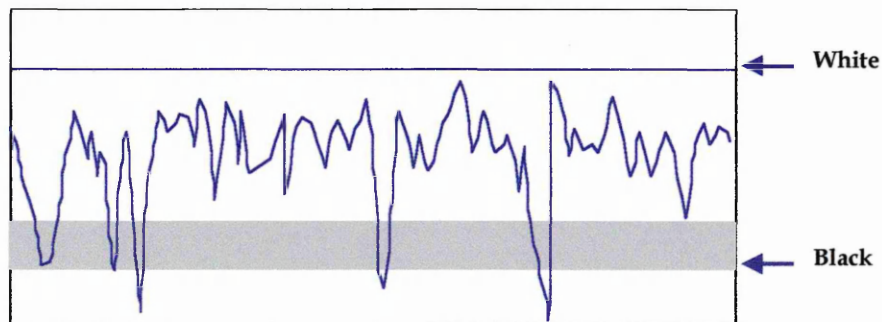


Figure 3.7: Use of the SEM wave-form meter to ensure image consistency.

The operational procedure for the SEM and Feature Scan image analysis software was as follows:

- i) Allow SEM chamber to de-evacuate
- ii) Home stage
- iii) Place specimen on the microscope stage with the notch facing west.
- iv) Evacuate chamber
- v) Optimise image
 - a) check filament saturation
 - b) Set gun tilt
- v) Image specimen at x1000 (screen mag.), focus (slow scan) and adjust stigmators.
- vi) Place notch tip in screen centre using cross hairs.
- vii) Use "measurement" function to determine distance from notch to top of field of view e.g. $\sim 87\mu\text{m}$ (Feature Scan software gives image dimensions)
- viii) Using "position" move image so that notch tip is just out of view, e.g. $\sim 87\mu\text{m}$.
- ix) Note the stage x,y co-ordinates.
- x) Set up the BSE image as detailed in microscope conditions above.
- xi) Go to external x,y, signal controlled by image analysis software.
- xii) Select Feature Scan programme in digital imaging programme.
- xiii) Set up detection conditions or call up conditions file, e.g. TB samples.
 - a) features smaller than 10 pixels excluded
 - b) noise reduction = 20 samples
 - c) thresholding - collect digital image in slow Kalman (5 frames); levels set to distinguish between the grey levels of features of interest and background.
E.g. Typical threshold band for detection of voids = 0-140 grey levels.
- xiv) Set up measurement conditions
 - a) no. of feret projections for measurements = 36
 - b) measurement derived - feature area as % of field, centre of gravity positions (x,y), feature length and breadth, orientation (radians with respect to horizontal axis¹), perimeter and aspect ratio.

¹ This value was subsequently recalculated to give orientation with respect to the notch tip.

- xv) Set up feature filter conditions - used to differentiate between low atomic number inclusions and voids (chemical classification bins set up for elements of interest e.g. sulphides in ferrite / pearlite samples).
- xvi) Set up image calibration.
E.g. Typical calibration
Field width = 187.778 μm , field height = 185.082 μm ,
Field area = 34754.2 μm^2 .
Image resolution = 1024 x 1024 (i.e. 1 pixel = 0.18338 μm x 0.18074 μm)
- xvii) Analyse live image.

3.6.2 Transmission and Scanning Transmission Electron Microscopy

Transmission electron microscopy (TEM) and scanning transmission electron microscopy (STEM) were performed using a Jeol 100CX microscope with a tungsten filament electron gun and a Philips CM 20 microscope with an LaB₆ electron gun. Both microscopes were fitted with energy dispersive X- ray, (EDX), analysis facilities.

TEM was generally employed to examine and identify the micro-structural features of interest in the starting materials, temper trial samples and creep tested specimens. The Jeol 100CX in STEM mode and associated EDX feature detection software, was specifically employed to carry out an assessment of the evolution of carbide morphology in the bainite tempering investigation.

Image contrast in the TEM is due to density and thickness variations in the specimen or diffraction effects due to the interaction of features in the microstructure with the primary electron beam, i.e. kinematic and dynamic conditions.

Specimens for TEM examination generally take the form of either a 3mm diameter solid disc partially thinned to a few nm thick for electron penetration,

thin foils, or extraction replicas in which particles from the bulk material are extracted onto a carbon film and supported on 3mm diameter copper grids.

The majority of the work carried out in this study necessitated the preparation and examination of extraction replicas with only the occasional requirement for preparation and examination of thin foil type specimens.

3.6.2(a) Preparation of Carbon Extraction Replicas

Extraction replicas consist of particles extracted from the specimen of interest, supported on 3mm squares of carbon film. TEM examination of the extracted particles can provide information about their type, morphology, crystallography and chemical analysis.

Specimens for examination were prepared in the conventional metallurgical manner, by grinding and polishing to a 1 μ m diamond finish. After polishing the specimens were immediately subjected to a light etch in 2% Nital. The area of interest was then isolated using masking tape, as illustrated in Figure 3.8 for selective extraction of carbides in the notch tip and reference regions. The sample was then placed in an Edwards carbon evaporation coating unit for at least 12 hours to achieve a high vacuum of $\sim 1 \times 10^{-8}$ bar and, on reaching this, carbon was evaporated over the specimen from a height of 100mm in 0.5 second blasts, allowing the vacuum to recover between each layer. Coating at high vacuum is essential to maintain a fine grained carbon structure which will remain intact during subsequent operations.

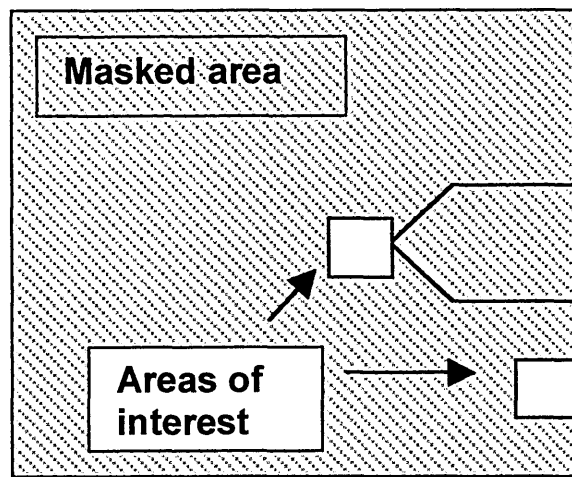


Figure 3.8: Selective preparation of notch tip and reference region extraction replicas.

After carbon coating, the masking tape was removed from the specimen and a sharp scalpel was used to score a 3mm x 3mm area on the coated surface of interest. The specimen was then immersed in 2% Nital reagent until the surface carbon layer began to blister. At this point, the specimen was transferred via a dish containing analar methanol, to a dish containing distilled water. Separation of the carbon from bulk specimen, was achieved by angling the specimen surface at 45° to the water surface during immersion and allowing the surface tension of the water to provide the force for separation.

After removing the bulk specimen from the water 3mm diameter copper grids were used to "catch" the floating carbon squares which were then dried carefully and stored in a clean dry environment until required for TEM examination.

3.6.2(b) Preparation of Thin Foils

TEM examination was necessary to characterise the structure of the 100% bainite starting material produced by heat-treatment. The specimens for this work were produced by conventional jet electro-polishing, using chilled 2% perchloric acid in methanol solution.

3.6.2(c) Microstructural Examination in the TEM

General microstructural assessment of the as received material, tempered bainite material and CT tested specimens was performed on extraction replicas using a Philips CM20 TEM/STEM with EDAX analysis. An accelerating voltage of 200keV was used for the investigation, with the specimen positioned at eucentric height and tilted at an angle of 25° towards the detector for chemical analysis.

The carbide classification scheme for this part of the investigation was based upon the ratios of $Fe_{k\alpha}/Cr_{k\alpha}$, $Mo_l/Cr_{k\alpha}$ and $Fe_{k\alpha}/Mo_l$ detected in each of the carbide types, that is M_3C , M_2C , M_7C_3 , $M_{23}C_6$, M_6C . The ratios used, as detailed in Table 3.4, were determined by carrying out a series of EDX spot analysis trials on carbides extracted from both starting material and tempered bainite specimens. The procedure for the analysis involved focusing the electron beam, of spot size 6, onto the carbide of interest and collecting the emanating signal utilising the EDAX software. The result of the analysis was displayed in the form of an X-ray spectra that allowed the elements of interest to be identified and X-ray windows in the relevant KeV ranges to be created. The net number of X-ray counts contributing to each of the elemental windows specified in the spectra, as described in section 3.6.2(d), was then displayed and the key elemental ratios determined. The raw data for this determination is shown in Appendix 2.

Carbide Type	Elemental Ratio Range		
	Fe / Cr	Mo / Cr	Mo / Fe
M_3C	2.00 – 6.00	0.20 – 0.60	0.05 – 0.25
M_2C	0.02 – 0.60	1.50 – 4.50	7.50 – 30.00
M_7C_3	0.50 – 0.90	0.05 – 0.50	0.05 – 0.35
$M_{23}C_6$	1.10 – 1.50	0.15 – 0.60	0.10 – 0.35
M_6C	5.00 – 15.00	5.00 – 15.00	0.75 – 1.50

Table 3.4: Elemental ratios determined by EDX spot analyses and used for carbide identification.

3.6.2(d) Carbide Characterisation by Image Analysis in the STEM

To study the carbide evolution process in the alloy, an image analysis procedure was developed for use with the Jeol 100CX STEM allowing the size, chemical composition and type of carbide particles to be assessed. For this part of the work the STEM unit was used with a LINK Instruments EDX software package called Digiscan, a feature detection and analysis programme that converts an electron microscope image into a digitised image displayed as a range of grey levels. The microscope conditions were set up so that the features of interest, i.e. the carbides, fell within an acceptable grey level band within the STEM image, as illustrated in Figure 3.9(a). The corresponding digital image, see Figure 3.9(b), was then thresholded, i.e. a range of grey levels was selected, to identify more precisely which features were to be considered in the analysis.

Once the thresholds had been set, the microscope beam was controlled by the Digiscan programme and made to scan a grid of points superimposed on the thresholded image. The X-Y co-ordinates of all the features detected were stored, subsequently allowing the beam to return and perform a sizing and analysis routine. All relevant size and compositional information was stored in a file to which data from subsequent image fields was added.

Sizing of the features was based on mean diameter measurements derived from 20 feret projections. Calibration for sizing was achieved by entering the screen width corresponding to the Digiscan rastered area and the working magnification.

The analysed field width was equivalent to $5.6\mu\text{m}$ and 1024 pixels each pixel measured approximately $0.005\mu\text{m} \times 0.005\mu\text{m}$. Only features having an area >10 grid points, i.e (pixels) were considered for the analysis.

The determination of the composition of microstructural features using Digiscan involved energy dispersive X-ray analysis in conjunction with user determined window files and chemical classification bins. EDX analysis data, displayed in

the form of a spectra, as illustrated in Figure 3.10 was used to define the X-ray energy limits of elements of interest and regions of background radiation. Areas defined by these limits are known as "windows".

Each element window contains X-ray counts for both the element of interest and background radiation and therefore, background windows are necessary to calculate the net contribution of specified element. For this purpose the background fraction of X-ray counts contributing to a specific element window was determined as follows:

$$\text{Background fraction in element window} = \left(\frac{X - \text{ray counts in element window on carbon film}}{X - \text{ray counts in background window on carbon film}} \right)$$

In the case where two elements in the alloy have X-ray energies that overlap, and therefore contribute to the same EDX window, a factor to calculate the contribution of each element has to be made. This was achieved by calculating the contribution of pure element standards to the specified window using bulk samples in the SEM. For example, in the case of 2.25%Cr-1%Mo steel, Figure 3.10, the K_{β} peak for chromium contributes to the window specified for manganese and the overlap fraction is calculated as follows:

$$\text{Overlap frac}^n \text{ for } Mn_{K\alpha} = \frac{\text{Net X-ray counts from Mn std to } W_1}{(\text{Net X-ray counts from Mn std to } W_1) + (\text{Net X-ray counts from Cr std to } W_1)}$$

Where:

W_1 = specified window for the element manganese

The elemental factors in each case are detailed in Appendix 3.

Chemical classification by Digiscan image analysis was achieved by setting up chemical classification bins, each of which defined the range of element mass

percentages for a particular class of feature; in this case the mass % of elements in each carbide type.

It has been reported that the types of carbides expected in this alloy are M_3C , M_2C , M_7C_3 , $M_{23}C_6$ and M_6C ^[17] and that the composition of these carbides is known to vary ^[28]. Based on this knowledge and the EDX spot analyses trials, as described in section 3.6.2c, the classification bins for the image analysis process were derived, as detailed in Table 3.5 .

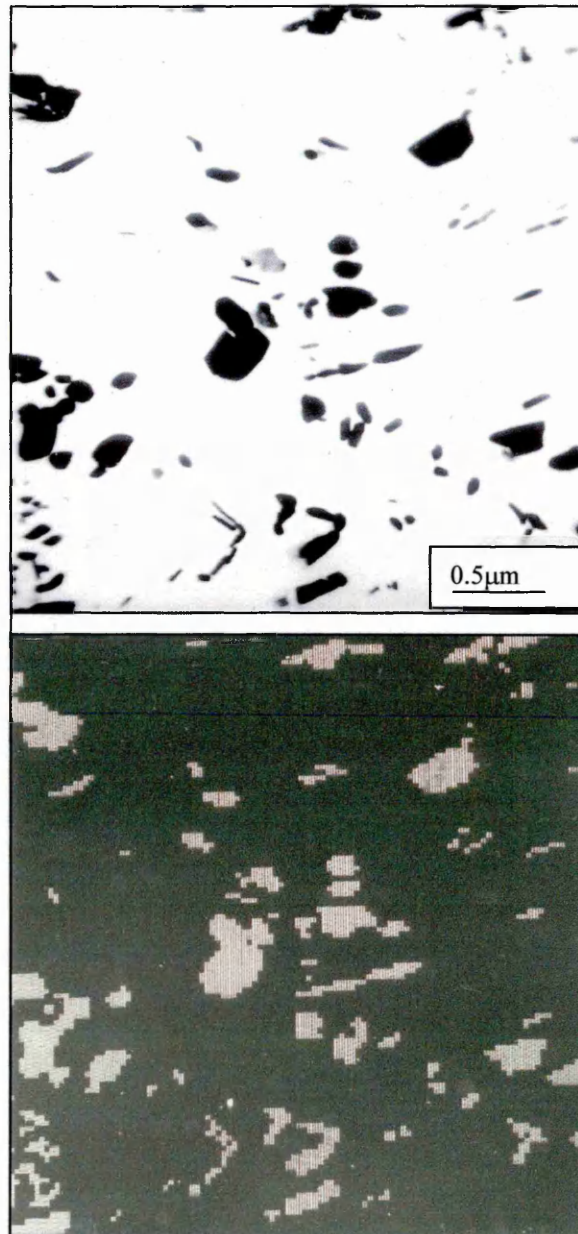


Figure 3.9: STEM images of a) carbide precipitates and b) the corresponding digitised image.

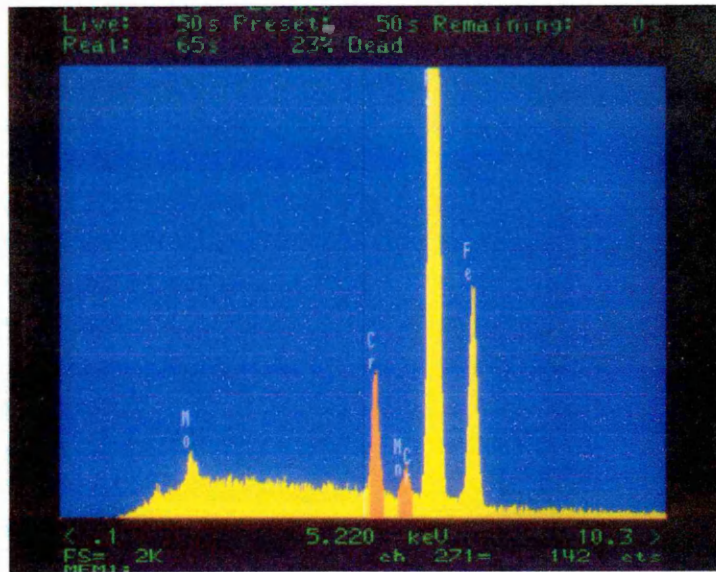


Figure 3.10: EDX spectra of 2.25%Cr-1%Mo steel showing identification of elements of interest by formation of “windows”.

Carbide Type	Chemical Composition Classification Bins (element mass %)		
	Fe	Cr	Mo
M_3C	56 - 85	10 - 20	0 - 10
M_2C	0 - 10	15 - 35	55 - 75
M_7C_3	25 - 45	50 - 65	5 - 15
$M_{23}C_6$	45 - 60	30 - 50	5 - 15
M_6C	35 - 50	0 - 15	40 - 55

Table 3.5: The compositional range of various metal carbides encountered in 2.25%Cr-1%Mo steel, as used in conjunction with EDX-Digiscan image analysis.

4.1 Introduction

The experimental work involved in this investigation progressed in three stages, as explained in detail in Section 3.1, namely:

- a) the characterisation of the starting materials
- b) a study of the tempering characteristics of the steel with a fully bainitic structure
- c) creep testing and microstructural investigation

The results obtained from these three phases of the work are described in detail in the subsequent sections.

4.2 Characterisation of the Starting Materials

Samples of 2.25%Cr-1%Mo steel exhibiting the following microstructural profiles provided the raw material for this investigation:

- i) Pro-eutectoid ferrite + pearlite
- ii) Pro-eutectoid ferrite + bainite
- iii) 100% bainite.

The source, detailed compositions and prior heat-treatment to obtain these structures have been described in detail in sections 3.2 and 3.3.

In order to determine the affect of such microstructural variations on the creep deformation behaviour of material ahead of a defect in 2.25%Cr-1%Mo steel it was necessary to first obtain an understanding of the initial microstructures, and their subsequent evolution at elevated temperatures, and establish the basic mechanical properties of the starting materials.

Hardness and tensile tests were carried out on the starting materials and a combination of optical and electron microscope techniques were used to examine the microstructures.

4.2.1 Mechanical Properties

The room temperature Vickers hardness and tensile test behaviour at room temperature and 550°C were determined as described in section 3.4.1 and 3.4.2 respectively. The results obtained are summarised in Table 4.1.

Sample Identity	Average HV _{20Kg}	0.2% Proof Stress (MPa)		Ultimate Tensile Strength (MPa)		Elongation %		Young's Modulus (GPa)	
		RT	550°C	RT	550°C	RT	550°C	RT	550°C
Ferrite + Pearlite	142	278	190	488	400	33	29	197	124
Ferrite + Bainite	136	256	176	492	296	30	28	208	131
100% Bainite	170	413	298	551	380	30	24	208	112

Table 4.1: Hardness and tensile properties.

The sample exhibiting the fully bainitic structure was found to possess the highest hardness value followed by the sample consisting of the mixed ferrite / pearlite structure and finally the ferrite / bainite sample. The determination of these values was considered relevant to the project in terms of providing a possible link between room temperature hardness and creep brittle /ductile behaviour.

The room temperature tensile properties, for all three structures, were superior to those determined at 550°C. The bainitic structure resulted in the highest room temperature properties but exhibited the most significant reduction in properties on raising the test temperature to 550°C. The decrease in tensile strength and Young's modulus at the elevated temperature was expected but it was notable that the high temperature ductility of all three structures was lower than that at room temperature. It was anticipated that the bainite constituent of

the mixed ferrite / bainite material would render this structure harder and stronger than that of the ferrite / pearlite structure. Unexpectedly, with the exception of the Young's modulus values, the hardness and tensile properties of the ferrite / pearlite structure were similar or better to those of the ferrite / bainite structure. The reason for this discrepancy may be due to the relative maturity of the carbides in the predominant ferrite phase of these structures. This will be discussed later in section 5.2 in conjunction with a description of the carbide morphology results.

4.2.2 Optical Microscopy

Optical microscopy was carried out on samples extracted and metallurgically prepared from the starting materials as detailed in section 3.5 to determine the microstructural phase constituents, grain-size and phase proportions in each of the materials.

Plates 4.1 - 4.3 are photomicrographs representative of the microstructures of each of the starting materials.

A qualitative metallurgical assessment of the materials, using magnifications up to x800, indicated that the microstructures required for this project had been achieved. With the resolution capability of the optical microscope it was not possible to determine the morphological type of bainite present in the latter sample and, consequently, this was assessed further in the scanning electron and transmission electron microscopes as reported in sections 4.2.3 and 4.2.4 respectively .

The grain size and phase proportions of the micro-structures observed in Plates 4.1 - 4.3 were assessed on a Vickers 55 optical microscope using mean linear intercept and 2D point counting methods as described in sections 3.5.2 and 3.5.3 respectively.

The grain-size and phase volume fraction results are summarised in Table 4.2.

Micro-structure	Average Grain-Size (mm)	Average Phase Proportions
Pro-eutectoid ferrite / pearlite	0.035	90% ferrite + 10% pearlite
Tempered, pro-eutectoid ferrite / bainite	0.064	75% ferrite + 25% bainite
Tempered 100% bainite	0.066	100% bainite

Table 4.2: Grain size and phase proportions of starting materials.

The average grain size determined for the tempered bainite and mixed ferrite / bainite structures were found to be similar. The ferrite / pearlite microstructure, however, which was derived from a different source, was found to possess a significantly finer grain structure. This may be significant later in relation to the mechanisms of creep cavity formation and crack initiation.

The phase proportions present in each of the structures is indicative of the relative number of grain boundary types. In the mixed ferrite / pearlite structure the pearlite occurs as discrete islands in the ferrite matrix and the majority of grain boundaries are ferrite / ferrite in nature. In the ferrite / bainite structure the ferrite structure is broken by an almost continuous network of bainite grains and there is a mixture of ferrite / ferrite and ferrite / bainite boundaries with occasional boundaries of bainite / bainite. In the structure classified as fully bainitic no other major phases were observed.

These structures represent the range of microstructures that may occur in a large casting of quality heat-treated 2.25%Cr-1%Mo steel and were, therefore, considered satisfactory for the purpose of this study.

4.2.3 Scanning Electron Microscopy

A major part of the creep damage assessment procedure in this programme of work was to be carried out using scanning electron microscopy. It was

necessary, therefore, to establish the appearance of the starting material structures prior to the application of the creep stress and elevated temperature. SEM examination of the starting materials was carried out using a Philips XL40 microscope as described in section 3.6.1. Examples of the structures observed are shown in Plates 4.4 - 4.9.

In the ferrite / pearlite structure, as shown in Plates 4.4 and 4.5, a network of relatively coarse carbides can be seen clearly delineating the position of the prior austenite grain boundaries. Regions of pearlite were found to be homogeneously distributed throughout the structure and were identifiable by the presence of a dense mass of lamella carbide. Growth of the pearlitic lamellae could be seen to occur either into one or both of the adjacent ferrite grains. The ferritic regions could be identified by the presence of a fine, less dense, distribution of carbides which were more globular in nature than those observed in the pearlite.

Plates 4.6 and 4.7 show SEM images of the mixed pro-eutectoid ferrite / bainite microstructure. The regions of ferrite and bainite were, again, easily distinguished by the difference in their carbide size and population. The bainite regions possessed a structure of relatively large carbides which decorated the boundaries of the prior, upper bainite laths. The ferrite, however, exhibited a fine distribution of very small carbides that were uniformly dispersed. The boundaries between the two regions were outlined by a network of globular carbides .

The carbide morphology in the fully bainitic structure, as shown in Plates 4.8 and 4.9, was similar to that described above for the bainite in mixed ferrite / bainite structure. In the case of the fully bainitic structure, however, the carbides in the intra-granular regions appeared to be slightly larger in size and less densely populated.

4.2.4 Transmission Electron Microscopy

Transmission electron microscopy was carried out on all three starting materials using the techniques described in section 3.6.2.

Bainite can exist in two forms, upper bainite and lower bainite. It was necessary to establish the type of bainite formed by the heat treatment regimes employed in this work, as described in section 3.3.1, to produce the 100% bainite starting material.

Examination of a thin foil specimen produced from the bainite structure in the normalised condition, Plate 4.10, showed that carbides existed at the boundaries of the bainite laths. This inter-lath precipitation is indicative of the structure being upper bainite.

One of the primary objectives of this investigation was to assess the role of carbides and their evolution process on the mechanism of creep crack initiation and growth in the presence of a pre-existing defect. It was, therefore, necessary to assess the carbide compositional morphology of the three starting micro-structures. This assessment was achieved by examining extraction replicas, taken from each of the three materials, in the TEM and analysing, where possible, the carbides in terms of their chemical composition and type. Chemical analysis of the carbides was by semi-quantitative EDX analysis based on elemental ratios as described in section 3.6.2c of the experimental procedures. Plates 4.11- 4.14 illustrate the typical microstructures observed and Tables 4.3 - 4.5 detail the carbide compositions found in each case.

Plate 4.11 shows a typical ferrite / pearlite boundary in the mixed pro-eutectoid / ferrite microstructure. The lenticular shaped precipitates in the ferrite regions, designated 'A' in Plate 4.11, were analysed and found to be rich in chromium and molybdenum. Comparison of the elemental ratios for this carbide with those detailed in Table 3.4 of the experimental procedures suggested that their composition was similar to that of M_2C but with a greater chromium

concentration. The lamellar carbides observed in the pearlitic regions, designated 'B' in Plate 4.11, were found to have compositions typical of $M_{23}C_6$, being richer in iron and chromium than would be expected for M_3C . Carbides existing at the prior austenite grain boundaries were also found to be predominantly $M_{23}C_6$ type, for example carbide 'C', in Plate 4.11.

Plates 4.12 and 4.13 show typical images of the carbide morphology observed in the mixed ferrite / bainite structure. The precipitates in the ferritic regions were predominantly of one morphology, that is, small, lenticular-shaped carbides, rich in molybdenum. Comparison of the elemental ratios determined by EDX analyses for these carbides with the data in Table 3.4 suggested that these carbides were M_2C . Occasional fringes of carbide of a similar composition, but larger in size, were also found adjacent to the ferrite / bainite grain boundaries.

The carbides present in the bainitic regions of the ferrite / bainite structures had a range of morphologies and chemistries including the lenticular-shaped, M_2C , carbides observed in the ferrite regions. In addition small and large globular carbides plus stick-like carbides were observed as indicated in Plate 4.13. The stick-like and globular precipitates exhibited a range of overlapping compositions based on iron, chromium and molybdenum which meant that it was impossible to identify the type of carbide on shape alone. Based on the EDX analyses ranges in Table 3.4 the small globular precipitates were found to be predominantly M_7C_3 , the stick-like precipitates either M_7C_3 or $M_{23}C_6$ and the large grain boundary precipitates $M_{23}C_6$ or M_6C . The carbides at the ferrite / ferrite boundaries were found to be chromium rich and of the type M_7C_3 . This was in contrast to the carbides at the ferrite / ferrite boundaries in the ferrite / pearlite structure which were iron rich and typical of $M_{23}C_6$.

Plate 4.14 shows the carbide morphology observed in the fully bainitic structure. As described previously for the SEM images in section 4.2.3, the fully bainitic structure was found to be less densely populated in terms of the carbide distribution than was that in the mixed ferrite / bainite structure. The

types of carbides present were consistent with those detected in the bainite phase region in the ferrite / bainite samples described above , however, it was noted

that the relative proportions of M_7C_3 and $M_{23}C_6$ carbides in the intra-bainitic regions differed. The majority of carbides in the intra-bainitic regions of the fully bainitic structure were of the $M_{23}C_6$ type with only occasional M_7C_3 type carbides being identified, whereas, in the mixed structure there was almost an equal amount of the two carbides. Typical EDX analyses spectra for the range of carbides detected are shown in Figure 4.1.

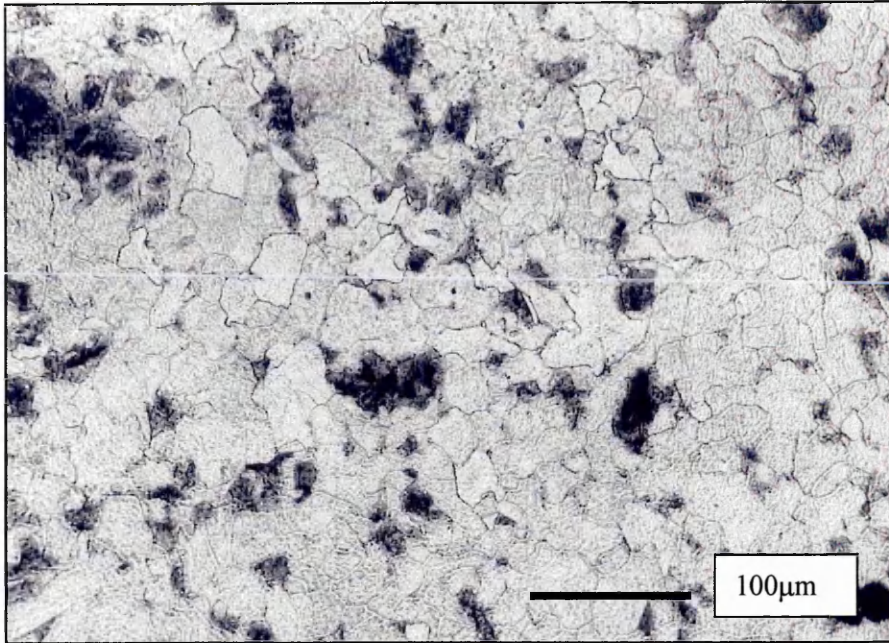


Plate 4.1: Optical micrograph of the mixed pro-eutectoid ferrite / pearlite structure derived from pipe section fully annealed at 960°C.

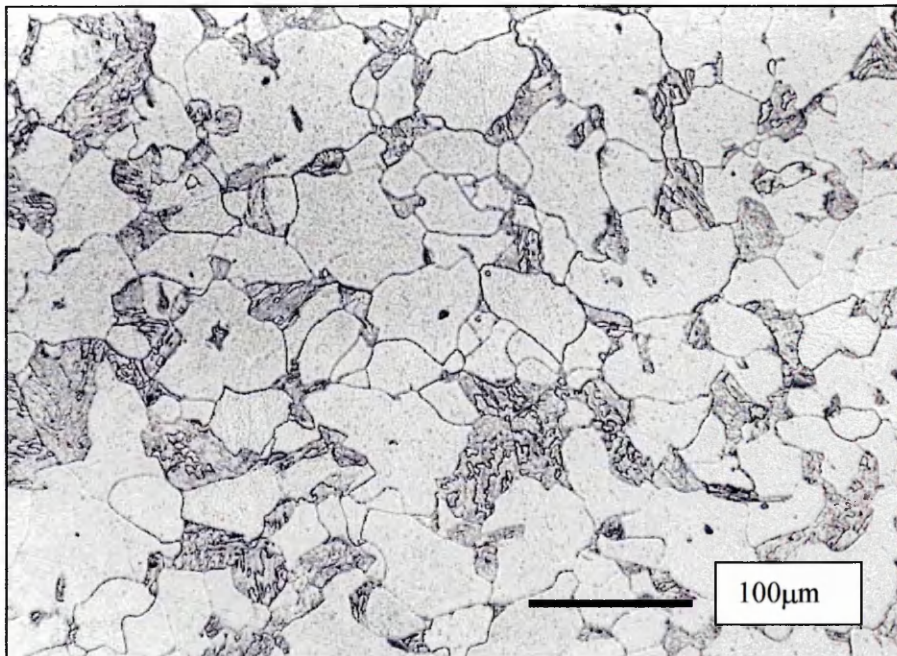


Plate 4.2: Optical micrograph of the mixed pro-eutectoid ferrite / bainite structure derived from as-received bar normalised at 960°C, tempered at 705°C and stress relieved at 700°C .

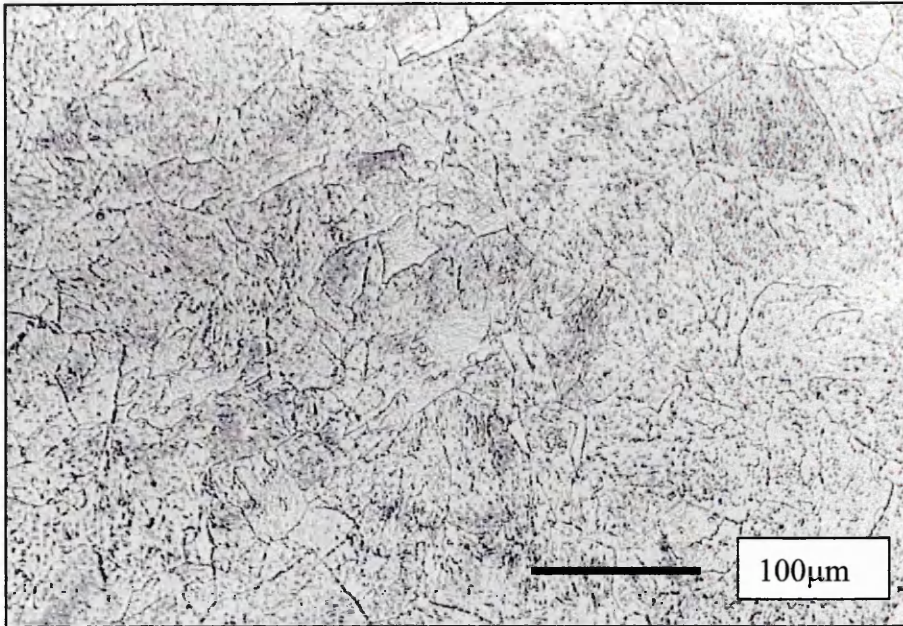


Plate 4.3: Optical micrograph of the 100% bainite structure produced by normalising at 960°C and tempering at 700°C for 24h.

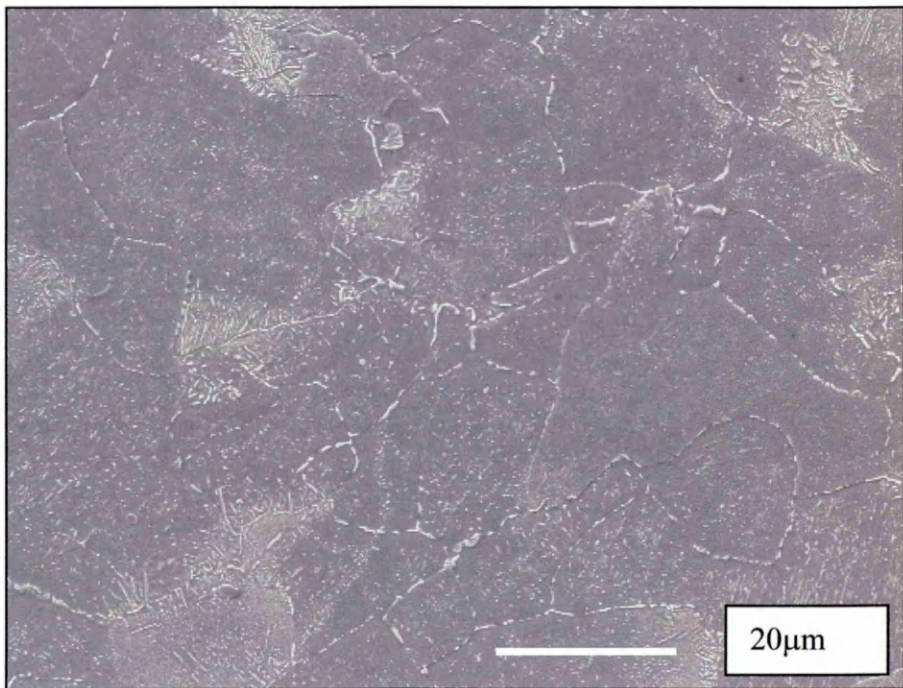


Plate 4.4: Low magnification SEM image of the ferrite / pearlite starting microstructure.

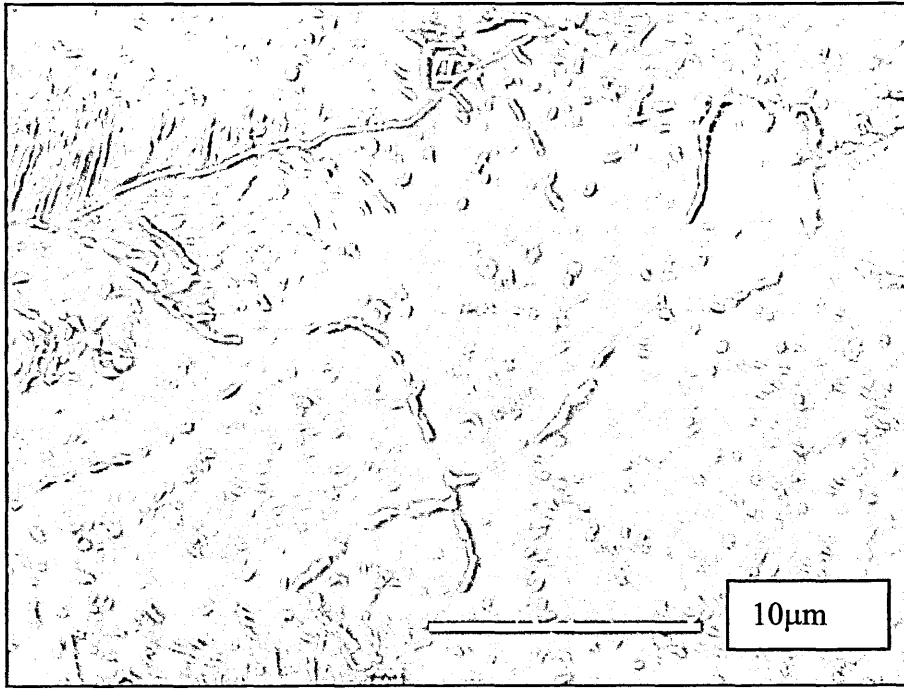


Plate 4.5: High magnification SEM image of the ferrite / pearlite starting microstructure.

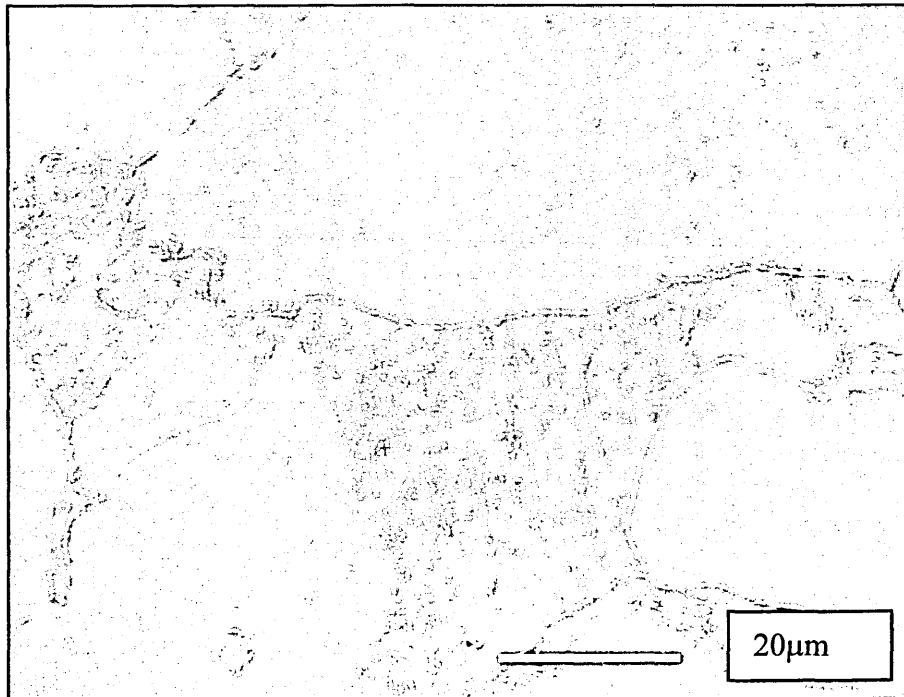


Plate 4.6: Low magnification SEM image of the ferrite / bainite starting microstructure.

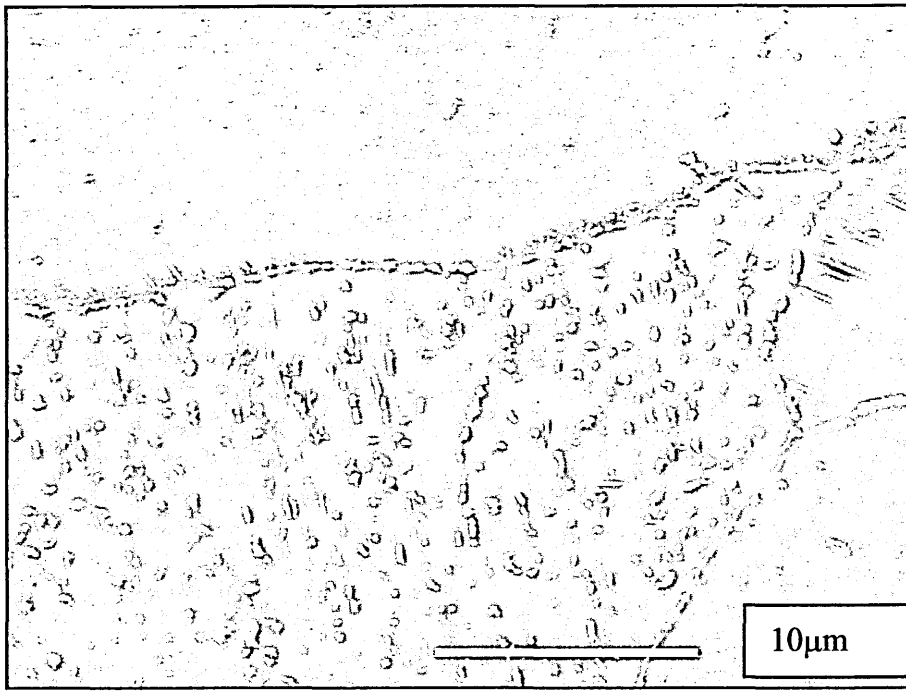


Plate 4.7: High magnification SEM image of the ferrite / bainite starting microstructure.

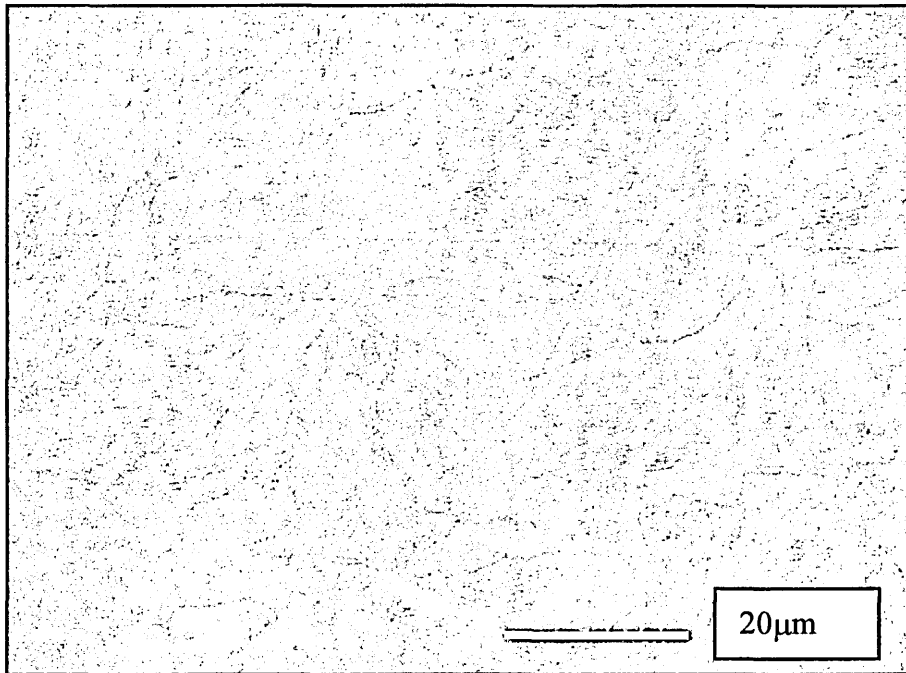


Plate 4.8: Low magnification SEM image of the fully bainitic starting microstructure.

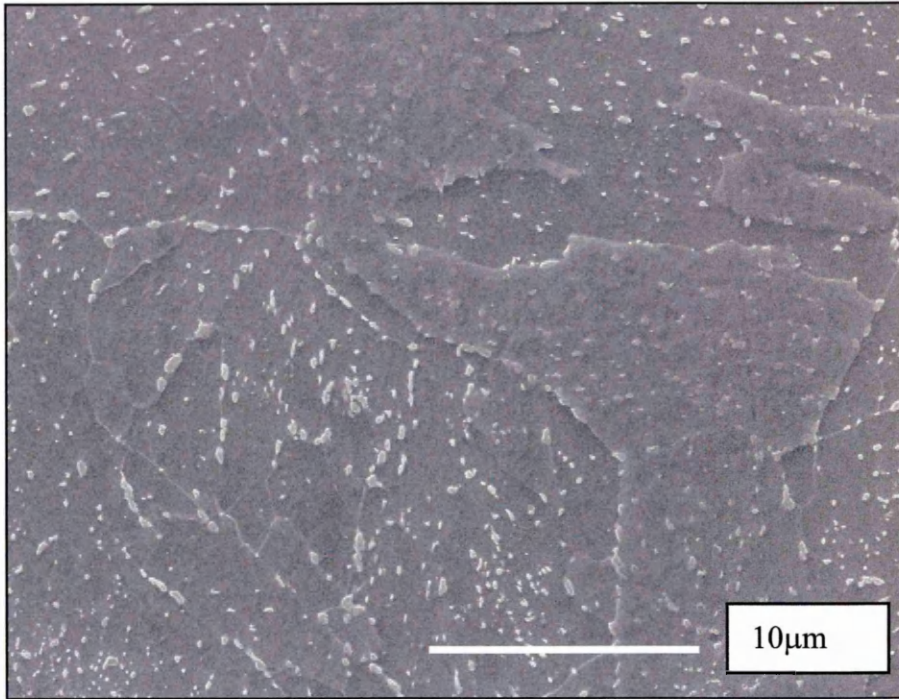


Plate 4.9: High SEM magnification image of the fully bainitic starting microstructure.

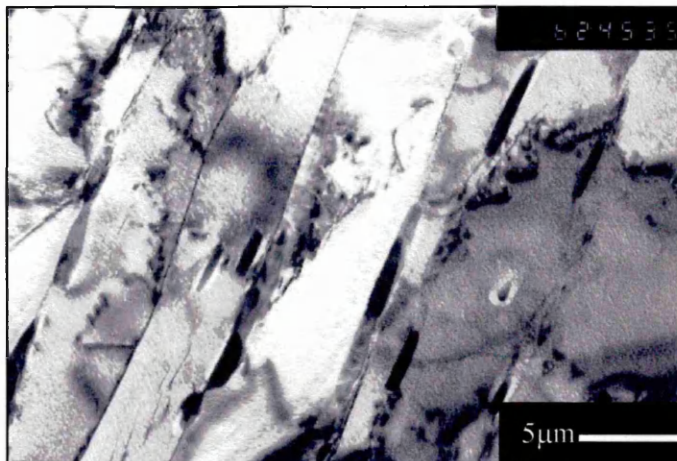


Plate 4.10: TEM bright field Image of a thin foil specimen extracted from the as normalised material . Carbide precipitation observed between the ferrite laths identified the structure as upper bainite.

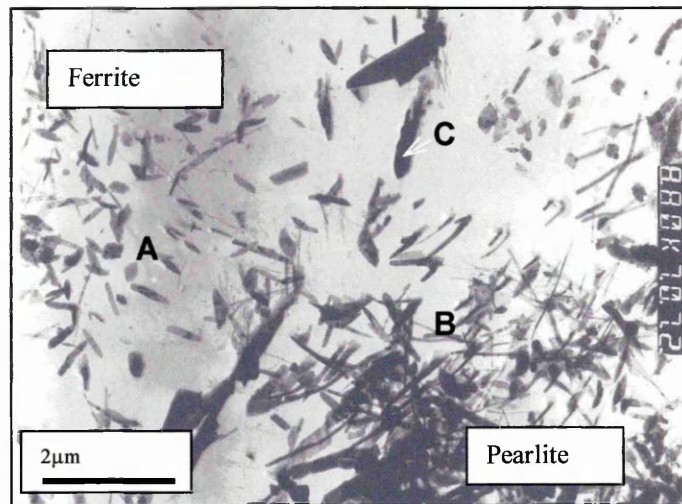


Plate 4.11: TEM micrograph of the carbide morphology in the ferrite / pearlite starting material .

Carbide Designation	Typical Elemental Ratios			Carbide Type
	Fe:Cr	Mo:Cr	Mo:Fe	
A	0.11	0.68	6.07	M ₂ C
B	0.95	0.34	0.36	M ₂₃ C ₆
C	1.41	0.32	0.22	M ₂₃ C ₆

Table 4.3: Elemental ratios for the carbides observed in the ferrite / pearlite structure as indicated in plate 4.11.

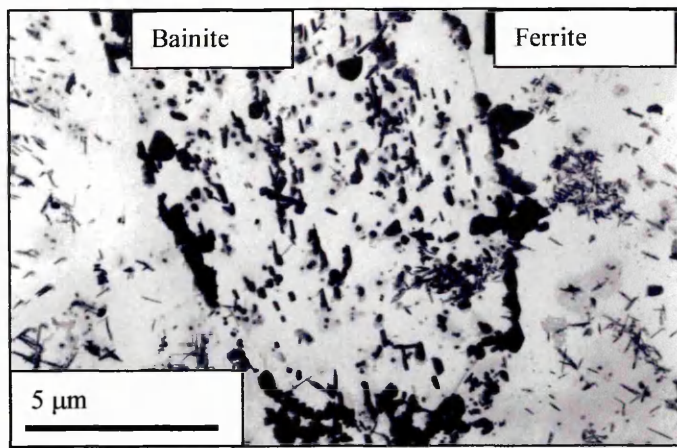


Plate 4.12: TEM micrograph of the carbide morphology in the tempered mixed pro-eutectoid ferrite / bainite starting material.

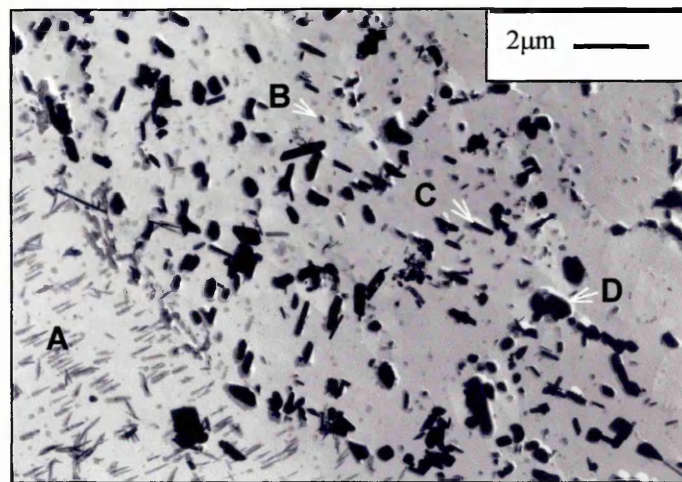


Plate 4.13: TEM micrograph of the carbide morphology in the tempered, mixed pro-eutectoid ferrite / bainite starting material.

Carbide Designation	Typical Elemental Ratios			Carbide Type
	Fe:Cr	Mo:Cr	Mo:Fe	
A	0.21	2.03	9.92	M_2C
B	0.62	0.11	0.18	M_7C_3
C	1.34	0.17	0.13	$M_{23}C_6$
D	6.89	5.60	0.81	M_6C

Table 4.4: Elemental ratios for the carbides observed in the ferrite / bainite structure as indicated in plate 4.13.

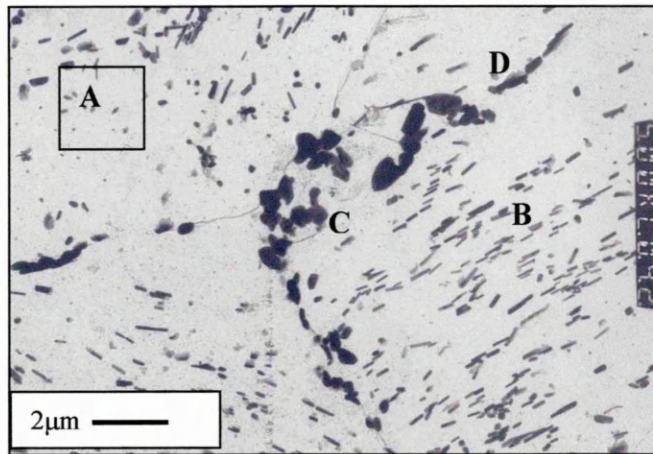


Plate 4.14: TEM micrograph of the carbide morphology in the tempered 100% bainite starting material.

Carbide designation	Typical Elemental Ratios			Carbide Type
	Fe:Cr	Mo:Cr	Mo:Fe	
A	0.59	0.05	0.09	M_7C_3
B	1.22	0.10	0.09	$M_{23}C_6$
C	1.13	0.12	0.10	$M_{23}C_6$
D	5.25	3.74	0.71	M_6C

Table 4.5: Elemental ratios for the carbides observed in the ferrite / bainite structure as indicated in plate 4.14.

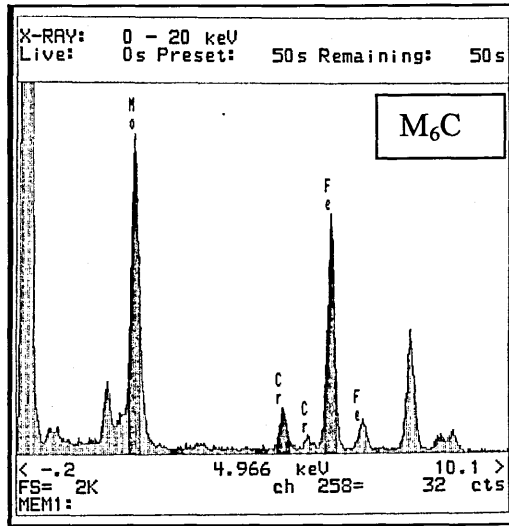
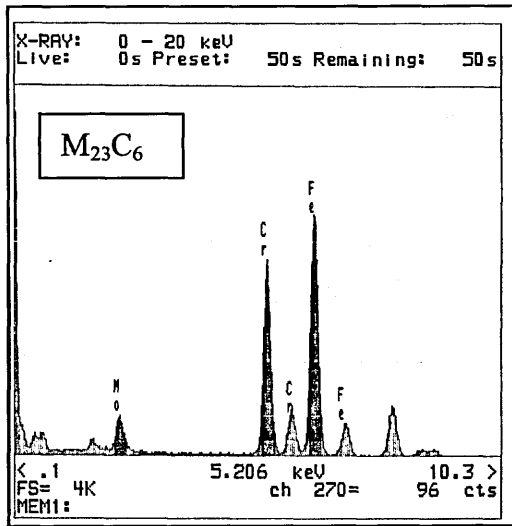
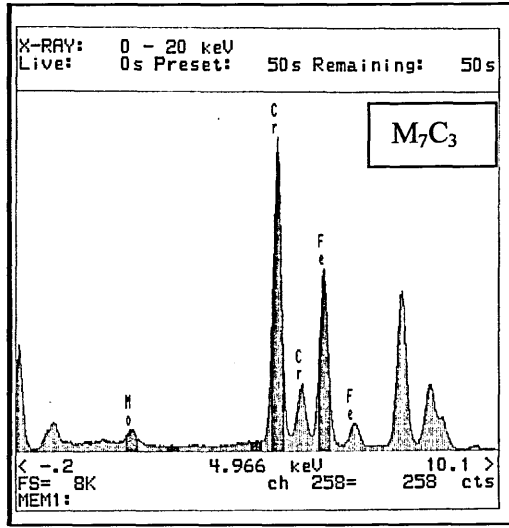
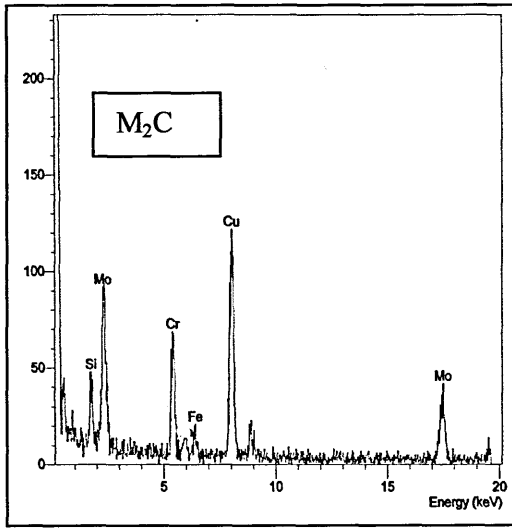


Figure 4.1: Typical EDX spectra for the carbides in 2.25%Cr-1%Mo alloy.

4.3 The Tempering Behaviour of Fully Bainitic 2.25%Cr-1%Mo Alloy Steel

Exposure of the bainite phase to elevated temperatures results in a dispersion of carbides, which progressively coarsen with time. To facilitate a comparison with microstructural changes during subsequent creep tests, when there is the added complication of both external and localised internal stresses, a tempering trial on samples initially with the fully bainitic microstructure, was carried out. Details of the experimental procedures used for this trial are given in section 3.3.2.

Samples of the 100% bainite starting material were tempered at temperatures of 650°C, 700°C and 750°C for times up to 5000 hours as shown below in Table 4.6.

Tempering Duration (h)	Tempering Temperatures (°C)		
	650	700	750
0.5	√	√	√
1.0	√	√	√
5	√	√	√
10	√	√	√
25	√	√	√
50	√	√	√
100	√	√	√
1000		√	
5000		√	

Table 4.6: Temper trial sample conditions.

After heat treatment the Vickers hardness of each sample was determined and specimens prepared for optical microscopy, SEM and TEM examination.

4.3.1 Hardness Test Results

Hardness tests were performed on each of the tempered, fully bainitic samples using a Vickers hardness testing machine and a load of 20Kg. The results are detailed below in Table 4.7 and presented graphically in Figure 4.2.

As can be seen from Figure 4.2 for each tempering temperature the hardness of the material was found to decrease with time at temperature. The rate of the reduction in hardness was highest in the initial period of leading to a period of almost constant hardness in the intermediate period and softening slightly at extended times. As might be expected, the degree of softening after any particular interval was increased with increasing tempering temperature.

No secondary hardening peaks due to the precipitation of M_2C , as described by Baker and Nutting^[17], were observed in these trials.

The hardness test data in Table 4.7 may be represented in the form of a Holloman – Jaffe plot, as described by Honeycombe^[23], in order to assess the combined effect of time and temperature on the carbide evolution process as shown in Figure 4.3.

Although the general trend observed, after the first 0.5 hour, is for a gradual reduction in hardness with increasing temperature the Holloman - Jaffe plot suggests that at extended times the samples tempered do not follow a linear relationship when a constant of 20 is used.

Temp. °C	Tempering Time (Hours) / Vickers Hardness No. (HV _{20kg})									
	0	0.5	1.0	5.0	10	25	50	100	1000	5000
650	233 ±2.55	219 ±6.39	212 ±4.79	206 ±5.99	192 ±1.70	186 ±1.21	183 ±2.69	168 ±2.57	n.a	n.a
700	233 ±2.55	194 ±4.11	194 ±2.07	192 ±1.81	192 ±1.95	173 ±3.81	169 ±2.56	161 ±2.40	159 ±2.76	136 ±3.77
750	233 ±2.55	185 ±4.24	184 ±2.94	175 ±4.37	176 ±4.93	164 ±4.22	163 ±3.33	148 ±3.26	n.a	n.a

Table 4.7: Hardness results for the tempered fully bainitic samples ($\pm 2\sigma$).

Note* - n.a = not applicable.

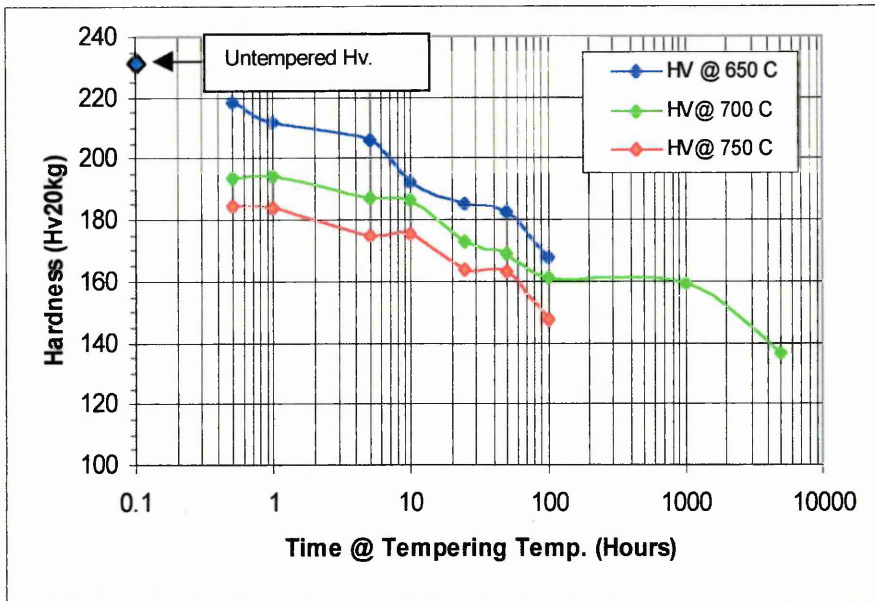


Figure 4.2: Graph showing Vickers hardness values against tempering temperature and time for the fully bainitic specimens.

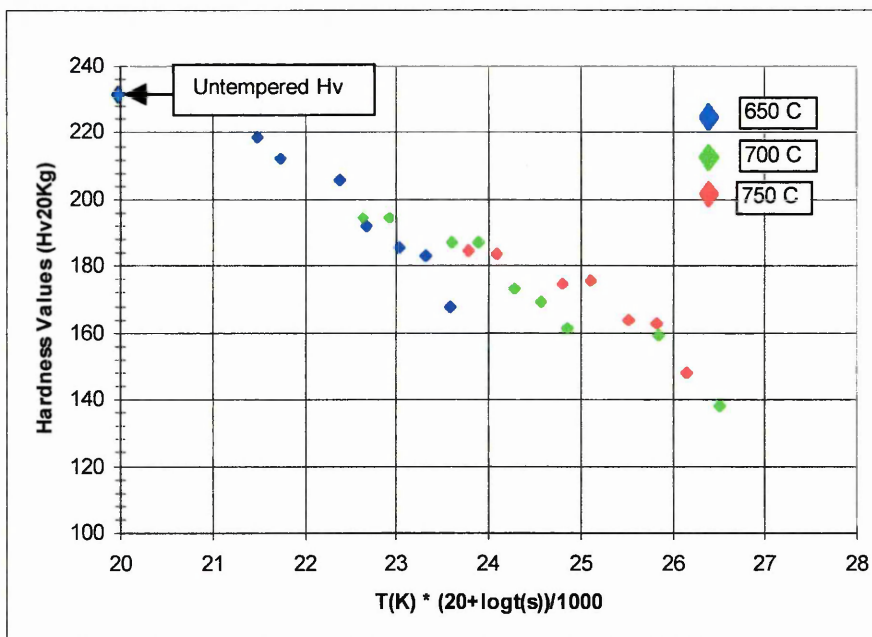


Figure 4.3: Graph showing Vickers hardness values against the Holloman - Jaffe parameter, $P = T \times (k + \log t)$, for the fully bainitic specimens.

Where: T = temp. (K), k = a constant taken to be 20 and t = time (secs).

4.3.2 Microstructural Changes During Tempering

Specimens were prepared from each of the heat treat samples for examination using both the scanning electron microscope and transmission / scanning transmission electron microscope.

4.3.2(a) Examination by Scanning Electron Microscopy

Scanning electron microscopy was utilised to study the general micro-structural changes taking place in the bainitic microstructure at all three tempering trial temperatures.

Plates 4.15 - 4.21 show micrographs of the samples tempered at 700°C for 0.5, 5, 50, 100 and 5000 hours. General microstructural assessment of the structures depicted in these micrographs indicated that for a constant tempering temperature the microstructure changes with time.

In the sample tempered for 0.5 hours, Plate 4.15, the intra-granular carbides were very fine and observed, generally, to decorate the original bainite lath boundaries. The carbides at the grain boundaries in the 0.5 hour were slightly larger and more globular than those at the intra-granular sites.

With increasing time from 0.5 hours to 5, 50 and 100 hours, Plates 4.15 - 4.18, the carbides at both intra and inter-granular sites were observed to spheroidise, grow and reduce in number rendering the original bainite lath boundaries indistinguishable. In addition the samples tempered at 50 and 100 hours clearly showed evidence of sub-boundary formation and the onset of recrystallization.

After 1000 hours the large grain boundary carbides were observed to be growing in an irregular shaped manner and at the expense of carbides in the

neighbouring regions. This is evident from the images shown in Plates 4.19 and 4.20.

After 5000 hours at 700°C, Plate 4.21, the original bainite morphology was no longer visible and the structure consisted of recrystallized ferrite grains delineated by large spheroidal carbides.

To consider the effect of varying the tempering temperature for a constant tempering time Plates 4.22 and 4.23, depicting the micrographs of the samples tempered for 50 hours at 650°C and 750°C respectively, were included for comparison with Plate 4.17. For a constant duration with increasing temperature the microstructure was observed to change in the same manner as that described above for a constant temperature and increasing time. The micrograph of the sample tempered at 750°C for 50 hours, Plate 4.23, showed a well developed sub-structure similar in nature to that observed in Plate 4.18 for the sample tempered at 700°C for 100 hours.

A general observation was that a degree of re-crystallisation was found to be occurring in samples having a Holloman - Jaffe parameter value of greater than about 25.

4.3.2.b Examination by Scanning Transmission Electron Microscopy

Scanning transmission electron microscopy was used to assess the changes in carbide precipitate morphology, size, number and density in the samples tempered at 700°C utilising the image analysis routine specifically devised for this project as described in section 3.6.2(d).

The samples tempered at 700°C for 0.5, 5, 50 and 5000 hours were selected for the analysis routine to show the progression of the carbide evolution process, described qualitatively in section 4.3.2.a.

Tables 4.8 - 4.11 and Figures 4.4 - 4.7 show the size distribution data and charts for the carbides classified in the analysis, Table 4.12 and Figure 4.8 show the change in carbide type with time at 700°C and Figures 4.9 - 4.13 show the combined results of percent carbide type against size distribution.

Figure 4.4 shows that after 0.5 hours at a tempering temperature of 700°C the carbides classified as M_7C_3 are the most prevalent and largest of the carbides existing at this stage. $M_{23}C_6$ carbides existed in smaller size ranges and in lesser amounts than M_7C_3 in this sample as did M_3C and M_2C . M_6C type carbides were not detected at this early stage of tempering.

M_3C carbides were absent in all other samples tempered for duration's longer than 0.5 hours.

With increasing time to 5 hours and subsequently 50 hours, Figures 4.5 and 4.6, the $M_{23}C_6$ carbides were observed to be dominant. The majority of carbides after tempering for 5 hours existed in the 0.1 - 0.3 micron size range with a lesser distribution in the 0.3 - 0.6 micron range. The occurrence of M_7C_3 and $M_{23}C_6$ carbides in this larger size range decreased with increasing time to 50 hours as the M_6C carbides began to evolve. Fine M_2C carbides were most abundant in the sample tempered for 5 hours and disappeared after 50 hours. After 5000 hours, as indicated in Figure 4.7, M_6C carbides were the major carbides remaining in the material tempered at 700°C, only a few $M_{23}C_6$ carbides coexisted at this stage. The evolution of the M_6C carbide at the expense of all other carbides is clearly represented in Figure 4.8 and appears to begin at a tempering duration of ~50 hours. The size distribution of each carbide type and their predominance at each stage of the tempering process up to 5000 hours is indicated in Figures 4.9 – 4.13.

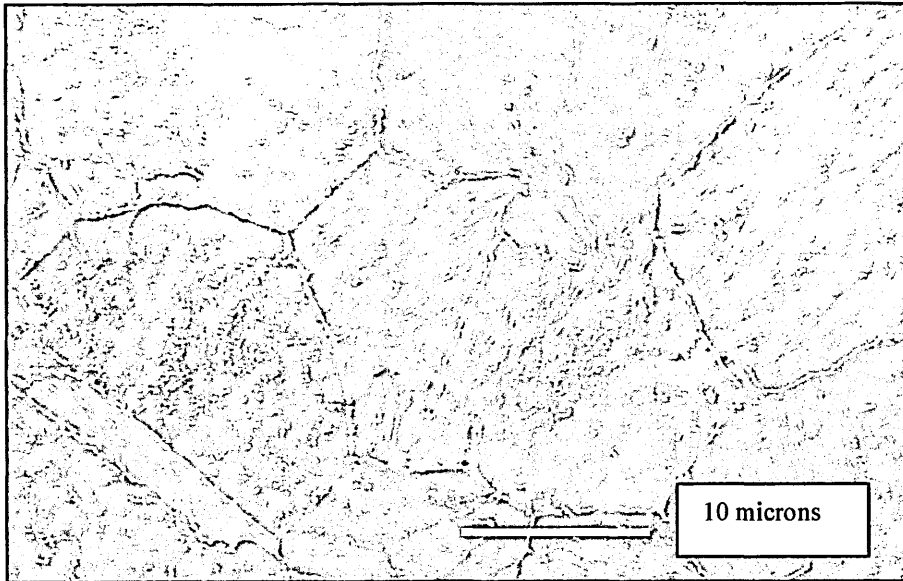


Plate 4.15: SEM micrograph of the fully bainitic sample tempered at 700°C for 0.5h.

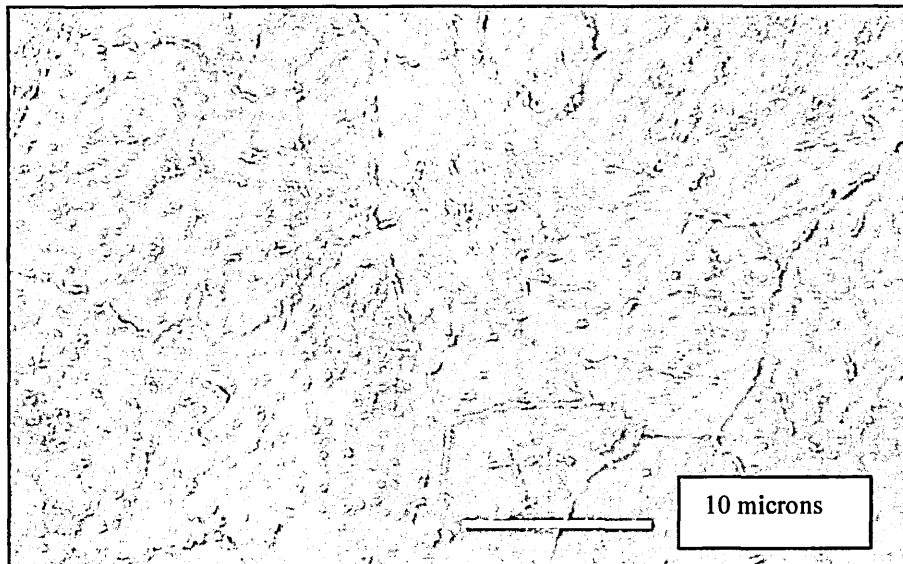


Plate 4.16: SEM micrograph of the fully bainitic sample tempered at 700°C for 5h.

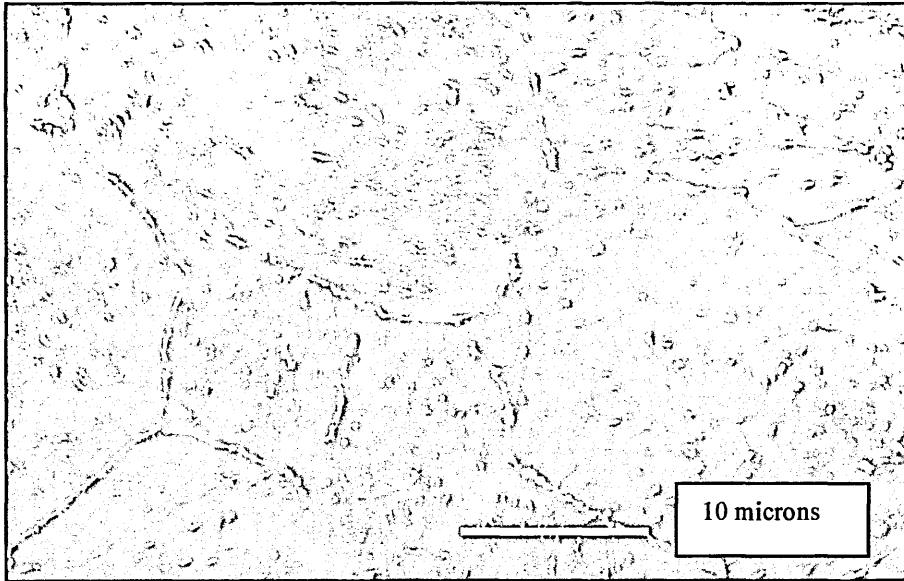


Plate 4.17: SEM micrograph of the fully bainitic sample tempered at 700°C for 50h.

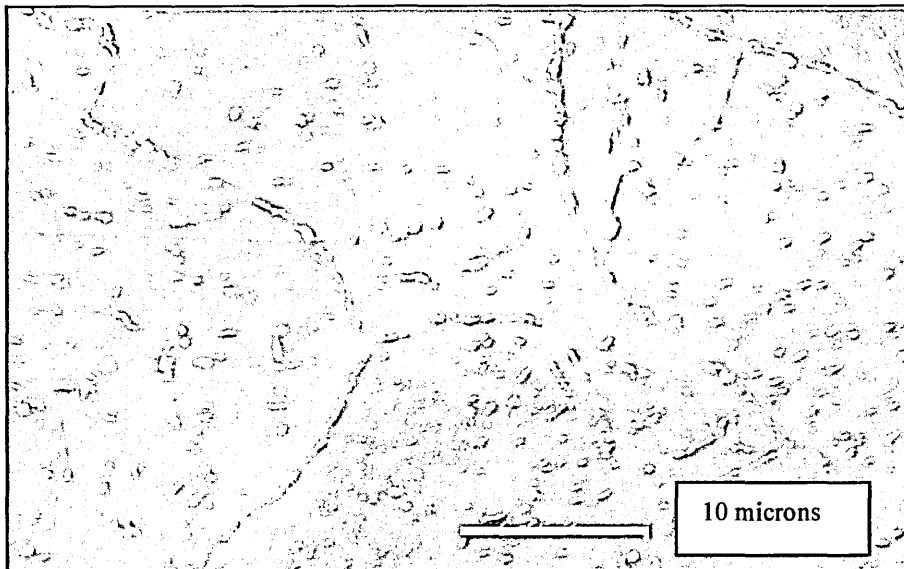


Plate 4.18: SEM micrograph of the fully bainitic sample tempered at 700°C For 100h.

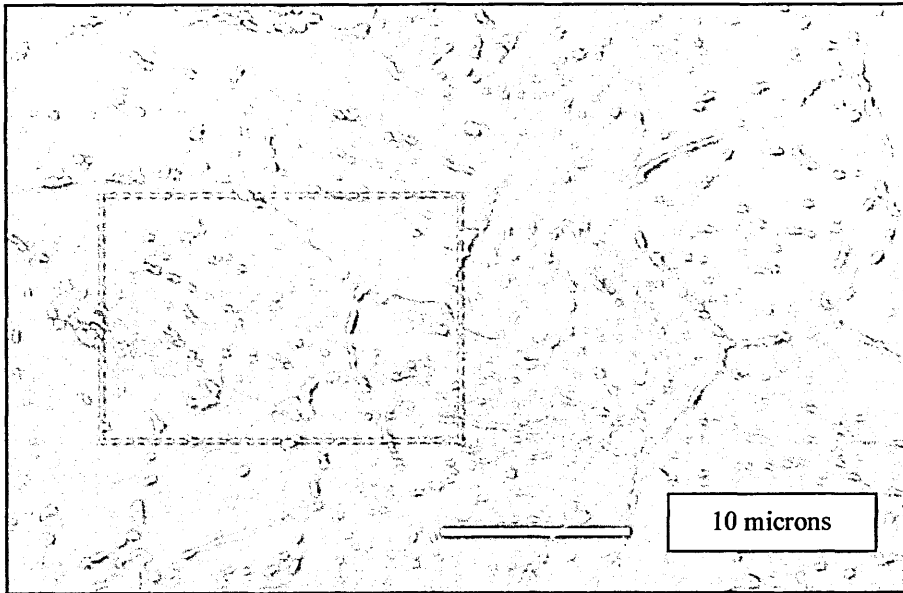


Plate 4.19: SEM micrograph of the fully bainitic sample tempered at 700°C For 1000h.

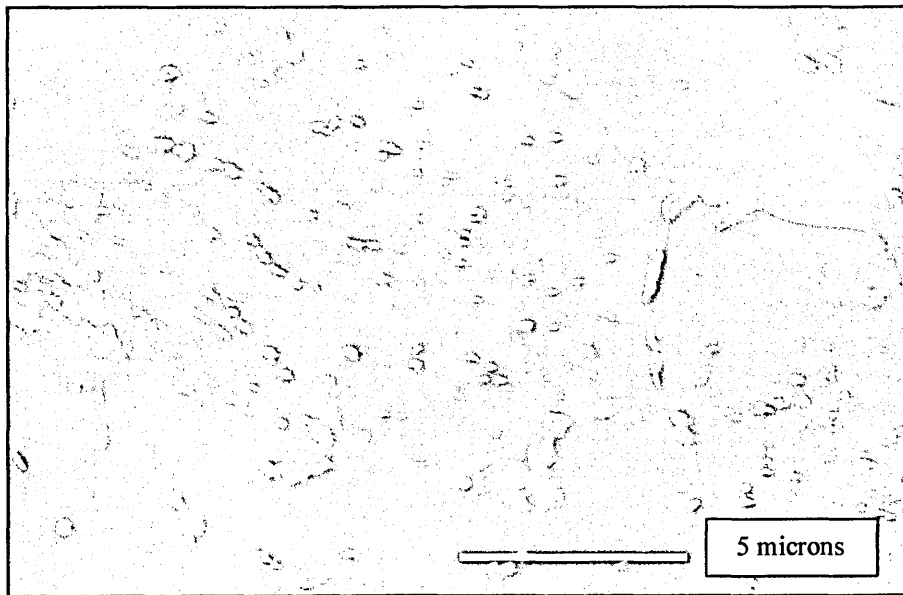


Plate 4.20: High magnification SEM image of the area out-lined in plate 4.19 showing irregular growth of grain boundary carbides and associated precipitate free zones.

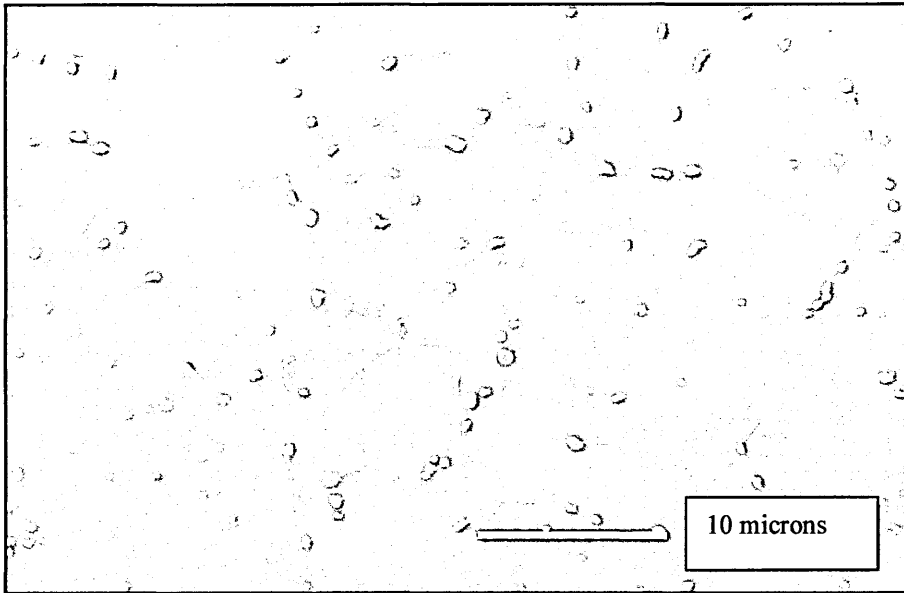


Plate 4.21: SEM micrograph of the fully bainitic sample tempered at 700°C For 5000h.

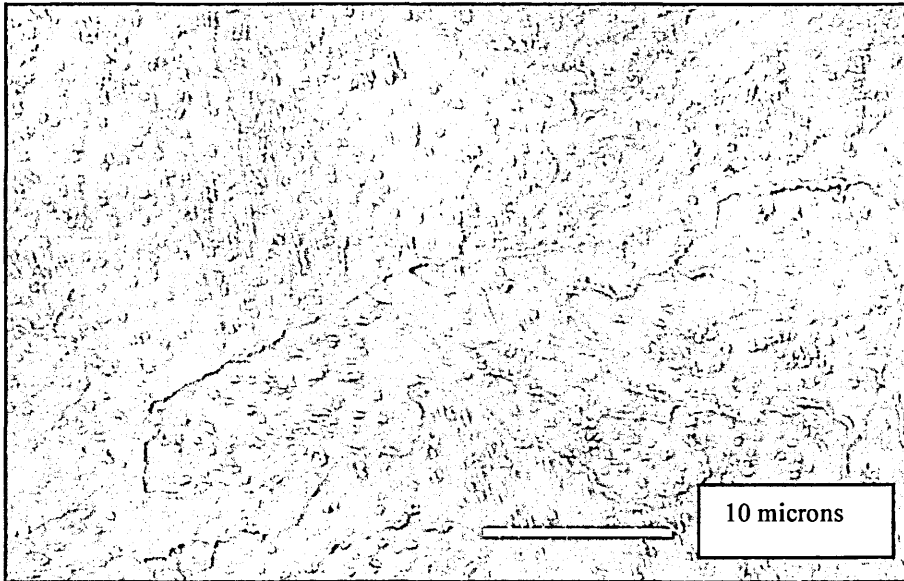


Plate 4.22: SEM micrograph of the fully bainitic sample tempered at 650°C for 50h.

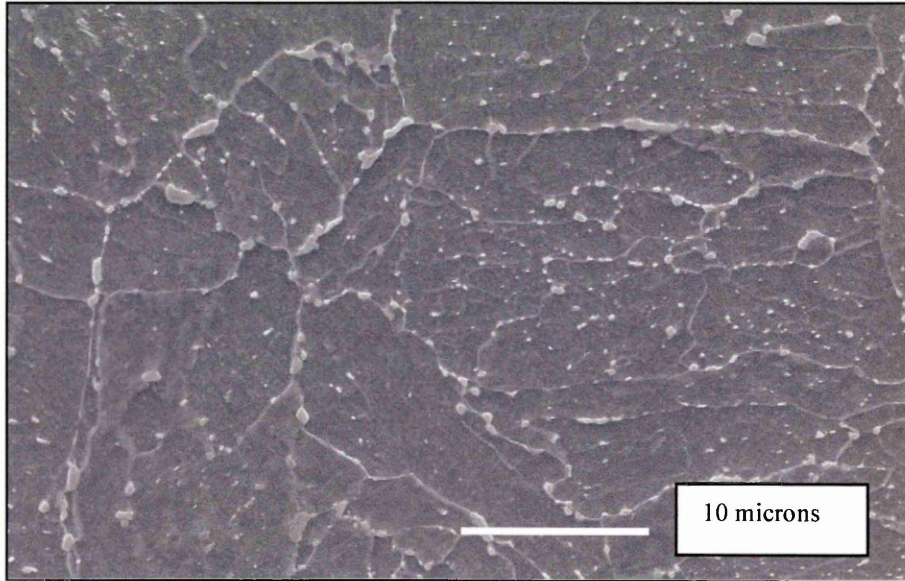


Plate 4.23: SEM micrograph of fully bainitic sample tempered at 750°C for 50h.

Particle Mean Diameter (microns)	Percentage Of Total No. Of Carbides				
	M ₃ C	M ₂ C	M ₇ C ₃	M ₂₃ C ₆	M ₆ C
0.0-0.1	1.8	2.1	4.8	7.4	0.3
0.1-0.2	2.7	0.0	17.2	11.6	0.0
0.2-0.3	1.8	0.0	18.2	7.4	0.0
0.3-0.4	0.0	0.0	12.8	1.8	0.0
0.4-0.5	0.0	0.0	6.0	0.0	0.0
0.5-0.6	0.3	0.0	2.1	0.0	0.0
0.6-0.7	0.0	0.0	1.2	0.0	0.0
0.7-0.8	0.0	0.0	0.6	0.0	0.0
0.8-0.9	0.0	0.0	0.0	0.0	0.0
0.9-1.0	0.0	0.0	0.0	0.0	0.0
Total %	6.6	2.1	62.9	28.2	0.3

Table 4.8: Carbide size distribution data for the fully bainitic sample tempered at 700°C for 0.5 hours.

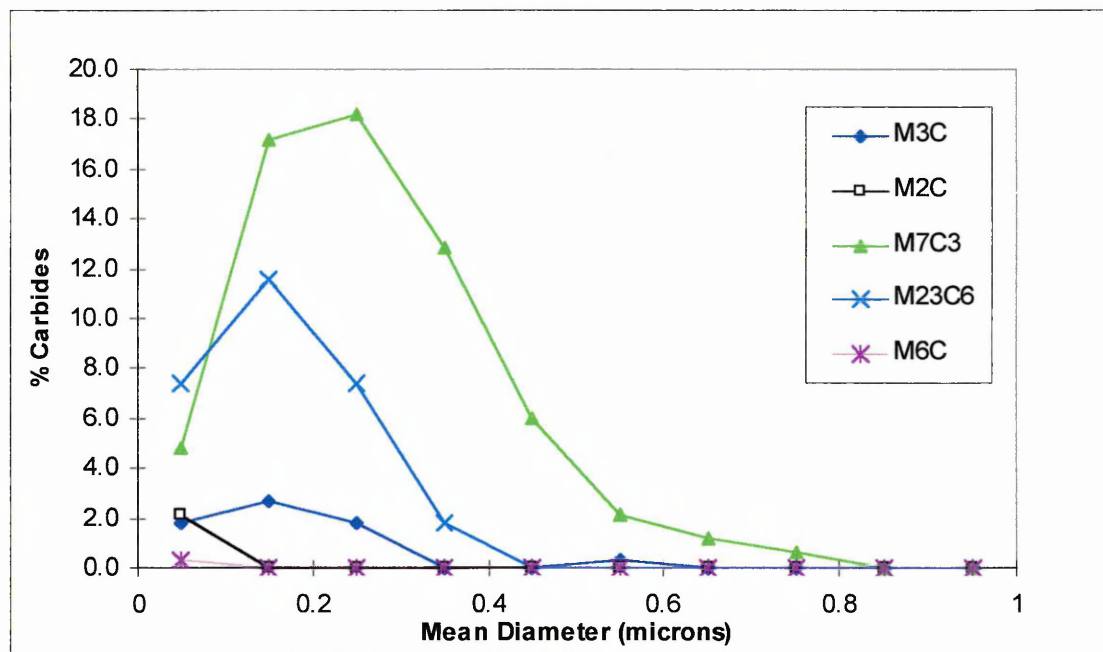


Figure 4.4: Size distribution curves for the various carbides identified in the fully bainitic sample tempered at 700°C for 0.5 hours.

Particle Mean Diameter (microns)	Percentage Of Total No. Of Carbides				
	M ₃ C	M ₂ C	M ₇ C ₃	M ₂₃ C ₆	M ₆ C
0.0-0.1	0.0	12.0	8.0	4.0	0.0
0.1-0.2	0.0	4.0	12.0	24.0	0.0
0.2-0.3	0.0	0.0	12.0	14.0	0.0
0.3-0.4	0.0	0.0	0.0	6.0	0.0
0.4-0.5	0.0	0.0	2.0	2.0	0.0
0.5-0.6	0.0	0.0	0.0	0.0	0.0
0.6-0.7	0.0	0.0	0.0	0.0	0.0
0.7-0.8	0.0	0.0	0.0	0.0	0.0
0.8-0.9	0.0	0.0	0.0	0.0	0.0
0.9-1.0	0.0	0.0	0.0	0.0	0.0
Total %	0.0	16.0	34.0	50.0	0.0

Table 4.9: Carbide size distribution data for the fully bainitic sample tempered at 700°C for 5 hours.

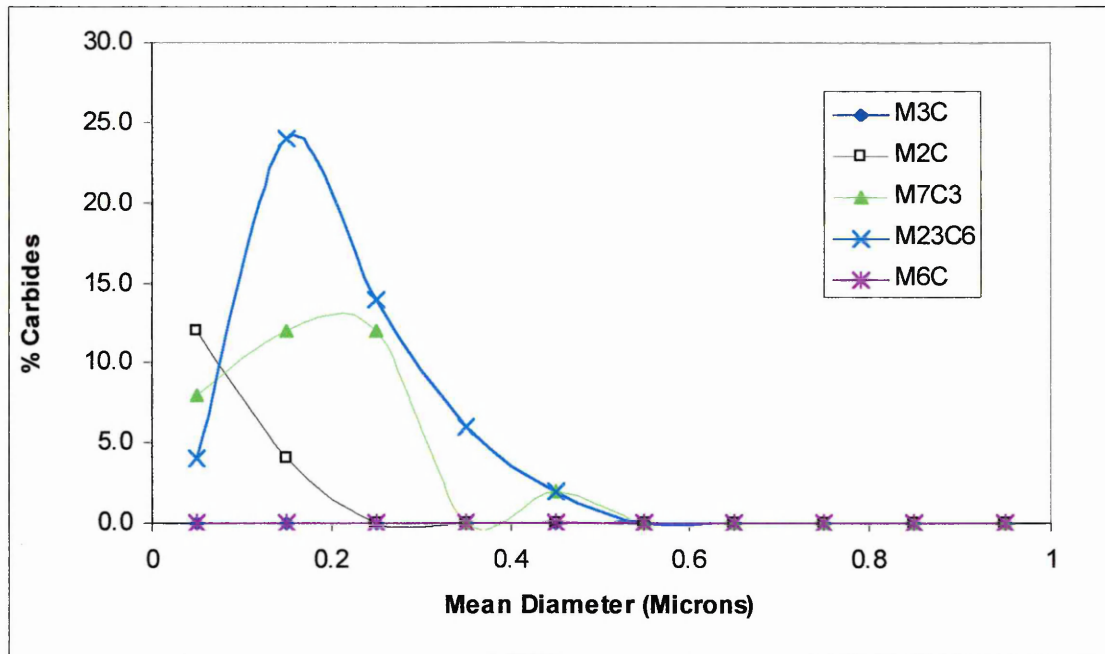


Figure 4.5: Size distribution curves for the various carbides identified in the fully bainitic sample tempered at 700°C for 5 hours.

Particle Mean Diameter (microns)	Percentage Of Total No. Of Carbides				
	M ₃ C	M ₂ C	M ₇ C ₃	M ₂₃ C ₆	M ₆ C
0.0-0.1	0.0	0.5	13.8	19.9	0.0
0.1-0.2	0.0	0.0	11.0	22.1	0.5
0.2-0.3	0.0	0.0	4.9	12.1	1.1
0.3-0.4	0.0	0.0	2.2	2.2	1.1
0.4-0.5	0.0	0.0	1.1	1.1	1.6
0.5-0.6	0.0	0.0	0.0	0.5	0.5
0.6-0.7	0.0	0.0	0.0	0.0	1.6
0.7-0.8	0.0	0.0	0.0	1.1	0.5
0.8-0.9	0.0	0.0	0.0	0.0	0.0
0.9-1.0	0.0	0.0	0.0	0.5	0.0
Total %	0.0	0.5	33.0	59.5	6.9

Table 4.10: Carbide size distribution data for the fully bainitic sample tempered at 700°C for 50 hours.

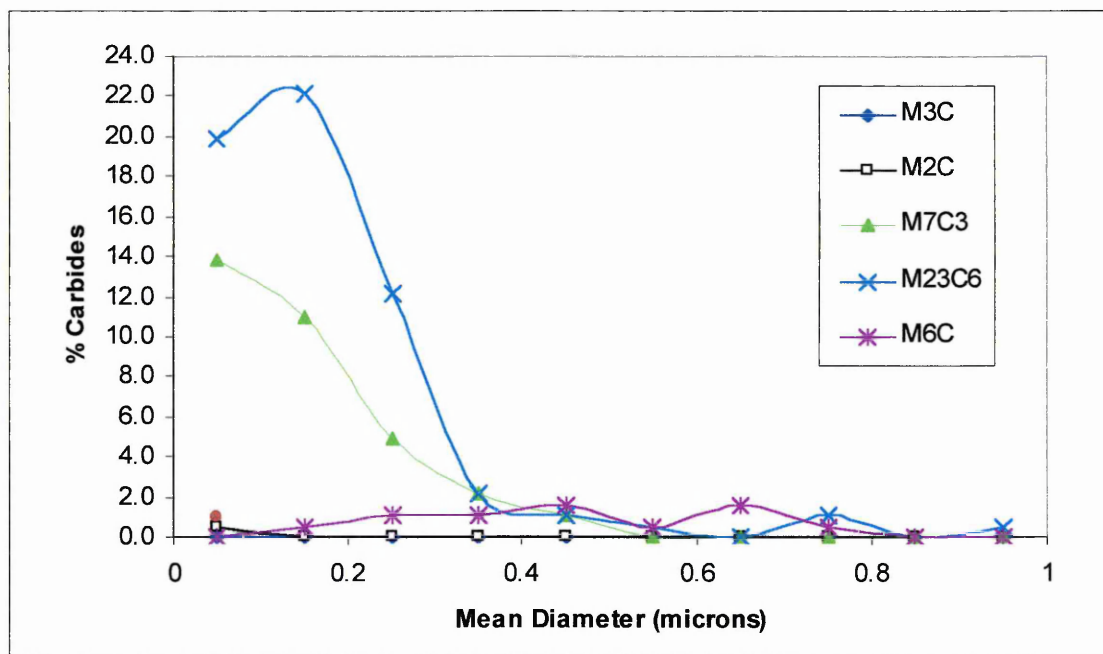


Figure 4.6: Size distribution curves for the various carbides identified in the fully bainitic sample tempered at 700°C for 50 hours.

Particle Mean Diameter (microns)	Percentage Of Total No. Of Carbides				
	M ₃ C	M ₂ C	M ₇ C ₃	M ₂₃ C ₆	M ₆ C
0.0-0.1	0.0	0.0	0.0	1.3	5.3
0.1-0.2	0.0	0.0	0.0	0.0	12.7
0.2-0.3	0.0	0.0	0.0	0.0	23.9
0.3-0.4	0.0	0.0	0.0	0.7	21.3
0.4-0.5	0.0	0.0	0.0	0.0	14.7
0.5-0.6	0.0	0.0	0.0	0.0	7.4
0.6-0.7	0.0	0.0	0.0	0.0	2.0
0.7-0.8	0.0	0.0	0.0	0.7	4.0
0.8-0.9	0.0	0.0	0.0	0.0	4.0
0.9-1.0	0.0	0.0	0.0	0.0	2.0
Total %	0.0	0.0	0.0	2.7	97.3

Table 4.11: Carbide size distribution data for the fully bainitic sample tempered at 700°C for 5000 hours.

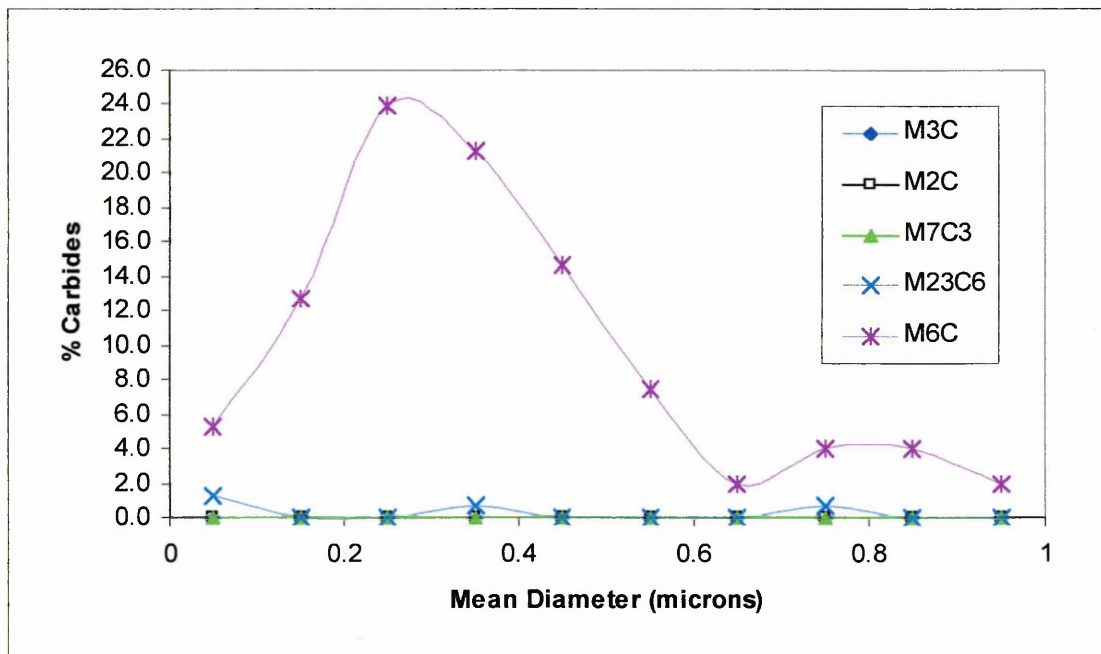


Figure 4.7: Size distribution curves for the various carbides identified in the fully bainitic sample tempered at 700°C for 5000 hours.

Time (Hours)	Percentage Of Total No. Of Carbides				
	M ₃ C	M ₂ C	M ₇ C ₃	M ₂₃ C ₆	M ₆ C
0.5	6.6	2.1	62.9	28.2	0.3
5	0.0	16.0	34.0	50.0	0.0
50	0.0	0.5	33.0	59.5	6.9
5000	0.0	0.0	0.0	2.7	97.3

Table 4.12: Change in carbide type with tempering time at 700°C for the fully bainitic samples.

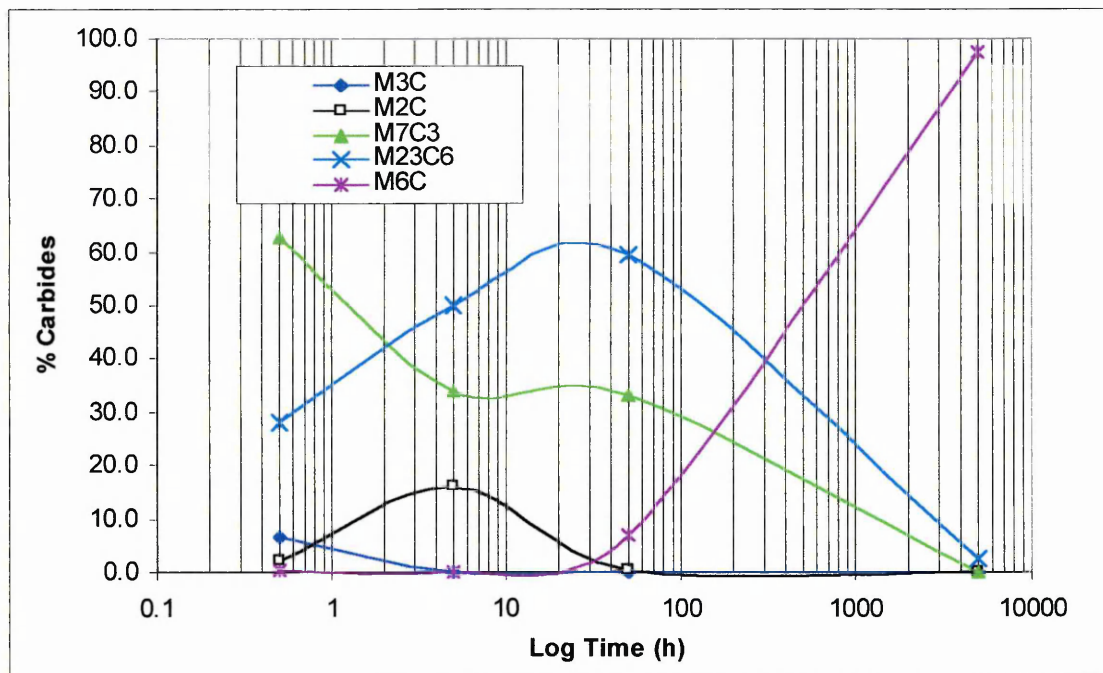


Figure 4.8: Change in carbide type with tempering time at 700°C for the fully bainitic samples.

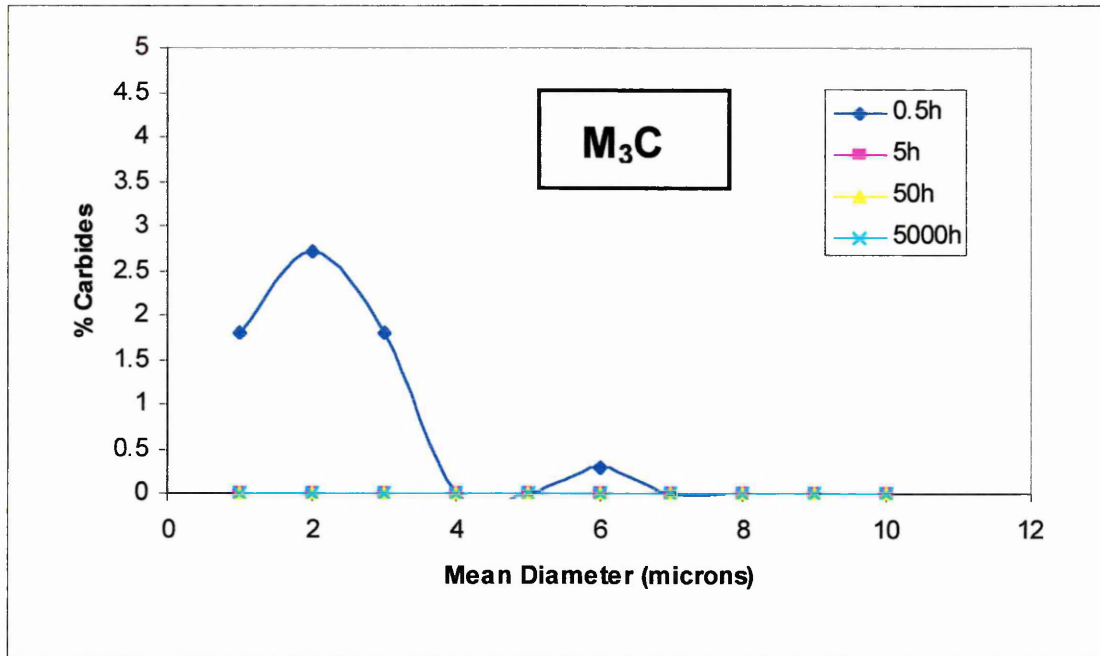


Figure 4.9: Graph showing M_3C type carbides as a percent of the total detected for each tempering duration plotted against mean diameter.

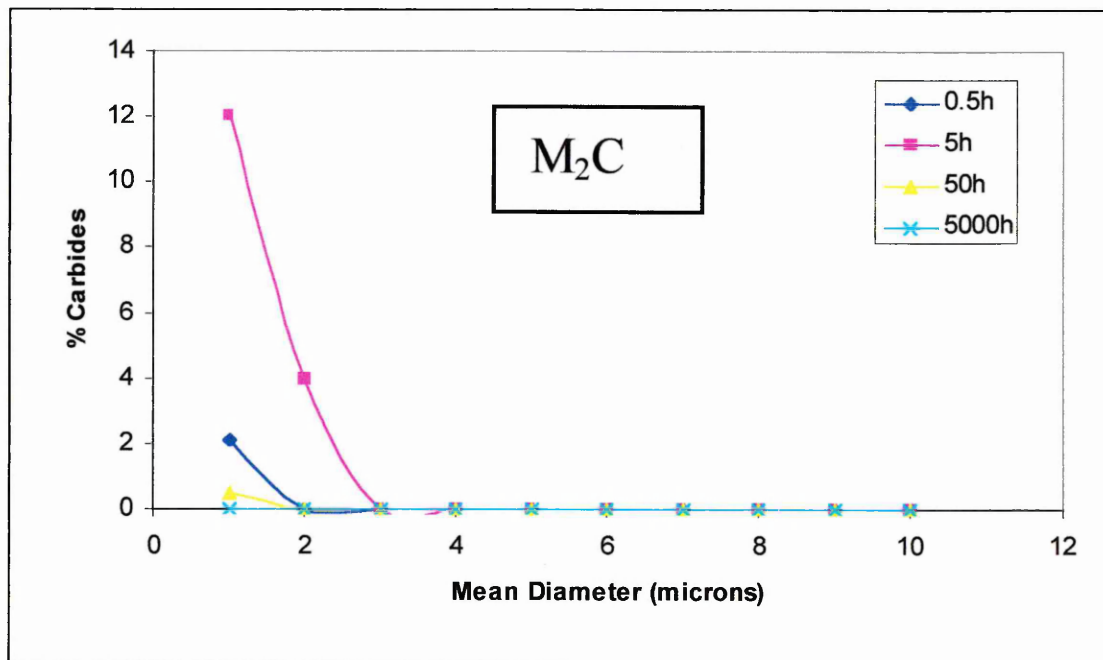


Figure 4.10: Graph showing M_2C type carbides as a percent of the total detected for each tempering duration plotted against mean diameter.

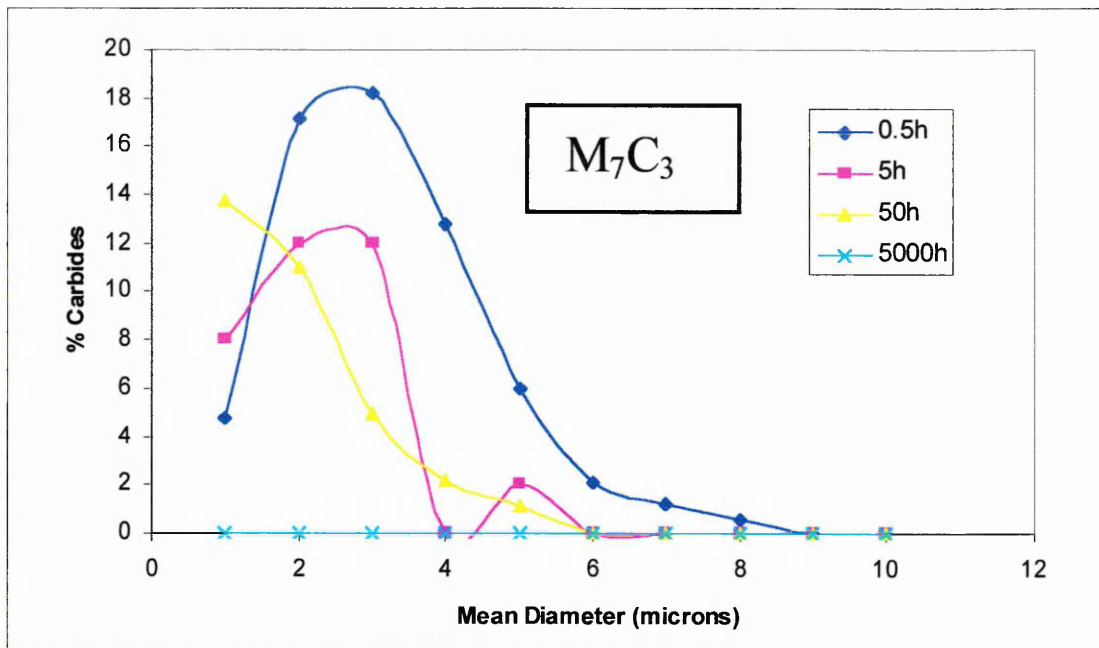


Figure 4.11: Graph showing M_7C_3 type carbides as a percent of the total detected for each tempering duration at 700°C plotted against mean diameter.

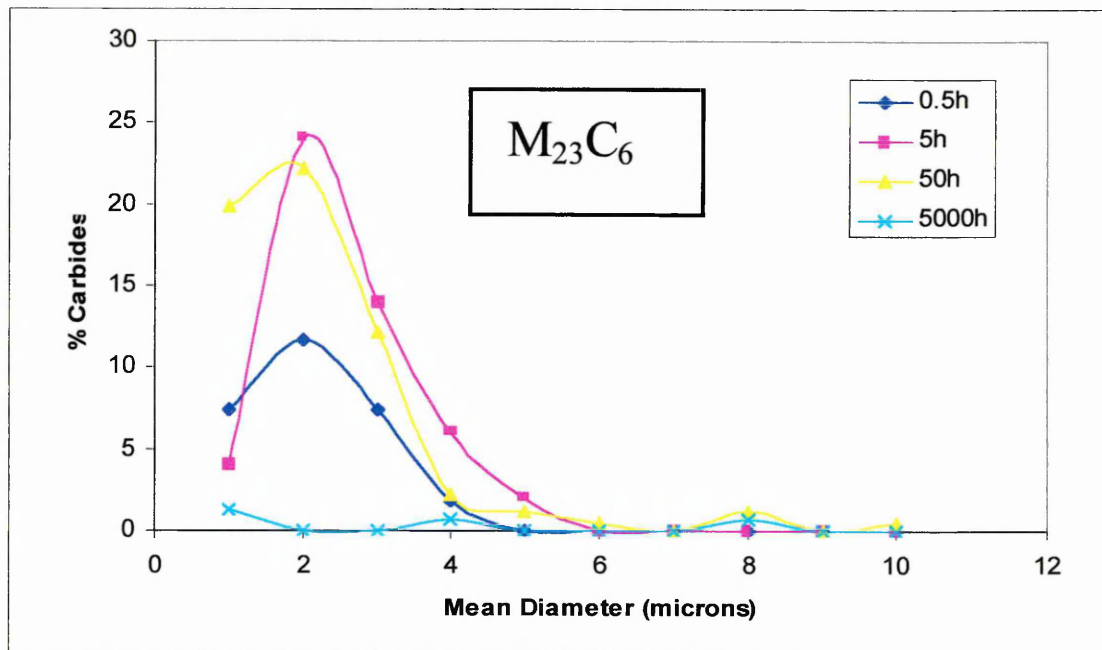


Figure 4.12: Graph showing $M_{23}C_6$ type carbides as a percent of the total detected for each tempering duration at 700°C plotted against mean diameter.

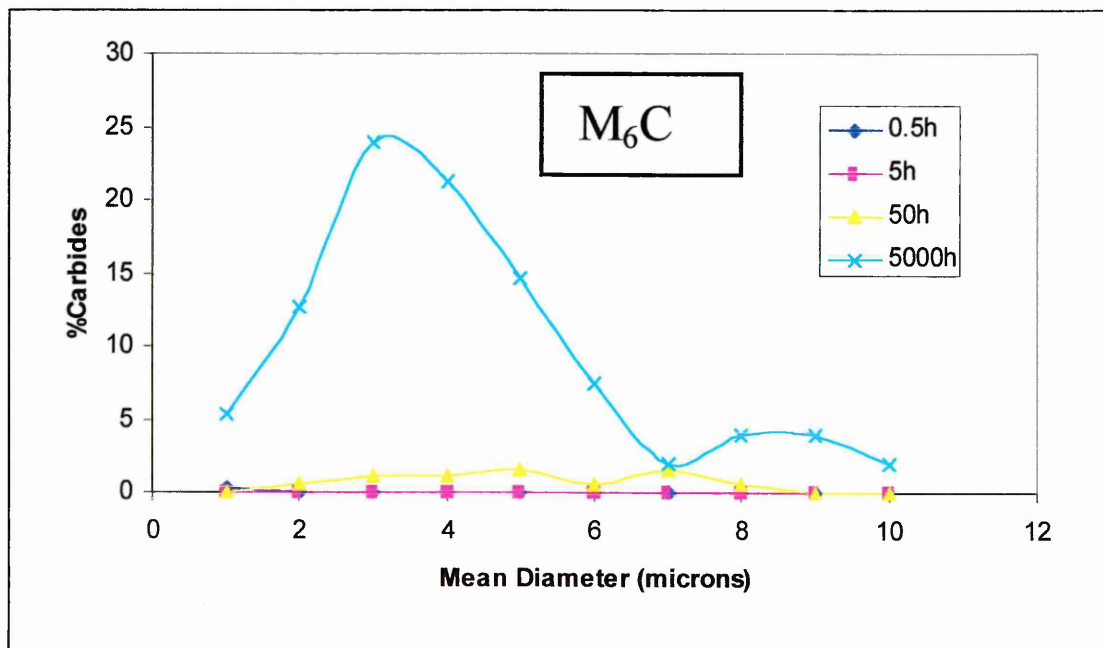


Figure 4.13: Graph showing M_6C type carbides as a percent of the total detected for each tempering duration at 700°C plotted against mean diameter.

4.4 Creep Testing and Deformation Assessment

4.4.1 Crack Opening Displacement Measurement

The experimental techniques adopted to assess the creep deformation behaviour of the steel being investigated have been described in section 3.4.3. Compact tension specimens of 2.25%Cr-1%Mo steel with the previously specified starting microstructures were prepared, each with a spark eroded notch tip to simulate the presence of a pre-existing defect. These were then creep tested to assess the affect of the presence the pre-existing defect on the creep crack initiation and growth process in samples exhibiting each of the three microstructural profiles.

Crack opening displacement values for each test specimen were determined by measuring the Y-axis displacement between two parallel lines of hardness indentations which had been made along the specimen width prior to the test as described in section 3.4.3(c).

Tables 4.13 and 4.14 present the results for the x/y displacement values versus time for creep tests carried out at 550°C on the 100% bainitic and ferrite / bainite specimens. The displacement values for the ferrite / pearlite test specimens, tested at the collaborating establishment, were not available for analysis and are, therefore, absent from this section of the results.

The y -axis displacement values were plotted against the x-axis position along the specimen width to produce charts as shown Figures 4.14 - 4.17. The positions of the CT specimen load point, (LP). and spark eroded notch tip, (NT), have been indicated on the charts to show the difference in the degrees of deformation at these two critical points. The y-displacement at the notch tip position also allowed an assessment of the relationship between notch tip opening displacement, creep cavity density and crack extension to be made.

For the crack opening displacement values of the 100% bainite and mixed ferrite / bainite samples two charts were plotted in each case. This was necessary to compare the deformation characteristics of all the test specimens in each microstructural condition concurrently and to assess the crack tip opening displacement values of the specimens tested for the shortest times. The specimens tested for the shorter duration's, in particular, gave information regarding the critical stages of creep crack initiation and early growth.

Comparison of the crack opening displacement values for the tempered bainite and mixed ferrite / bainite structures show a marked difference in the deformation behaviour of the two materials. Assessment of the deformation lines between the load point and notch tip points for the two materials showed that the 100% bainite structure was less ductile than the mixed ferrite / bainite structure. This is indicated by the straight line nature of the graph in Figure 4.15 as opposed to the curved line in Figure 4.17.

The crack, or notch, tip opening displacement values (CTOD's), as detailed in Table 4.15, were determined by extrapolating the deformation lines plotted on Figures 4.14 – 4.17 to the notch tip points. Although an absolute like for like comparison of the CTOD results was not possible due to the difference in loading stresses and test duration's it was noticeable that the CTOD values for the ferrite / bainite material, tested at a stress of 110MPa, were less than those observed for the fully bainitic structure, tested for similar test duration's and a stress of 100MPa.

No. Of Hours at 550° C	X/Y-Displacement (mm)							
	2.54	5.08	7.62	10.16	12.7	15.24	17.78	20.32
300	1	1	0.8	0.6	0.5	0.3	0.2	0.1
350	1.2	1.2	1	0.8	0.6	0.6	0.4	0.3
400	1.3	1.2	1	0.8	0.6	0.5	0.4	0.2
500	1.8	1.6	1.3	1.1	0.9	0.8	0.6	0.4
600	2	1.9	1.5	1	1	0.8	0.6	0.4
800	3.6	3.3	2.9	2.5	2	1.9	1.6	0.9
1000	4.9	4.5	3.8	3.8	2.9	2.6	2.1	1.6

Table 4.13: Y-displacement values of hardness indentations for 100% tempered bainite starting material tested at a stress of 100MPa for times between 300 and 1000 hours.

No.Of Hours at 550°C	X/Y Axis Displacement (mm)							
	2.54	5.08	7.62	10.16	12.7	15.24	17.78	20.32
300	1	1	0.7	0.6	0.5	0.3	0.2	0.1
700	2	1.7	1.4	1.2	0.9	0.6	0.3	0.2
850	2.3	1.9	1.5	1.3	1	0.7	0.5	0.3
1000	3.3	3	2.6	2	1.3	0.8	0.5	4
1500	10.2	9.4	8.2	6.9	5.7	4.6	3.8	2.9

Table 4.14: Y-displacement values of hardness indentations for mixed ferrite / bainite starting material tested at a stress of 110MPa for times between 300 and 1500 hours.

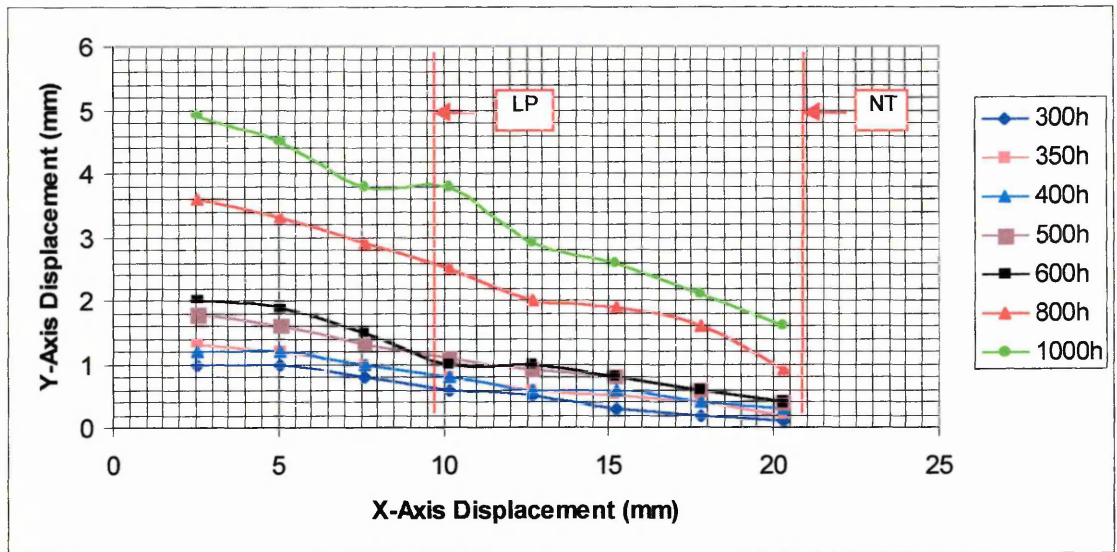


Figure 4.14: Crack opening displacement values for the fully bainitic sample tested at a stress of 100MPa and 550°C for times between 300 – 1000h.

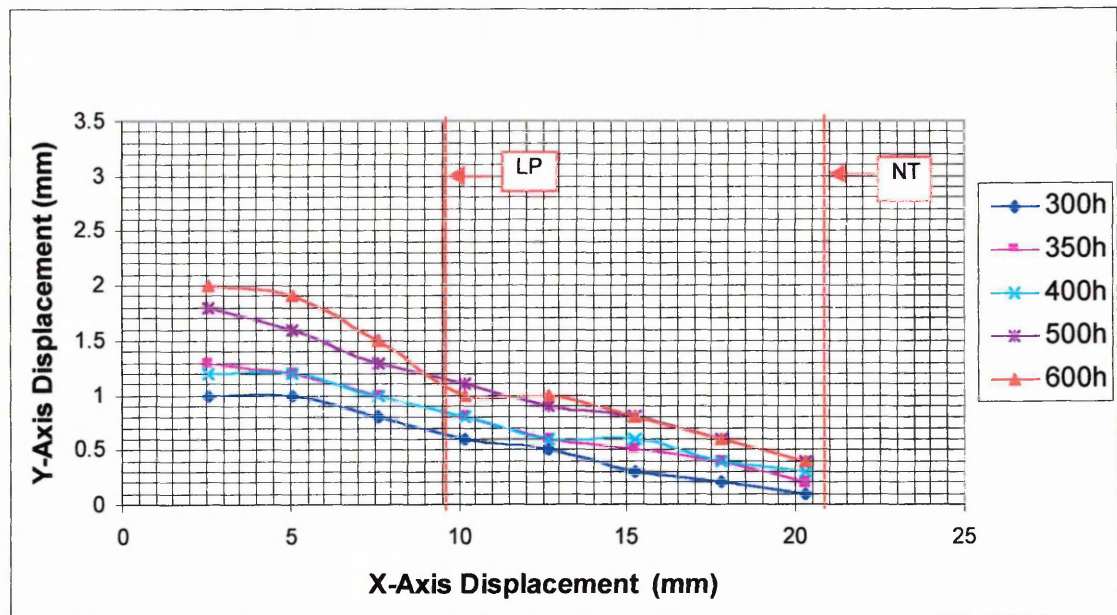


Figure 4.15: Crack opening displacement values for the fully bainitic sample tested at a stress of 100MPa and 550°C for times between 300 – 600h.

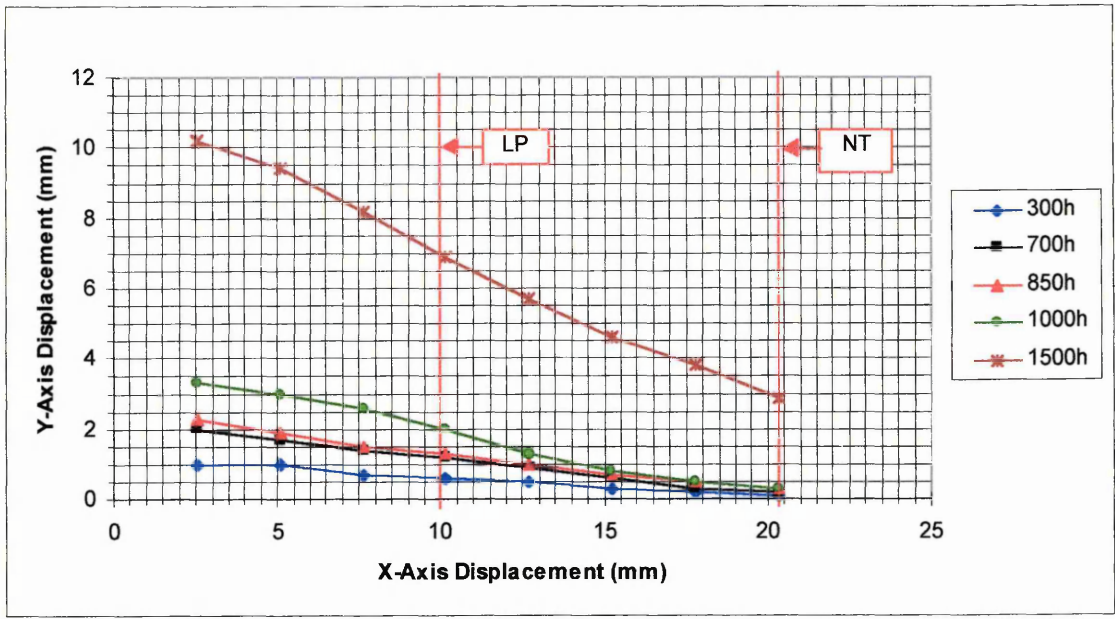


Figure 4.16: Crack opening displacement values for the ferrite / bainite sample tested at a stress of 110MPa and 550°C for times between 300 – 1500h.

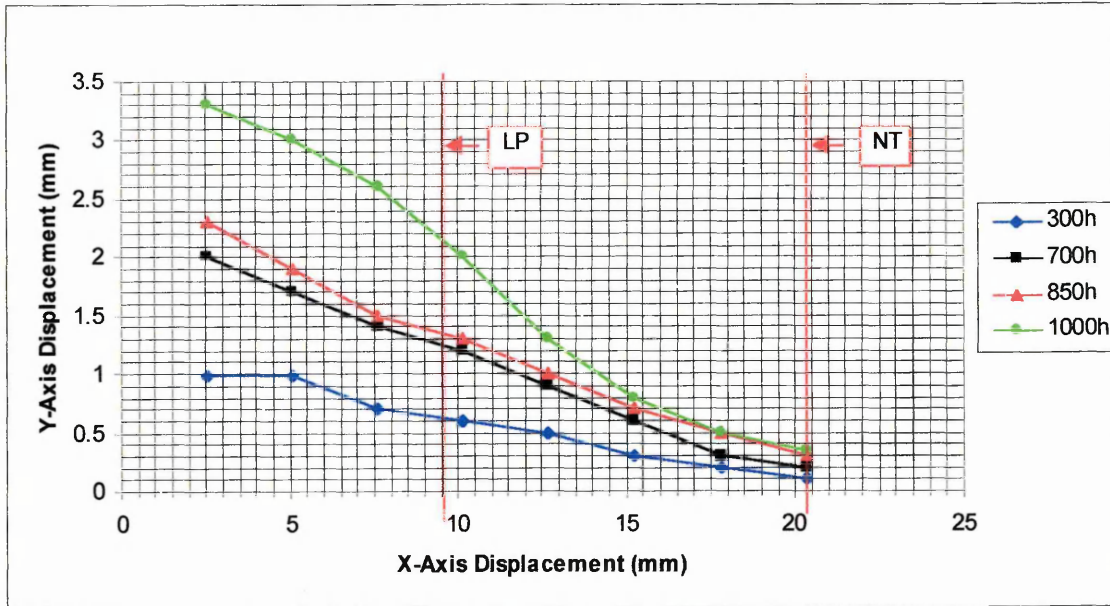


Figure 4.17: Crack opening displacement values for the ferrite / bainite sample tested at a stress of 110MPa and 550°C for times between 300 – 1000h.

	Ferrite / Bainite Tested at 110MPa					Bainite Tested at 100MPa							Pearlite Tested at 85MPa				
	0	300	700	850	1000	1500	0	300	350	400	500	600	800	1000	0	3680	6850
Test Duration (h)	0	300	700	850	1000	1500	0	300	350	400	500	600	800	1000	0	3680	6850
Crack Tip Opening Displacement (mm)	0.00	0.08	0.16	0.27	0.27	2.75	0.00	0.07	0.18	0.28	0.35	0.35	0.98	1.52	n.d	n.d	n.d

Table 4.15: Crack tip opening displacement results derived from CT specimens manufactured from the starting materials.

Note* - n.d = not determined

4.4.2 Creep Damage Assessment in the Scanning Electron Microscope

Scanning electron microscopy was used to assess the microstructure ahead of the CT notch in each of the tested specimens in order to assess the degree of creep damage and, hence, attempt to determine the mechanisms by which that damage had occurred. Samples were prepared from the test specimens and examined in the SEM, in the polished and etched condition, using the techniques as described in section 3.6.1.

In particular back-scattered electron imaging was used in conjunction with the image analysis routine outlined in section 3.6.1(c) to examine the extent of creep cavitation and its orientation with respect to the “pre-existing defect” created by the machined notch. The percentage of cavitation occurring in an area 1mm^2 around the notch tip was determined and graphically correlated against crack extension to ascertain the degree of creep ductility for the purpose of this project, creep crack initiation was considered to be taking place up to a crack extension of 1mm and therefore only specimens exhibiting $\leq 1\text{mm}$ of crack extension were considered for damage accumulation assessment.

Crack extension, measured using a linear measuring device incorporated in the SEM imaging software, was considered to have occurred if creep cavities had coalesced to give a micro-crack traversing more than one grain.

To help gain a better understanding of the mechanism of creep crack initiation a number of selected samples were examined in detail using high resolution secondary electron imaging.

4.4.2(a) 100% Bainite Specimens

Compact tension specimens of the steel initially with 100% bainite structure were creep tested at a constant applied stress of 100MPa and a temperature of 550°C for 300, 350, 400, 500, 600, 800 and 1000 hours.

Plate 4.24 shows a low magnification image of the microstructure in the specimen tested for 300 hours in the region close to the spark eroded notch tip. Although cracking had not yet occurred in this sample there was evidence of grain boundary voiding. Table 4.16 and Figure 4.18 show the analysis of void % in the vicinity of the notch and indicate that the densest region of void formation was in an area, 200 μ m x 200 μ m, immediately adjacent to the notch tip.

The microstructure of the sample tested for 350 hours, Plate 4.25, revealed a micro-crack emanating from a point approximately 50 μ m below the notch tip and slightly to the right of the notch tip centre. The crack extended up to a length of 0.49mm and appeared to follow an intergranular path. The corresponding void % data for the notch tip region for this sample is shown in Table 4.17 and Figure 4.19. Again the densest region of void formation is shown to be in the area closest to the notch tip with the distribution of voids in the surrounding area being slightly unevenly biased toward the right hand side.

After testing for 400 hours the degree of crack extension was found to have increased to a length of 0.62mm, the crack path being similar to that observed in the 350 hour specimen. In addition to the dominant 0.62mm crack a further crack was observed to have initiated, emanating from the left hand side of the notch and propagating towards the main crack path. Overall, as indicated in the void analysis results, Table 4.18 and Figure 4.20, the crack front and region of highest void density remained constrained to the material immediately ahead of the notch tip

The microstructures examined for the specimens tested for 500 hours and above showed crack extensions exceeding 1mm. These samples were not , therefore, analysed further in terms of void area % and distribution.

A summary of the crack extension values measured for all the 100% tempered bainite CT specimens and the area percent of voids detected in a region extending 1mm² around the notch tip centre is given in Table 4.19.

To assess the area around the notch tip in terms of its evolving microstructure and creep void orientation with respect to the stress axis a detailed microstructural analysis was carried out on the specimen tested for 400 hours. Plate 4.27 shows a montage of back scattered electron images depicting the areas assessed for void formation immediately ahead and to the right of the notch tip in the specimen tested for 400 hours, i.e. $0\mu\text{m}$ to $-800\mu\text{m}$ in the y-direction and $-100\mu\text{m}$ to $300\mu\text{m}$ in the x-direction. These images revealed that the main crack was extending in an intergranular manner at approximately 45° to the notch tip and, hence, 45° to the principal stress axis. Similarly, voiding observed in the area surrounding the crack appeared to be taking place preferentially on grain boundaries oriented at $\sim 45^\circ$ to the notch tip.

The incidence of void formation occurring in a particular orientation for the areas shown in Plate 4.27 was assessed in the SEM image analysis routine as described in section 3.6.1(c). The orientation of the voids, i.e., the orientation of the longest feret diameter of the void with respect to the notch tip, was subsequently plotted on a frequency chart as shown in Figure 4.21. The chart showed that the voids occurred most frequently at an orientation of $\pm 50 - 60^\circ$ with respect to the notch tip.

Plates 4.28 – 4.32 show high magnification secondary electron images resulting from the examination of selected grains exhibiting the initial stages of cavitation in the specimen tested for 400 hours. This examination was necessary to find evidence for the mechanisms of creep crack initiation ahead of the defect. In the majority of cases, as suggested by the low magnification image in Plate 4.27 the voiding occurred along grain boundaries having an angle of 45° to the notch tip. In Plate 4.28 the voids appear to have been initiated in the vicinity of large grain boundary carbides which are elongated in the direction of the boundary. Adjacent to these elongated, and quite often irregular shaped, carbides was evidence of an intra-granular substructure, as indicated by the red arrows in this plate, and a grain boundary area denuded zone. Further evidence of denudation and the presence of sub-structure boundaries adjacent to cavitating grain boundaries is shown in Plates 4.30 and

4.31 respectively. Plate 4.31 also shows evidence of void formation at a triple point. For comparison, Plate 4.32 shows the microstructure from a reference region in the CT specimen remote from the stress field. No evidence of cavitation was detected in this region

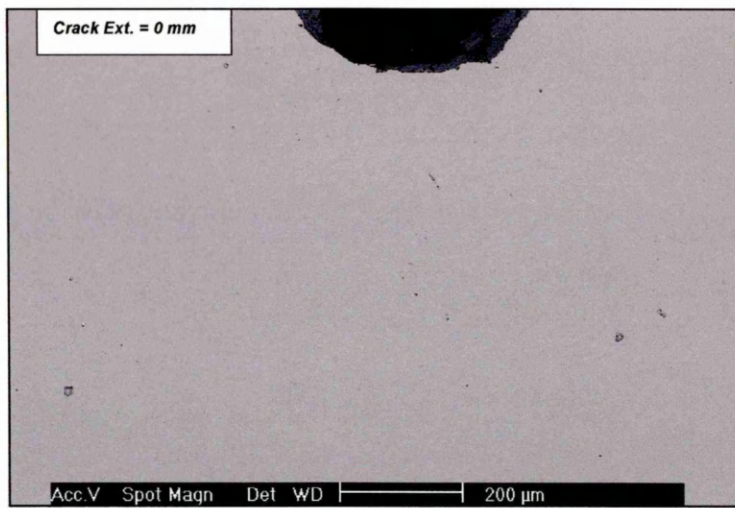


Plate 4.24 : Low magnification SEM image of the notch tip region in the fully bainitic sample tested at 550°C and 100MPa for 300 hours.

Y-Direction (microns)	X-Direction (microns) / Void%				
	-400	-200	0	200	400
0	0.014	0.075	0.097	0.07	0.005
-200	0.001	0.01	0.117	0.023	0.061
-400	0.055	0.012	0.084	0.018	0.018
-600	0.019	0.026	0.039	0.03	0.017
-800	0.04	0.047	0.001	0.01	0.01
-1000	0.041	0.016	0.001	0.009	0.003

Table 4.16 : Void % analysis results for the 100% tempered bainite sample tested at 550°C and 100MPa For 300h.

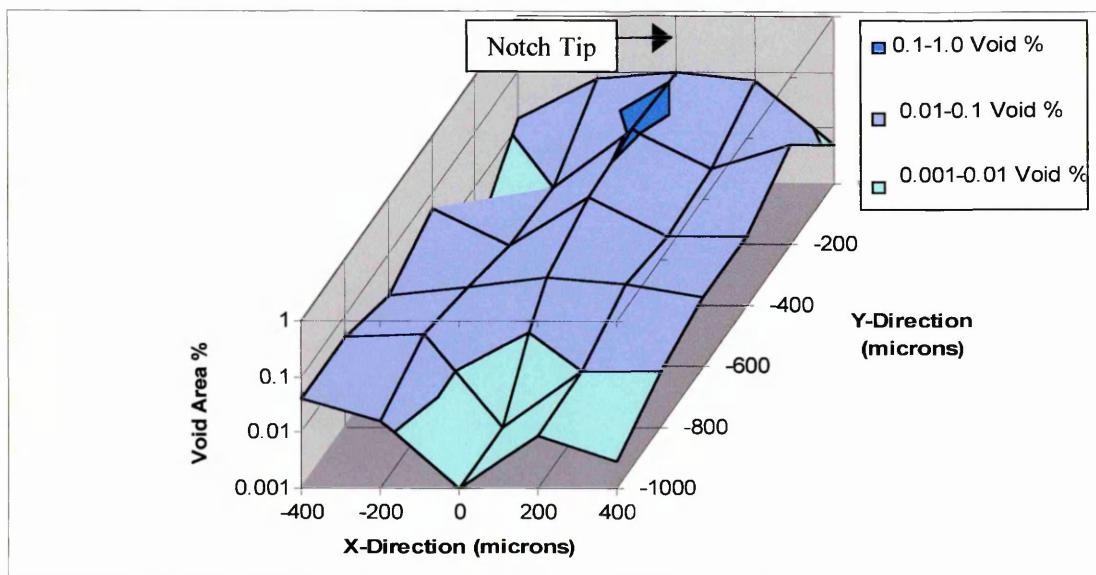


Figure 4.18: Void % analysis distribution chart for the 100% tempered bainite sample tested at 550°C and 100MPa for 300h.

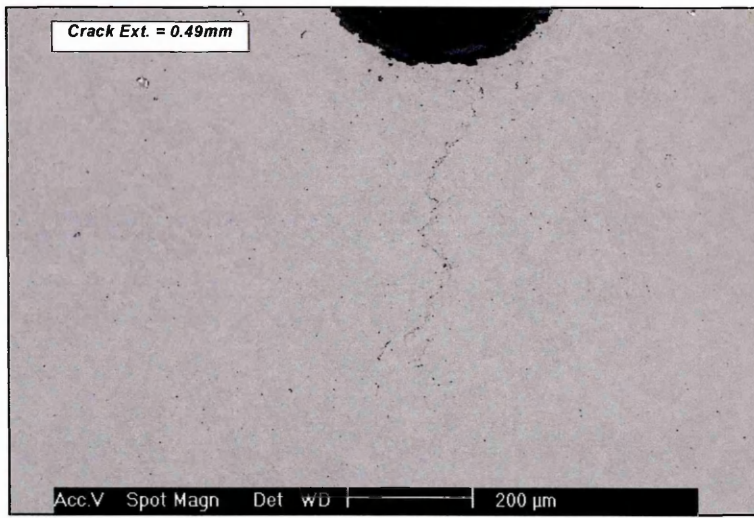


Plate 4.25: Low magnification SEM image of the notch tip region in the fully bainitic sample tested at 550°C and 100MPa for 350h.

Y- Direction (microns)	X-Direction (microns) / Void %						
	-600	-400	-200	0	200	400	600
0	0.107	0.092	0.283	1.126	0.063	0.097	0.055
-200	0.078	0.115	0.117	1.279	0.091	0.081	0.069
-400	0.093	0.143	0.326	0.857	0.058	0.082	0.048
-600	0.044	0.107	0.078	0.087	0.075	0.103	0.069
-800	0.039	0.067	0.084	0.080	0.063	0.100	0.087
-1000	0.042	0.151	0.098	0.105	0.049	0.046	0.083

Table 4.17: Void % analysis results for the 100% tempered bainite sample tested at 550°C and 100MPa for 350h.

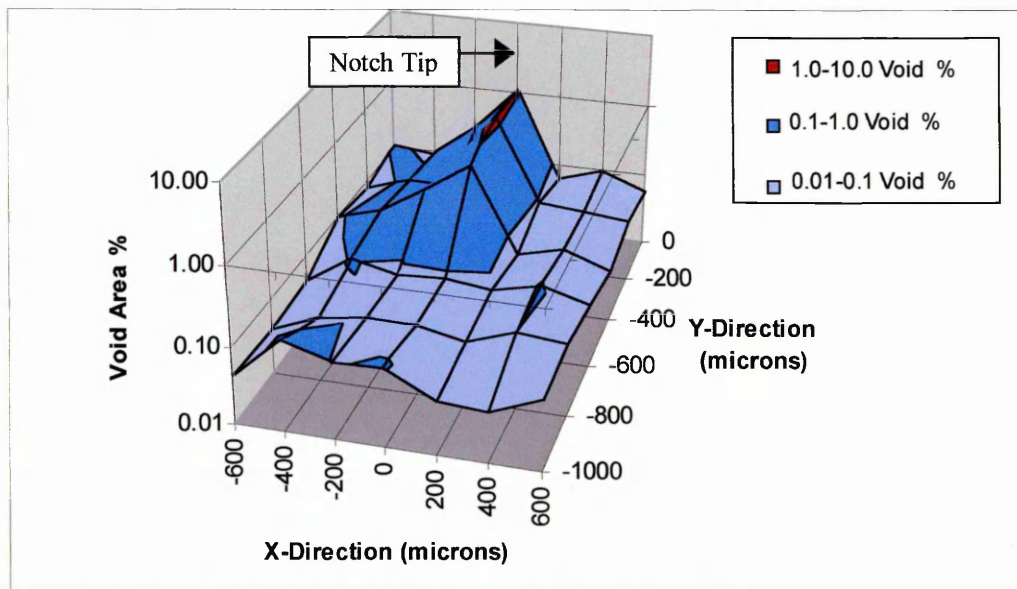


Figure 4.19: Void % analysis distribution chart for the 100% tempered bainite sample tested at 550°C and 100MPa For 350h.

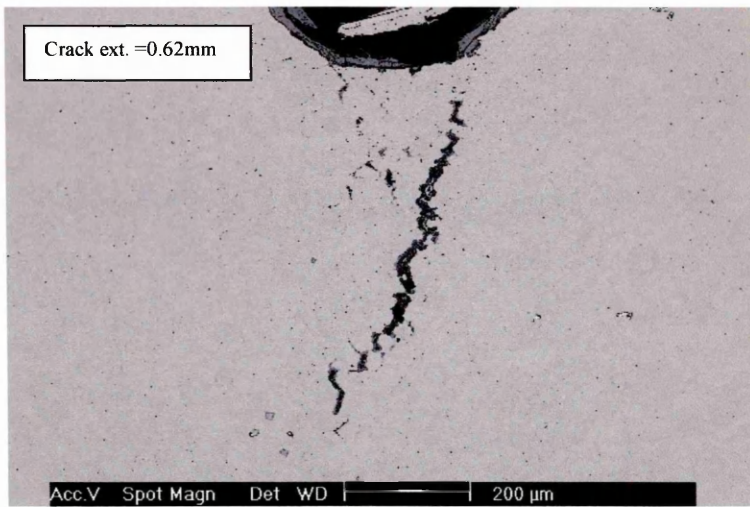


Plate 4.26: Low magnification SEM image of the notch tip region in the fully bainitic sample tested at 550°C and 100MPa for 400h.

Y Direction (microns)	X Direction (microns) / Void %										
	-1000	-800	-600	-400	-200	0	200	400	600	800	1000
0	0.081	0.075	0.147	0.259	0.419	8.86	0.648	0.248	0.255	0.11	0.079
-200	0.092	0.083	0.166	0.202	0.429	11.251	0.463	0.357	0.187	0.094	0.096
-400	0.121	0.505	0.173	0.285	0.249	7.779	0.513	0.324	0.177	0.131	0.221
-600	0.09	0.129	0.142	0.239	0.363	0.828	0.358	0.2	0.171	0.17	0.119
-800	0.085	0.649	0.177	0.195	0.171	0.339	0.261	0.318	0.098	0.22	0.094
-1000	0.087	0.077	0.618	0.176	0.112	0.215	0.159	0.217	0.122	0.144	0.094

Table 4.18: Void % analysis results for the 100% tempered bainite sample tested at 550°C and 100MPa for 400h.

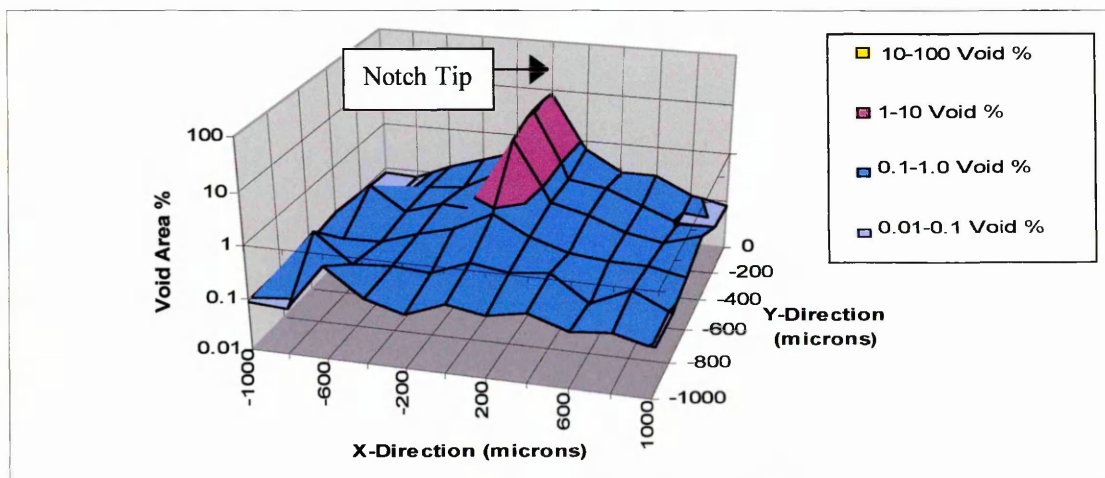
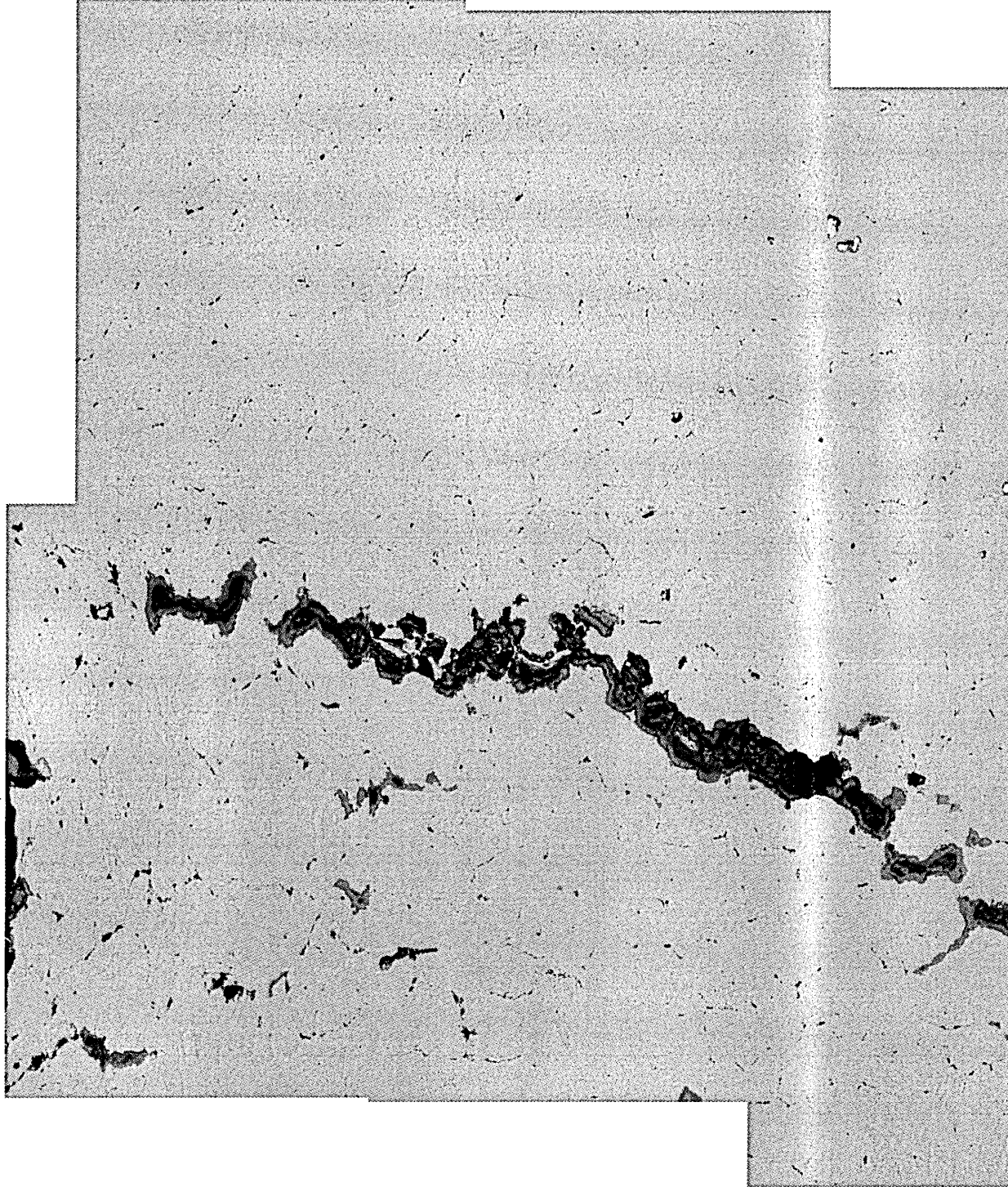


Figure 4.20: Void % analysis distribution chart for the 100% tempered bainite sample tested at 550°C and 100MPa for 400h.

Centre of notch tip



	100% Tempered Bainite (100MPa)							
Test Duration (h)	0	300	350	400	500	600	800	1000
Crack Ext. (mm)	0.00	0.00	0.49	0.62	2.50	4.00	6.17	6.81
Void Area %	0.00	0.04	0.22	1.42	n.d	n.d	n.d	n.d

Table 4.19: Crack extension and void area %² values for the tempered, fully bainitic, CT specimens.

Note* -n.d = values not determined

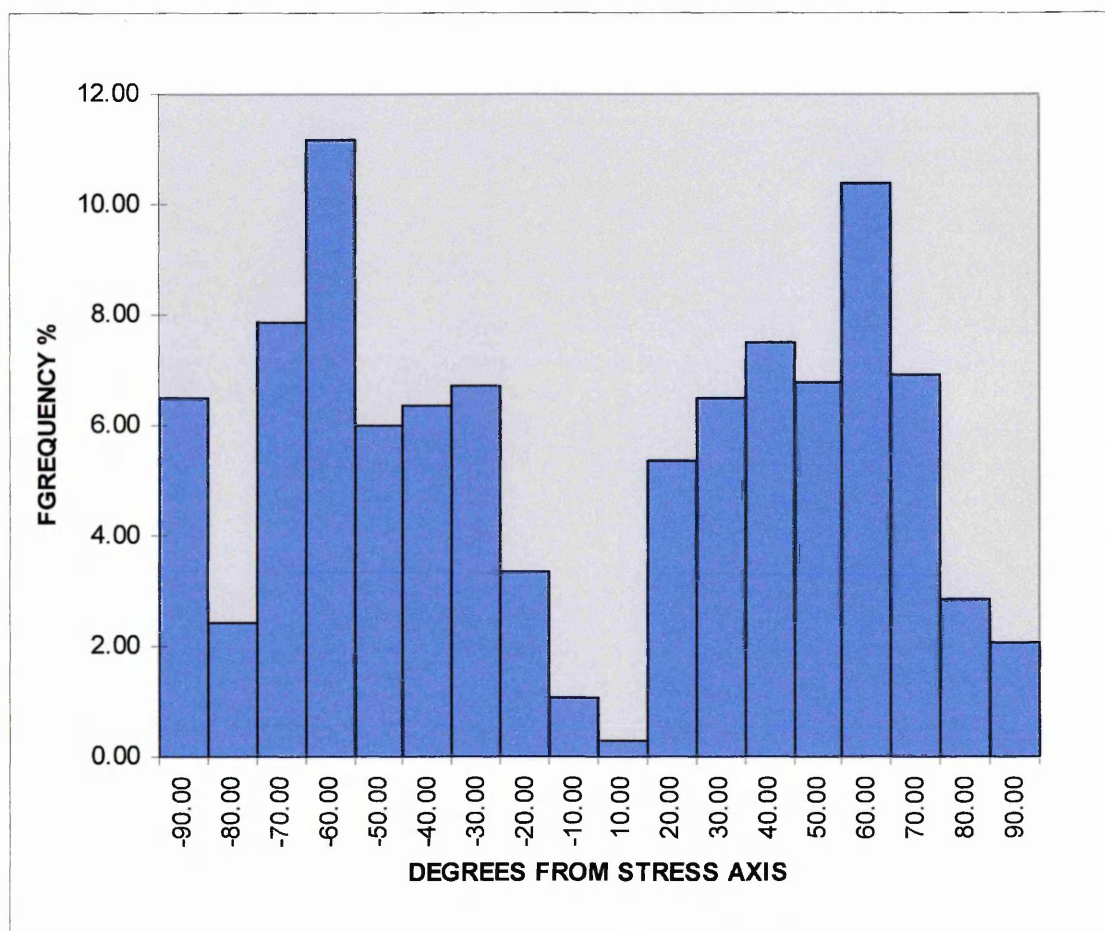


Figure 4.21: Frequency distribution analysis for void orientation in the fully bainitic sample tested at 550°C, 100MPa for 400h.

² Void area % values were taken from data determined in a region 1mm² ahead of the notch tip.

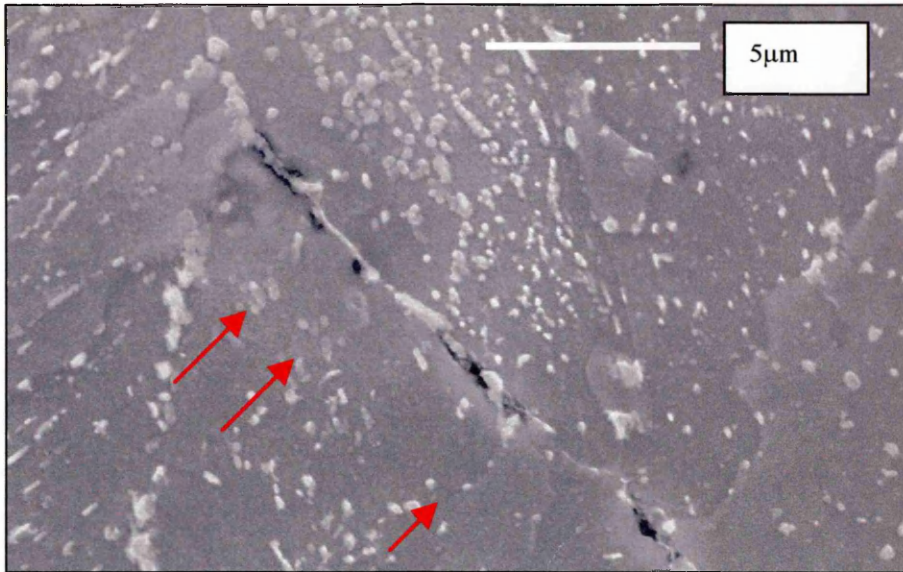


Plate 4.28: High magnification SEM image of grain boundary voiding evident in the tempered, fully bainitic, material tested at 550°C and 100MPa for 400h. The red arrows indicate evidence of sub-structure boundaries adjacent to the cavitating regions.

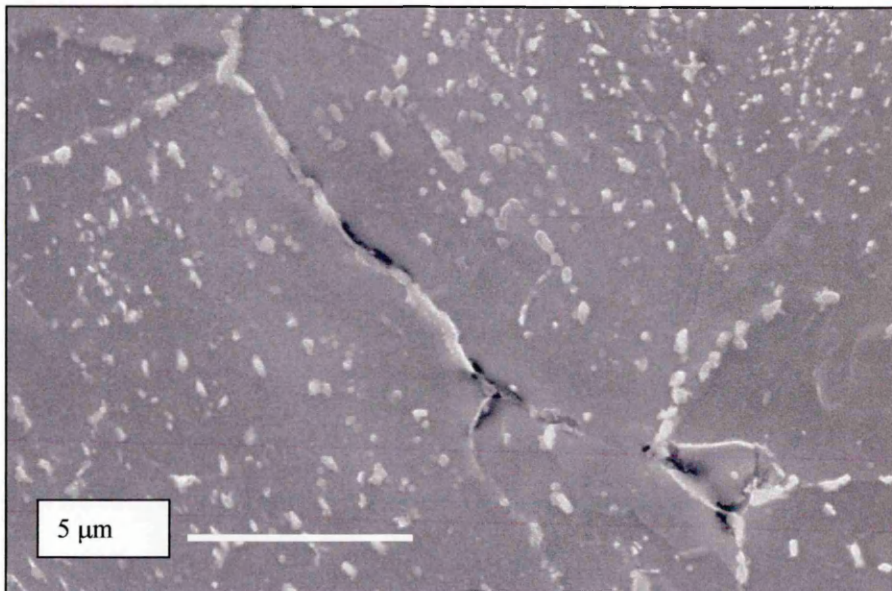


Plate 4.29: High magnification SEM image of voiding at a grain boundary in the tempered, fully bainitic, material tested at 550°C and 100MPa for 400h. Elongated carbides, adjacent to PFZ's, are evident in the vicinity of the voids.

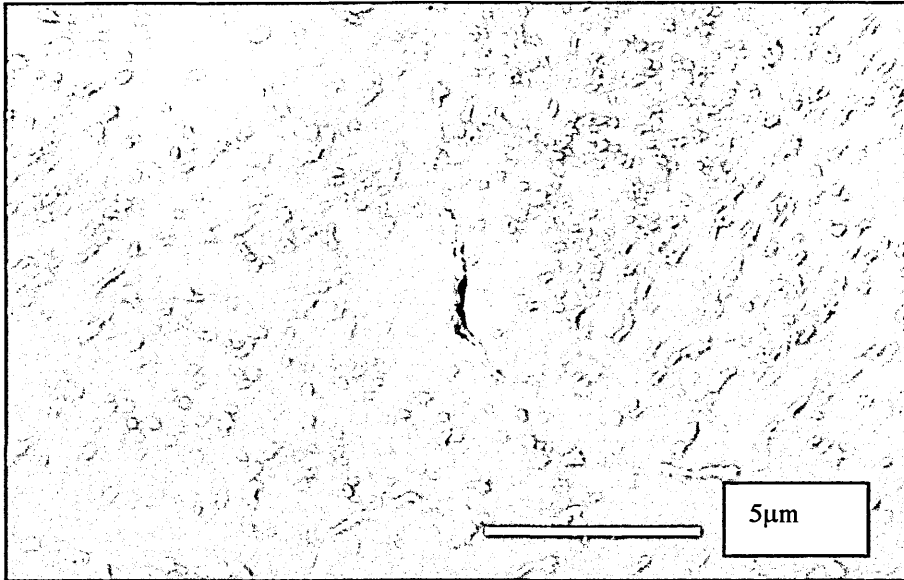


Plate 4.30: SEM micrograph showing a denuded zone adjacent to grain boundary voiding in the tempered, fully bainitic, material tested at 550°C and 100MPa for 400h.

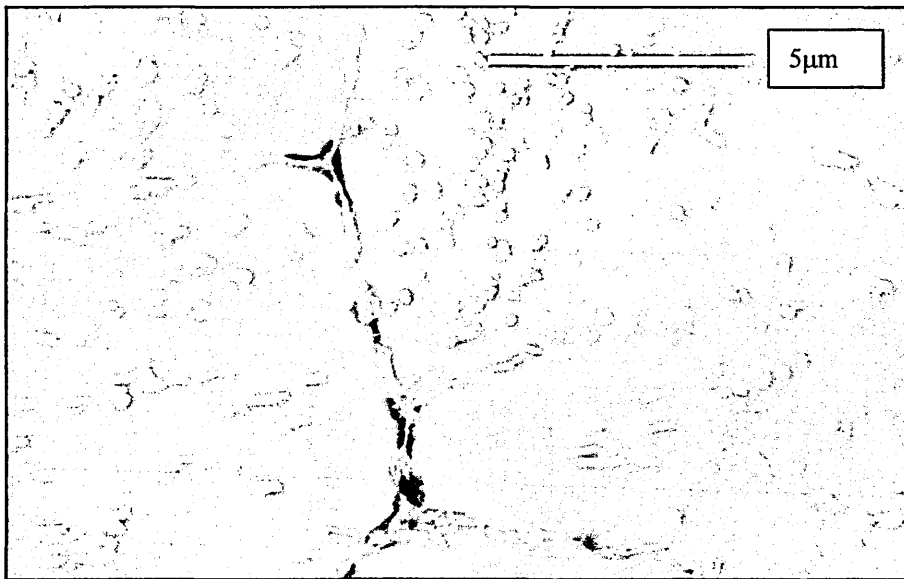


Plate 4.31: SEM image showing voids opening up at triple points and evidence of atom migration down sub-structure boundaries in the tempered, fully bainitic, material tested at 550°C and 100MPa for 400h.

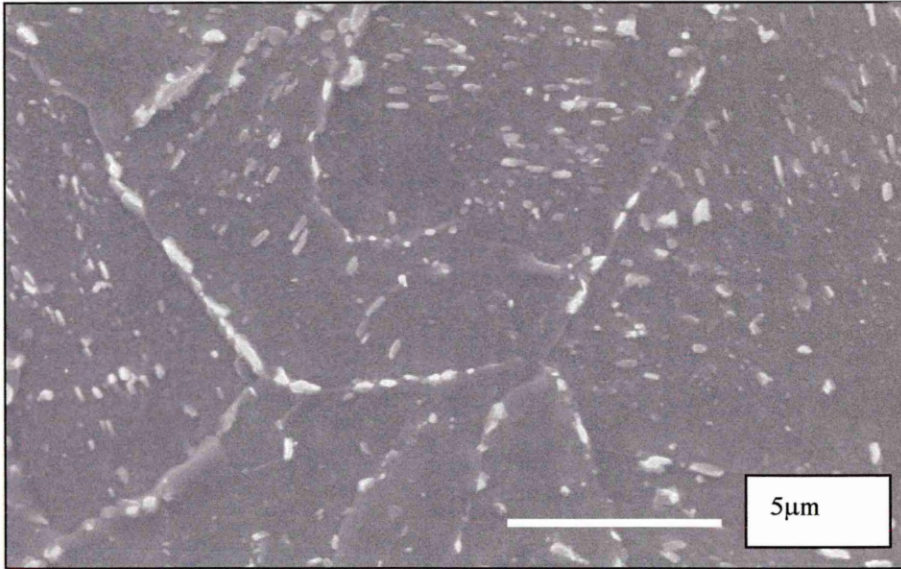


Plate 4.32: SEM micrograph showing the carbide morphology in a reference region remote from notch tip stress field in the tempered, fully bainitic, material tested at 550°C and 100MPa for 400h.

4.4.2(b) Mixed Pro-eutectoid Ferrite / Bainite Specimens

Compact tension specimens of the steel initially with a mixed ferrite / bainite structure were creep tested at a constant stress of 110MPa and a temperature of 550°C for 300, 700, 850, 1000 and 1500 hours. The specimen tested for 300 hours showed no evidence of crack extension and a minimal amount of cavitation, consequently this sample was not analysed further in terms of void analyses.

Plate 4.33 shows a low magnification image of the microstructure ahead of the notch in the specimen tested for 700 hours. In this specimen isolated cavities were visible uniformly distributed in an area approximately $400\mu\text{m}^2$ around the notch tip area, as indicated in Table 4.20 and Figure 4.22. The cavities in this specimen appeared to be less constrained by the stress concentration at the notch tip than that observed for the fully bainitic specimen tested for 300 hours which showed a similar density of voiding immediately ahead of the notch.

After 850 hours crack extension had occurred to a length of $\sim 0.39\text{mm}$, as shown in Plate 4.34. When compared to the initial crack observed in the tempered bainite specimen after 350 hours, as shown previously in Plate 4.25, this crack, although still propagating in an intergranular manner, appeared to be less acute in its directionality. A fairly large cavity was observed to have opened up approximately $150\mu\text{m}$ ahead of the notch tip in the crack path, possibly due to the presence of an inclusion, and in addition an oxidised crack could be seen adjacent to the notch tip at the left hand side. The void % data and corresponding distribution chart for this specimen are given in Table 4.21 and Figure 4.23 respectively.

Plate 4.35 shows the microstructure of the specimen tested for 1000 hours. In this specimen crack extension had occurred up to a length of 0.9mm. Again, as in the specimen tested for 850 hours, the crack emanated from a position close to the left hand side of the notch tip, it then propagated for approximately $300\mu\text{m}$ at an angle close to 45° and then changed direction through an angle of

~90°. The region surrounding the main crack exhibited widespread grain boundary cavitation as indicated in Table 4.22 and the void distribution chart, Figure 4.24.

A summary of the crack extension values measured for all the mixed ferrite / bainite specimens and the area percent of voids detected in a region extending 1mm² around the notch tip centre is given in Table 4.23.

For the mixed ferrite / bainite structure the CT specimen selected for detailed microstructural assessment was that tested for 1000 hours. Plate 4.36 shows a montage of back scattered electron images depicting the areas assessed for void formation immediately ahead and to the right of the notch tip in this specimen, i.e. an area extending from 0µm to -800µm in the y-direction and 0 to 300µm in the x-direction. As suggested previously for this specimen the angle of propagation of the dominant crack appears less constrained to the immediate notch tip centre than in the case of the 100% bainite specimens. Cavitation, once again, was observed to occur predominantly at grain boundary sites and in particular, in this mixed structure, at the boundaries between the ferrite and bainite grains. Occasional regions of bainitic intra-granular voiding were also observed.

The incidence of void formation, occurring at a specific orientation with respect to the notch tip for the areas depicted in Plate 4.36, was assessed in the manner described for the 100% tempered bainite specimens. Figure 4.25, showing the frequency of voids occurring at particular orientations, again suggests that the maximum feret diameter of the voids initiated occurred at an angle of ± 50 - 60° with respect to the notch tip centre.

Plates 4.37 – 4.42 show high magnification, secondary electron, images taken from regions of voiding in the specimen tested for 1000 hours. Plate 4.37 shows an image of both a ferrite / ferrite and ferrite / bainite grain boundary oriented at approximately 45° to the notch tip. The carbide at the ferrite / ferrite boundary, whilst delineated by elongated carbides, does not show any

evidence of cavitation. In contrast, as shown in detail in Plate 4.38 the ferrite / bainite boundary shows cavitation at a number of carbide sites. As described previously for the 100% tempered bainite structure, the large grain boundary carbides associated with the void formation appear to be in the vicinity of sub-structure boundaries formed within the bainite grain.

Plate 4.39 shows a large irregular carbide evident on a ferrite / ferrite grain boundary oriented at 90° to the notch tip. This carbide appears to be growing into both adjacent ferrite grains, perhaps with some preference towards the grain featured below the carbide. The material surrounding the carbide shows no signs of cavitation unlike the adjacent bainite grain where extensive denudation and cavitation have occurred. A high magnification image of this latter cavitating boundary is shown in Plate 4.40. From the shape of the cavity in the centre of this image it seems likely that it formed at the site of a carbide which grew away from the bainite grain into the ferrite, eventually losing coherency. Further evidence for the likely mechanism of void formation is also visible in Plate 4.41. Cavities can be seen to initiate at the cusp of grain boundary carbides, probably due to the grain boundary sliding, leading to decohesion between the carbides and matrix to one side. Plate 4.42 shows evidence for the fact that cavitation also occurred, very occasionally, at intra-granular sites along sub-boundaries in the bainite.

For comparison Plates 4.43 and 4.44 show images of the microstructure in a reference region of the specimen well away from the notch tip. No evidence of cavitation was found in this area. It was evident from Plate 4.44 that the carbides at the ferrite / bainite boundary were larger than those at the ferrite / ferrite boundary.

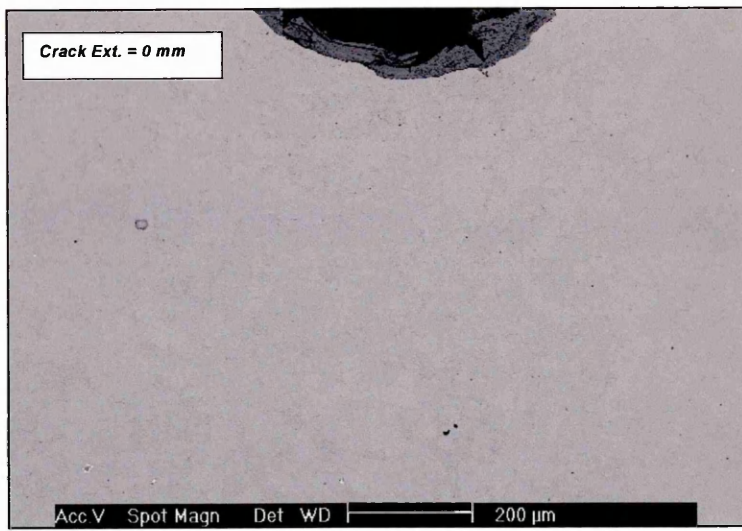


Plate 4.33: Low magnification SEM image of the notch tip region in the mixed ferrite / bainite sample tested at 550°C and 110MPa for 700h.

Y-Direction (microns)	X-Direction (microns) / Void %				
	-400	-200	0	200	400
0	0.271	0.114	0.095	0.069	0.065
-200	0.006	0.036	0.055	0.068	0.041
-400	0.012	0.094	0.062	0.050	0.078
-600	0.019	0.037	0.056	0.065	0.061
-800	0.060	0.012	0.017	0.028	0.012
-1000	0.127	0.041	0.094	0.039	0.100

Table 4.20: Void % analysis results for the mixed ferrite / bainite sample tested at 550°C and 110MPa for 700h.

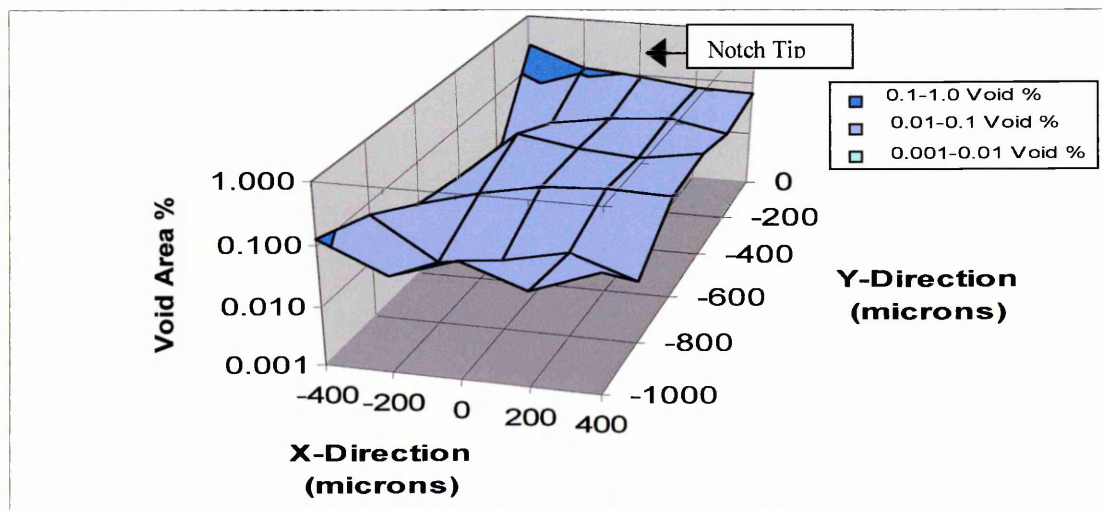


Figure 4.22: Void % analysis distribution chart for the ferrite / bainite sample tested at 550°C and 110MPa for 700h.

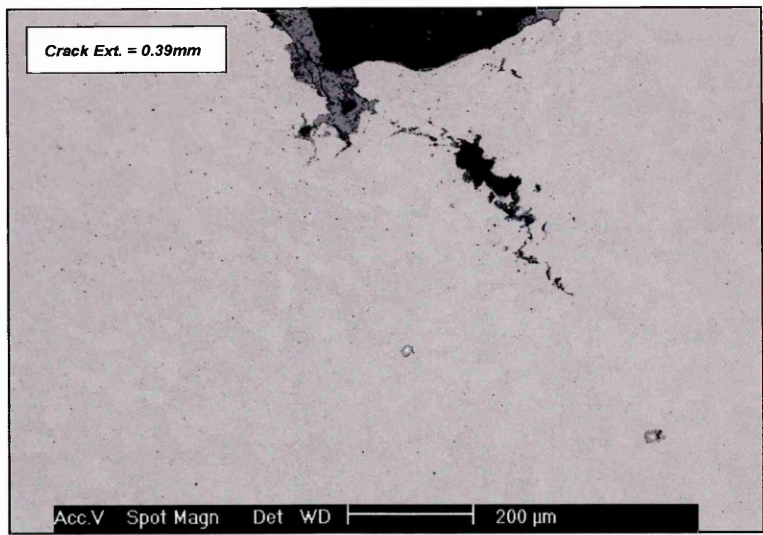


Plate 4.34: Low magnification SEM image of notch tip region in the ferrite / bainite sample tested at 550°C and 110MPa for 850h.

Y Direction (microns)	X Direction (microns)/Void %										
	-1000	-800	-600	-400	-200	0	200	400	600	800	1000
0	0.281	0.173	0.280	0.350	22.283	9.579	0.714	0.048	0.023	0.104	0.018
-200	0.330	0.190	0.379	0.248	0.296	0.582	6.589	0.044	0.054	0.050	0.062
-400	0.173	0.246	0.303	0.325	0.190	0.152	0.160	0.106	0.010	0.062	0.039
-600	0.114	0.224	0.266	0.244	0.205	0.146	0.113	0.047	0.322	0.092	0.082
-800	0.189	0.128	0.483	0.167	0.235	0.143	0.054	0.128	0.104	0.044	0.078
-1000	0.145	0.159	0.113	0.141	0.118	0.116	0.038	0.086	0.075	0.018	0.058

Table 4.21: Void % analysis results for the mixed ferrite / bainite sample tested at 550°C and 110MPa for 850h.

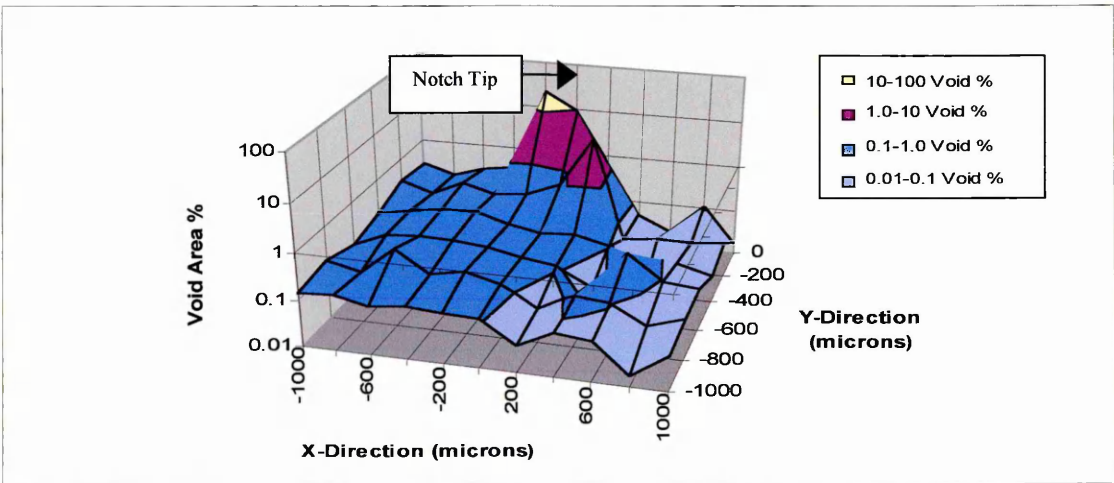


Figure 4.23: Void % analysis distribution chart for the mixed ferrite / bainite sample tested at 550°C and 110MPa for 850h.

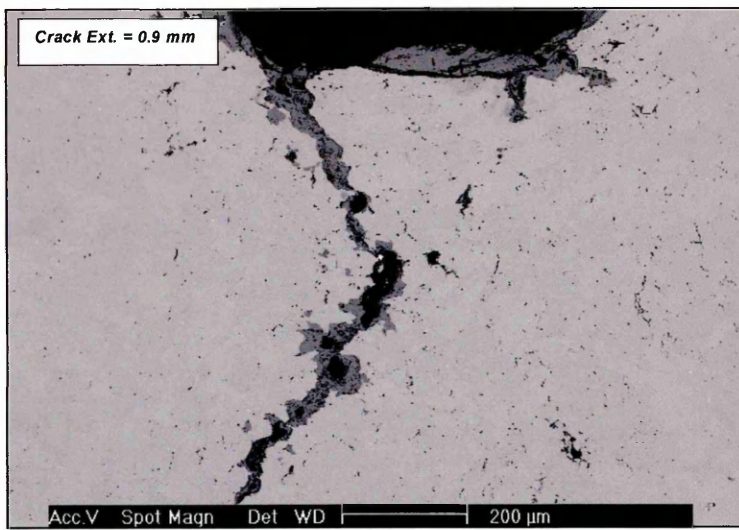


Plate 4.35: Low magnification SEM image of notch tip region in the mixed ferrite / bainite sample tested at 550°C and 110MPa for 1000h.

Y Direction (microns)	X Direction (microns) / Void %										
	-1000	-800	-600	-400	-200	0	200	400	600	800	1000
0	0.14	0.123	0.235	1.637	29.279	1.129	7.028	1.122	0.503	0.356	0.206
-200	0.302	0.209	0.292	0.443	6.299	16.559	0.83	1.396	0.587	0.32	0.287
-400	0.368	0.587	0.158	0.334	32.706	1.981	1.226	0.714	0.394	0.336	0.288
-600	0.345	0.461	0.264	1.235	10.07	0.379	3.233	0.589	0.272	0.451	0.472
-800	0.522	0.344	0.46	3.166	4.168	0.522	2.005	0.495	0.229	0.165	0.378
-1000	0.372	0.438	0.253	2.437	0.998	0.679	0.938	0.504	0.243	0.251	0.269

Table 4.22: Void % analysis results for the mixed ferrite / bainite sample tested at 550°C and 110MPa for 850h.

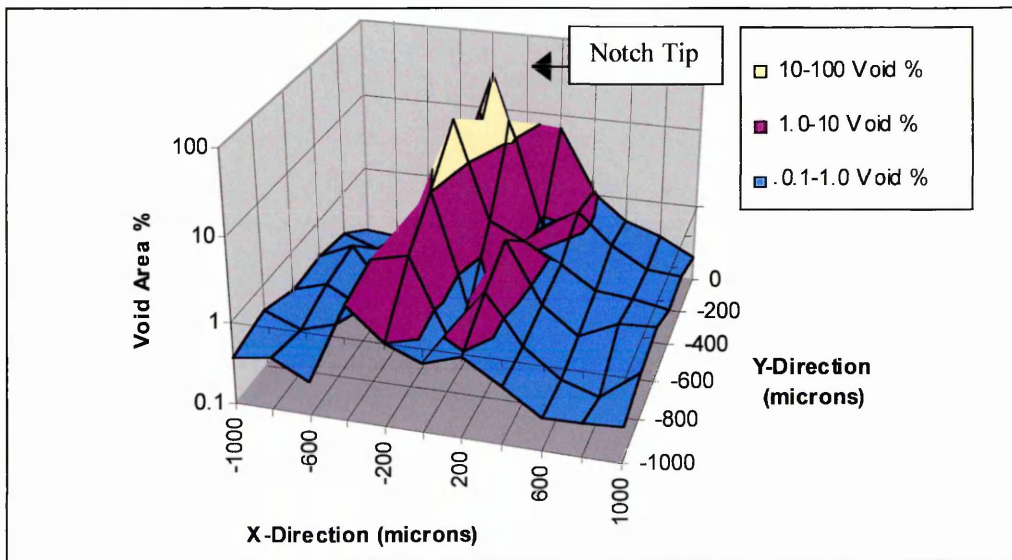
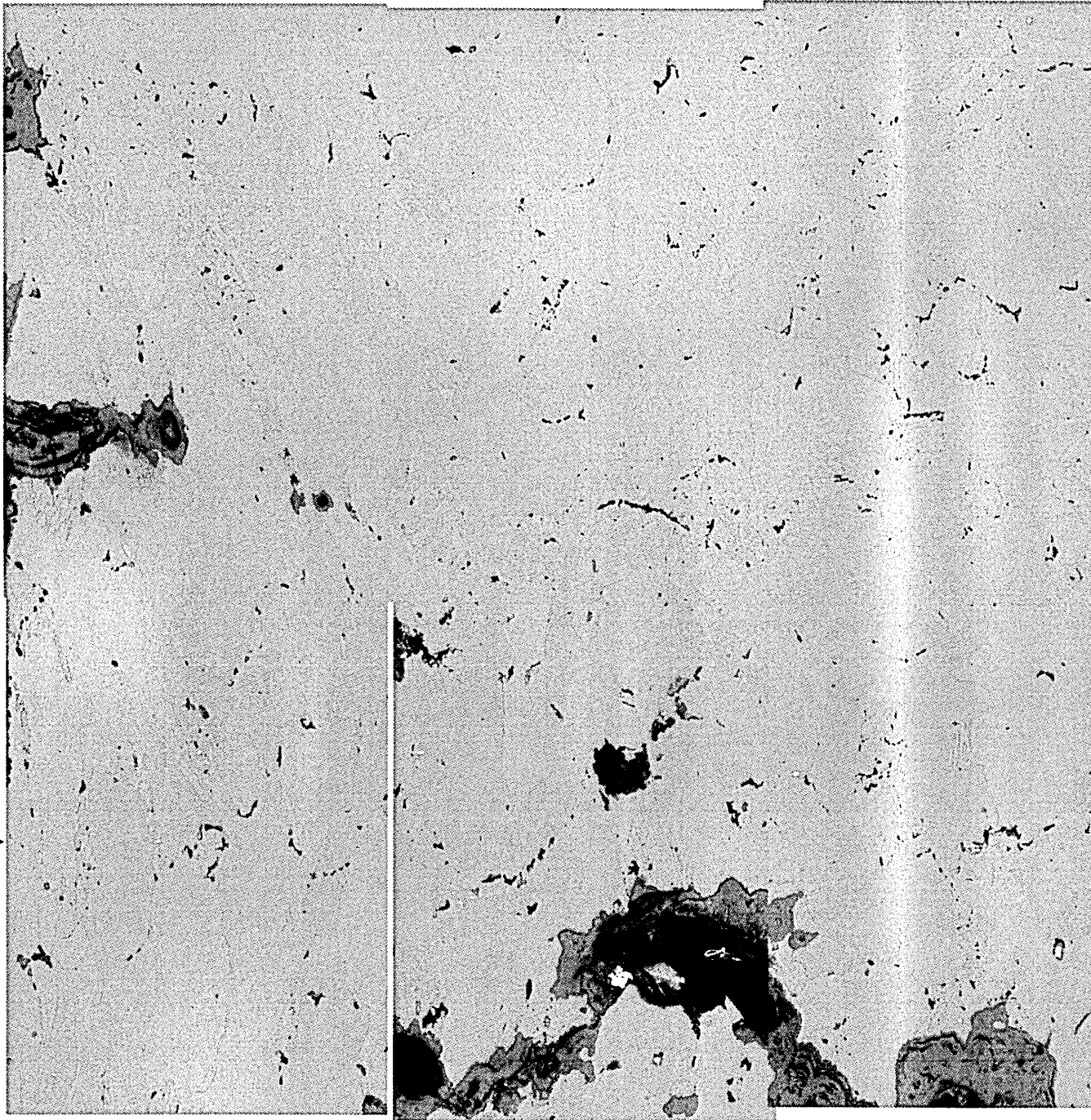


Figure 4.24: Void % analysis distribution chart for the mixed ferrite / bainite sample tested at 550°C and 110MPa for 1000h.

Centre of notch tip



	Mixed Ferrite/ Bainite (110MPa)					
Test Duration (h)	0	300	700	850	1000	1500
Crack Ext. (mm)	0.00	0.00	0.00	0.39	0.90	8.22
Void Area %	0.00	0.01	0.06	1.73	5.14	n.d

Table 4.23: Crack extension and void area %³ values for the mixed ferrite / bainite CT specimens.

Note* -n.d = values not determined

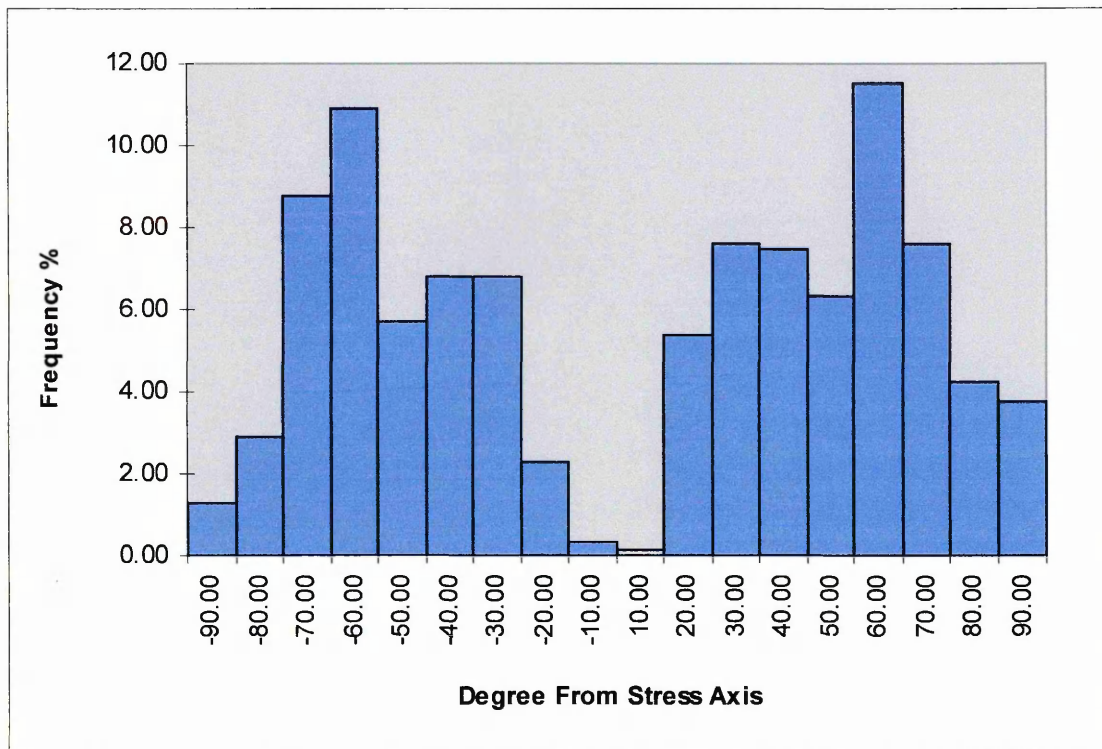


Figure 4.25: Frequency distribution analysis for void orientation in the ferrite / bainite sample tested at 550°C and 110MPa for 850h.

³ Void area % values were taken from data determined in a region 1mm² ahead of the notch tip.

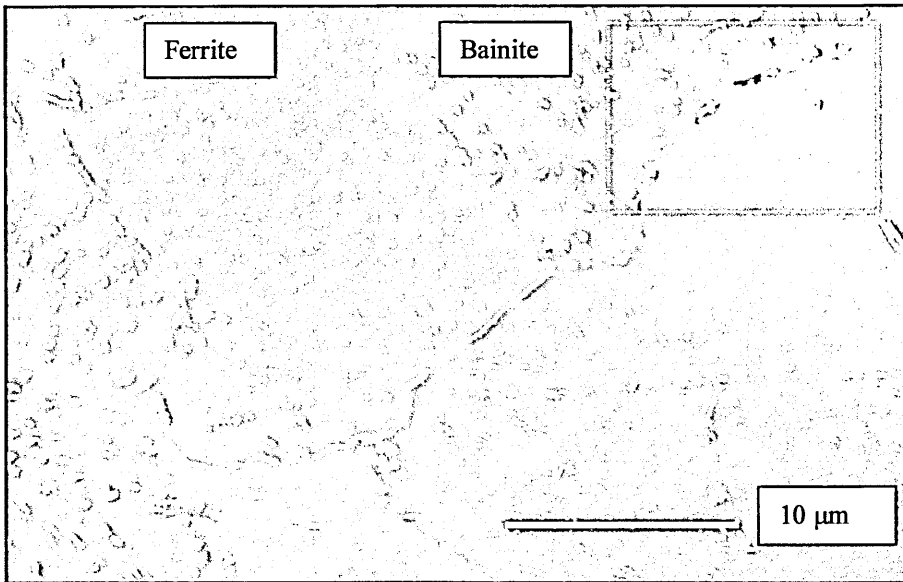


Plate 4.37: High magnification SEM image of voiding at a ferrite / bainite grain boundary .

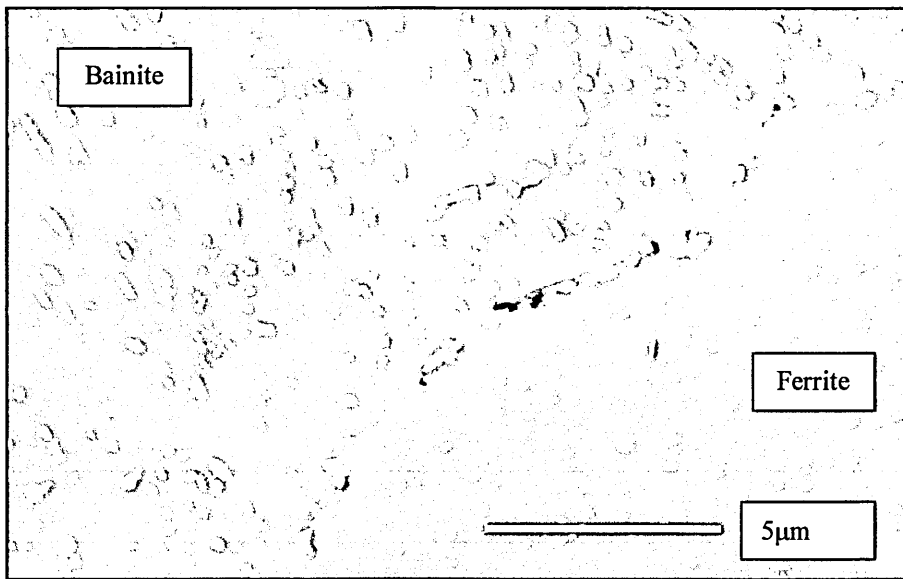


Plate 4.38: High magnification SEM image of an area indicated in plate 4.37 above showing voiding at a grain boundaries and evidence of sub-structure boundaries in the bainite phase.

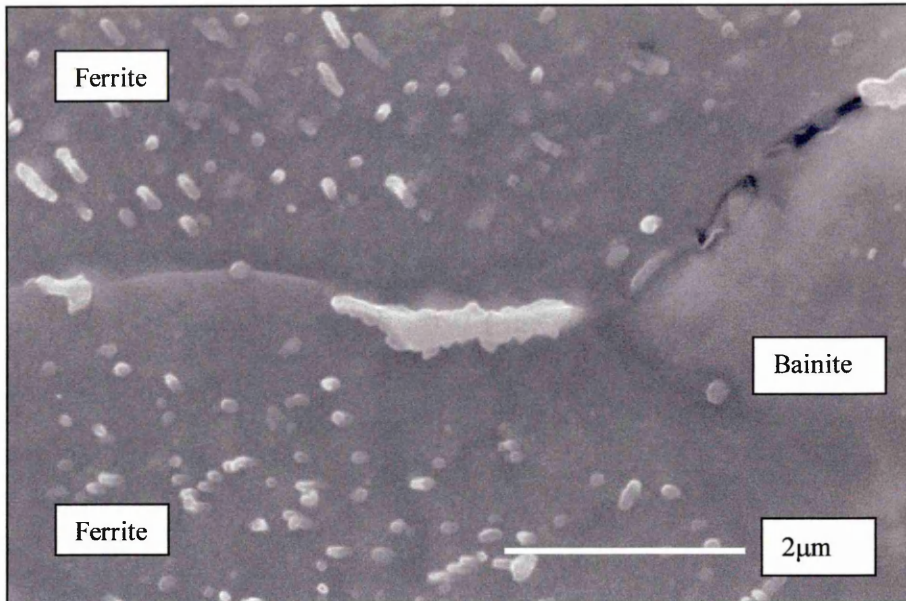


Plate 4.39: SEM micrograph showing large, irregular shaped, grain boundary carbide perpendicular to principal stress axis between two ferrite grains and adjacent to a denuded bainite grain.

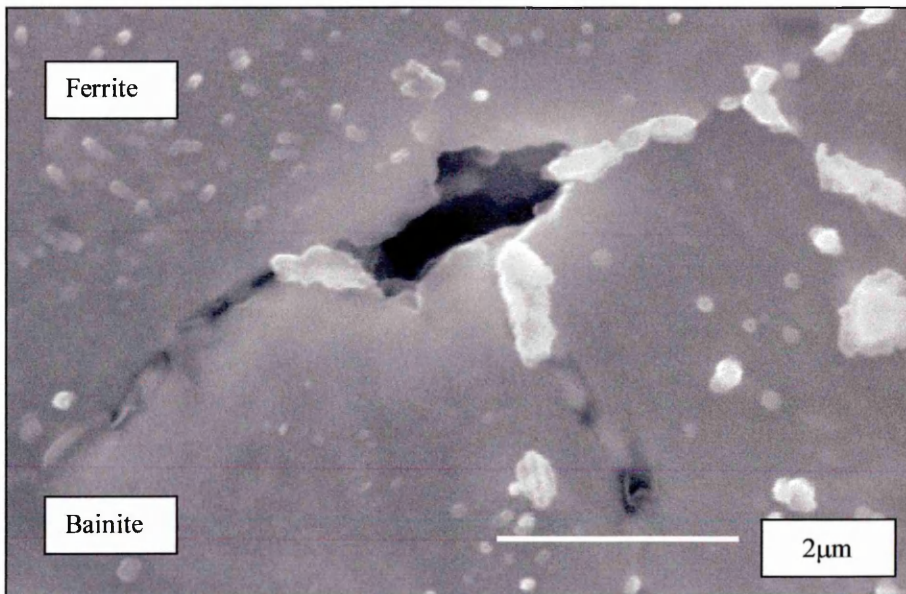


Plate 4.40: SEM micrograph showing cavitation on a ferrite / bainite grain boundary and associated denuded region.

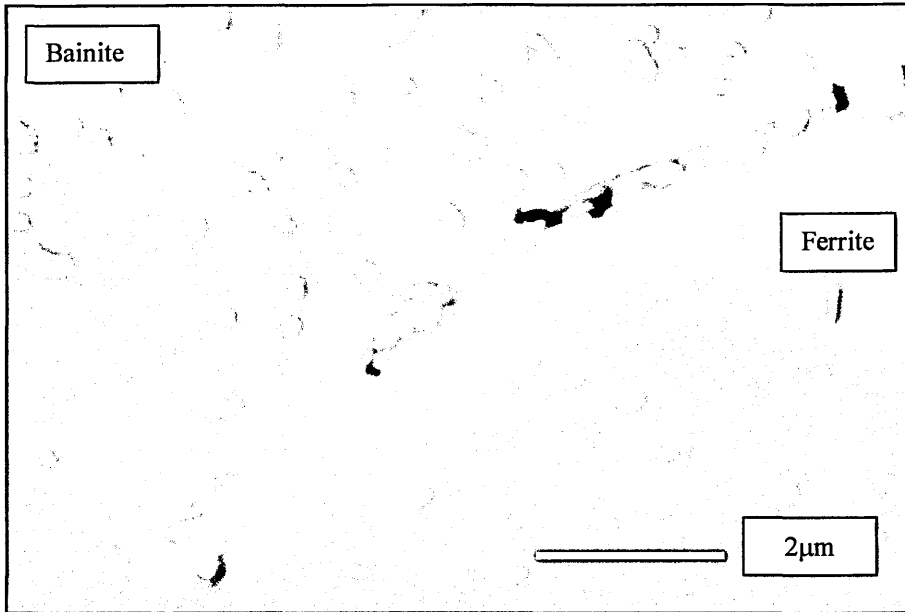


Plate 4.41: SEM image depicting cavitation on a ferrite / bainite grain boundary and growth of associated grain boundary carbides. PFZ evident in the ferrite grain adjacent to the grain boundary.

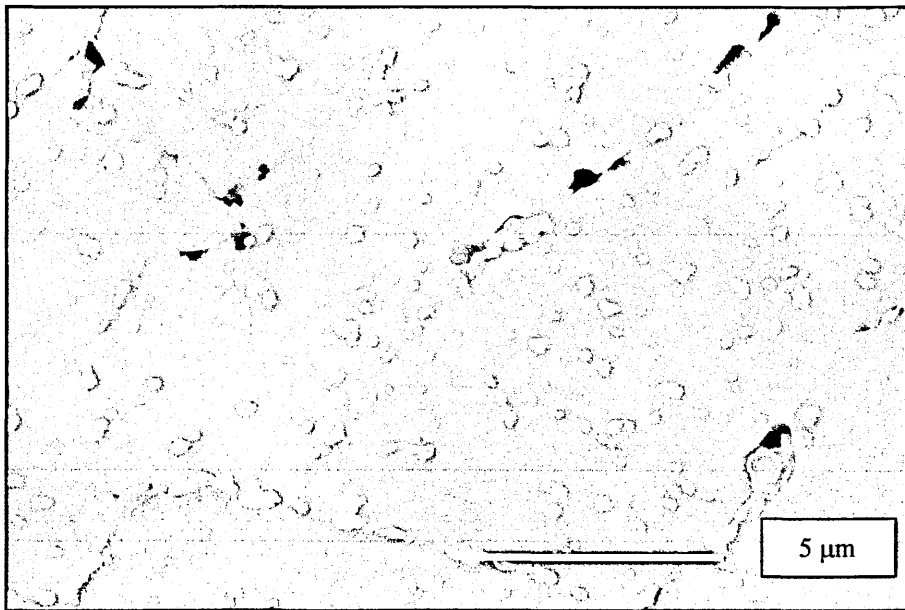


Plate 4.42: SEM image showing voiding in an intra-granular bainitic region of the mixed ferrite / bainite specimen tested for 1000 hours.

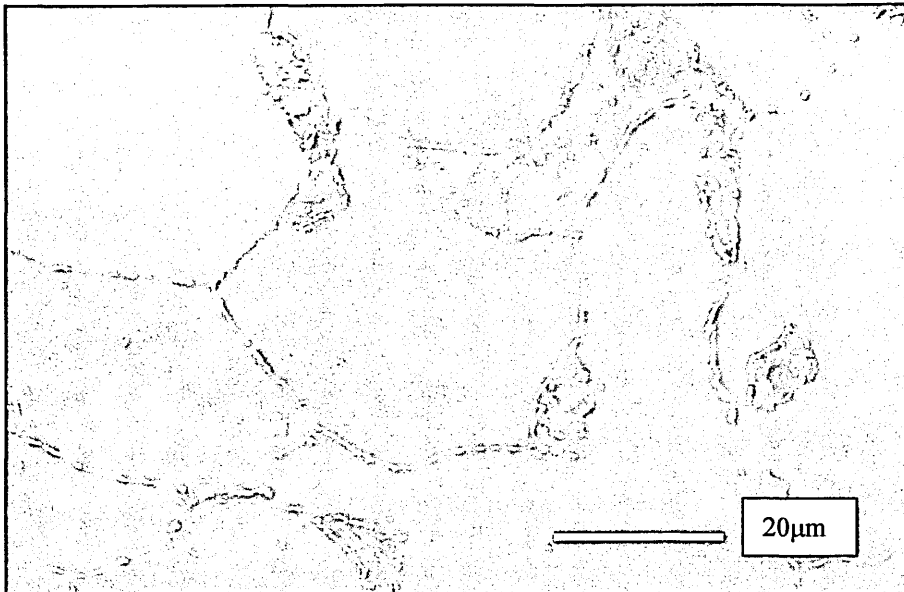


Plate 4.43: SEM micrograph showing carbide morphology in a reference region, remote from the notch tip stress field, of the ferrite / bainite specimen tested for 1000h.

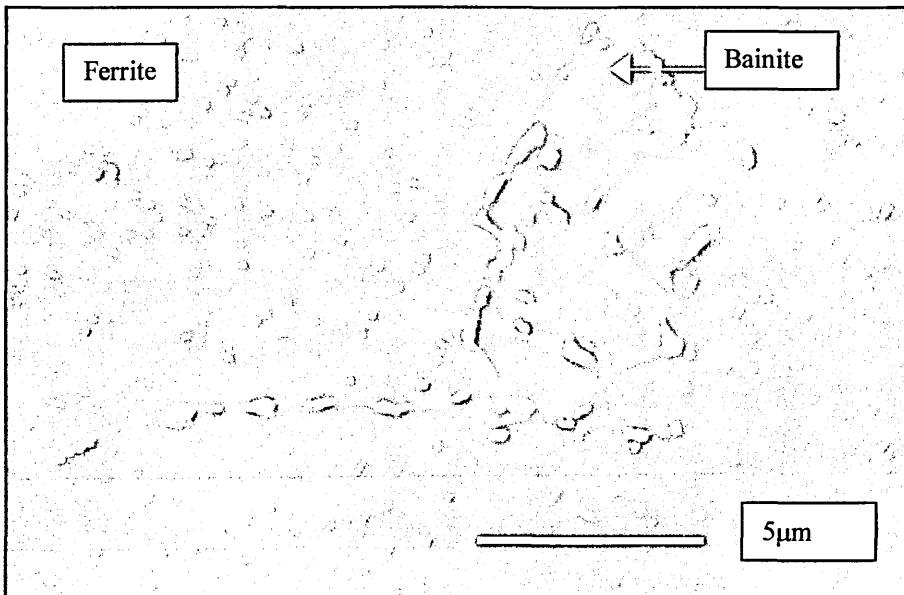


Plate 4.44: High magnification SEM micrograph showing the carbide morphology in a reference region, remote from notch tip stress field, of the ferrite / bainite specimen tested for 1000h.

4.4.2(c) Mixed Pro-eutectoid Ferrite / Pearlite Specimens

Compact tension specimens of the steel initially with mixed ferrite / pearlite structure were creep tested at a constant stress of 85MPa and a temperature 550°C for 1007, 2006, 3530, 3680h and 6850 hours. The first two of these specimens showed no evidence of creep damage and were not, therefore, considered for further analyses.

The samples tested for 3530, 3680 and 6850 hours all showed evidence of damage accumulation and <1mm of crack extension, however, due to the similarity, in terms of test duration, of the first two of these samples only the 3680h and 6850 h specimens were investigated.

Plate 4.45 shows a low magnification image of the notch tip region in the CT specimen tested for 3680 hours. Although cavity coalescence did not appear to have occurred to a length extending more than one grain, extensive voiding was observed, particularly in a region up to 300µm either side and 1mm ahead of the notch tip. The corresponding void % data and distribution chart for this specimen is given in Table 4.24 and Figure 4.26 respectively.

After testing for 6850 hours a small crack extending approximately 80µm, i.e. about 2-3 grain diameters, was observed to have initiated in a position approximately 300µm to the left of centre and below the notch tip, as visible in Plate 4.46. As denoted in the void % data table, Table 4.25, the area initiating the crack was found to be associated with the presence of a large MnS type inclusion as was the area indicated at the x,y co-ordinates (-200µm,-200µm). The area percent of voids detected in the surrounding regions was less than that observed in the previous specimen which had been tested for half the test duration.

A summary of the crack extension values measured for the ferrite / pearlite CT specimens and the area percent of voids detected in a region extending 1mm² around the notch tip is shown in Table 4.26.

For the mixed ferrite / pearlite structure the CT specimen selected for detailed microstructural assessment was that tested for 3680 hours. Plate 4.47 shows a

montage of back scattered electron images depicting the area assessed for void formation, as described previously in parts b) and c) of this section for the 100% bainite and ferrite / bainite structures. The montage of images show that cavity formation was widely distributed throughout the area examined. Although multiple cavities were frequently found to occur on adjacent grain boundaries, evidence of coalescence encompassing more than one grain was not observed. Sulphide inclusions were found to exist in most areas of the sample examined, for example the large inclusion evident in the right hand bottom quadrant of Plate 4.47. In the majority of cases the voids observed appeared to form on grain boundaries occurring between regions of ferrite and pearlite. In contrast to the 100% bainite and ferrite / bainite material, the orientation of the grains upon which cavitation was seen to initiate was not restricted to boundaries oriented at $\sim 45^\circ$. Many grains boundaries exhibiting cavitation appeared to be oriented at much lower angles of incidence. This was confirmed by the void orientation results, Figure 4.28, which showed that many of the voids in the ferrite / pearlite structure initiated at angles between $30^\circ - 50^\circ$ with respect to the notch tip.

Plates 4.48 - 4.51 show high magnification secondary electron images resulting from the examination of selected grains exhibiting the initial stages grain boundary voiding and coalescence in the specimen tested for 3680 hours. In Plate 4.48 cavities were observed to be forming on grain boundaries between a ferrite and pearlite region in the microstructure. The cavities did not, however, appear to be uniquely linked to specific grain boundary carbides and in fact in some areas, as shown in Plates 4.49 and 4.50, the carbides appeared to be pinning the boundaries. Plate 4.52 shows the microstructure taken from a reference region of the 3680 hour CT specimen for comparison.

In contrast to the carbides observed in the ferrite and bainite regions of the ferrite / bainite CT specimens, the carbides present in the two phase regions in the ferrite / pearlite structure are similar in size. Additionally, the boundaries between the ferrite / pearlite regions of the structure were not always clearly delineated by globular grain boundary carbides.

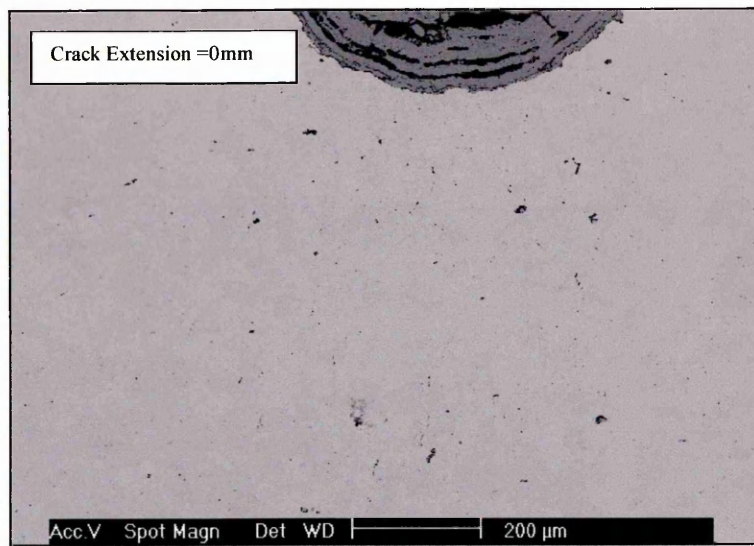


Plate 4.45: Low magnification SEM image of the notch tip region in the ferrite / pearlite sample tested at 550°C and 85MPa for 3680h.

Y Direction (microns)	X Direction (microns) / Void %						
	-600	-400	-200	0	200	400	600
0	0.062	0.041	0.215	0.582	0.483	0.083	0.218
-200	0.046	0.069	0.208	0.243	0.319	0.150	0.055
-400	0.094	0.095	0.119	0.642	0.292	0.207	0.089
-600	0.085	0.076	0.168	0.169	0.230	0.184	0.042
-800	0.083	0.090	0.148	0.225	0.253	0.141	0.076
-1000	0.047	0.097	0.099	0.223	0.097	0.216	0.056

Table 4.24 : Void % analysis results for the mixed ferrite / pearlite sample tested at 550°C and 85MPa for 3680h.

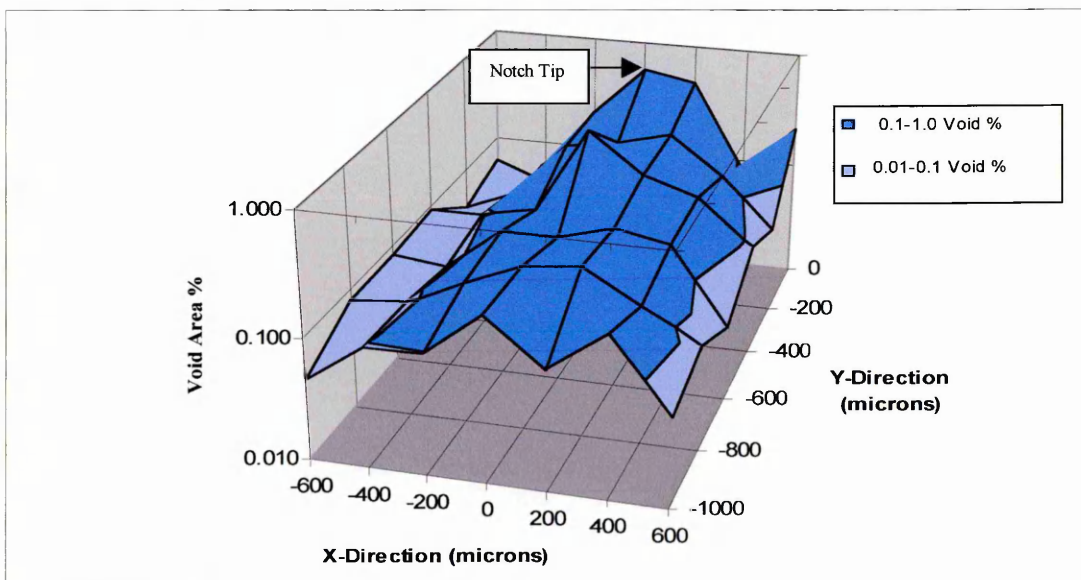


Figure 4.26: Void % analysis distribution chart for the ferrite / pearlite sample tested at 550°C and 85MPa for 3680h.

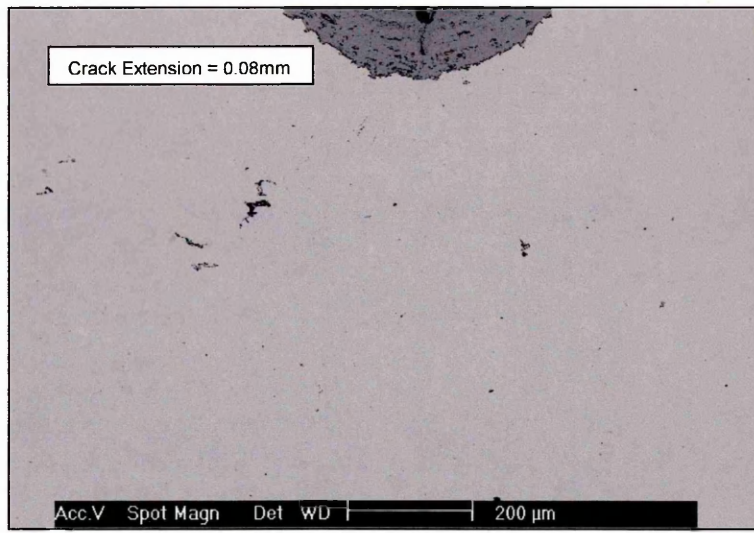


Plate 4.46: Low magnification SEM image of the notch tip region in the ferrite / pearlite sample tested at 550°C and 85MPa for 6850h.

Y Direction (microns)	X Direction (microns) / Void %						
	-600	-400	-200	0	200	400	600
0	0.009	0.033	0.089	0.224	0.056	0.020	0.030
-200	0.022	0.019	1.480	0.095	0.035	0.024	0.028
-400	0.053	0.048	0.079	0.149	0.031	0.022	0.026
-600	0.029	0.017	0.035	0.044	0.291	0.028	0.028
-800	0.012	0.021	0.031	0.020	0.023	0.021	0.034
-1000	0.021	0.017	0.034	0.109	0.031	0.021	0.025

Table 4.25 : Void % analysis results for the mixed ferrite / pearlite sample tested at 550°C and 85MPa for 6850h.
(Note- Shaded area denote areas containing large cavities due to the presence of sulphide inclusions.)

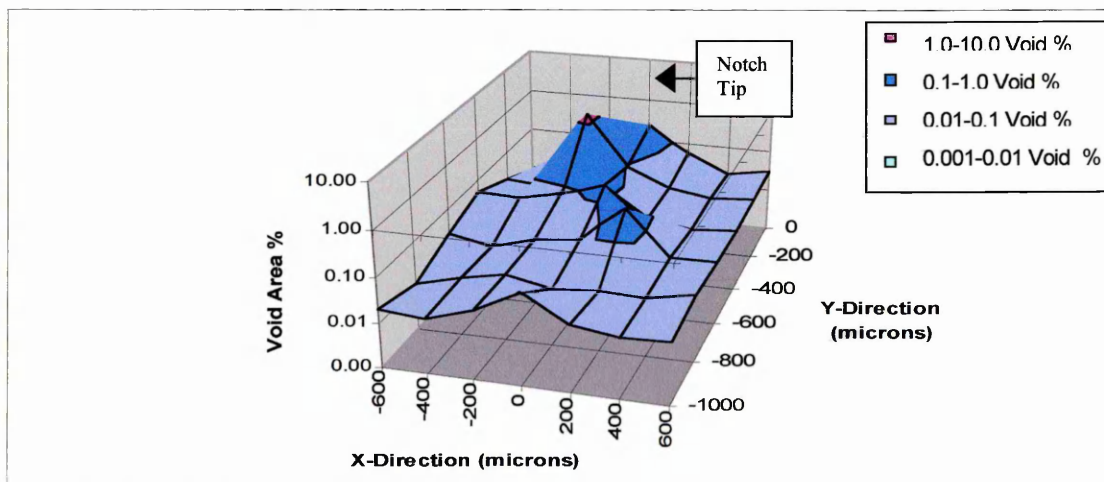
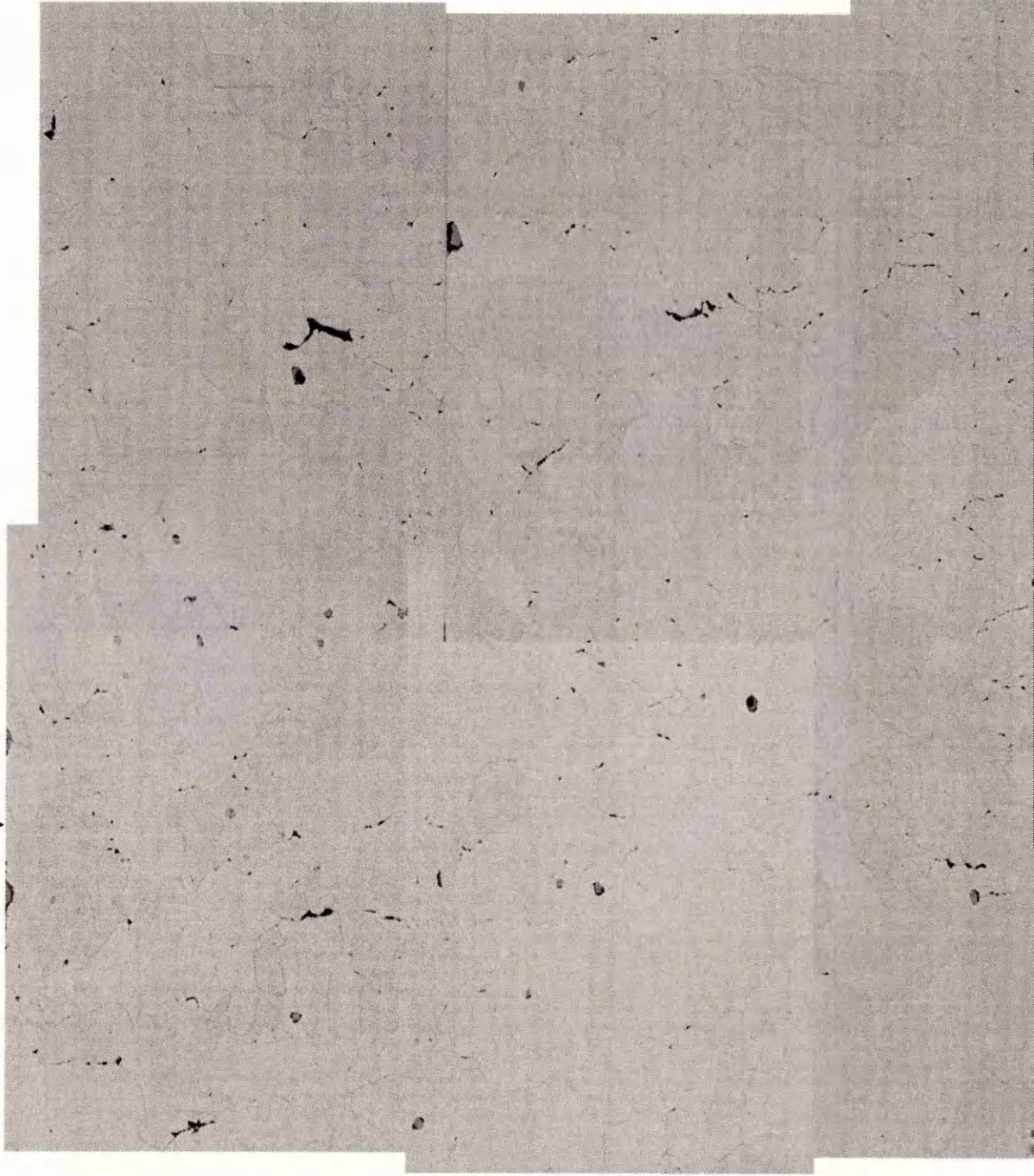


Figure 4.27: Void % analysis distribution chart for the ferrite / pearlite sample tested at 550°C and 85MPa for 6850h.

Centre of notch tip



	Mixed Ferrite / Pearlite (85MPa)		
Test Duration (h)	0	3680	6850
Crack Ext. (mm)	0	0	0.08
Void Area %	0	0.22	0.05

Table 4.26: Crack extension and void area %⁴ values for the mixed ferrite / pearlite CT specimens.

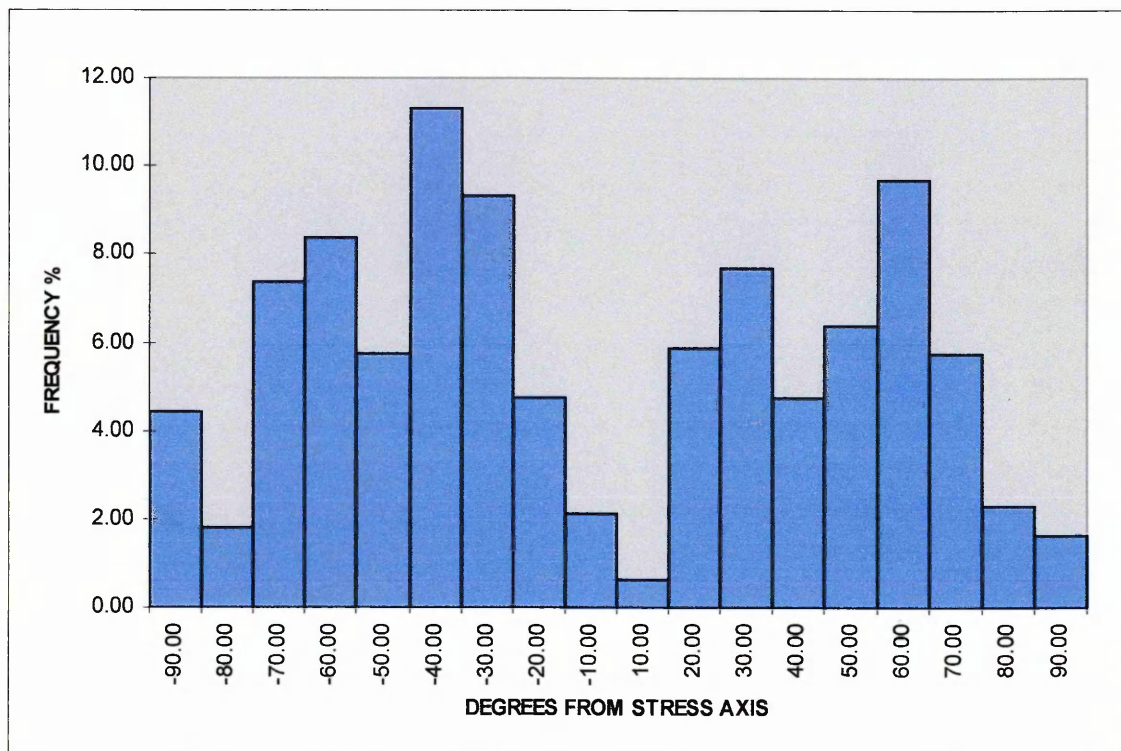


Figure 4.28: Frequency distribution analysis for void orientation in the ferrite / pearlite sample tested @ 550°C, 85MPa and 3680h.

⁴ Void area % values were taken from data determined in a region 1mm² ahead of the notch tip.

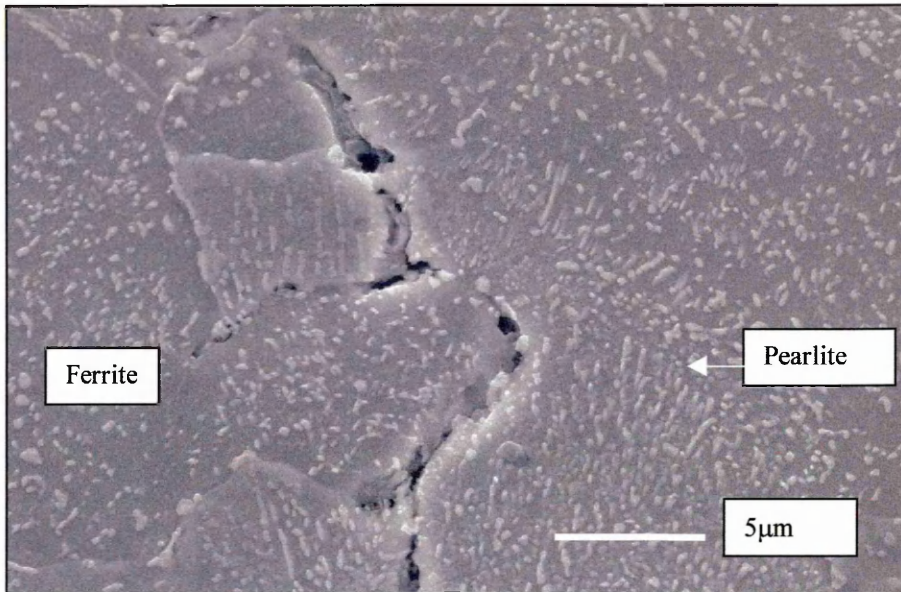


Plate 4.48: SEM image showing voiding at a grain boundary between the ferrite and pearlite phase.

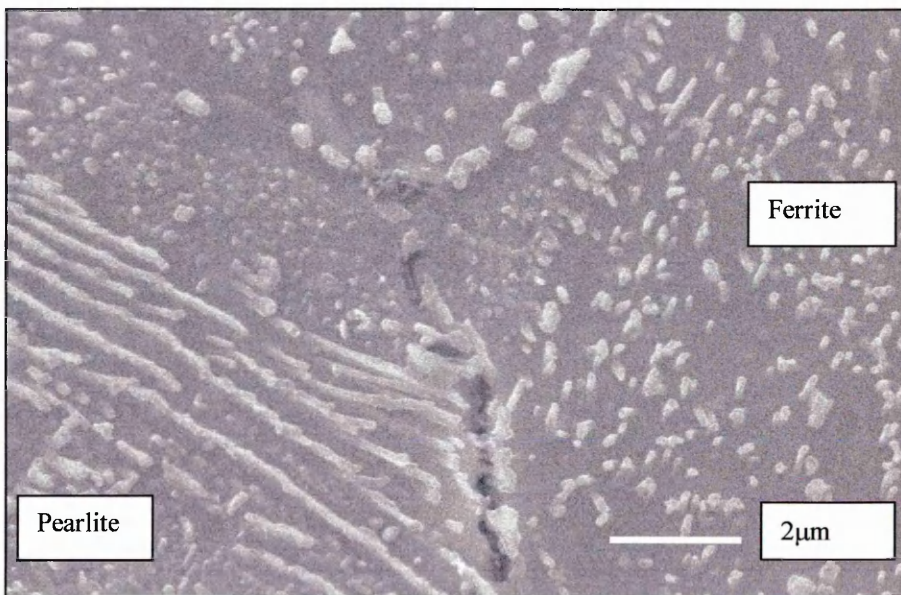


Plate 4.49: Voiding at a grain boundary between the ferrite and pearlite phase.

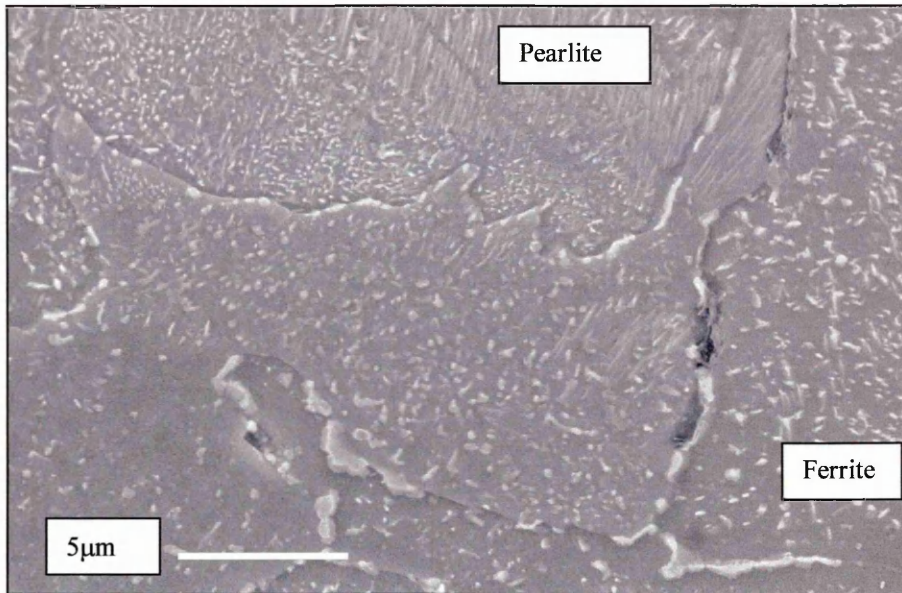


Plate 4.50: Voiding at a grain boundary between the ferrite and pearlite phase.

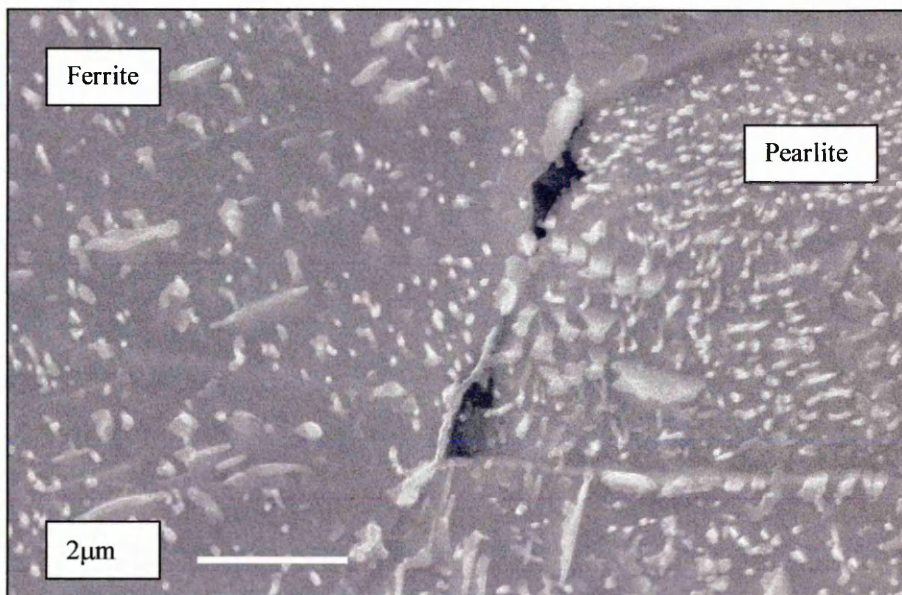


Plate 4.51: Voiding at a grain boundary between the ferrite and pearlite phase.

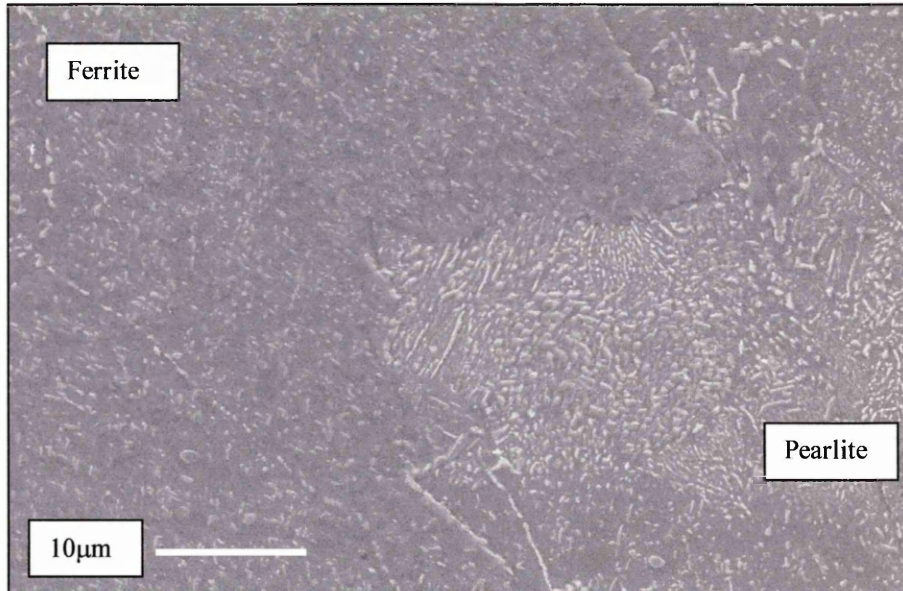


Plate 4.52: SEM micrograph showing the carbide morphology in a reference region, remote from notch tip stress field, of the ferrite / pearlite specimen tested for 3680h.

4.4.3 Correlation and Summary of the Creep Test Investigation Data

The crack tip opening displacement, crack extension and void analysis results, for all three microstructural variables, as described in sections 4.4.1 and 4.4.2, are summarised in Table 4.27.

The crack opening displacement data for the mixed ferrite / pearlite specimens, tested at the collaborating establishment, were not available for further analysis and are, therefore, absent from this table and subsequent charts. The only data comparison that could be made for all three microstructural variables was that for the crack extension and void area %.

The ability of the microstructure to sustain creep cavities in the structure, prior to the onset of crack initiation, was observed to occur in the following order: ferrite / pearlite > ferrite / bainite > 100% bainite.

Figure 4.29 shows the crack tip opening displacement, crack extension and void area % results plotted against test duration for the 100% tempered bainite structure and the mixed ferrite / bainite structure. As described in section 3.4.3, to achieve a crack extension of about 1mm in 1000 hours, the ferrite / bainite CT specimens were tested at a temperature of 550°C and a creep stress of 110 MPa and the 100% bainite specimens at 550°C and a stress of 100MPa. The results show that even though the ferrite / bainite specimens were tested at a higher stress than the fully bainitic specimens the occurrence of a specific value of CTOD, crack extension or void area % was delayed with respect to the bainitic structure.

In Figure 4.29a it can be seen that the time to achieve a critical CTOD of 0.3mm was ~ 1000 hours in the ferrite / bainite specimens and only ~400 hours in the fully bainitic specimens. Similarly, from Figure 4.29b, a crack extension of a 1mm occurred in the ferrite / bainite specimens after ~1000 hours but after only ~400 hours in the fully bainitic structure. Once the cracks had extended to a length of ~1mm the void area % was observed to increase rapidly as indicated in Figure 4.29.

Overall the results described above suggest that the mixed ferrite / bainite structure was more resistant to ductility exhaustion, i.e. was more creep ductile, than the fully bainitic structure. This was substantiated by further analysis of the CT test results as presented in Figures 4.30 and 4.31.

Figure 4.30a shows that crack extension, i.e. coalescence of grain boundary voids extending more than one grain boundary, occurred upon the attainment of only a very small percent of voiding in the area 1mm^2 around the notch tip in the fully bainitic structure. In the mixed structure a greater % of voids were found to exist prior to the onset of crack extension.

Figure 4.30b indicates that, for CTOD's less than 0.2mm, a greater CTOD was required to generate the same creep damage, in the form of voids and microcracks, for the ferrite / bainite specimen than for the fully bainitic structure.

Correlation of the data derived for CTOD and crack extension, as shown in Figures 4.31a and b, suggested that although CTOD initiation was delayed in the ferrite / bainite sample an almost linear relationship existed for the two structures once a critical CTOD had been reached, i.e. upon the attainment of a CTOD value of $\sim 0.3\text{mm}$ and a crack extension of $\sim 1\text{mm}$.

	Ferrite / Bainite (110MPa)						Bainite (100MPa)						Pearlite (85MPa)				
	0	300	700	850	1000	1500	0	300	350	400	500	600	800	1000	0	3680	6850
Test Duration (h)	0.00	0.08	0.16	0.27	0.27	2.75	0.00	0.07	0.18	0.28	0.35	0.35	0.98	1.52	n.a	n.a	n.a
CTOD (mm)	0.00	0.00	0.00	0.39	0.90	8.22	0.00	0.00	0.49	0.62	2.50	4.00	6.17	6.81	0	0	0.08
Crack Ext. (mm)	0.00	0.01	0.06	1.73	5.14	n.d	0.00	0.04	0.22	1.42	n.d	n.d	n.d	n.d	0	0.22	0.05

Table 4.27: Summary of creep testing investigation results.

Note* - n.a = data not available,
n.d = data not determined

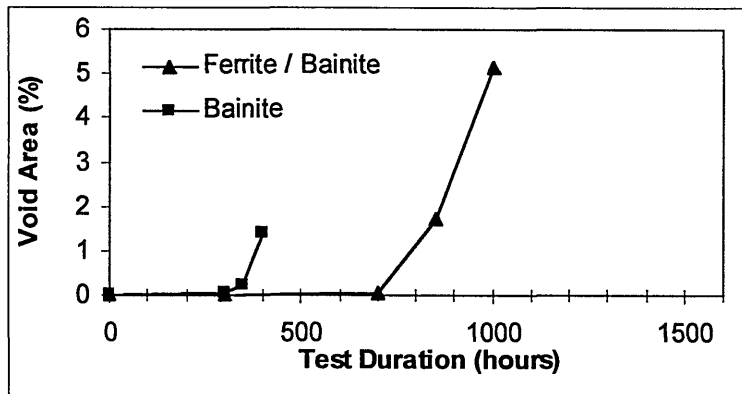
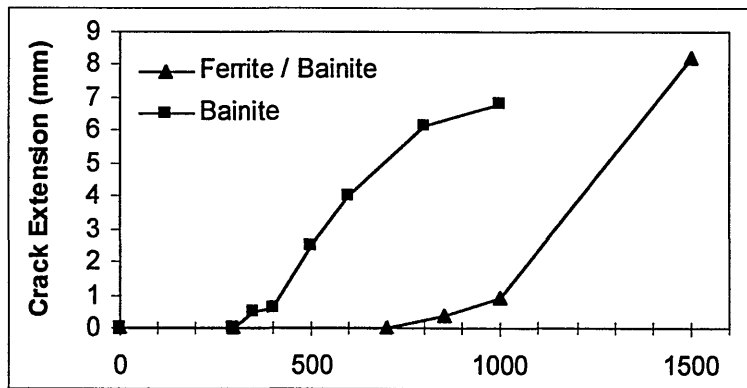
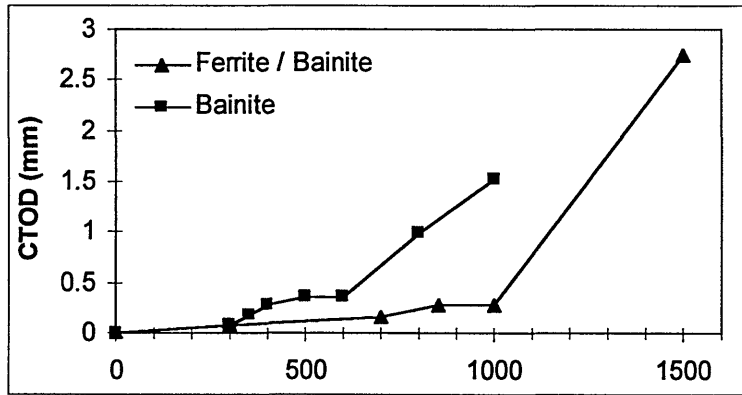


Figure 4.29: Variation of a) CTOD, b) Crack extension and c) Void area %, with test duration for 100% tempered bainite and mixed ferrite / bainite specimens.

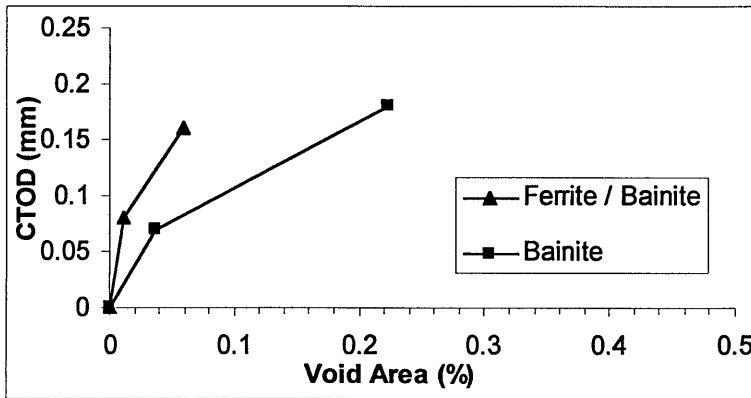
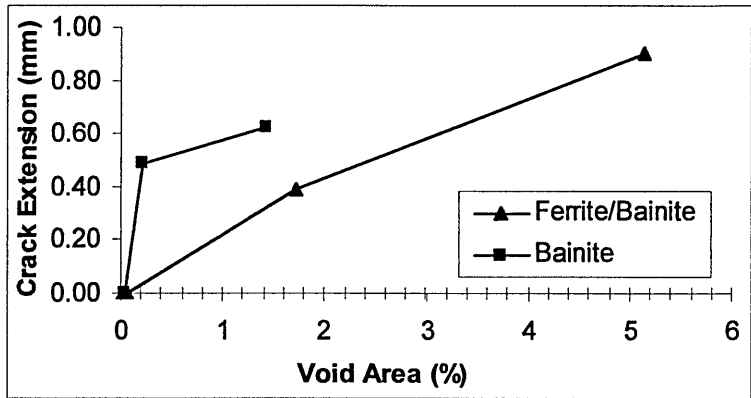


Figure 4.30: Variation of a) CTOD and b) Crack extension with void area % for 100% tempered bainite and mixed ferrite / bainite specimens.

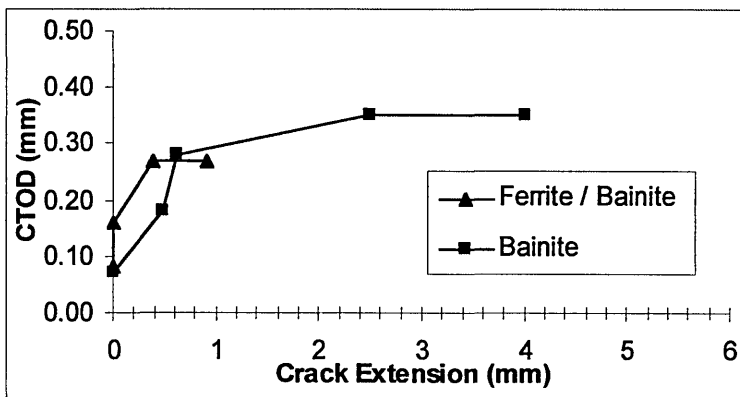
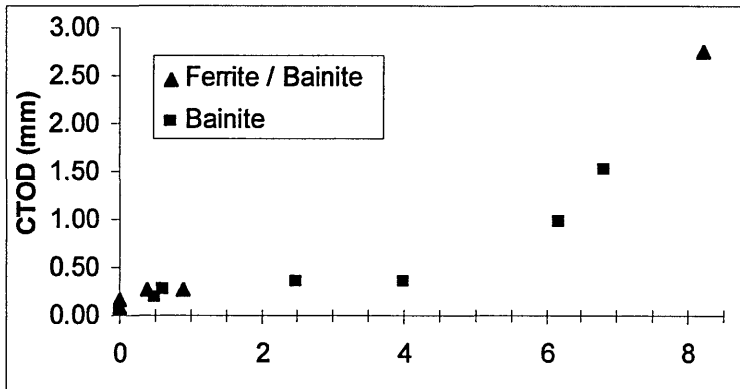


Figure 4.31: CTOD against crack extension for a) all samples, b) expanded scale delineating crack initiation region, i.e. <1mm of crack extension.

4.4.4 Carbide Analysis of Creep Tested Materials in the TEM

Cavitation due to the presence of a creep stress acting at the notch tip in the CT specimens was found, in the SEM study, to be associated with the grain boundary carbides. To study these carbides in more depth it was necessary to produce extraction replicas from the specimens of interest and analyse them in the TEM as described in section 3.6.2. To establish the effect of the stress on the grain boundary carbide evolution process replicas were taken from an area immediately ahead of the notch tip and from a reference region remote from the stress concentration. The assessment of the replica samples included a study of the distribution, morphology and type of carbides occurring in the two regions. The classification of the carbides detected was based on the ratios of Fe, Cr and Mo found in the carbides, as described in section 3.6.2(c) and detailed in Table 3.4, page 87.

This study was carried out on the specimens tested in the ferrite / bainite and fully bainitic structures only.

4.4.4(a) Carbide Analysis of the 100% Bainite Specimens

The fully bainitic CT specimen analysed in this study was that tested for a duration of 350 hours.

Plates 4.53 and 4.54 show typical grain boundary regions in the reference and notch tip areas of the fully bainitic CT specimen. The intra-granular carbide distribution was similar in both areas, each showing regions consisting of the following:

- i) densely populated directional carbides, predominantly $M_{23}C_6$ in type
- ii) occasional globular carbides, $M_{23}C_6$ / M_6C in type
- iii) denuded areas adjacent to large carbides situated at grain boundaries.

In the notch tip and reference regions large carbides observed at the grain boundaries were found to be either $M_{23}C_6$ or M_6C carbides or of a composition somewhere between the two. Analysis of a number of carbides existing along a typical grain boundary in each region showed no significant difference in the number of carbides of a particular type. This suggests that the rate of the $M_{23}C_6 \rightarrow M_6C$ evolution process was not affected by the effective stress acting at the notch tip.

Plate 4.55 shows a typical grain boundary, in the notch tip region of the specimen, oriented at an angle with respect to the principal stress axis. To evaluate the evolutionary state of the carbides in this region a number of the carbides were analysed in terms of their key element ratios, i.e. Fe:Cr, Mo:Cr and Mo:Fe using EDX analysis. High magnification images of the carbides analysed, identified by the letters A-C in Plate 4.55 are shown, along with their elemental ratios, in Plates 4.56 – 4.58.

Carbide A, as shown in Plate 4.56, was an 'L' shaped carbide which appeared to have evolved from the diffusion of atoms across the interface between a grain boundary and sub-grain boundary carbide. The dark regions in the carbide had a composition which was typical of $M_{23}C_6$ whereas the lighter, diffuse, regions were typical of M_6C , the equilibrium carbide.

Carbide B, a large irregular shaped carbide positioned along a sub-grain boundary, was mainly found to be of a chemistry which was consistent with that of M_6C . In this case, however, it appeared to have evolved from an M_7C_3 type carbide, the remnants of which could be observed in dark field imaging mode as shown in Plate 4.57.

Carbide C, which lies directly upon the grain boundary, was identified as an M_6C type carbide and, as shown in Plate 4.58, could be seen to be growing along the bainite / bainite interface.

In contrast to the latter carbide, the carbide shown in Plate 4.59 was found to lie on a grain boundary which was parallel to the notch tip / principal stress axis. Although the chemical analysis of this carbide was similar to that of carbide C in Plate 4.58 its growth appeared to be occurring in finger like

protrusions away from the original $M_{23}C_6$ carbide and into the adjacent grain. Plate 4.60 shows the effect of a triple point on the growth characteristics of M_6C .

The main difference observed between the notch tip and reference regions was that in the notch tip area there was evidence of carbides elongated along grain boundaries which were oriented at an angle with respect to the notch tip, These carbides were considered to be the ones that were associated with the initiation of grain boundary cavitation as observed in the SEM study section 4.4.2 and as such were investigated further. Plate 4.61 shows a montage of images and elemental ratios derived from an elongated carbide which appeared to be associated with cavitation to one side. The elemental ratios determined for Fe, Cr and Mo along the length of this carbide suggests that, as for carbide C in Plate 4.58, the evolution and growth of M_6C from $M_{23}C_6$ occurs along the grain boundaries. The denuded regions surrounding these large carbides suggest that the atoms necessary for this evolutionary process are provided by the dissolution of carbides in the adjacent grains.

In all the examples outlined above it apparent that the equilibrium carbide, M_6C , evolves from existing carbides by the dissolution of carbides in adjacent regions and that growth occurs in the direction of easiest diffusion.

4.4.4(b) Carbide Analysis of the Mixed Ferrite / Bainite Specimens

The ferrite/ bainite CT specimen analysed in this study was that tested for a duration 850 hours.

As for the fully bainitic specimen a number of grain boundary carbides in both a reference and notch tip region were analysed to determine any differences between the carbide compositions and morphologies. No significant difference between the number of carbides of a particular type was detected.

For reference Plate 4.62 shows a typical ferrite / bainite grain boundary from a region remote from the notch tip. As described in the TEM study of the starting material, section 4.2.4, the ferrite regions were densely populated with fine M_2C type carbide and were separated from the coarse carbide structure of the bainite regions by large globular grain boundary carbides, predominantly $M_{23}C_6$ or M_6C in nature. The carbides in the bainite were again predominantly $M_{23}C_6$ type carbides with occasional M_7C_3 and M_6C . Carbides at the ferrite / ferrite grain boundaries were found to be predominantly M_7C_3 in nature.

Once again the main difference observed between the notch tip and reference region was the morphology of the evolving carbides on grain boundaries oriented at an angle with respect to the notch tip. Elongated carbides apparently associated with cavitation were observed on ferrite / bainite boundaries, as shown in Plates 4.63 and 4.64. Cavitation associated with grain boundary carbides was not observed on ferrite / ferrite boundaries. The carbide depicted in the montage of Plate 4.64 is similar to that observed for the fully bainitic specimen in Plate 4.61. Growth of the evolving M_6C carbide occurs along the grain boundary between the existing $M_{23}C_6$ carbide and by the corresponding dissolution of surrounding carbides.

Plate 4.65 shows the growth process occurring on a carbide which was not oriented at a critical angle with respect to the notch tip. Carbides adjacent to the grain boundary $M_{23}C_6$ can be seen to be absorbed by the evolving carbide. The growth of an M_7C_3 type carbide at a ferrite / ferrite grain boundary is shown in Plate 4.67.

A significant difference between the ferrite / bainite structure and the fully bainitic structure was the presence of ferrite / ferrite boundaries in the former and the type of carbides precipitated there. The carbides at the ferrite / ferrite boundaries were found to be predominantly M_7C_3 in nature, as depicted in Plate 4.66, and as such appeared to be more resistant to change. This fact was considered to be due to the difference in the concentration of elements in the immediate vicinity of the grain boundary carbides.

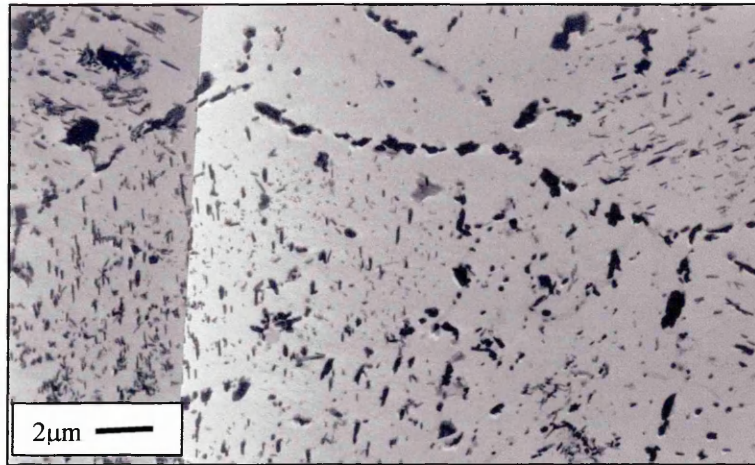


Plate 4.53: TEM micrograph showing the typical carbide morphology observed in a reference region of the tempered bainite CT specimen tested at a temperature 550°C and a stress of 100MPa for 350 hours.

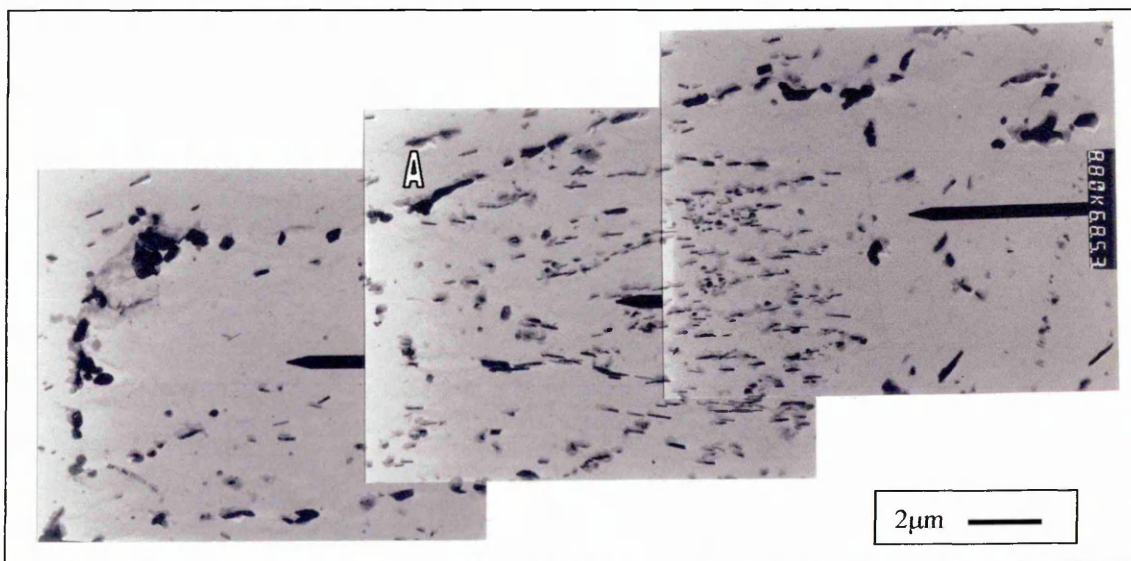


Plate 4.54: TEM micrograph showing the typical carbide morphology observed in the notch tip region of the tempered bainite CT specimen tested at a temperature 550°C and a stress of 100MPa for 350 hours.

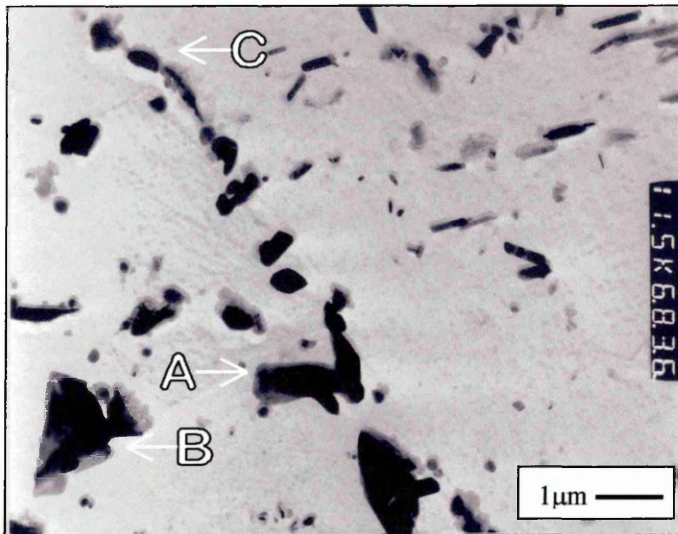


Plate 4.55: Typical boundary oriented at an angle with respect to the notch tip in the fully bainitic CT specimen tested at a temperature 550°C and a stress of 100MPa for 350 hours. Evolving carbides identified for EDX analysis in Plates 4.56 – 4.58.

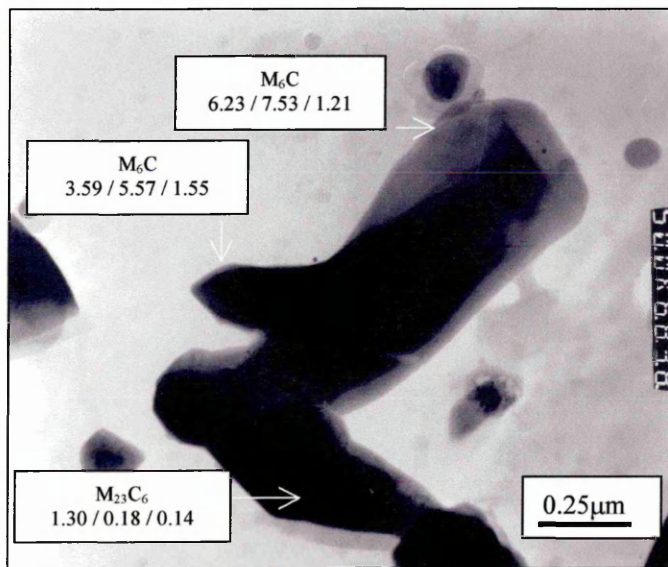


Plate 4.56: Brightfield image of feature A in micrograph depicted in plate 4.55 and the corresponding elemental ratios for Fe:Cr, Mo:Cr and Mo:Fe determined by EDX analysis.

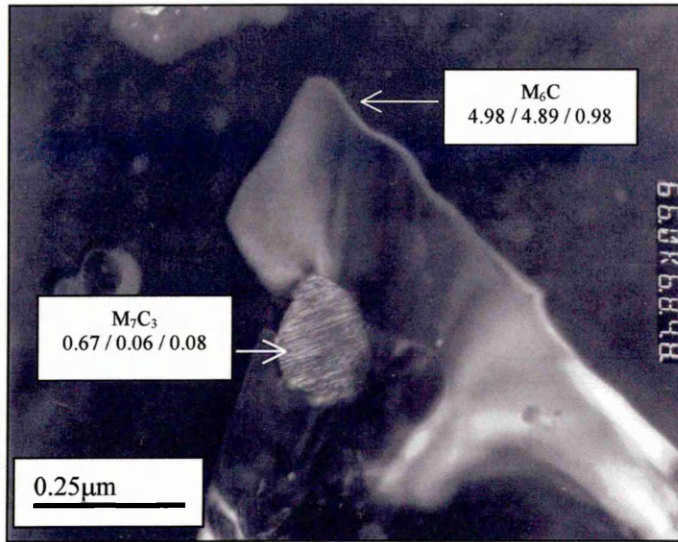


Plate 4.57: Dark field image of feature B in micrograph depicted in plate 4.55 and the corresponding elemental ratios for Fe:Cr, Mo:Cr and Mo:Fe from EDX analysis.

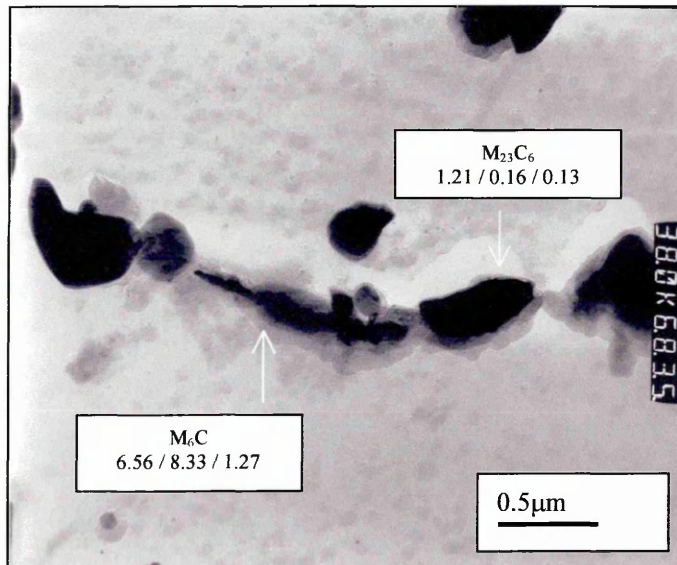


Plate 4.58: Bright field image of feature C in micrograph depicted in plate 4.55 and the corresponding elemental ratios for Fe:Cr, Mo:Cr and Mo:Fe from EDX analysis.

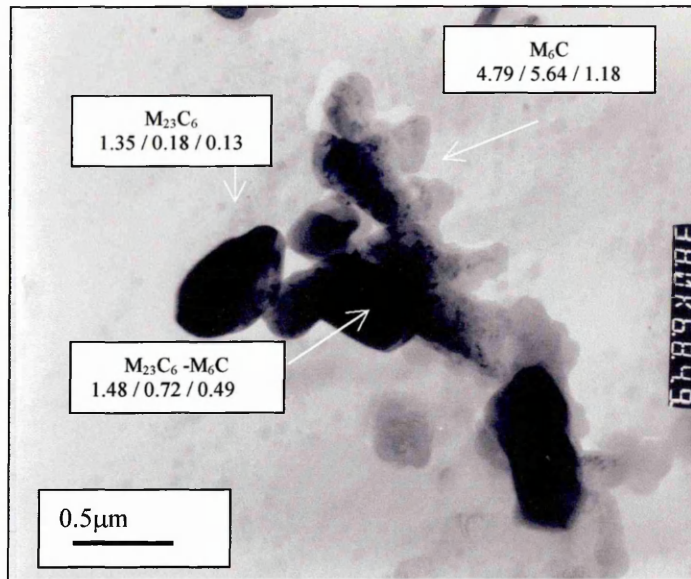


Plate 4.59: Growth of M_6C from $M_{23}C_6$ on a grain boundary almost parallel to the maximum principal stress in the notch tip region of the fully bainitic CT specimen tested at a temperature of $550^\circ C$ and a stress of 100MPa for 350 hours and corresponding elemental ratios for Fe:Cr, Mo:Cr and Mo:Fe determined by EDX analysis.

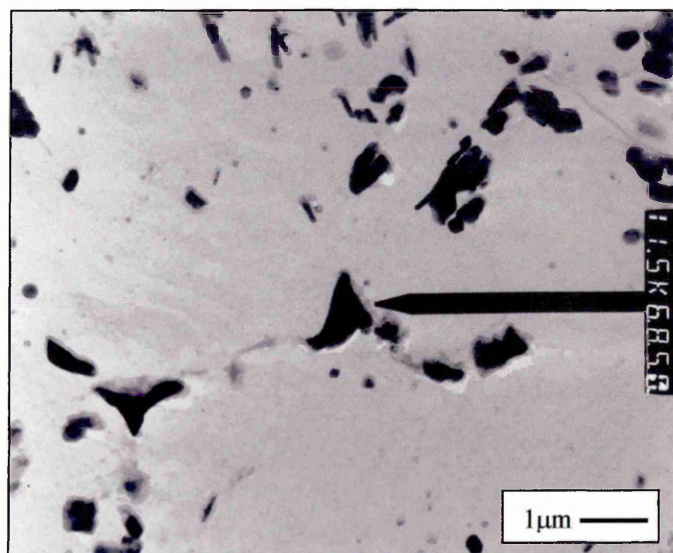


Plate 4.60: M_6C type carbides at grain boundary triple points in the fully bainitic CT specimen tested at a temperature of $550^\circ C$ and a stress of 100MPa for 350 hours.

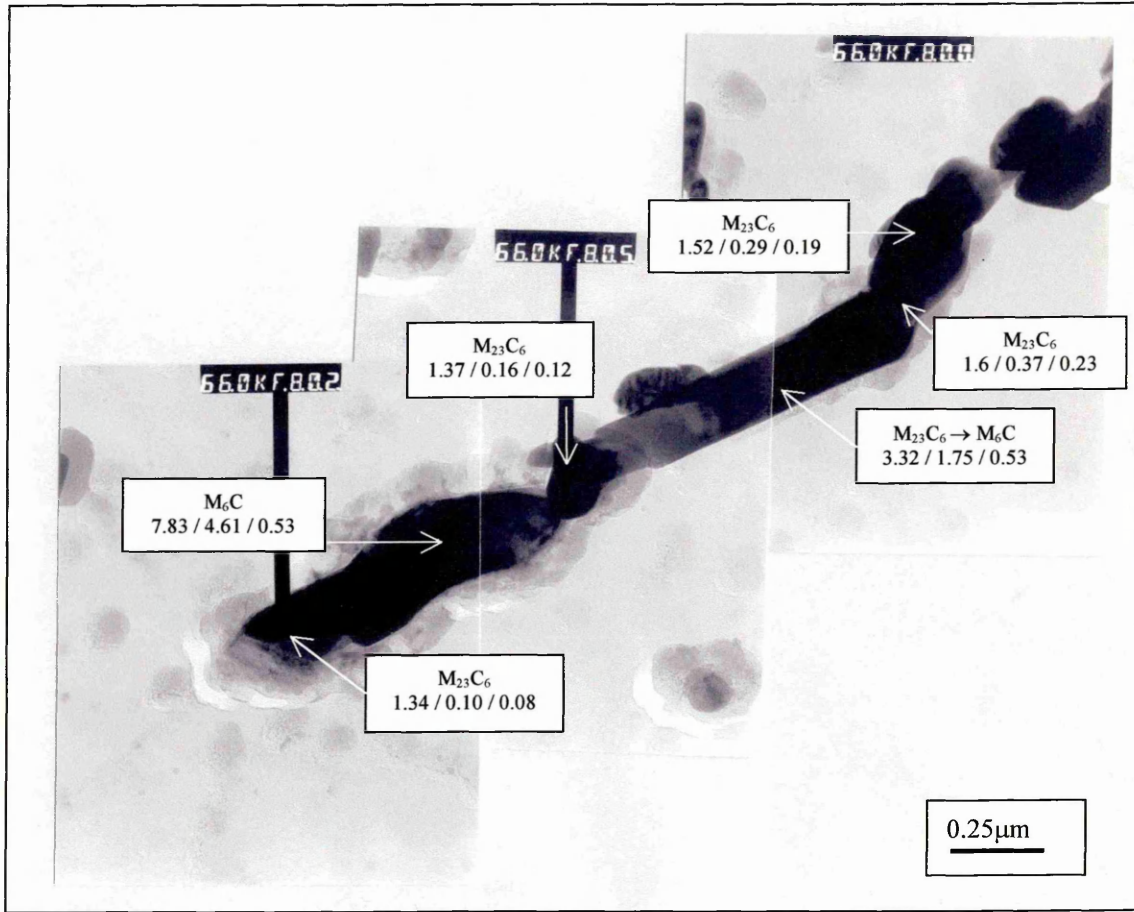


Plate 4.61: High magnification TEM image of an elongated grain boundary carbide in the notch tip region of the fully bainitic CT specimen. The elemental ratios of Fe:Cr, Mo:Cr and Mo:Fe, determined by EDX analysis, are indicated in this micrograph.

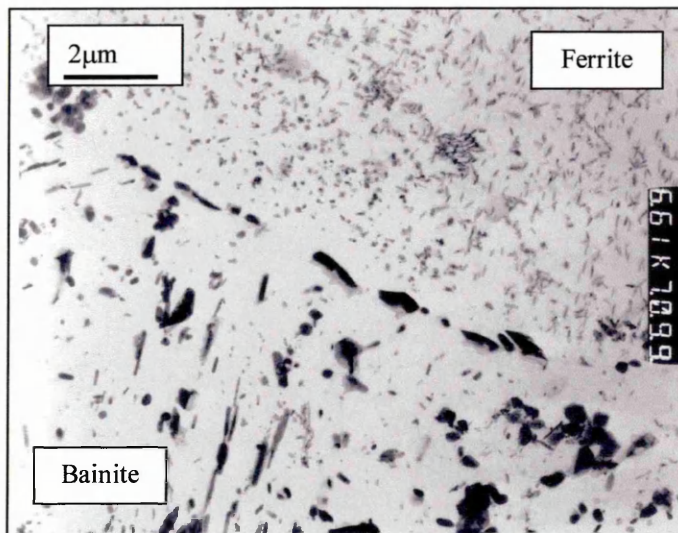


Plate 4.62: TEM micrograph showing the typical carbide morphology observed in a reference region of the ferrite / bainite CT specimen tested at a temperature 550°C and a stress of 110MPa for 850 hours.

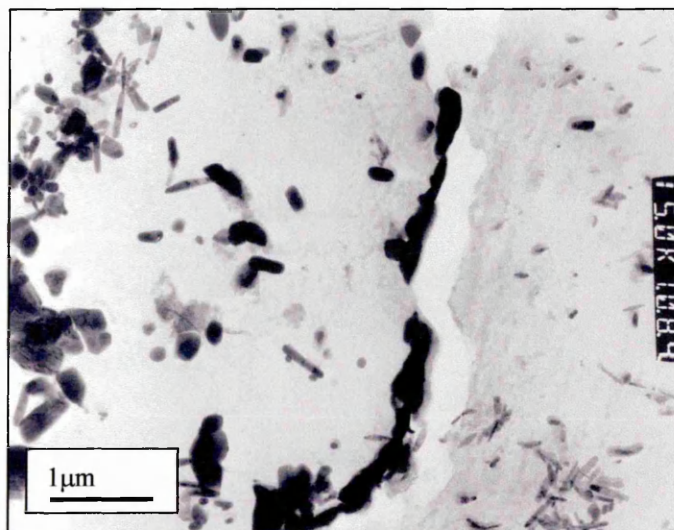


Plate 4.63: TEM micrograph showing elongated carbides along a ferrite / bainite grain boundary oriented at an angle with respect to the notch tip and maximum principal stress.

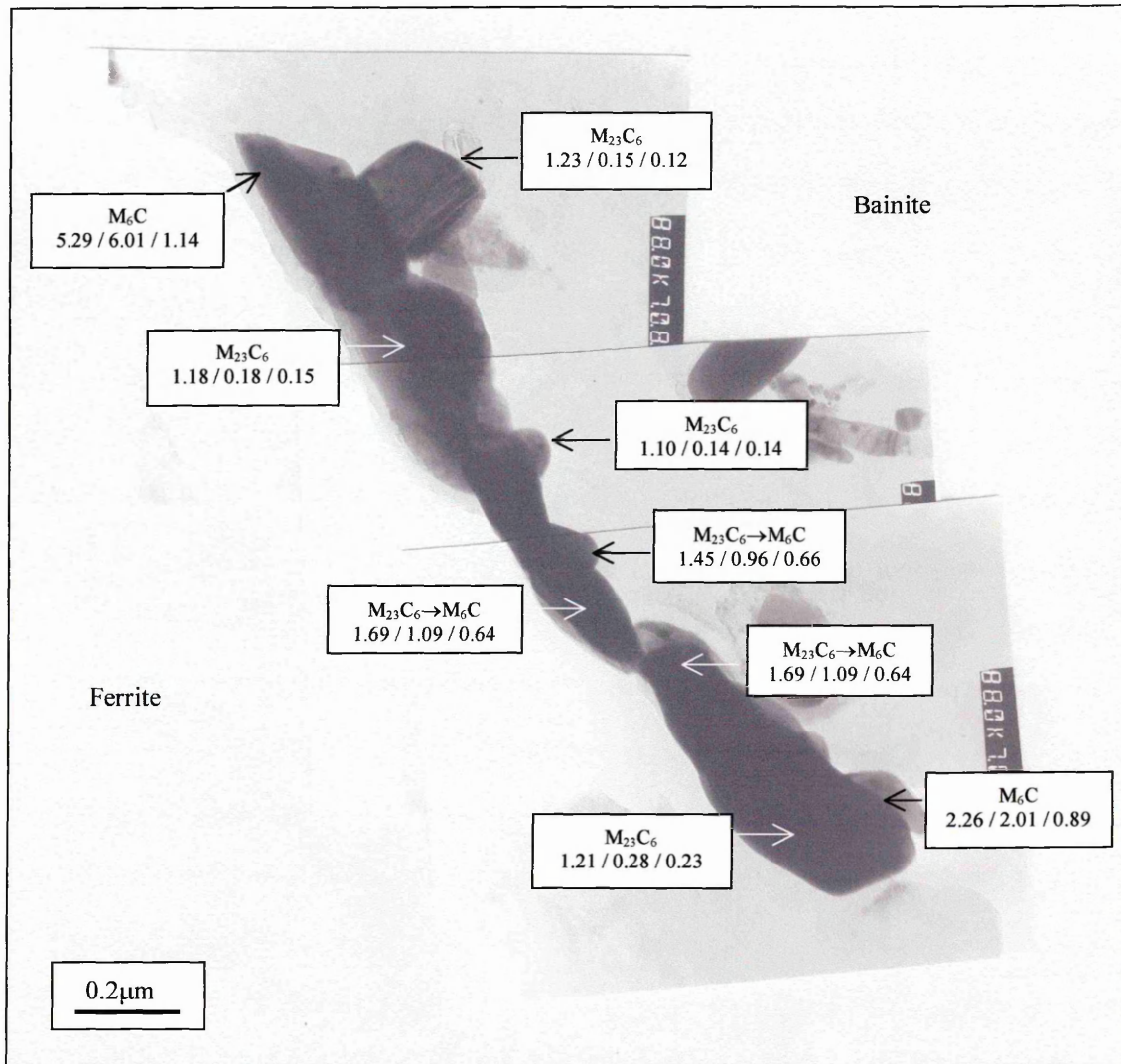


Plate 4.64: High magnification TEM image of the elongated grain boundary carbide observed in plate 4.63 and corresponding elemental ratios for Fe:Cr, Mo:Cr and Mo:Fe determined by EDX analysis.

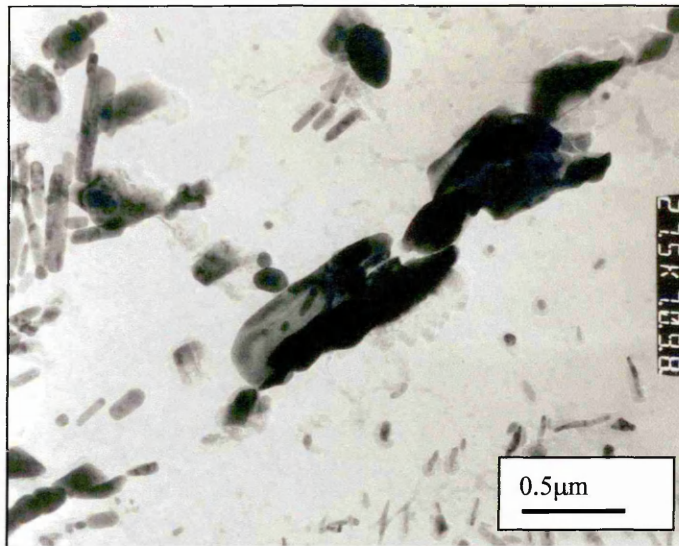


Plate 4.65: Evolution of $M_{23}C_6$ to M_6C by the gradual absorption of elements from adjacent carbides on a non-critically oriented ferrite / bainite grain boundary.

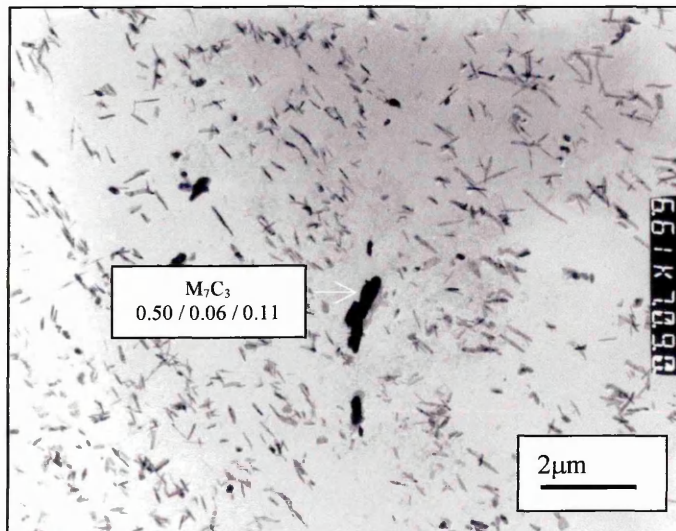


Plate 4.66: M_7C_3 type carbide at a typical ferrite / ferrite grain boundary in the ferrite / bainite CT specimen and corresponding elemental ratios for Fe:Cr, Mo:Cr and Mo:Fe.

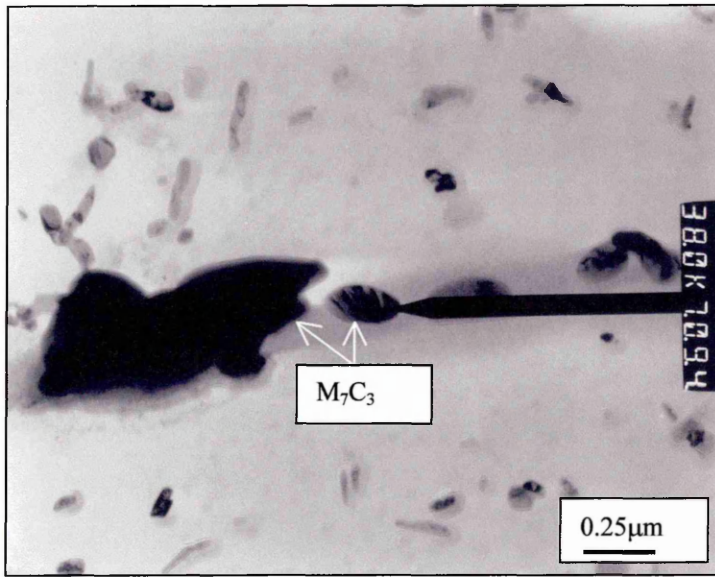


Plate 4.67: Growth of M_7C_3 type carbide at a ferrite / ferrite grain boundary by absorption of adjacent M_2C carbides in the ferrite / bainite CT specimen.

5.1 Starting Structures and Basic Mechanical Properties of 2.25%Cr-1%Mo Steel

In large, ferritic alloy steel, cast components a range of microstructures may exist ranging from pro-eutectoid ferrite + pearlite structures, in thick sections, to fully bainitic structures, in thin sections.

In this study, three microstructural variants of 2.25%Cr-1%Mo steel, a material utilised for power plant applications, were selected to assess the effect of the presence of a pre-existing defect on the creep resistance of the alloy. To make this assessment it was first necessary to characterise the starting structures in terms of their microstructural constituents and basic mechanical properties and to consider the principles behind their formation.

5.1.1 Transformation Structures

The three transformation structures generated for this study, i.e. ferrite / pearlite, ferrite / bainite and 100% bainite, were a result of varying the cooling rate of the alloy from the austenitising phase field, above the A_{c3} . The grain size of the resulting structures was a direct consequence of the austenitising temperature and duration and was determined in this study using the mean linear intercept method.

As anticipated the grain-size of the ferrite / bainite and fully bainitic structures were similar having an average grain diameter of $\sim 0.065\text{mm}$. The ferrite / pearlite structure, however, being from an alternative material source, was found to possess a significantly finer grain structure of average grain diameter $\sim 0.03\text{mm}$. Although the grain size is only regarded as having a small influence on the creep resistance of ferritic, alloys ^{[21] [75]}, it may have had a significant effect on the tensile properties, as discussed later.

In accordance with the CCT diagram for the alloy ^[140], cooling to room temperature from above the Ac_3 results in the transformation of FCC austenite to BCC ferritic phases, the elemental additions in the alloy either remaining in solid solution or precipitating out as discrete second phase particles. The propensity of the elements to be situated in one or the other of these sites depends upon the solubility of the alloying elements in the BCC crystal lattice and the cooling rate from the Ac_3 to the Ac_1 .

In ferritic, 2.25%Cr-1%Mo, alloy steel the elements that are of particular interest, with respect to the creep resistance of the alloy, are C, Mo and Cr. When precipitation of these elements is suppressed on cooling from above the Ac_3 , C is held interstitially in the Fe lattice, while Cr and Mo substitute for Fe. In both interstitial and substitutional solid solutions the elements create a strain field in the BCC iron lattice leading to solid solution hardening effects.

On slow cooling from above the Ac_3 to form the ferrite / pearlite transformation structure the pro-eutectoid ferrite formed first, nucleating at the austenite grain boundaries and rejecting carbon into the remaining austenite. On reaching the Ac_1 any remaining austenite underwent the eutectoid reaction to pearlite, precipitating the majority of carbon as Fe_3C or alloy carbide. The relative amounts of pro-eutectoid ferrite and pearlite in the final structure were dependent upon the cooling rate between the Ac_1 and Ac_3 . In this study only ~10% pearlite phase was found to exist, the dominant phase in the pearlite / ferrite structure being that of newly formed pro-eutectoid ferrite grains.

During the transformation process to pro-eutectoid ferrite + bainite, by faster cooling than that experienced for the ferrite / pearlite structure, the pro-eutectoid ferrite was again formed first. The pearlite reaction was prevented by the faster cooling rate and the remaining austenite, enriched in carbon, transformed to bainite. In the case of upper bainite, as was confirmed for the material in this study, the carbon was held in both interstitial solid solution sites and precipitated out as cementite between the upper bainitic ferrite laths. The Mo and Cr in the as-cooled structure existed in solid solution sites uniformly

dispersed between the pro-eutectoid ferrite and the bainite, in line with the theory of non-partitioning as described by Honeycombe ^[23]. The volume fraction of the pro-eutectoid ferrite and bainite formed was again dependent upon the cooling rate from above the A_{c3} , and in this investigation a structure consisting of 75 % ferrite and 25% bainite was observed.

In the case of the fully bainitic structure, where the cooling rate was sufficiently high to by-pass the pro-eutectoid ferrite and pearlite transformation curves, the austenite transformed directly to bainite and the carbon, for upper bainite, was distributed as described above for the bainite in the mixed structure. In this case, however, due to the absence of the pro-eutectoid ferrite phase there was less interstitial saturation of carbon in the bainite. Cr and Mo were, again uniformly dispersed in the solid solution structure.

5.1.2 Carbide Structure

In the case of the ferrite / bainite and fully bainitic material, the as cooled structures were, subsequently, subjected to a stress relief and tempering treatment. This treatment allowed some of the elements saturated in the solid solution to precipitate out as alloy carbides. As the carbide type, size and distribution in these structures has a significant effect on its mechanical properties the starting structures were also characterised in these terms.

In the mode of Titchmarsh ^[138], Pilling and Ridley ^[30] and Abdel-Latif et al ^[39] semi-quantitative EDX analysis of carbides extracted from the temper trial samples and starting structures enabled a carbide classification scheme, based on the ratios of Fe, Cr and Mo, to be derived. These classification ratios, as detailed in Table 3.4, p87, were then used to identify the carbides in the alloy for the remainder of the study.

From the SEM and TEM studies of the starting structures it became clear that although the various carbide types detected in each structure were similar their distribution and, in some cases, maturity varied.

The carbides in the pro-eutectoid ferrite phase of both the mixed ferrite / pearlite and ferrite / bainite structures were identified as M_2C by their lenticular shape and composition rich in molybdenum and chromium. It was noted, however, that the M_2C in the ferrite phase of the ferrite / pearlite structure was richer in chromium than that detected in the ferrite / bainite structure. This was considered to be due to the increased chromium concentration of the ferrite in the slow cooled structure, that is the slower cooling may have allowed partitioning of the ferrite former.

The pearlitic regions in the ferrite / pearlite specimens were found to exhibit a lamellar structure of eutectoid ferrite and alloy carbide with large, globular or elongated, $M_{23}C_6$ carbides at the prior austenite grain boundaries. The boundaries between the pearlite and pro-eutectoid ferrite regions that did not coincide with those of the prior austenitic structure were not delineated by large carbides. At the ferrite / ferrite boundaries carbides typical of $M_{23}C_6$ were found. No evidence of M_6C carbides were detected in this structure.

From the analysis of the carbides in the bainitic regions of both the mixed ferrite / bainite and fully bainitic structures it became clear that, not only was there a higher density of carbides in the bainite of the mixed structure but that the proportion of carbides of a particular type varied.

The bainitic regions in both structures exhibited a mixture of M_2C , M_7C_3 and $M_{23}C_6$ carbides, the occurrence of M_2C being minimal compared to that observed in the ferrite grains and also to that of the M_7C_3 and $M_{23}C_6$. $M_{23}C_6$ was widely detected in the bainitic regions of both structures but M_7C_3 was more prevalent in the mixed structure.

As determined in the tempering trials of this investigation, and described by previous authors ^[17] ^[30], M_7C_3 in this alloy nucleates in the early stages of tempering in the vicinity of M_3C by absorption of Cr from the surrounding matrix. At extended times and elevated temperatures the M_7C_3 carbide begins to dissolve giving way to the independent nucleation and growth of $M_{23}C_6$, having a lower C:metal atom ratio. With this evidence in mind it can be surmised that the increased carbide density and persistence of M_7C_3 to longer times observed in the bainite region of the mixed structure was due to an increased C: metal atom ratio compared to that in the fully bainitic structure.

It is proposed that, during the austenite to pro-eutectoid ferrite transformation the remaining austenite was enriched in carbon. On further cooling, when the remaining austenite transformed to upper bainite, the carbon in solution precipitated out between the bainite laths as cementite and, to a lesser extent, remain trapped interstitially in the bainitic ferrite. The increased concentration of carbon in the remaining austenite led to a corresponding increase in the density of carbides in the bainite of the mixed structure.

Evidence for the stabilising effect of carbon on the $M_7C_3 - M_{23}C_6$ evolution process was reported previously by Beech and Warrington ^[32]. They proposed a relationship between the alloy composition and the time to achieve 50% transformation of the M_7C_3 carbides to $M_{23}C_6$, such that:

$$t_{50} = \exp 13.7(1 + C - 0.12Cr) \quad - \text{Equation 5.1}$$

Carbides existing at the bainite / bainite boundaries and ferrite / bainite boundaries in both bainite containing structures were found to be predominantly $M_{23}C_6$ in nature with occasional M_6C . Analysis of the carbides at the ferrite / ferrite boundaries in the mixed ferrite / bainite structure, however, were found to be chromium rich and of the type M_7C_3 .

The explanation for the retention of M_7C_3 at the ferrite / ferrite boundaries in the mixed structure may again be linked to the relative carbon: metal atom ratio in this region and the evidence for this comes from a comparison of the current work with that of Thomson [35]. In contrast to the current work Thomson reported that $M_{23}C_6$ was present at the ferrite / ferrite grain boundaries during the early stages of tempering a mixed ferrite / bainite, 2.25%Cr-1%Mo steel. The mixed structure in the Thomson study, however, was that of 50% ferrite / 50% bainite and not 75% ferrite / 25% bainite as in this case.

During the formation of the pro-eutectoid ferrite in the mixed structure of the current study less remaining austenite was available to absorb the carbon displaced from the ferrite, i.e. only 25% austenite remained compared to 50% in the study by Thomson [35]. The outcome of this was that carbon became trapped at the ferrite / ferrite boundaries, increasing the carbon : metal atom ratio of the carbides that formed there, allowing them to persist in the structure to longer times.

Table 5.1 summarises the types and locations of carbides identified in the various starting structures.

Locations	Transformation Structures		
	Ferrite / Pearlite	Ferrite / Bainite	100% Bainite
Ferrite Intra-granular Regions	M_2C	M_2C	n.a.
Pearlite Intra-granular Regions	Lamellar alloy carbides	n.a.	n.a.
Bainite Intra-granular Regions	n.a.	M_7C_3 , $M_{23}C_6$	$M_{23}C_6$
Ferrite / Ferrite Grain Boundaries	$M_{23}C_6$	M_7C_3	n.a.
Ferrite / Pearlite Grain Boundaries (prior γ)	$M_{23}C_6$	n.a.	n.a.
Ferrite / Pearlite Boundaries (not prior γ)	Not delineated by carbides	n.a.	n.a.
Ferrite / Bainite Grain Boundaries	n.a.	$M_{23}C_6 + M_6C$	$M_{23}C_6 + M_6C$
Bainite / Bainite Grain Boundaries	n.a.	n.a.	$M_{23}C_6 + M_6C$

Table 5.1: Type and location of carbides detected in the three starting structures investigated in the current study.

5.1.3 Basic Mechanical Properties

In light of the evidence given above for the microstructural variables in the three structures studied, the variation in room temperature and elevated temperature properties can now be discussed.

The room temperature hardness and strength of the fully bainitic structure were superior to those of the ferrite containing structures as anticipated. Bainite, and in this particular case upper bainite, is rich in carbon some of which is held interstitially in solid solution and some precipitated out as alloy carbide. The strengthening in such structures results from the strain fields around the interstitial C sites, and precipitate structures, reacting with mobile dislocations, ^[23]. The effectiveness of precipitates acting as barriers to dislocation movement is dependent on their size which is in turn controlled by Ostwald ripening. In the fully bainitic starting structure the carbides were only in the early stages of evolution and the structure was, therefore, relatively hard and strong.

The room temperature hardness and strength of the ferrite / pearlite and ferrite / bainite structures were similar. This result could not be anticipated from the explanation for strengthening mechanisms given above for bainite as it would be expected that the faster cooled bainite transformation product in the ferrite / bainite structures would be harder and stronger than that of the pearlite in the ferrite / pearlite structure. The grain size of the two structures, however, must also be taken into consideration as this has a direct effect on these properties.

The well known Hall – Petch relationship, as described by Honeycombe ^[23], shows that the yield strength, σ_y , increases linearly for a decrease in grain diameter and it is this factor that was considered to be dominating the tensile behaviour in this case. The smaller grain-size of the ferrite / pearlite structure led to an increase in the number of barriers to dislocation movement per unit length of material. The carbide size and distribution at the grain boundaries may also have had an effect on the fracture stress but this was regarded as being of only minor significance here.

The elongation to breaking point was found to be similar in each structure indicating the relative insensitivity of the test to any variation in grain boundary carbide morphology present at this stage.

At 550°C the results of the tensile results were quite different to those of the room temperature tests. The ultimate tensile strength of the bainitic containing structures reduced significantly compared to that of the ferrite / pearlite structure, that became the stronger material at this temperature. This effect was considered, predominantly, to be due to the loss of carbon from the interstitial solid solution sites in the bainite and, secondly, to the growth of existing carbides at the elevated temperature. The ferrite / pearlite structure, being closer to the equilibrium state for the alloy, did not suffer a similar loss in strength, the advantage of the fine grain structure being dominant.

The elongation to breaking point at the elevated temperature was surprising in that the values obtained for all three structures were lower than those obtained at room temperature. This result was also found in tests carried out on this alloy by other authors ^[143] ^[144] but was not explained. It may be possible that an increase in the size of the carbides at the grain boundaries, due to the elevated temperature, had an effect on the fracture initiation and growth process but there is insufficient evidence to substantiate this at this time.

It became apparent that even when studying the basic mechanical properties of 2.25%Cr-1%Mo steel, variations in grain-size, transformation products and carbide type and distribution make trends in behaviour very difficult to establish.

5.2 Tempering Characteristics and the Carbide Evolution Process in 2.25%Cr-1%Mo Steel.

To gain an understanding of the carbide evolution process in this alloy a tempering trial was carried out on the fully bainitic structure generated for this

study. It was necessary to achieve this understanding in order to assess the effect of a tri-axial state of stress, as exists ahead of a pre-existing defect, on the microstructural evolutionary process in a power plant component.

Although it was appreciated that the evolutionary process may vary from structure to structure, the fully bainitic structure was selected for the tempering trial on the basis that it possessed, at some stage during tempering, all of the carbides types reported to exist in this alloy. The trial consisted of tempering normalised 2.25%Cr-1%Mo steel for various times and temperatures and examining the resultant microstructures and hardness values.

Vickers hardness values were determined for all the specimens tempered in the trial and plotted concurrently on charts showing the change in hardness with time at temperature and against the Holloman -Jaffe parameter, as described in section 4.3.1

The similar trends in softening apparent for the specimens tempered at all three tempering temperatures suggested that the same softening mechanisms were occurring but at different rates dependent upon the temperature. The largest reduction in hardness was observed in the first 0.5 hours of tempering for all specimens and was the greatest for the specimens tempered at 750°C., as indicated in Figure 4.2, p112. There was no evidence of a peak in the hardness values due the secondary hardening as described for the study on this alloy by Baker and Nutting ^[17]. As the softening mechanisms were considered to be consistent for all specimens tempered at the various temperatures the remainder of the discussion concentrates on the specimens tempered at 700°C only.

A qualitative assessment of the tempered specimens in terms of their general microstructure, carbide size and distribution was made by SEM examination. The carbide evolution process, however, was assessed by setting up an image analysis programme in the STEM and characterising the carbides in terms of

their size and type. The carbide classification scheme in this trial was based on the key elemental constituents in the carbides.

The microstructure of the bainitic starting structure for the tempering trials was that of the as normalised 2.25%Cr-1%Mo alloy. The carbides present between the upper bainitic, ferrite, laths were Fe and Cr rich and, therefore, believed to be either ϵ - carbide or Fe_3C as described in the study of Baker and Nutting^[17]. The intra-lath regions were free of any precipitation.

After tempering the bainite structure for only 0.5 hours at 700°C a distribution of both small, uniformly dispersed, carbides and larger, grain boundary and lath boundary, carbides were evident throughout the structure. The majority of the small carbides were found to be Fe rich with some contribution from Cr that identified them as M_3C type carbides. The remainder of the small carbides were identified as M_2C type by their lenticular shape and Mo / Cr rich composition. The large carbides were observed to be either rod-like, trapezoidal or globular in shape and analysed to contain a range of Fe, Cr, and Mo concentrations. This evidence was consistent with these larger carbides being either M_7C_3 or M_{23}C_6 type.

The results of the image analysis routine on the carbides extracted from the 0.5 hour sample, as shown in Figure 4.4, p121, indicated that the most abundant carbides at this very early stage of tempering were M_7C_3 in nature with a significant presence of M_{23}C_6 carbides. The fine dispersion of M_3C and M_2C carbides represented only a small percentage of the total of carbides detected in this sample. M_6C carbide, the equilibrium carbide in this alloy, was not evident at this stage of tempering.

After tempering for 5 hours at 700°C the image analysis results, as shown in Figure 4.5, p122, indicated that the small M_3C carbides had already dissolved at the expense of the other carbides and that M_{23}C_6 was now the most abundant carbide. A slight increase in the amount of M_2C was detected at this

stage of tempering but the quantity of M_7C_3 had decreased. Again no evidence for the evolution of the M_6C carbide was found in this sample.

The simultaneous dissolution of M_7C_3 and precipitation $M_{23}C_6$ supports the theory that $M_{23}C_6$ grows at the expense of M_7C_3 . Although the mechanism for the $M_7C_3 - M_{23}C_6$ process, in this study and from literary evidence, is unclear the most support appears to be for the theory that $M_{23}C_6$ precipitates independent of the M_7C_3 carbides but may only do so when sufficient Cr has been released back into solution during the dissolution of the M_7C_3 [32].

After 50 hours the quantity of M_7C_3 carbides remained approximately the same but their size was diminishing as indicated by a comparison of the graphs depicted in Figures 4.6, p123, and Figure 4.8, p125. In contrast the incidence of $M_{23}C_6$ type carbides was on the increase with many more small carbides of this type being detected. The number of large $M_{23}C_6$ carbides, greater than $0.3\mu\text{m}$ in diameter, however, appeared to be decreasing at the expense of the evolving equilibrium carbide, M_6C .

As confirmed at a later stage of the study when analysing the creep tested specimens, and as reported by previous authors [17] [29] [30] [138], M_6C is found to evolve from other carbides, predominantly M_2C in the pro-eutectoid ferrite and $M_{23}C_6$ in bainite. The evolutionary process takes place by the gradual absorption of Mo from the surrounding regions and at the expense of the smaller non-equilibrium carbides. Hence, the significant reduction in the number of M_2C type carbides detected at this stage is likely to be a result of its dissolution at the expense of the larger $M_{23}C_6$ and M_6C carbides.

The growth of the larger $M_{23}C_6$ and M_6C carbides at grain boundaries and sub-boundaries was particularly evident in the tempered microstructures observed after extended times and at higher temperatures, for example; after 1000h at 700°C , as shown in Plate 4.19, p118, and after 50 hours at 750°C , as shown in Plate 4.23, p120. The carbides at the grain boundaries were observed to grow in an irregular manner and at the expense of carbides in the adjacent

grains. Their growth rate appeared to be faster than those of like-carbides in intragranular regions of the structure due to the increased rate of atom diffusion at the grain boundary interface.

After 5000h at 700°C only a small percentage of $M_{23}C_6$ carbides remained in the structure in addition to the equilibrium carbide M_6C , that had taken on a more rounded morphology as shown in Plate 4.21, p119. These remaining carbides existed almost exclusively at the prior austenite and recrystallized grain boundaries.

The reduction in hardness trend described previously for the tempered specimens can now be related to the change in microstructure. The initial rapid decrease in hardness coincided with the rapid dissolution of the ϵ -carbide / M_3C carbide and the corresponding loss of carbon and other alloying elements from solution by the precipitation of M_2C , M_7C_3 and $M_{23}C_6$ type carbides. Subsequent softening, considered to be due to a further loss in solid solution hardening elements from the matrix and growth of the alloy carbides, occurred at a much slower rate but continued gradually up to extended times when M_6C , the equilibrium carbide, was fully formed.

In the tempering trials on 2.25%Cr-1%Mo steel carried out by Baker and Nutting^[17] the bainite region in the normalised steel was shown to soften rapidly and then slow down immediately prior to the precipitation of the M_7C_3 . Once precipitation of the M_7C_3 had taken place the softening rate increased again. This may have been due to an effect of the carbon from the M_3C going back into solid solution and for a short period of time forming solute pairs with Cr prior to the precipitation of the Cr rich carbide.

In the well publicised carbide precipitation sequence for normalised 2.25%Cr-1%Mo steel, by Baker and Nutting^[17], M_2C and M_7C_3 were shown to persist for significantly longer times than those reported here. This anomaly is due to the fact that the normalised structure in the Baker and Nutting study was that of 55% ferrite and 45% bainite, and not 100% bainite as in this case. M_2C is

known to persist in ferrite for extended times and eventually to dissolve only at the expense of the equilibrium carbide, M_6C . The existence of pro-eutectoid ferrite in the normalised structure also meant that the resulting bainite was enriched in carbon and that this, in turn led, to the stabilisation of M_7C_3 to longer times^{[30] [32]}.

5.3 Creep Deformation in the Presence of a Pre-existing Defect

To compare the creep deformation response of the three structures selected for this investigation, CT specimens were tested under creep conditions and the material ahead of the spark machined fine notch subsequently assessed in terms of 'damage' accumulation.

The deformation of the CT specimen was monitored by measuring the physical displacement of hardness indentations made parallel to the notch, in the mode of Holdsworth and Cunnane^[19], and the mechanisms of damage accumulation were assessed by qualitative and quantitative microstructural examination of the notch tip material after removing the specimens, sequentially, from test.

Testing of the ferrite / pearlite specimens was carried out at the collaborating establishment and, as a consequence, only micro-samples prepared from the tested specimens were available for further investigation. The ferrite / bainite and fully bainitic specimens were tested in house utilising a creep rig specifically designed for this project, as described in section 3.4.3(a). These specimens were, therefore, fully assessed by all the techniques described in section 3.6 .

5.3.1 Creep Damage Response

When a creep load is applied to a body containing a defect, the stress intensity at the defect tip is dependent upon a number of factors^{[14] [95]}.

- i) the load transmitted to the defect tip
- ii) the defect tip profile
- iii) the constraint exerted at the defect tip by the surrounding material.

In the creep tests carried out in this study the load was applied to the specimens by two diametrically opposite loading pins either side of a machined notch, as shown in Figure 3.4, p73, and the load was transmitted along the load line to the notch tip simulating the defect. The ability of the material surrounding the defect tip to resist creep crack initiation and growth describes the materials creep ductility where the greater the notch opening to creep crack length ratio the more ductile the situation ^[96].

Evidence from the COD evaluation for the 100% bainite and mixed ferrite / bainite CT specimens gave an early indication that the ferrite / bainite structure was more creep ductile than the fully bainitic structure. Examination of the COD curves, depicted in Figure 4.15, p132, and Figure 4.17, p133, showed an almost linear relationship for the displacement of the fully bainitic specimens and a non-linear load line / displacement relationship for the ferrite / bainite specimens. This difference in deformation behaviour highlighted the greater ductility of the mixed ferrite / bainite structure. It also confirmed the observation of Holdsworth et al ^[19] that, values of CTOD determined from load point displacement measurements, as opposed to physical displacement measurements at the crack tip, are inaccurate for materials exhibiting a high creep ductility.

As described in the literature, section 2.4.2, the application of a steady load to a pre-cracked creep ductile structure at high temperature leads to the progressive build up of a damage zone ahead of the crack tip, subsequent crack propagation and eventually failure of the remaining ligament. The spread of the damage zone, prior to crack initiation, is dependent upon the ability of the material ahead of the defect to redistribute the stress intensity ^{[124] [125] [126]} that, in turn, is dependent upon the elastic – plastic characteristics of the material and the degree of notch constraint.

As the geometry of the CT test specimens was the same for all the three microstructural variables studied the constraint due to this factor could be considered equivalent. The test temperature in each case was 550°C and, therefore, the only inconsistency between the specimens, that was non-microstructural, was that of the applied stress used to induce crack initiation in less than 1000 hours, as detailed in section 3.4.3b.

Although it was recognised that the difference in applied stress, and hence the creep deformation rate, may have had an effect on the stress redistribution at the notch tip, it was considered that the observations recorded from the creep tested material were still relevant and significant to the determination of the mechanisms of creep crack initiation and growth ahead of a pre-existing defect in the alloy.

As described by Reidel ^[40], a crack may be perceived to have initiated at the absolute minimum when only two adjacent cavities coalesce or, on the other hand, as described by Holdsworth ^[11], when the crack is detectable by non-destructive testing techniques, that is approximately 0.2mm for the electrical potential drop method. In this study a crack was considered to have initiated if grain boundary cavity coalescence spanned more than one grain. Initiation was then considered to be in progress up to 1mm of detectable crack extension, after which the crack was considered to be propagating.

The creep damage analysis results for the 100% bainite, ferrite / bainite and ferrite / pearlite CT specimens were detailed in sections 4.4.2(a)–(c) respectively.

Comparison of the SEM micrographs and void analysis data for the three microstructures showed that the propensity for cavitation in the notch tip region varied from structure to structure.

In the notch tip region of the fully bainitic structure cavitation, and subsequent crack initiation, was constrained predominantly to an area immediately ahead of the notch tip and into the remaining ligament as shown in the SEM image

and corresponding void analysis chart, Figure 4.20 and Plate 4.26, p141. In the ferrite / bainite structure less constraint was apparent and the damage zone was more widely dispersed, Plate 4.35 and Figure 4.24, p152.

In both the fully bainitic and ferrite / bainite structures cavities were found to have initiated on grain boundaries that were oriented at approximately 45° to the notch tip, or principal stress axis, and the area % of cavities was observed to increase with increasing test duration. High resolution, SEM, secondary electron imaging of the cavitating boundaries indicated that cavitation was nearly always associated with the presence of large, and quite often elongated, carbides. Once initiated, the cavities were observed to extend along the interface between the initiating grain boundary carbide and one of the adjacent grains, suggesting a weakness or loss of coherency of the carbide with matrix.

When carbides nucleate and grow at the interface between two adjacent grains they do so by maintaining a degree of coherency with one of the grains, and in the absence of an applied stress, grow preferentially into the other with which the coherency is low. In the two bainite containing structures, the carbides on the boundaries oriented at $\sim 45^\circ$ to the principal stress axis were observed to grow preferentially along the boundaries and the explanation for this phenomenon lies in the consideration of paths of easy diffusion.

As indicated in Plate 4.28, p144, for the fully bainitic structure, growth of the grain boundary carbides appeared to be occurring at the expense of other carbides in the adjacent grain by atom diffusion down the original, bainitic, lath boundaries. However, rather than the grain boundary carbide growing into an adjacent grain, growth appeared to occur along the line of least resistance, i.e. along the grain boundary. The grain boundaries oriented at 45° to the principal stress axis in the CT specimen were subjected to the maximum shear stresses in the test specimens and, as such, were attempting to slide, thereby acting as a source of dislocations. The dislocation structure, thus created, then acted as an ideal path for atom redistribution, or vacancy migration.

In the mixed ferrite / bainite structure cavitation was rarely observed on the ferrite / ferrite boundaries, even though elongated carbides were found to occur on the boundaries oriented at 45° to the principal stress axis. This phenomenon was considered to be due to the increased stability of the M_7C_3 , detected at these boundaries compared with that of $M_{23}C_6$, $M_{23}C_6$ showing a greater propensity to evolve to the equilibrium carbide, M_6C .

Analysis of the void orientation results for the two bainite containing structures showed that although the creep voids occurred on boundaries oriented at 45° to the principal stress axis the highest frequency of voids detected was for those oriented at angles between $\pm 50^\circ$ to 60° . It was considered that this angle was that related to the longest, feret, diameter of the newly initiated voids, i.e. the angle of the void at the cusp of the carbide, as described by Evans and Wilshire^[50].

In the case of the ferrite / pearlite structure an increase in the area % of cavities with test duration was not found for the limited number of ferrite / pearlite specimens examined. The ferrite / pearlite specimen tested at 85MPa for 3689 hours showed extensive cavitation in the notch tip region, as indicated in Plate 4.45 and Table 4.24, p161, but the structure resisted crack initiation by cavity coalescence. In contrast, the ferrite / pearlite sample tested at 85MPa for 6850 hours showed little cavitation in the area ahead of the notch, however, a crack measuring $\sim 0.08\text{mm}$ was found to have initiated, as shown in Plate 4.46, p162. Examination of this crack, using high resolution secondary electron imaging in the SEM and complementary EDX analysis, revealed that it was associated with the presence of a large sulphide inclusion that appeared to have caused its initiation. In a microstructure such as this, that allows gross cavitation to take place without extensive coalescence, it was considered that the incoherent interface between the sulphide and the matrix may have acted as a sink for stress induced dislocations rendering the surrounding material relatively stress and cavity free. This evidence also highlights the importance of fine microstructure on the creep properties of a material containing a defect

in that a large inclusion, under the action of a triaxial state of stress, may nucleate a crack prematurely.

In contrast to the ferrite / bainite and fully bainite specimens, that exhibited cavitation on boundaries that were approximately 45° to the principal stress axis, cavitation in the ferrite / pearlite specimens took place on grain boundaries which were oriented at much lower angles, the angle of the first formed voids being $\sim 30^\circ$ - 40° with respect to the notch tip. This difference in orientation could not be explained mechanistically but it was considered that it may have been due to a preferred orientation effect resulting from the manufacture of the pipe material from which it was derived.

A further difference in the creep deformation behaviour between the two bainite containing structures and the ferrite / pearlite structure was the apparent mechanism by which the initiated grain boundary cavities appeared to be "growing". Whilst cavity growth and crack extension in the aforementioned structures appeared to be a result of concurrent decohesion of elongated carbide / matrices and subsequent coalescence; in the ferrite / pearlite structure cavity growth was considered to be a result of ductile tearing along the carbide / matrices interface.

Due to the lack of data available for ferrite / pearlite specimens the final correlation between the void area %, CTOD and crack extension results was made only for the ferrite / bainite and 100% bainitic microstructures.

A comparison of the behaviour of the two bainite containing structures was made by plotting the creep deformation results on the same axes as shown, and described, in section 4.4.3. The results plotted for the CTOD against crack extension data showed that a CTOD value of $\sim 0.3\text{mm}$ gave crack initiation of 1mm in both bainite containing structures, Figure 4.31, p173. The time to generate this degree of crack extension, however, was found to be only ~ 400 hours in the fully bainitic structure tested at the lower stress of 100MPa, compared to ~ 1000 hours in the mixed structure tested at 110MPa.

In the preliminary stages of initiation, i.e. up to 0.5mm of crack extension, cracking was found to proceed for a lesser degree of voiding and CTOD in the bainitic structure than in the ferrite / bainite structure as shown in Figure 4.30a, p172, and Figure 4.31b, p173, respectively. The values of $\Delta a/\Delta CTOD$ and $\Delta a/\text{void area \%}$ in this period give an indication of the constraint and, hence, creep ductility of the microstructure in the vicinity of the defect tip and have, therefore, been determined and displayed below in Table 5.2 for the two bainite containing structures. The larger the ratio value the greater the microstructural constraint and the lower creep ductility.

Transformation Structure	Ratio Values Determined Upon the Attainment of 0.5mm Crack Extension	
	$\Delta a/\Delta CTOD$	$\Delta a/\text{void area \%}$
75% Ferrite / 25% Bainite	1.85	0.21
100% Bainite	2.78	2.0

Table 5.2: Values of $\Delta a/\Delta CTOD$ and $\Delta a/\text{void area \%}$, determined from the ferrite / bainite and 100% bainite CT specimens at a crack extension of 0.5mm.

All the above factors confirm the superior creep ductility of the mixed structure up to a critical CTOD of ~0.3mm. Once this critical value has been obtained crack extension in both structures appeared to progress at a similar rate, Figure 4.29b, p171.

The difference in the deformation behaviour of a material exhibiting either a ferrite / bainite or a fully bainitic microstructure in the presence of a triaxial state of stress was also studied by Gooch and King ^[95]. In this study on a 0.5%Cr-0.5%Mo-0.25%V steel a microstructure consisting of 100% tempered bainite was found to exhibit a crack extension to COD ratio, ($\Delta a/\Delta COD$), three times the value of that determined for a 15% bainite + pro-eutectoid ferrite. It was considered that, although this observation supports the findings of the

current study, the deformation effects in the work of Gooch and King were exaggerated by the method used for evaluating the COD, i.e. displacement at the loading pins and not physical displacement measurements at the crack tip as in this work.

5.3.2 The Effect of Microstructural Variables on the Creep Crack Initiation and Growth Process

In this section the relationship between the microstructural evolution and the onset of creep crack initiation and growth will be considered for the three microstructural variants investigated.

The difference in the early deformation response of the microstructural variables was considered to be the key to understanding the mechanisms of creep damage in the presence of a pre-existing defect in this alloy.

When a defect is present in a large component operating under creep conditions the stress intensity at the defect tip is dependent upon the ease with which that stress can be redistributed in to the surrounding material, i.e. dependent upon the constraint of the material. With reference to the deformation map of Maruyama ^[67] it was considered that, in the temperature and stress regime relevant to this study, creep stress redistribution was related to the ease that dislocations could glide through the structure and bypass inherent obstacles.

In the microstructures studied, dislocation mobility was restricted by interaction with solid solution atoms, precipitates, other dislocations and grain boundaries and was released by diffusion of atoms, by dislocation climb, leading to power law creep. At elevated temperatures a further degree of freedom to deform was activated by the ability of the grain boundaries to slide past one another.

In the presence of grain boundary carbides, sliding can only occur if there is sufficient driving force for atoms in the vicinity to circumnavigate the obstructing carbide. The driving force for this to occur is provided by the heat in the system which is, generally, less for movement of atoms down dislocation cores, (Coble creep), than diffusion through the bulk, (Nabarro-Herring creep).

From a consideration of the above factors, the following microstructural aspects were regarded to be of importance to evaluate the creep behaviour of the material under investigation in this study:

- The elements in solid solution in the pro-eutectoid ferrite, pearlite and bainitic regions of the structures.
- The chemistry, morphology and distribution of the carbides in the intra-granular regions of the pro-eutectoid ferrite, pearlite and bainite.
- The chemistry, morphology and distribution of the carbides at the ferrite / ferrite, ferrite / pearlite, ferrite / bainite and bainite / bainite grain boundaries.
- The presence, or absence, of precipitates in the zones immediately adjacent to the grain boundaries in the structures.

The resistance to dislocation movement in the intra-granular regions of the structures will be considered first.

By comparing the microstructural constituents of the ferrite / pearlite structure with that of the ferrite / bainite structure and, in turn, the ferrite / bainite structure with that of the 100% bainite structure, the contribution of each phase region to the creep resistance of the alloy could be assessed.

The main difference in the creep response of the ferrite / pearlite and ferrite / bainite structures was attributed to the relative maturity of the carbides in the pearlite and bainite phase regions. The slower cooling regime that produced the ferrite / pearlite structure allowed the majority of the alloying elements in

that structure to precipitate out as alloy carbides, reducing the solid solution strengthening capability and leaving it susceptible to creep deformation.

The presence of the faster cooled bainite phase regions in the ferrite / bainite structure were comparatively creep resistant, the carbides existing there being in a less mature state.

Similarly, the significant difference between the two bainite containing structures studied was the presence of pro-eutectoid ferrite grains in the mixed structure.

In terms of the passage of dislocations through the bainite containing structures the presence of the ferrite phase may have had two distinct effects:

- i) To impart a restriction to dislocation movement in the ferrite by the precipitation of a fine distribution of M_2C .
- ii) To cause, during its formation, an increase in the saturation of carbon in the remaining austenite resulting in additional solid solution and/or precipitation hardening in the, finally formed, bainite .

In the starting condition these structures were in a tempered state and the carbides had already undergone a degree of evolution with respect to original transformation structures.

M_2C was the only carbide found to exist in the ferrite of the mixed structure but it had almost completely disappeared at the expense of M_7C_3 and $M_{23}C_6$ type carbides in the bainitic regions. If restriction of dislocation movement by the M_2C precipitates was the dominant strengthening mechanism, as has been described for many long term tests, the ferrite / bainite specimens would have been more resistant to creep deformation than the fully bainitic specimens. This was not the case, the ferrite / bainite specimens exhibiting the greater creep ductility.

In addition to the presence of the pro-eutectoid ferrite another difference between the two bainite containing structures was identified. The bainite in

the mixed structure was found to consist of a more dense dispersion of carbides and, as mentioned previously, a higher $M_7C_3 / M_{23}C_6$ carbide ratio than that in the fully bainitic structure. This was evident from the TEM images for the ferrite / bainite and fully bainitic structures, as shown in Plate 4.12, p107, and Plate 4.14, p108, respectively. The variation in the amount of each carbide type present and the increased density of carbides was attributed to the fact that the bainite in the mixed structure was enriched in carbon with respect to that in the fully bainitic condition. The fact that the additional carbon in the bainite of the mixed structure appeared to have precipitated out, as indicated by the greater density of carbides in the bainite of this structure, suggests that its subsequent effect on interstitial solid solution hardening would be minimal, however, an effect of precipitation strengthening may have occurred.

The principle difference in the response to a creep stress of the two bainite containing structures, then, appears to be the percentage of bainite present.

Two strengthening mechanisms may be operable in the bainite, that is:

- i) precipitation strengthening from the alloy carbides and
- ii) solid solution strengthening from the C, Cr and Mo in solution.

It has been reported by Kleuh^[16] and Jones^[64] that Cr and Mo may form solute pairs with C leading to dislocation drag and, hence, creep strengthening. In the relatively short term tests of the current study, i.e. where the applied stress was relatively high, this was considered to be a likely mechanism for the strengthening as a substantial amount of C, Cr and Mo still existed in the solid solution. The argument against this theory may be that if a substantial amount of Mo was still present in the solid solution then M_2C would naturally precipitate next as a consequence of this. This was not the case. In this study M_2C was shown to be virtually absent in the bainite after the tempering treatment and prior to creep testing. It was considered unlikely, from existing knowledge, that Cr alone would have this strengthening effect and, therefore, it was believed that in the bainite M_2C dissolved early in the

tempering process, re-enriching the solid solution in Mo, from where it was gradually absorbed by the pre-existing $M_{23}C_6$. Finally when the Cr in the matrix was depleted the continuing enrichment of Mo led to the evolution of the M_6C equilibrium carbide. This enrichment behaviour was observed in the final stages of evolution in this study during the investigation of the grain boundary carbides of the creep tested specimens.

Comparison of the Fe:Cr, Mo:Cr and Mo:Fe elemental ratios for the evolving carbides depicted in Plate 4.59, p181, Plate 4.61, p182, and Plate 4.64, p184, indicated how the carbide could exist in a transition state between the equilibrium compositions of the $M_{23}C_6$ and M_6C carbides. The Fe:Cr and Mo:Cr elemental ratios in the evolving carbides were shown to gradually increase indicating the gradual enrichment of the evolving carbide in molybdenum.

In addition to the solid solution strengthening in the bainite, it was considered that strengthening may also have been afforded by the M_7C_3 and $M_{23}C_6$ precipitates. Compared to the M_2C in the ferrite these carbides were relatively coarse, however, it is known that optimum creep strengthening is not always afforded by a fine dispersion of precipitates but, "rather by a somewhat over-aged structure", [6].

In summary, dislocation mobility in the intra-granular regions of the specimens tested was considered to be limited by:

- i) Mo, Cr and C atoms in solid solution, possibly at atom clusters [5] [16] [65].
- ii) M_2C precipitates in the pro-eutectoid ferrite.
- iii) M_3C , M_2C , M_7C_3 , $M_{23}C_6$ precipitates in the pearlitic and bainitic regions.

Once freed from barriers, dislocations were able to glide through the structure until they impinged upon a grain boundary. At boundaries the dislocations then piled up creating a stress that may have been sufficient to cause grain boundary sliding and, or, initiation of mobile dislocations in adjacent grains; and so the plastic zone propagated.

Resistance to grain boundary sliding during creep was dependent on two main factors:

- i) grain boundary carbide pinning
- ii) stress accommodation by precipitate free zones

As described previously in section 5.1.2, large carbides existed, in most cases, at the grain boundary sites of the three starting microstructures investigated in this study. The exception to this was at the ferrite / pearlite boundaries that did not coincide with those of the prior austenitic structure. The effect of these 'pinning' carbides was to resist the sliding motion exerted by the shear stress acting ahead of the notch in the CT specimens. Once the carbides, or the interface between the carbides and the matrix, could no longer support the stress, sliding occurred eventually leading to the onset of cavitation and creep crack initiation. This process has been reported to occur in bursts ^[40] due to the time taken for a stress concentration to build up at the interface between the grain boundary carbide and slip band within the grain.

In a creep study by Cane and Fidler ^[22] on uniaxial test specimens in 2.25%Cr-1%Mo alloy steel it was noted that a significant amount of shear took place at grain boundaries during creep. This deformation mechanism was observed to appear, occasionally, as pure grain boundary sliding but also, more generally, as deformation in precipitate free zones (PFZ's) adjacent to the boundaries. Cavity density was shown to decrease with increasing mean PFZ width suggesting local stress accommodation by these zones.

Evidence of PFZ's were observed in this study in the microstructures of the fully bainitic and ferrite / bainite CT tested specimens, as shown in Plate 4.29, p144 and Plate 4.41, p157, respectively. The width of these zones was found to be narrow, $\sim 1\mu\text{m}$, compared to those affording low cavitation densities in the study by Cane and Fidler. It is believed, therefore, that although the stress at the grain boundaries may have been briefly accommodated by the PFZ's most of the stress induced will have been acting directly on the grain boundary itself, and, in particular on the carbide / matrix interface. The resistance to grain

boundary sliding, then, was effected by the presence of the alloy carbides M_7C_3 , $M_{23}C_6$ and to a lesser extent, M_6C .

The types of carbide present at the boundaries between the various microstructural regions of the specimens were dependent upon the local concentration of elements either side of the boundary and the temperature and duration of the elevated temperature exposure. No literary evidence was found to suggest that the carbide type evolving during the creep process is affected by the mode or size of the stress field acting on the grain boundary.

The carbides present at the grain boundaries of the starting structures were, as described above in section 5.1.2, predominantly $M_{23}C_6$ at ferrite / pearlite, ferrite / bainite and bainite / bainite boundaries and M_7C_3 or $M_{23}C_6$ at ferrite / ferrite boundaries. Both these carbides are believed to be effective at preventing grain boundary sliding provided that they remain semi-coherent with the adjacent grains. At extended times at elevated temperatures, as demonstrated in the tempering trial, these carbides tend to evolve to the equilibrium carbide M_6C , at which time, it has been reported ^[28], that coherency with the matrix is lost.

5.3.3 The Contribution of Grain Boundary Carbides to the Creep Crack Initiation Process

To ascertain the reason why some carbides, on critically oriented boundaries, initiated creep cavities a TEM investigation was instigated. Carbide replicas, extracted from the 100% bainitic specimen tested for 350 hours and the mixed ferrite / bainite specimen tested for 850 hours, were examined to identify any differences in the composition, morphology or distribution of carbides on the grain boundaries in both notch tip and reference regions of the specimens. Particular attention was paid to those carbides on the grain boundaries orientated at $\sim 45^\circ$ to the principal stress axis in the notch tip specimens.

As indicated in the SEM study on these structures, the majority of voids detected were found to have initiated at carbides present at either bainite / bainite or ferrite / bainite grain boundaries. It was also evident from this study that, the carbides associated with cavitation were often elongated in the direction associated with grain boundary sliding. It was with this knowledge that the carbides of interest were located for examination in the TEM.

EDX analyses taken from several positions along representative elongated carbides, as indicated in Plate 4.61, p182 and Plate 4.64, p184, showed that the carbides were composed of a number of $M_{23}C_6$ carbides that had grown along the boundary and evolved, at their extremes, to the equilibrium carbide M_6C . The additional elements required for the evolutionary process were made available from the dissolution of carbides in the adjacent grains, as indicated by the presence of PFZ's described previously.

Grain boundary carbides not oriented at a critical angle with respect to the notch tip, and those analysed in the reference regions, were also found to be evolving to M_6C but with less propensity to grow in the direction of grain boundary. For example, the carbides depicted in Plates 4.59, p181 and Plate 4.65, p185 show growth and evolution by dissolution and absorption of the adjacent carbides but with markedly less directionality. In fact, the carbides growing on these non-critical boundaries were observed to follow the growth mechanism expected, i.e. that of protrusions into the adjacent grains as described by Honeycombe^[23] and Benevenuti et al^[145].

This evidence shows that it is the grain boundary sliding action that encourages growth of the grain boundary carbides along the boundary, probably due to the increased driving force for diffusion imparted by the atomic disorder created there. By implication then it can be stated that, the effect of the triaxial state of stress in the creeping material was to increase the grain boundary sliding element, thereby, encouraging growth of the grain boundary carbides in the direction of the sliding.

No evidence was found to suggest an increase in the frequency of the $M_{23}C_6$ - M_6C transformation due to grain boundary sliding, the numbers of both carbides being similar in the notch tip and reference regions.

Although elongated carbides were found to exist at critically oriented ferrite / ferrite boundaries no evidence of the equilibrium carbide was found. These carbides were determined to be M_7C_3 and, as described for the starting structure, appeared to be more resistant to the evolutionary process if formed between two ferrite grains.

From the evidence presented, the onset of grain boundary cavitation, ahead of a pre-existing defect, appears to be related to both the $M_{23}C_6$ - M_6C evolutionary process and the growth of the carbide along the sliding grain boundary.

From theory it is known that, normally, precipitates grow in the direction of the interface with which there is least coherency. In the absence of grain boundary sliding then, the grain boundary carbides grew into one of the adjacent grains. Under the influence of sliding, however, due to the increased disorder, growth occurred along the boundary. As the majority of the structure was still resisting deformation by grain boundary sliding there was an increased stress concentration at the extremes of the elongated carbides and, when this coincided with the evolution to M_6C , cavitation began. Once initiated, with increasing stress, the cavities associated with the evolving carbides were observed to coalesce and grow by dissociation of the carbide with one of the adjacent grains.

Evidence of large voids in the shape of pre-existing carbides, as shown in Plate 4.40, p156, were considered to be indicative of the poor coherency of the grain boundary carbides that caused cavitation.

5.4 Contribution to Life Assessment Strategy

The accurate prediction of component life-time and remaining lifetime necessitates knowledge gained from both accurate microstructural evaluation and mathematical manipulations based on fracture / continuum damage concepts. With this in mind it was considered that the information gained in this current study will aid lifetime assessment strategies in several ways;

- i) To add to the knowledge base an appreciation of how certain microstructural variables can affect the degree of constraint at the notch tip of a pre-existing defect loaded in creep and to consider whether these variables have been accounted for, to date, in existing life-time prediction models.
- ii) To propose the mechanisms of creep deformation occurring ahead of a pre-existing defect in 2.25%Cr-1%Mo steel so that the microstructural characteristics affecting these can be quantified to aid life-time predictions.
- iii) To consider that the observation of the evolving microstructure in a power plant material may give an early indication for the onset of creep crack initiation and growth from a pre-existing defect .

Each of these contributions will now be considered in turn with a view to assessing the time for creep crack initiation and growth in components containing a pre-existing defect.

5.4.1 The Effect of Notch Tip Constraint and Life-Time Prediction

The assessment of creep deformation in CT specimens containing a simulated “pre-existing defect” has shown that the constraint at the defect tip varies with microstructure as described in section 5.3 above. The constraint imparted has

been shown to have a dramatic effect on the initial response of the material ahead of the defect tip in terms of its resistance to creep crack initiation.

The concept of local creep constraint has previously been addressed by Wang and Wu ^[101] who defined a creep constraint factor ξ where:

$$\xi = \left(1 - \frac{\epsilon_f^*}{\epsilon_f} \right)^{(n-1)/n} \quad \text{-Equation 5.1} \quad [101]$$

And

ϵ_f^* = local rupture strain with creep constraint

ϵ_f = creep ductility in uniaxial tension

n = material constant of the creep law

The authors demonstrated that if the value of ξ can be determined for a particular material, based on the creep constant, 'n', and a particular specimen geometry, then, knowing the creep ductility value for uniaxial creep failure, the value of ϵ_f^* can be determined and used in an equation for crack growth rate, \dot{a} .

Where:

$$\dot{a} = \frac{4C^{*0.85}}{\epsilon_f^*} \quad \text{-Equation 5.2} \quad [130]$$

And

$$C^* = \frac{2n}{n+1} \frac{P\dot{\Delta}}{B(W-a)} \quad \text{-Equation 5.3} \quad [130]$$

Comparing calculated and measured values for ε_f^* and, hence, crack growth rate, Wang and Wu ^[101] showed that the equations postulated gave reasonably accurate predictions.

In the current study it is not the crack propagation rate that is being considered but the time to initiate a crack from a pre-existing defect. The mathematical criteria for estimating the constraint factor during the crack initiation, or incubation phase, therefore, may be different to that proposed by Wang and Wu and a further study is required to quantify this.

Due to the possibility of non-linear displacement between the load point and the crack tip, particularly in creep ductile materials, C^* should be calculated from CTOD data as described in this work and by Holdsworth ^{[11] [132]}. In equation 5.3 the load point opening displacement rate, $\dot{\Delta}$, is replaced by the crack tip opening displacement rate, $\dot{\delta}$, up to the point of crack initiation, $\delta_{i,x}$. If the crack length at crack initiation, defined as x_c , is then put equal to the minimum crack extension, Δa , the incubation period, t_i , becomes:

$$t_{i[x_c]} = \frac{\Delta a \varepsilon_f^*}{4C^{*0.85}} \quad \text{-Equation 5.4}$$

To test the validity of this, and any mathematical models postulated for life-time prediction of components containing defects, it is necessary to carry out both uniaxial and notched specimen creep tests. From the evidence portrayed in this study it has been shown that creep performance is critically dependent upon the microstructure of the tested material and, therefore, to ensure accuracy when comparing test data, all test specimens must be extracted from micro-structurally equivalent material.

5.4.2 The Mechanisms of Creep Deformation Occurring Ahead of a Pre-existing Defect and Life-Time Prediction

In this study the mechanisms of creep deformation, up to the point of crack initiation, have been shown to be similar to those experienced in uniaxial creep specimens.

It has been shown that the variation in creep deformation behaviour of the three microstructural variables examined was due, predominantly, to the difference in:

- a) the solid solution strengthening effects and
- b) the grain boundary carbide stability .

In both cases the success of the resistance to deformation was related to the ability of the molybdenum in the alloy to stay in solid solution. Once the dislocations were freed from the strain field surrounding the solid solution elements they were free to migrate to the grain boundaries. At the boundaries sliding was initially restricted by grain boundary carbide pinning until such a time that the equilibrium carbide, M_6C , evolved. At this time it is believed that the effect of the triaxial state of stress acting on the M_6C grain boundary carbide had a significant effect on the subsequent stage of deformation leading to earlier creep crack initiation times that would have been expected in uniaxial specimens.

For the important evolving microstructural variables to be built into mathematical models for life prediction it is necessary to link them to a suitable mathematical variable. As described by Dyson and McLean ^[113] this can be achieved by using continuum damage mechanics equations involving the use of $\dot{\epsilon}$. Each parameter affecting $\dot{\epsilon}$ can be summed to give the total life expectancy in the mode of Grounes and Liberman ^{[111] [112]}. In the case of 2.25%Cr-1%Mo steel, then, strain rate ahead of a pre-existing defect should be based initially on damage accumulation in the form of multiplication of mobile dislocations and / or particle coarsening and evolution to M_6C at the grain boundaries. Using these parameters, the final total strain could be estimated

for the material creeping in uniaxial tension and then this value could be used, subsequently, in equations for components containing a pre-existing defect, such as that proposed by Wang and Wu ^[101]. Finally, once the effect of notch tip constraint had been determined, the time to initiate a creep crack, $t_{i_{xc}}$ could be estimated.

5.4.3 Carbide Evolution and Life-Time Prediction

A detailed microstructural analysis was carried out in this study to relate the change in carbide morphology in three microstructural variables of 2.2%Cr-1%Mo steel to the creep deformation and creep crack initiation process. It was found that in each case the mechanism of deformation and crack initiation was related to the evolutionary process of the carbides present at each stage. In particular it was related to the depletion of Mo from the solid solution in the bainite phase and, to a lesser extent, the precipitation strengthening of the fine M_2C precipitates in the ferrite.

With respect to the two bainite containing structures the dominant creep weakening mechanism was considered to be signalled by the growth of the inter and intragranular $M_{23}C_6$ carbides and their subsequent evolution to the equilibrium carbide, M_6C . Cavitation was nearly always associated with the decohesion of grain boundary M_6C carbides at their interface with an adjacent grain. Consequently any method which could predict the time to evolve M_6C at a particular temperature could aid in the prediction of creep life / remanent life.

Such methods have already been proposed and described by Bhadeshia et al ^[121] ^[119] based on thermodynamic calculations using programmes such as MTDATA.

5.5 Experimental Considerations and Suggestions for Further Work

From the experimental and literary evidence described in this study a number of important factors affecting the validity of experimental studies in this area have been noted.

It has become apparent that the fine microstructure critically affects the properties of creep resistant alloys. As such any comparisons between results derived from various sources must recognise these differences. For example the proportion of phases in the alloy can have a significant bearing on the distribution of carbon in the microstructure and, hence, the relative maturity of the precipitate structures within those phases.

Reference stress values must be taken from uniaxial specimens having equivalent chemistries and thermal histories to those to be tested under complex loading conditions.

The effect of varying the volume fraction of transformation structures, and hence microstructural constituents, on the microstructural constraint imposed at the tip of a pre-existing defect could be assessed by carrying out a detailed creep testing and microstructural analysis programme.

It is suggested that for further work, CT and uniaxial creep specimens should be manufactured from material consisting of a range of pro-eutectoid ferrite / bainite contents. Reference stress, creep index and creep ductility's could then be determined from uniaxial test data and used / correlated to creep deformation data obtained from creep testing CT specimens containing spark eroded defects in exactly the same microstructural condition. From this study the contribution of the various microstructural constituents could be assessed and quantified, subsequently, to be included in models for predicting creep or remanent lifetime.

In the assessment of void area percent, or cavitation damage, it is essential that all micro-specimens are prepared via the same routine. As described by

Silveira and May ^[135] and Samuels and Le Mann ^[136] variations in polishing or etching time can alter the size of the cavities detected and as such the value of the damage parameter determined.

In ductile materials local deformation at the crack tip of a notched specimen should be determined from the physical measurement of indentation marks made parallel to the crack opening front, i.e. CTOD measurements should be made by the similar triangles method described by Holdsworth ^[132]. If the displacement between the loading pins is utilised for the determination of CTOD non-linear deformation results in values of CTOD which are artificially large.

As discussed by Abdel-Latif ^[39] care must be taken when quoting absolute values for the elemental compositions of carbides analysed by EDX methods in the TEM. Due to the complexity of determining the necessary constants to quote absolute values characterisation of carbides in this study was made only by comparison of the elemental ratios present in the carbides with those derived from a series of experimental trials and by comparison with literary evidence ^{[30] [138]}. Accuracy was ensured by consistency in sample preparation and TEM operating conditions. In most cases the carbides were considered to be sufficiently thin, i.e. less than 5000 \AA , to avoid significant absorption and fluorescence effects.

The aim of this study was to assess the effect of a pre-existing defect on the creep deformation response of three microstructural variables of 2.25%Cr-1%Mo alloy steel. It is believed that the findings of this work will make a significant contribution to the understanding of how the presence, or absence, of key microstructural constituents can affect the deformation response of a component operating under creep conditions and, specifically, a component containing a pre-existing defect.

The conclusions of this study are as follows:

- The local creep constraint at the tip of a pre-existing defect in 2.25%Cr-1%Mo steel has been shown to vary with the microstructural condition of the alloy.

The greatest constraint of the three microstructures examined was that exerted by the fully bainitic structure. This was followed by the mixed proeutectoid ferrite + bainite structure and, finally, the annealed ferrite + pearlite.

- The magnitude of the constraint imposed at the defect tip was related to the ease with which the stress concentration was redistributed into the surrounding structure. This, in turn, was related to the microstructural constituents in the alloy preventing the processes of dislocation glide and climb.

SEM and TEM analysis of the creep damaged structures indicated that the microstructural constituent most effective in restricting dislocation mobility was that of Mo in solid solution in the bainitic ferrite .

- During the early stages of creep crack initiation from a pre-existing defect, the creep ductility of the alloy was inversely related to the constraint exerted by the material in the vicinity of the defect tip.

A high creep ductility, or low constraint, was indicated by a small value of $\Delta a/\Delta CTOD$ or a small value of $\Delta a/\text{void area } \%$.

In the ferrite / pearlite structure, that imparted only a small degree of constraint, cavitation was observed to occur over a large area surrounding the 'defect' tip. Gross plastic deformation was observed and yet crack initiation did not occur.

In the ferrite / bainite structure more constraint was evident, cavitation was confined to smaller area and a crack was observed to initiate after exceeding a CTOD of $\sim 0.16\text{mm}$. For a crack extension of 0.5mm the ratios of $\Delta a/\Delta\text{CTOD}$ and $\Delta a/\text{void area \%}$ were determined to be 1.85 and 0.21 respectively.

In the fully bainitic structure, where constraint was the highest, cavitation occurred in a confined area close to the 'defect' tip and crack initiation occurred after the CTOD exceeded $\sim 0.07\text{mm}$. For a crack extension of 0.5mm the ratios of $\Delta a/\Delta\text{CTOD}$ and $\Delta a/\text{void area \%}$ were determined to be 2.78 and 2.0 respectively.

- Crack extension occurred at a slower rate in the ferrite / bainite structure than in the fully bainitic structure up to a critical CTOD value of $\sim 0.3\text{mm}$, and a crack extension of $\sim 1\text{mm}$. Once these values had been attained crack extension occurred at a similar rate in both structures.
- The presence of an incoherent sulphide inclusion in the vicinity of the defect in the ferrite / pearlite structure resulted in poor stress redistribution and premature creep crack initiation. This occurrence was considered to be due to the inclusion acting as a sink for the dislocations induced at the notch tip.
- Creep cavitation ahead of the pre-existing defects occurred, predominantly, at the interface between grain boundary carbides and their adjacent grains. High resolution SEM and TEM examination, in conjunction with energy dispersive X-ray analysis, showed that the carbides most frequently linked to the cavitation process were large, elongated carbides exhibiting signs of evolution to the equilibrium carbide M_6C .

- A triaxial state of stress, created by the presence of a pre-existing defect in a component subject to creep conditions, imparted a significant grain boundary sliding element to the creep deformation process.

This was indicated by the large number of cavitating grain boundaries that were detected oriented at 45° to the principal stress axis in the fully bainitic and ferrite / bainite creep damaged specimens.

- Grain boundary sliding affected the growth direction of the carbides on critically oriented boundaries. i.e. those at 45° to principal stress axis. This reduced the effectiveness of the carbides pinning the grain boundaries allowing further sliding and, as a consequence, grain boundary cavity initiation and cavity growth.
- Crack initiation occurred when adjacent grain boundary cavities coalesced. High resolution SEM imaging of the cavitating structures indicated that the likely mechanisms for cavity coalescence were:
 - In the ferrite / bainite and fully bainitic structures: vacancy diffusion along paths of least resistance, i.e. along the interface formed between the elongated carbides and the adjacent grains.
 - In the ferrite / pearlite structure: plastic tearing of the matrix material adjacent to the grain boundary carbides
- The volume fraction of transformation products in the alloy affects the distribution and maturity of the alloy carbides at inter and intra-granular sites in the microstructure.

This was inferred by comparing the types of carbides detected in the microstructures of the current study with those reported by other workers. In particular, with reference to the mixed ferrite / bainite microstructure, the greater the volume fraction of pro-eutectoid ferrite the more stable the carbides in the intra-granular regions of bainite and at the ferrite / ferrite grain boundaries. The main significance of this is to the comparison of

creep rupture data derived from a number of sources. It is evident from these studies that, an appreciation of the fine micro-structure of a alloy is crucial to predict the operative mechanisms of creep deformation and, hence, component lifetime.

- It was possible to identify numerous carbides, based on their elemental ratios, quickly and accurately utilising the STEM / EDX image analysis routine developed in this study.

This routine may also be suitable to determine the carbides existing in power plant components at stages of component life by the examination of extraction replicas.

- Image analysis in the SEM was used, successfully, to determine the area % of voids occurring ahead of a pre-existing defect in creep damaged material. The method developed necessitated the analysis of bulk material extracted from the creep damaged specimens. It may, however, be possible to adapt the procedure to assess surface replica specimens extracted from power plant to aid lifetime prediction.

- The lifetime of a large cast component operating in a creep environment can be significantly reduced by the presence of a pre-existing defect in the microstructure. Lifetime, or remanent lifetime, prediction methods should, therefore, include parameters to account for this effect.

Models should include not only a parameter to account for the triaxial state of stress at the defect tip but also a parameter to account for the constraint imposed by the evolving component microstructure.

1. Nelkon, M. and Parker, P., (1989). *Advanced Level Physics*. 6th ed, Heinemann, Oxford.
2. Ingo, P., (2000). *Supercritical Coal Fired Power Plants* [Online]. Available: www.worldbank.org/html/fpd/em/supercritical/supercritical.htm [2000, March 26].
3. Scarlin, R.B., (1997). Improved Materials For High Efficiency Steam Turbines, Proc. 4th International Charles Parsons Turbine Conference, (Newcastle upon Tyne, UK), Nov 4-6. 242-256.
4. Coble, R.L., (1963). A Model For Diffusion Controlled Creep In Polycrystalline Materials, *Acta Metall.*, 1963. *J. Appl. Phys.*, 34, 1679-1684.
5. Frost, H.J. and Ashby, M.F., (1982), *Deformation Mechanism Maps, The Plasticity and Creep Of Metals and Ceramics*, Pergamon Press, Oxford, New York.
6. Pickering, F.B., (1990). Some Aspects Of Creep Deformation and Fracture In Steels, Proc., Rupture Ductility Of Creep Resistant Steels, (York, UK), Dec 4-5. 17-48.
7. Haigh, J.R., 1975. The Mechanisms Of Macroscopic High Temperature Crack Growth, Part II, *Mat. Sci. Eng.*, 20, 225-235.
8. Goodall, I.W. and Chubb E.J., (1976). The Creep Ductile Response Of Cracked Structures, *Int. J. Fracture*, 12, 289-303.
9. Ainsworth, R.A., (1982). The Initiation Of Creep Crack Growth, *Int. J. Solids Structures*, 18, 873-881.
10. Webster, G.A., Nikbin, K.M., Chorlton, M.R., Celard N.J.C. and Ober, M. (1998). A Comparison Of A High Temperature Defect Assessment Methods, *Materials At High Temperatures*, 15, (3/4), 337-346.
11. Holdsworth, S.R., (1992). Initiation And Early Growth Of Creep Cracks From Pre-existing Defects, *Materials At High Temps.*, 10, 127-137

- 12 Vilhelmsen, T. and Webster, G.A., (1994). Prediction Of The Early Stages Of Creep Crack Growth In High Temperature Plants, *ASME. PVP.*, 288, 291-295.
- 13 Turner, C.E. and Webster, G.A., (1974). Applied Fracture Mechanics To Creep Crack Growth, *Int. J. Fract.*, 10, 455-458.
- 14 Ellison, E.G. and Harper, M.P., (1978). Creep Behaviour Of Components Containing Cracks - A Critical Review, *J. Strain Analysis*, 13, 35-51.
- 15 Gope, N., Chatterjee, A., Mukherjee, T. and Sarma, D.S., (1993). Influence Of Long Term Ageing And Superimposed Creep Stress On The Microstructure Of 2.25%Cr-1%Mo Steel, *Met. Trans. A*, 24A, 315-326.
- 16 Kleuh, R.L., (1978). Interaction Solid Solution Hardening In 2.25%Cr-1%Mo Steel, *Mat. Sci. and Eng.*, 35, 239-253.
- 17 Baker, R.G. and Nutting, J., (1959). The Tempering Of 2.25%Cr-1%Mo Steel After Quenching And Tempering, *J.I.S.I.*, July, 257-267.
- 18 Ainsworth, R.A and Budden, P.J., (1998). R5 and British Standards Defect Assessment Procedures, *Materials At High Temperatures*, 15, (3/4),291-297.
- 19 Holdsworth, S.R. and Cunnane, D.J. (1993). Lifetime Prediction Of Components Containing Defects, Cost Report RM93/006, March.
- 20 Orr, J., Beckitt, F.R. and Fawkes, G.M., (1978). The Physical Metallurgy Of Chromium-Molybdenum Steels For Fast Reactor Boilers, Proc. Ferritic Steels For Fast Reactor Boilers. BNES, (London, UK), 92-109.
- 21 Irvine, K.J., Murray, J.D. and Pickering, F.B., (1961). *ISI*, Special Report 70, 246.
- 22 Cane, B.J. and Fidler, R.S., (1977). The Effect Of Microstructure And Grain Size On The Creep And Rupture Properties Of 2.25Cr-Mo and 9Cr-Mo Steels, Proc. Ferritic Steels for Fast Reactor Steam Generators. BNES, (London, UK), 193-199.
- 23 Honeycombe, R.W.K., (1981). *Steels - Microstructure and Properties*, Edward Arnold, London.

- 24 Thomson, R., (1992). *Carbide Composition Changes In Power Plant Steels As A Method Of Remanent Creep Life Prediction*, PhD Thesis, Cambridge University, UK.
- 25 Aaronsson, H.I., (1961). *Steel Strengthening Mechanisms*, Climax Molybdenum Company.
- 26 Bhadeshia, H.K.D.H., (1992). *Bainite In Steels*, Institute Of Materials, London, UK.
- 27 Nutting, J., (1998). The Structural Stability Of Low Alloy Steels For Power Generation Applications, Proc. Advanced Heat Resistance Steel For Power Generation, (San Sebastian, Spain), April, 12-30.
- 28 Woodhead, J.H and Quarrell, A.G., (1965). Role Of Carbides In Low-Alloy Creep Resisting Steels, *J.I.S.I.*, June, 605-620.
- 29 Murphy, M.C. and Branch, G.D., (1971). Metallurgical Changes In 2.25%Cr-1%Mo Steels During Creep-Rupture Test, *J.I.S.I.*, July, 546-561.
- 30 Pilling, J. and Ridley, N., (1982). Tempering Of 2.25%Cr-1%Mo Low Carbon Steels, *Met. Trans. A.*, 13A, 557-563.
- 31 Yu, J. (1989). Carbide Stability In 2.25%Cr-1%Mo Steels, *Met. Trans. A*, 20A, 1561-1564.
- 32 Beech, J. and Warrington, D.H., (1966). M_7C_3 to $M_{23}C_6$ Transformation In Chromium Containing Alloys, *J.I.S.I.*, May, 460-468.
- 33 Race J.M. and Bhadeshia H.K.D.H. (1992), Precipitation Sequences During Carburisation Of Cr-Mo Steel, *Mat. Sci. and Tech.*, 8, 875-882.
- 34 Thomson, R.C. and Bhadesia, H.K.D.H., (1994), Changes In Chemical Composition Of Carbides In 2.25Cr-1Mo Power Plant Steel - Part 1 Bainitic Microstructure, *Mat. Sci and Tec.*, 10, 193-203.
- 35 Thomson, R.C. and Bhadesia, H.K.D.H., (1994). Changes In Chemical Composition Of Carbides In 2.25Cr-1Mo Power Plant Steel - Part 2 Mixed Microstructure, *Mat. Sci and Tec.*, 10, 205-208.

- 36 Hodson, S.M., (1989). Metallurgical And Thermochemical Databank, National Physics Laboratory, UK.
- 37 Robson, J.D. and Bhadeshia, H.K.D.H., (1997). Kinetics of Precipitation Reactions In Ferritic Power Plant Steels, Proc. Microstructural Stability Of Creep resistant Alloys For High Temperature Plant Applications, (Sheffield, UK.) March 24-26, 395-429.
- 38 Varin, R.A and Haftek, J., (1984). Structural Changes In A Ferritic Heat- resistant Steel After Long Term Service, *Mat. Sci. and Eng.*, 62, 129-136.
- 39 Abdel-Latif, A.M., Corbett, J.M. and Taplin, D.M.R., (1982). Analysis Of Carbides Formed During Accelerated Ageing Of 2.25%Cr-1%Mo Steel, *Met. Sci.*, 16, 90-96.
- 40 Reidel, H., (1987), *Fracture At High Temperature*, Springer and Verlag, Heidelberg, Germany.
- 41 Monkman, F.C. and Grant, N.J., (1969). An Empirical Relationship Between Rupture Life And Minimum Creep Rate In Creep-Rupture Tests, *Proc. ASTM*, 56, 593 – 605.
- 42 Mukherjee, A.K., Bird, J.E. and Dorn, J.E. (1969). Experimental Correlation's For High Temperature Creep, *Trans. ASM*, 62, 155 – 179.
- 43 Sherby, O.D., Orr, R.L. and Dorn, J.E., (1954). Creep Correlations Of Metals At Elevated Temperatures, *Trans. AIME*, 200, 71-
- 44 Larson, F.R. and Miller, J. (1952). A Time-Temperature Relationship For Creep Rupture And Creep Stresses, *Trans. ASME*, 74, 765 – 775.
- 45 Dieter, G.E., (1976). *Mechanical Metallurgy*, 2nd ed., McGraw-Hill, Tokyo, Japan, 484 - 486.
- 46 Ashby, M.F. and Jones, D.R.H., (1996), *Engineering Materials Vol. 1, An Introduction To Their Properties & Applications*, 2nd ed., Butterworth & Heinemann, Oxford, UK, 188 -189.
- 47 Mullenore, A.W., and Grant, N.J., (1954), Creep Rupture Characteristics Of Al-Mg Solid Solution Alloys, *Trans. AIME*, 200, 973 - 979.

- 48 Brunner, H. and Grant, N.J., (1959). Deformation Resulting From Grain Boundary Sliding, *Trans. AIME*, 215, 48 - 56.
- 49 Garofalo, F. (1965), *Fundamentals Of Creep Rupture in Metals*, McMillan, 136.
- 50 Evans, R.W and Wilshire, B., (1985). *Creep of Metals and Alloys*, The Institute Of Metals, London.
- 51 Crossman, F.W. and Ashby, M.F., (1975). Non-Uniform Flow of Polycrystals by Grain-Boundary Sliding Accommodated by Power-Law Creep, *Acta. Met.* 23, (4), 425-440.
- 52 Langton, T.G. and Vastava, R.B. (1982). in *Mechanical Testing for Deformation Modelling Development*, Eds. Rhode, R.W. and Swearingen, J.C., ASTM. STP765, 435.
- 53 Gifkins, R.C., (1973). Grain-Size Dependence of Creep Rate in Recovery Creep, *J. Australian Inst. Metals*, 18, (3), 137-145.
- 54 Nabarro, F.R.N. (1948), Report On Conference On Strength of Solids, 1948, Physical Soc., London, 75
- 55 Ashby, M.F., (1972). First Report on Deformation-Mechanism Maps. *Acta. Met.* 20, (7), 887-897.
- 56 Townend, R.D., Timmins, R. and Brear, J.M., (1997). Condition Assessment Of Long Serviced High Temperature Components. Proc. Microstructural Stability Of Creep resistant Alloys For High Temperature Plant Applications, (Sheffield, UK), March 24-26, 145-172.
- 57 Mclean, D. (1962). Deformation At High Temperatures, *Metallurgical Reviews*, 7, 481 - 525.
- 58 Williams, K.R and Wiltshire, B., (1973). Stress and Temperature-Dependence of Creep of Nimonic 80A, *Met. Sci.*, 7, 176-179.
- 59 Henderson, P.J. and McLean. M., (1983), Microstructural Contributions To Friction Stress And Recovery Kinetics During Creep Of The Nickel-Base Superalloy IN738LC, *Acta Met.*, 31 (8), 1203-1220.

- 60 Dyson, B.F. and McLean, M., (1983). Particle-Coarsening, σ_0 and Tertiary Creep. *Acta Met.*, 31, (1), 17 – 27.
- 61 Yagi, K. and Abe, F., (1996). Long Term Creep and Rupture Of Heat Resisting Steels and Alloys, Proc. 6th International Conference On Creep and Fatigue, April 15-17, 41-50.
- 62 Abe, F. and Yagi, K., (1997). Evaluation of Long Term Creep and Rupture Properties of Heat Resisting Steels, Proc. 4th International Charles Parsons Turbine Conference, (Newcastle upon Tyne, UK), 750-765.
- 63 Kimura, K., Kushima, H, Yagi, K. and Tanaka, C., (1993). Proc. Aspects Of High temperature Deformation and Fracture In Crystalline Materials, The Japan Inst. Metals, 309 –312.
- 64 Jones, W. B. and Van Den Avyle, J.A., (1980). Substructure and Strengthening Mechanisms In 2.25%Cr-1%Mo Steel at Elevated Temperatures, *Met. Trans. A*, 11A, 275-1285.
- 65 Kleuh, R.L., (1985), Creep-Rupture Strength Of Annealed 2.25%Cr-1%Mo Steel, *Metallurgia*, 19, 789-793.
- 66 Yamauchi, M., Chuman, Y., Nishimura, N. and Masuyama, F., (1996). A Study On Larson-Miller Parameter Constant For 2.25Cr-1Mo steel Creep Rupture Data, Proc. 6th International Conference On Creep and Fatigue, April 15-17, 511-519.
- 67 Maruyama, K., Sawada, K., Koike, J., Sato, H. and Yagi, K., (1997). Examination of Deformation Mechanism Maps in 2.25Cr-1Mo Steel By Creep Tests at Strain rates of 10^{-11} to 10^{-6} s⁻¹, *Mat. Sci and Eng.*, A224, 166-172.
- 68 Ashby, M.F. and Dyson, B.F., (1984). Creep Damage Mechanics And Micromechanisms, Proc. Int. Conf. On Fracture, (New Delhi, India), Dec. 4-10, 3-30.
- 69 Ashby, M.F. (1977). *Fracture*, Ed., D.M.R. Taplin, University of Waterloo Press, Waterloo, Canada, 1-14.

- 70 Wray, P.J., (1969). Strain -Rate Dependence Of The Tensile Failure Of Polycrystalline Material At Elevated Temperatures, *J. Appl.Phys.*, 40, (10), 4018 – 4029.
- 71 Fields, R.J., Weerasooriya T., and Ashby, M.F., (1980). Fracture Mechanisms in Pure Iron, Two Austenitic Steels and One Ferritic Steel, *Metall. Trans.*, 11A, (2), 333-347.
- 72 Goods, S.H. and Brown, L.M., (1979). The Nucleation of Cavities by Plastic Deformation, *Acta Metall.*, 27, (1), 1-15.
- 73 Knott, J.F., (1973). *Fundamentals of Fracture Mechanics*, Butterworths, London.
- 74 Lagnebourg, R, (1981). In *Creep Fatigue In High Temperature Alloys*, Ed. J. Bressers, Applied Science Publishers, (London, UK), 41.
- 75 Cane, B.J., (1976). Creep-Fracture Initiation in 2.25%Cr-1% Mo Steel, *Met. Sci.*, 10, (1), 29-34.
- 76 Lonsdale, D. and Flewitt, P.E.J., (1979). Damage Accumulation and Microstructural Changes Occurring During the Creep of a 2.25Cr-1Mo Steel, *Mat. Sci Eng.*, 39, (2), 217-229.
- 77 Perry, A.J., (1974). Review, Cavitation in Creep, *Mat. Sci.*, 9, 1016 -1039.
- 78 Bendick, W., (1991). Analysis Of Material Exhaustion And Damage By Creep, *Int. J. Pres. Ves. & Piping*, 47, (1), 57-78.
- 79 Beere, W.B., (1980). Inhibition of Intergranular Cavity Growth in Precipitate-Hardened Materials, *J. Mat. Sci*, 15, (3), 657-669.
- 80 Beere, W.B and Speight, M.V., (1978). Creep Cavitation by Vacancy Diffusion in Plastically Deforming Solid, *Met. Sci.* 12, (4), 172-176.
- 81 Tipler, H.R., Taylor, L.H. and Hopkins, B.E. , 1970. Some Direct Observations On The Metallography Of Creep-Cavitated Grain Boundaries, *Met. Sci.* 4, 167 – 170.
- 82 Taplin D.M.R. (1965). A Note On The Relationship Between Cavitation And Ductility, *J. Australian Inst. Met*, 10,(4), 336-339.

- 83 Hull, D. and Rimmer, D.E., (1959), the Growth Of Grain Boundary Voids Under Stress, *Phil. Mag.*, 4, 673-687.
- 84 Dyson, B.F., (1976). Constraints on Diffusional Cavity Growth Rates (During Creep), *Met. Sci.*, 10, 349-353.
- 85 Dyson, B.F. (1979). Constrained Cavity Growth, Its Use in Quantifying Recent Creep Fracture Results, *Canad. Metall. Qu.*, 18, (1). 31-38.
- 86 Hancock, J.W., (1976). Creep Cavitation Without A Vacancy Flux, *Met. Sci.*, 10, (9), 319-325
- 87 Needleman, A. and Rice, J.R., (1980). Plastic Creep Flow Effects In The Diffusive Cavitation Of Grain Boundaries, *Acta Met.*, 28, 1315 – 1332.
- 88 Cane, B.J and Williams, J.A., (1987). Remaining Life Prediction of High Temperature Materials, *Int. Mat.Rev.*, 32, (5), 241-262.
- 89 Cane, B.J. (1976). The Effect Of Transformation Structure On The Creep And Rupture Behaviour Of 2.25%Cr - 1%Mo Steel, CEGB Report no. RD/L/N 236/75, March.
- 90 Siverns, M.J. and Price, A.T., (1973). Crack Propagation Under Creep Conditions In A Quenched 2.25Cr-Mo Steel, *Int. J. Fract.*, 9, (2), 199-207.
- 92 Rice, J.R., (1968). *Fracture An. Advanced Treatise*, Ed. H. Liebowitz, Academic Press, New York, 2, 191-311.
- 93 Landes, J.D and Begley, J.A., (1976), *Mechanics Of Crack Growth*, ASTM STP, 590, American Society For Testing and Materials, 47-62.
- 94 Nikbin, K.M., Smith, D.J. and Webster, G.A., (1986). An Engineering Approach To The Prediction Of Creep Crack Growth, *Trans. ASME*, 108, April, 186-191.
- 95 Gooch, D.J. and King, B.L., (1977). Relationship Between Engineering and Metallurgical Factors in Creep Crack Growth, *Met. Sci.*, Nov., 545-550.
- 96 Ellison, E.G and Neate, G.J., (1976), Life Prediction Methods For Cracked Components Operating In A Creep range, *Proc. Failure Of Components Operating In The Creep Range*, I. Mech E., 39 – 46.

- 97 Siverns, M. and Price, A.T., (1970). Crack Growth Under Creep Conditions, *Nature*, 228, 760-761.
- 98 Marriot, D.J., (1970). IUTAM, Symp. On Creep, Berlin, Springer and Verlag, Berlin.
- 99 Haigh, J.R., (1974). CERL Report RD/LN118/74, Leatherhead, Surrey.
- 100 Ewing, D.J.F and Richards, C.E. (1974). Yield-Point Loads of Singly-Notched Pin-Loaded Tensile Strips, *J. Mech, Phys. Solids*, 22, (1), 27-36.
- 101 Wang, Z. and Wu, D., (1991). A Damage Mechanics Approach To The Prediction Of Creep Crack Growth, *Int. J. Of Pres. Ves. & Piping*, 48, (3), 305 - 319.
- 102 Nguyen, B.N., Onck, P.R. and Van Der Giessen, E., (1998), Study Of Higher-Order Crack Tip Fields In Intergranular Creep Fracture, Proc. Modelling Of Microstructural Evolution In Creep Resistant Materials, (London, UK.) , Sept. 29 - 30, 341-355.
- 103 Dobrzanski, J. and Hernas, A., (1996). Relationship Between Microstructure and Residual Life Of Low Alloy Cr-Mo Steels, Proc. 6th International Conference On Creep And Fatigue, April 15-17, 451-461.
- 104 Freres, P. and El-Magd, E., (1996), Investigation Of The Influence of a Multiaxial State Of Stress On The Behaviour Of Intercrystalline Creep Microcracks, *Computational Materials Science*, 5, 101-110.
- 105 Sham, T.L. and Needleman, A., (1983). Effects Of Triaxial Stressing On Creep Cavitation Of Grain Boundaries, *Acta Metall.* 31, (6), 919-926.
- 106 Van Der Giessen, E. , Van Der Burg, M.W.D., Needleman, A. and Tvergaard, V., (1995). Void Growth Due To Creep and Grain Boundary Diffusion At High Triaxialities, *J.Mech. Phys. Solids*, 43, (1) ,123-165.
- 107 Maille, K., (1996). Influence Of Multiaxiality On Damage And Failure Behaviour Of Components Operating In The Creep Range, *Trans. Indian Inst. Met.*, 49, (4), 371-375.

- 108 Molinie, E. Martel, P. Duquenez, C. Dupas, P. and Prunier, V., (1998). Creep Behaviour Of Seam Welded Reheat Steam Pipes In Thermal Fossil Power Plant: Feedback Analysis and Life Assessment Methodology, *Materials At High Temperatures*, 15, (3/4), 375-384.
- 109 Robinson, E.L., (1952). Effect Of Temperature Variation On The Long-Term Rupture Strength Of Steels, *Trans. ASME*, 74, 777-781.
- 110 Hart, R.V., (1977). Concept of Area-Modified Stress for Life-Fraction Summations During Creep, *Met. Technology*, 4, (9), 447-448.
- 111 Grounes, M. (1969), A Reaction-Rate Treatment Of The Extrapolation Methods In Creep Testing, *J. Basic Eng.*, 91, (1) 59-62.
- 112 Liberman, L., (1962). *Metallov. Term. Obrab. Met.*, 1962, 4, .6
- 113 Dyson, B.F and Mclean, M., (1997). Microstructural Evolution and Its Effects On The Creep Performance Of High Temperature Alloys, Proc. Microstructural Stability Of Creep Resistant Alloys For High Temperature Plant Applications, (Sheffield, UK.), March 24-26, 371-393.
- 114 Egger, G., (1990). Creep Damage Quantification And Damage Localization, Proc., Rupture Ductility Of Creep Resistant Steels, (York, UK.), Dec. 4-5, 55 – 64.
- 115 Neubauer, B and Wedel, U., (1983). Rest Life Estimation Of Creeping Components By Means Of Replicas, Proc. ASME Int. Conf. On Advances In Life Prediction Methods, ASME, New York, 307 – 313.
- 116 Sandstrom, R., (1998). Modelling Of Creep Damage Development In Ferritic Steel, Proc. Technical Research Centre Of Finland, Baltica IV: Plant Maintenance For Managing Life And Performance, Finland, Sept. 7-9, 587-97.
- 117 Hale, K.F., (1975). Creep Failure Prediction From Observation Of Microstructure In 2.25%Cr - Mo Steel, *Physical Metallurgy Of Reactor Fuel Elements*, Metals Society, London, 193 – 201.
- 118 Benvenuti, A. Bontempi, P. Corti, S. and Ricci, N., (1996). Assessment Of Material Thermal History In Elevated Temperature Components, *Mat. Characterization*, 36, 271-278.

- 119 Strang, A., Voderek, V. and Bhadeshia, H.K.D.H., (1998). Modelling Of Microstructural Degradation In Creep Resistant 12%Cr Power Plant Steels, Proc. Modelling Of Microstructural Evolution In Creep Resistant Materials, (London, UK.), Sept. 29 - 30, 129-150.
- 120 Sugita, Y., Kato, Y., Yokoyama, T., Sada, T., Sasuyama, F. and Nishimura, N., (1990). Evaluation Of Creep Damage Progress By Metallurgical Examination In Aged Power Boiler Pressure Parts, *I.S.I.J.*, 30, (10), 895-904.
- 121 Bhadeshia, H.K.D.H., (1998). Estimation Of The Microstructure And Properties Of Ferritic Creep-Resistant Steels, Proc. Modelling Of Microstructural Evolution In Creep Resistant Materials, London, UK., Sept. 29-30, 15-38.
- 122 Bhadeshia, H.K.D.H., (1997). Power Plant Steels: Remanent Life Assessment And The Approach To Equilibrium, Proc. 4th Int. Charles Parsons Turbine Conference, (Newcastle upon Tyne, UK.), Nov. 4-6, 718-741.
- 123 Vilhelmsen, T. and Webster, G.A., (1994). Prediction Of The Early Stages Of Creep Crack Growth In High Temperature Plants, *ASME. PVP.*, 288, 291-295.
- 124 Molinie, E., Piques, R. and Pineau, A., (1991). Behaviour Of 1Cr-1Mo-0.25V Steel After Long Term Exposure – II. *Fatigue Fract. Engng. Mater. Struct.* 14, (5), 547-563.
- 125 Austin, T.S.P and Webster, G.A., (1992). Prediction Of Creep Crack Growth Incubation Periods, *Fatigue Fract. Engng. Mater. Struct.* 15, (11), 1081 –1090
- 126 Ainsworth, R.A., (1993), The Use Of A Failure Assessment Diagram For Initiation And Propagation Of Defects At High Temperatures, *Fatigue. Fract. Engng. Mater. Struct.*, 16, (10), 1091 – 1108.
- 127 Cocks, A.C.F. and Ashby, M.F., (1982), The Growth Of A Dominant Crack In A Creeping Material, *Scripta Metallurgia*, 16, (1), 109 –114.
- 128 Nikbin, K.M. and Webster, G.A., (1984), *In Micro and Macro Mechanics of Crack Growth*, Ed. K. Sadananda, B. B. Rath and D.J. Michel.
- 129 Nikbin, K.M., Smith, D.J and Webster, G.A., (1984). Prediction Of Creep Crack Growth From Uniaxial Creep Data, Proc. R. Soc. (London, UK.) . A396, 183-197.

- 130 Kubo, S., (1975), PhD Thesis, University of Osaka, Osaka, Japan.
- 131 ASTM E1457-92, (1997). Standard Test Method For Measurement Of Creep Crack Growth Rate In Metals, ASTM 03.01.
- 132 Holdsworth, S.R., (1998). Creep Crack Growth In Alloy Steel Weldments, *Materials At High Temperatures*, 15, (3/4), 203-209.
- 133 NORDTEST N NDT 010, (1991). Remanent Life Assessment Of High Temperature Components In Power Plant By Means Of Replica Inspection.
- 134 Corti, S., Benvenuti, A. and Ricci, N., (1995). In-Field Applications Of The Extraction Replica Technique To Assess Material Thermal History In Components Operated At Elevated Temperature, Proc. International Metallography Conference, (Colmar, France), May 10-12, 29 - 34.
- 135 Silveira, T.L. da and May, I. Le, (1992). Effects Of Metallographic Preparation Procedures On Creep Damage Assessment, *Materials Characterization*, 28, 75-85.
- 136 Samuels, L.E. , Coade, and Mann, S.D., (1997). Pre-cracking Structures In A Creep Ruptured Low Carbon Cr-Mo Steel, *Materials Characterization*, 39, 631-651.
- 137 Titchmarsh, J.M., (1978). Proc. 9th Int. Congress On Electron Microscopy, Ed. J.M Sturgess, The Microscopical Soc. Of Canada, 618-619.
- 138 Titchmarsh, J.M., (1979). The Identification Of Second Phase Particles In Steels Using An Analytical Transmission Electron Microscope, AERE Report 9661, Dec.
- 139 Li, C., (1996). Effect Of Heat Treatment On The Microstructure Of A 2Cr-Mo-Ni-W-V Rotor Steel, PhD Thesis, Sheffield Hallam University, Sheffield.
- 140 Atkins, M., (1980). Atlas Of Continuous Cooling Transformation Diagrams or Engineering Steels, ASM: British Steel Corporation.
- 141 *High Temperature Design Data for Ferritic Pressure Vessel Steels*, (1983). The Creep of Steels Working Party of the Institution of Mechanical Engineers, Mechanical Engineering.

- 142 Pickering, F.B., (1976). *The Basis Of Quantitative Metallography*, Monograph No.1, Publ. Metals and Metallurgy Trust For The Institute Of Metallurgical Technicians, London
- 143 Gemmill, M.G. and Murray, J.D., (1956). The Properties Of 2.25% Cr-1%Mo Steel, *Iron and Steel*, , April, 150-152.
- 144 Wada, T. and. Biss, V.A, (1983). Restoration Of Elevated Temperature Tensile Strength In 2.25Cr-1Mo Steel, *Met. Trans. A*, 14A, 845-855.
- 145 Benvenuti, A, Angelo, D . Feleli, G. and Ricci, N., (1993). Microstructural Changes In Long Term Aged Steels, Proc., Microstructures and Mechanical Properties Of Ageing Material, The Minerals, Metals And Materials Society, 143 – 148.

Appendix 1 – Creep Data For The Derivation Of σ_{ref}

Time	Strain %	Time	Strain %
0	0	1050	9.9373
18	0.3343	1074	10.4839
42	0.6496	1098	11.0095
66	0.9033	1122	11.341
90	1.0811	1146	11.6479
114	1.2428	1170	11.9092
138	1.3905	1194	12.4496
162	1.5319	1218	13.1079
186	1.6656	1242	13.5045
210	1.796	1266	13.8575
234	1.9187	1290	14.3852
258	2.2234	1314	15.227
282	2.5038	1338	15.7139
306	2.7631	1362	16.1491
330	2.9691	1386	17.179
354	3.1291	1410	17.4793
378	3.2798	1434	18.9457
402	3.4326	1458	19.6635
426	3.5637	1482	20.9761
450	3.6937	1507	21.9371
474	3.8193	1530	23.6802
498	4.0671	1554	25.8442
522	4.42	1578	30.0659
546	4.7213	1580	30.4803
570	4.9568	1589	Rupture
594	5.1392		
618	5.3084		
642	5.4701		
666	5.6243		
690	5.7739		
714	5.9172		
738	6.3862		
762	6.7582		
786	7.0267		
810	7.2371		
834	7.436		
858	7.6251		
882	7.8068		
906	8.0832		
930	8.5974		
954	8.9899		
978	9.2557		
1002	9.5001		
1026	9.7252		

Table A1.1: Creep data for as received 2.25%Cr-1%Mo steel tested at 550°C and 110MPa by courtesy of Alstom Energy, UK. Ltd.

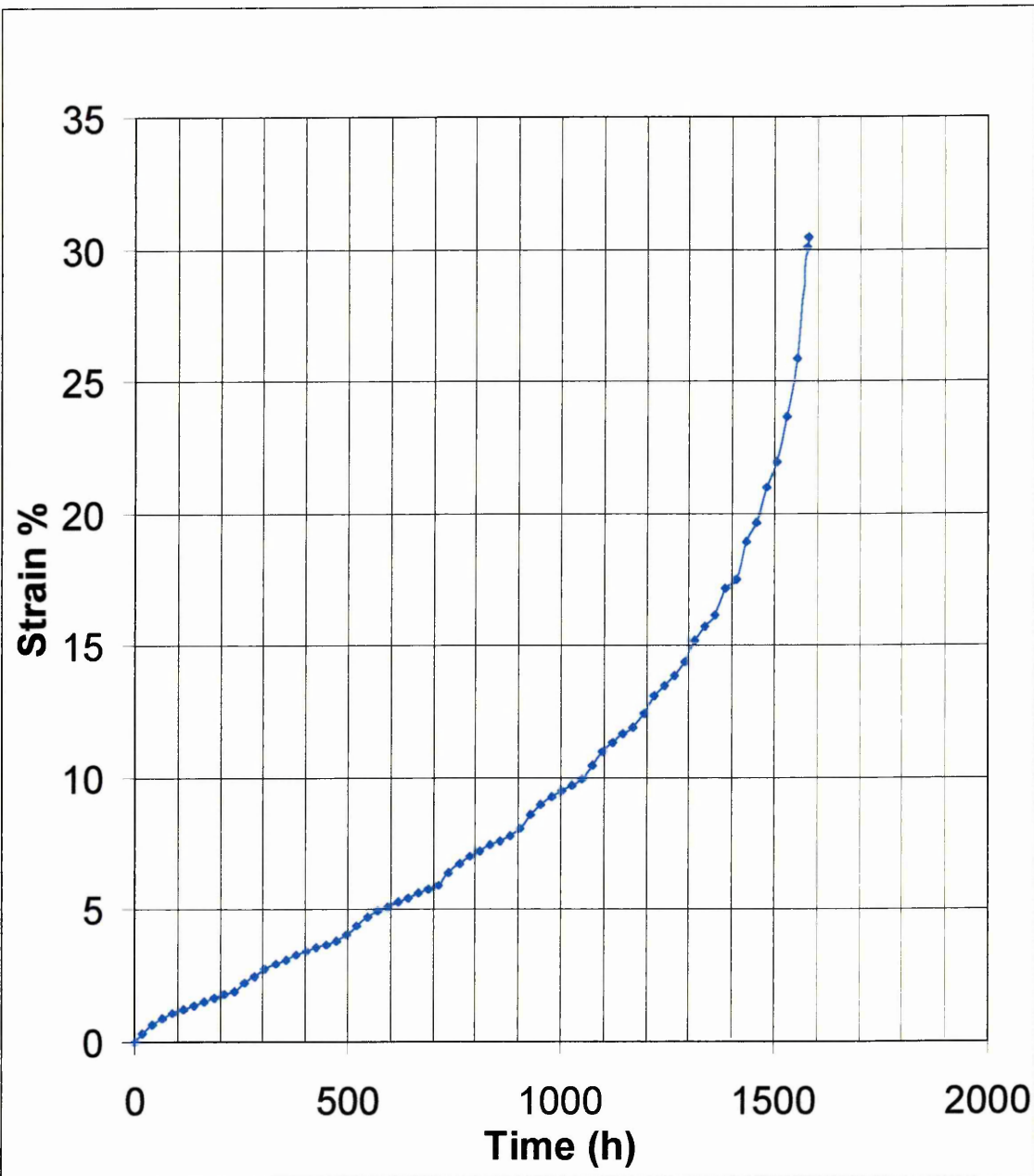


Figure A1.1: Creep curve plotted from data detailed in Table A1 - 2.25%Cr-1%Mo steel tested at 550°C and 110MPa, by courtesy of Alstom Energy, UK. Ltd.

APPENDIX 2 - EDX Spot Analysis For The Determination Of Carbide Classification Schemes

Fe%	Cr%	Mo%	Fe/Cr	Mo/Cr	Mo/Fe
73.98	18.48	7.55	4.00	0.41	0.10
76.81	16.57	6.62	4.64	0.40	0.09
79.17	14.79	6.04	5.35	0.41	0.08
76.04	17.22	6.74	4.42	0.39	0.09
75.81	17.29	6.90	4.38	0.40	0.09
75.73	17.43	6.84	4.35	0.39	0.09
75.85	16.85	7.30	4.50	0.43	0.10
75.73	17.43	6.84	4.35	0.39	0.09
75.85	16.85	7.30	4.50	0.43	0.10
76.70	16.39	6.91	4.68	0.42	0.09
76.23	16.85	6.93	4.52	0.41	0.09
74.14	18.02	7.85	4.12	0.44	0.11
64.22	24.81	10.97	2.59	0.44	0.17
64.18	29.76	6.06	2.16	0.20	0.09
66.46	24.31	9.24	2.73	0.38	0.14
69.68	22.02	8.30	3.16	0.38	0.12
66.00	24.02	9.98	2.75	0.42	0.15
69.99	21.25	8.76	3.29	0.41	0.13
59.78	26.08	14.14	2.29	0.54	0.24
65.63	19.87	14.50	3.30	0.73	0.22
71.34	20.29	8.37	3.52	0.41	0.12
71.46	20.60	7.94	3.47	0.39	0.11
72.23	19.75	8.02	3.66	0.41	0.11

Table A2.1: Fe₃C Type Carbides (Determined from an intra-granular region of the fully bainitic specimen tempered @ 650°C for 1h)

Fe%	Cr%	Mo%	Fe/Cr	Mo/Cr	Mo/Fe
0.57	25.51	73.91	0.02	2.90	129.67
5.19	27.24	67.57	0.19	2.48	13.02
4.12	25.43	70.45	0.16	2.77	17.10
3.86	37.93	58.21	0.10	1.53	15.08
8.03	27.58	64.39	0.29	2.33	8.02
3.91	31.56	64.54	0.12	2.04	16.51
5	26.27	68.73	0.19	2.62	13.75
9.45	16.62	73.93	0.57	4.45	7.82
2.43	26.89	70.68	0.09	2.63	29.09
6.33	30.87	62.8	0.21	2.03	9.92
5.34	27.24	67.42	0.20	2.48	12.63
4.92	23.81	71.27	0.21	2.99	14.49
3.94	30.74	65.32	0.13	2.12	16.58
7.39	23.35	69.35	0.32	2.97	9.38

Table A2.2 : M₂C Type Carbides (Determined from the α region of the as-received mixed ferrite / bainite structure).

Fe%	Cr%	Mo%	Fe/Cr	Mo/Cr	Mo/Fe
34.15	60.31	5.54	0.57	0.09	0.16
31.04	60.66	8.3	0.51	0.14	0.27
43.11	51.91	4.98	0.83	0.10	0.12
35.75	57.69	6.56	0.62	0.11	0.18
37.97	55.83	6.2	0.68	0.11	0.16
35.97	60.95	3.08	0.59	0.05	0.09
33.57	57.93	8.49	0.58	0.15	0.25
34.15	55.1	10.75	0.62	0.20	0.31

Table A2.3: M_7C_3 Type Carbides (Determined from the bainite region of the as-received mixed ferrite / bainite structure)

Fe%	Cr%	Mo%	Fe/Cr	Mo/Cr	Mo/Fe
49.6	42.1	8.3	1.18	0.20	0.17
55.77	37.57	6.65	1.48	0.18	0.12
53.66	35.99	10.36	1.49	0.29	0.19
49.59	41.24	9.17	1.20	0.22	0.18
54.48	38.76	6.75	1.41	0.17	0.12
53.16	36.33	10.51	1.46	0.29	0.20
53.33	39.88	6.79	1.34	0.17	0.13
52.82	39.9	7.28	1.32	0.18	0.14
53.82	40.33	5.85	1.33	0.15	0.11
53.31	29.49	17.2	1.81	0.58	0.32
51.86	39.68	8.47	1.31	0.21	0.16

Table A2.4: $M_{23}C_6$ Type Carbides (Determined from the bainite region of the as-received mixed ferrite / bainite structure)

Fe%	Cr%	Mo%	Fe/Cr	Mo/Cr	Mo/Fe
52.95	4.99	42.06	10.61	8.43	0.79
52.57	4.75	42.68	11.07	8.99	0.81
53.83	4.42	41.75	12.17	9.44	0.78
49.86	3.85	46.29	12.95	12.03	0.93
48.15	4.26	47.59	11.30	11.17	0.99
49.54	3.78	46.68	13.11	12.35	0.94
48.69	4.15	47.16	11.73	11.36	0.97
48.46	3.90	47.64	12.43	12.22	0.98
48.73	3.74	47.53	13.03	12.71	0.98
49.39	3.85	46.76	12.84	12.16	0.95
45.15	5.81	49.04	7.77	8.44	1.09

Table A2.5: M_6C Type Carbides (Determined from an intra-granular region of the fully bainitic specimen tempered @ 700°C for 10,000h)

Appendix 3 – Elemental Factors Determined for Use in the STEM Image Analysis Routine.

Element / Background Window	Window Identification	Window span (ev)	Background Window	Background Fraction	Overlap window	Overlap Fraction
Si	1	1580 - 1900	3	1.57	n.a	0
Mo	2	2120 - 2520	3	2.14	n.a	0
BG1	3	2760 - 3000	3	1.00	n.a	0
BG2	4	4840 - 5140	4	1.00	n.a	0
Cr	5	5200 - 5620	4	1.18	n.a	0
Mn	6	5680 - 6120	4	0.96	5	0.13
Fe	7	6160 - 6640	4	1.18	n.a ¹	0

Table A3.1: Data For Calculation Of Factors Required For STEM Image Analysis Routine.

¹ Overlap contribution from Mn_{Kβ} to Fe_{Kα} considered to be negligible and therefore not calculated for the purposes of this analysis.

Creep damage quantification of 2·25Cr–1Mo steel using scanning electron microscopy

R. A. Collington, J. Cawley, and S. R. Holdsworth

The material 2·25Cr–1Mo alloy steel has been used extensively for high temperature applications in power generation plant for over five decades owing to its long term creep resistance. It has been recognised that the lifetime of a high temperature component containing pre-existing defects is dependent not only upon the material's crack propagation resistance but also upon an incubation period before crack growth during which a damage zone ahead of the defect tip develops. The extent of the damage occurring during this incubation period, before crack propagation, is dependent upon the stress intensity at the defect tip, the ductility of the material, and the microstructure in the damage zone. The present paper details a technique for quantifying the early stages of creep damage using image analysis in the scanning electron microscope, and compares the degree, distribution, and orientation of creep damage occurring in two microstructural variables of 2·25Cr–1Mo alloy steel. The paper describes the procedures necessary for generating consistent and reproducible quantitative analysis results, including specimen preparation, defect detection, and measurement criteria. The image analysis process, its accuracy, and application to the study of creep damage mechanisms occurring ahead of defects are discussed.

MST14741

Ms Collington and Dr Cawley are at the Materials Research Institute, Sheffield Hallam University, Sheffield, UK and Dr Holdsworth is with Alstom Power, Rugby, Warwickshire, UK. Based on a presentation at the conference on 'Quantitative microscopy of high temperature materials' held at Sheffield Hallam University on 22–24 November 1999; this meeting was one of the Microstructure of High Temperature Materials series sponsored by The Institute of Materials. The full proceedings will be published as an IoM book.

© 2000 IoM Communications Ltd.

Introduction

Assessment of the remaining lifetime of components in a creep environment has been the subject of much research during the past few decades, two approaches to prediction being the use of crack growth models based on time dependent fracture mechanics concepts¹ and microstructural evaluation.² To predict accurately the lifetime of a component, it has become clear that these two approaches should not be studied in isolation, and that detailed microstructural evidence is required to model creep damage and failure mechanisms of materials of interest.

A number of methods are available to predict the lifetime of a component containing defects using mathematical models based on the theory of fracture mechanics,³ and assessment procedures based on the use of the C^* loading parameter and critical crack opening displacement (COD) have been established.⁴ The importance of estimating the time to initiate a crack t_i as well as the time for crack propagation t_g has now been recognised^{4,5} and, therefore, to estimate this period more accurately more detailed microstructural evidence is required.

During the incubation period before crack propagation, a creep damage zone develops at the crack tip and there is a redistribution of the stress intensity. The structural degradation that occurs in the incubation period is dependent upon the operating stress and temperature regime, and includes changes in chemistry, size distribution, and spacing of second phase particles and nucleation and growth of cavities and cracks.

The present paper details experimental procedures designed to assess the progress of cavitation damage in two microstructures of 2·25Cr–1Mo steel at 550°C in the vicinity of a pre-existing defect, and correlates the results from the study with corresponding crack tip opening displacement and crack initiation data.

Experimental procedure

MATERIAL INVESTIGATED

The material for the present study was extracted from the flange of a fully heat treated cast steam turbine casing in 2·25Cr–1Mo steel. Composition of the steel was Fe–0·11C–0·35Si–0·59Mn–0·006P–0·005S–2·34Cr–1·00Mo (wt-%), heat treated as given in Table 1.

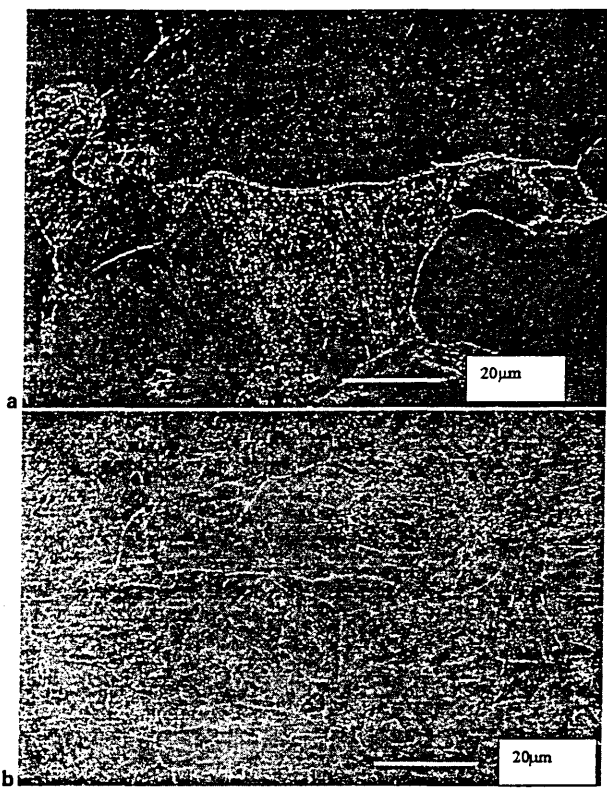
The microstructure of quality heat treated, complex shaped castings, such as those used for turbine generator casings in the power industry, may range from fully bainitic structures in thin sections to ferrite–pearlite structures in the core of the casting. This microstructural variation results from differences in the cooling rate experienced by these regions when cooling from the normalising temperature, relative to the position of the ferrite nose in the continuous cooling transformation (CCT) diagram for 2·25Cr–1Mo steel. For the purpose of the present study, two possible microstructural variables were assessed:

- (i) the as received microstructure of tempered 25% bainite + 75% proeutectoid ferrite (Fig. 1a)
- (ii) a fully bainitic structure derived from renormalising at 960°C and tempering at 700°C (Fig. 1b)

CREEP DAMAGE TEST PROGRAMME

The aim of the creep test programme was to simulate the stress situation ahead of a pre-existing defect in 2·25Cr–1Mo steel and generate creep damage up to the point of 1 mm crack extension $t_{1,mm}$. Analysis of the tested specimens would then allow the degree, distribution, and orientation of creep damage to be determined and related to the strain at the defect tip (crack tip opening displacement) and the onset of cracking (crack initiation).

To simulate the stress situation occurring ahead of such a defect, compact tension specimens, containing fine spark eroded notches <0·2 mm dia., were subjected to



a mixed ferrite-bainite; b 100% bainite

1 Original microstructures of test materials

creep loads at a temperature of 550°C. Crack tip opening displacement (CTOD)^{6,7} was assessed by measuring the displacement of hardness indentations placed at each side of the compact tension specimen notch before and after the creep test⁸ (Fig. 2).

Creep loads applied were based on plain strain reference stress criteria⁹ σ_{ple} , equation (1), and then finally adjusted to give a crack extension of ~1 mm in 1000 h

$$\sigma_{ple} = P/m_{ple} B_n W \dots \dots \dots (1)$$

where P is the applied load, m_{ple} is the yield ratio in plane strain, B_n is the net section thickness, and W is the specimen width, and

$$m_{ple} = [1 + 1.702(a/W)] + [2.702 + 4.599(a/W)^2]^{1/2}$$

where a is crack length.

To assess the progress of damage accumulation, CTOD, and crack initiation, up to four compact tension specimens were tested in series and then removed sequentially at various life fractions for evaluation. Damage accumulation was assessed using image analysis in the scanning electron microscope, and CTOD and crack initiation measurements were made using calibrated scalar devices in the optical and scanning electron microscopes.

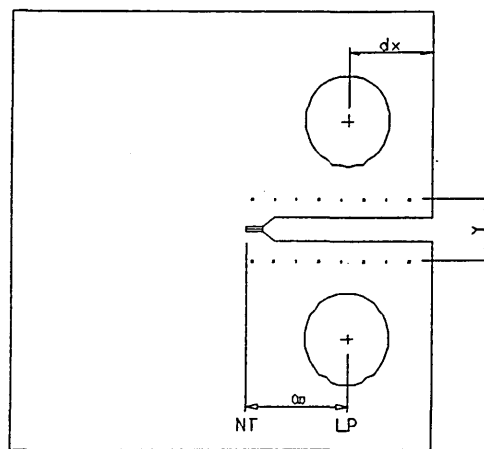
CREEP DAMAGE ACCUMULATION BY IMAGE ANALYSIS IN SEM

Specimen preparation

To obtain an accurate appraisal of the microstructural damage induced during the creep process, it was essential to prepare the specimens for examination with the minimum

Table 1 Heat treatment condition of as received material

Normalise	960 °C, air cool +
Temper	705 °C, furnace cool +
Stress relieve	700 °C, furnace cool



2 Compact tension specimen showing position of hardness indentations for crack tip opening displacement (CTOD)

amount of deformation. Sections from around the damaged defect tip were removed from the test specimens using a fine alumina abrasive wheel, mounted in conducting Bakelite, and ground to a 600 grit finish using conventional silicon carbide abrasive papers. After thorough cleansing, the specimens were polished to a 1 µm finish on diamond impregnated cloths and etched in 2% nitric acid in methanol. The specimens were then subjected to two further polish-etch sequences to ensure that the burred surface had been removed, but without artificially enlarging the voids and microcracks present.¹⁰ After the final etching process, the specimens were coated with a thin evaporated layer of carbon to prevent charging of the oxide layer in the scanning electron microscope (SEM).

Image analysis routine

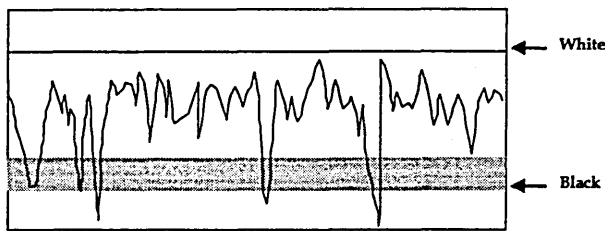
Microstructural examination and damage accumulation of the creep tested compact tension specimens was carried out using a Philips XL40 SEM and Oxford Instruments image analysis software. The microspecimens prepared were examined using both backscattered electron (BSE) and secondary electron (SE) imaging modes. The BSE imaging allowed creep voids and microcracks to be clearly delineated from general microstructural features for quantification purposes, while the SE imaging enabled the operator to determine whether damage was present at inter- or intragranular sites.

The accuracy of the analytical process relied on imaging conditions remaining consistent between consecutive fields of view and between specimens, and, therefore, a systematic routine was devised to ensure reproducible image contrast and brightness and feature detection.

The following microscope conditions were maintained during the analytical procedure:

- working distance 15 mm
- accelerating voltage 20 keV
- beam current ~85 µA
- probe size spot size 6 (large)
- image type backscattered electron
- magnification × 1000
- scan rate 200 ms/line

As the stability of the beam current cannot be guaranteed over long periods of time, or from specimen to specimen, it was necessary to establish a datum for the contrast and brightness levels to ensure consistency. This was achieved by using the waveform meter on the SEM control panel to ensure that the average contrast and brightness signal for



3 Use of SEM waveform meter to ensure image consistency

the general microstructure was at a known position with respect to the 'white' level and that the signal from the voids and microcracks fell into the 'black' level (Fig. 3).

The analytical programme was set up to detect the voids and microcracks using a function which isolates the features of interest from the remaining microstructure, known as grey level thresholding. Once set, the threshold levels remained valid, providing that the contrast and brightness levels in the BSE image were maintained.

To assess quantitatively the creep damage, the analysis routine was used to carry out morphological measurements based on a series of 36 Feret projections. The use of a large number of measurements allows the features of interest to be accurately assessed in terms of their size and shape and, specifically for the present study, the area percentage of the voids and microcracks and their orientation with respect to the stress axis. During the image analysis routine, a BSE signal was collected from the field of interest and displayed as a digital image having an image resolution of 1024×1024 pixels and an area $\sim 185 \times 185 \mu\text{m}$, i.e. 1 pixel $\approx 0.18 \times 0.18 \mu\text{m}$.

Figure 4 shows typical BSE, SE, and digital images of cavitation and microcracking in a specimen of 2.25Cr-1Mo alloy steel.

For this particular exercise, up to 36 fields of view were studied on each specimen, extending to 1 mm each side of the notch tip and 1 mm into the remaining ligament.



Figure 4. a backscattered electron (BSE); b secondary electron (SE); c digital

4 Typical images of cavitation and microcracking

Table 2 Test data* derived from compact tension specimens creep tested at 550°C

Test duration, h	CTOD, mm	Crack extension, mm	Cavity area, %
Ferrite-bainite (110 MPa)			
0	0.00	0.00	0.00
300	0.08	0.00	0.01
700	0.16	0.00	0.06
850	0.27	0.39	1.73
1000	0.27	0.90	5.14
1500	2.75	8.22	ND
Bainite (100 MPa)			
0	0.00	0.00	0.00
300	0.07	0.00	0.04
350	0.18	0.49	0.22
400	0.28	0.62	1.42
500	0.35	2.50	ND
600	0.35	4.00	ND
800	0.98	6.17	ND
1000	1.52	6.81	ND

*CTOD is crack tip opening displacement, ND is data not determined.

Results

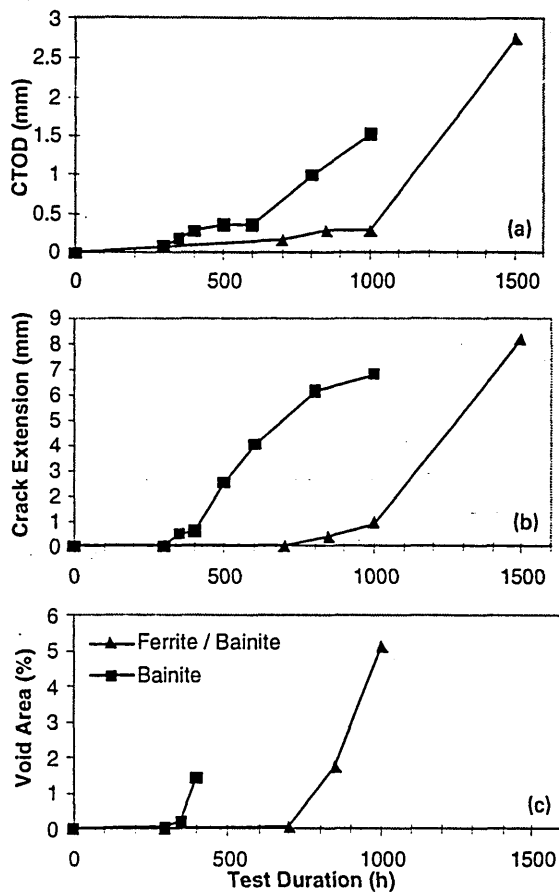
At predetermined intervals, the compact tension specimens were removed from the creep test and assessed for crack opening displacement. Microspecimens were then extracted and prepared from the 'defect' tip region and analysed in terms of their microstructure, void area percentage, and void orientation in the SEM.

CTOD, CRACK EXTENSION, AND VOID AREA PERCENTAGE

The results determined for CTOD, crack extension, and void area percentage are given in Table 2.

From the results (Fig. 5) it was evident that the onset of CTOD, crack extension, and void nucleation in the ferrite-bainite material was delayed with respect to that in the fully bainitic condition, suggesting that the duplex structure is more resistant to ductility exhaustion (more creep ductile) than the single phase structure. This was substantiated by examination of the results plotted in Fig. 6b for CTOD against void area percentage. This showed that, for CTODs less than 0.2 mm, a greater CTOD was required to generate the same creep damage, in the form of voids and microcracks, for the ferrite-bainite specimen than for the fully bainitic structure.

In the fully bainitic structure, crack extension advanced for a minimal amount of voiding and then appeared to slow down, while in the case of the ferrite-bainite structure there



a CTOD; b crack extension; c void area percentage

5 Variation of given parameters with test duration

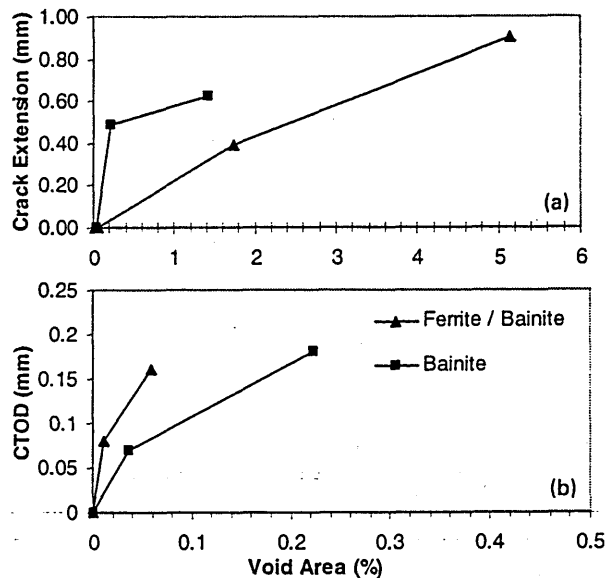
was an almost linear relationship between crack extension and void percentage (Fig. 6a).

Correlation of the data derived for CTOD and crack extension (Fig. 7) suggested that, although CTOD initiation was delayed in the ferrite-bainite specimen, an almost linear relationship existed for the two structures once a critical CTOD had been reached.

MICROSTRUCTURAL EXAMINATION AND VOID ORIENTATION

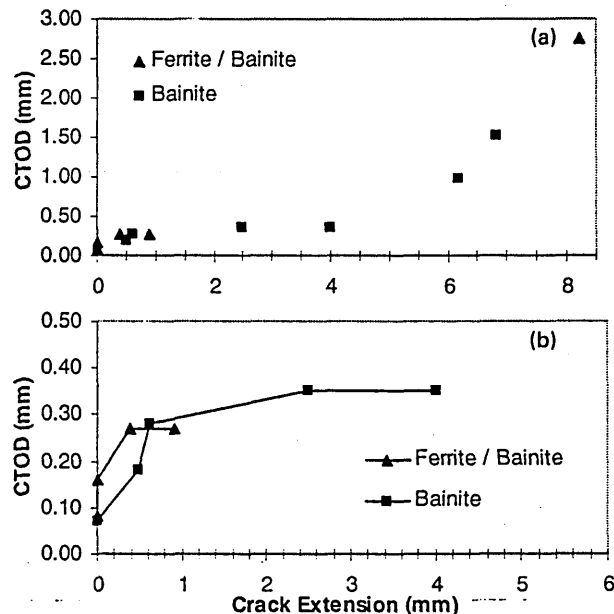
Low magnification imaging of the notch tip region in each of the specimens analysed showed that voiding and microcrack extension in the fully bainitic structure was constrained to a narrower field width than in the ferrite-bainite specimen (Fig. 8). The degree of constraint was also evident on plotting the void area percentage data against position relative to the notch tip, as shown in Fig. 9.

Frequency distribution charts showing void orientation with respect to notch tip position (Fig. 10) suggested that void elongation occurred predominantly at angles of 50–60° with respect to the notch tip in both microstructural variables. Microstructural evidence, however, suggested that the orientation of the grain boundaries, along which voiding occurred, was close to the 45° shear axis as might have been predicted in these short term tests (Fig. 11). The occurrence of voids and microcracking in all cases was predominantly intergranular, being detected mainly at the proeutectoid ferrite/bainite boundaries in the mixed structure (Fig. 11a) and at the prior austenite grain boundaries in the fully bainitic structure (Fig. 11b). Examination of the precipitate morphology depicted in Fig. 11 showed that the carbides in the ferrite region of the mixed structure were much finer than those present in the bainite phase of either material condition. This was also evident from extraction



a crack extension; b CTOD

6 Variation of given parameters with void area percentage



a all results; b expanded scale delineating crack initiation region, i.e. <math>< 1\text{ mm}</math> of crack extension

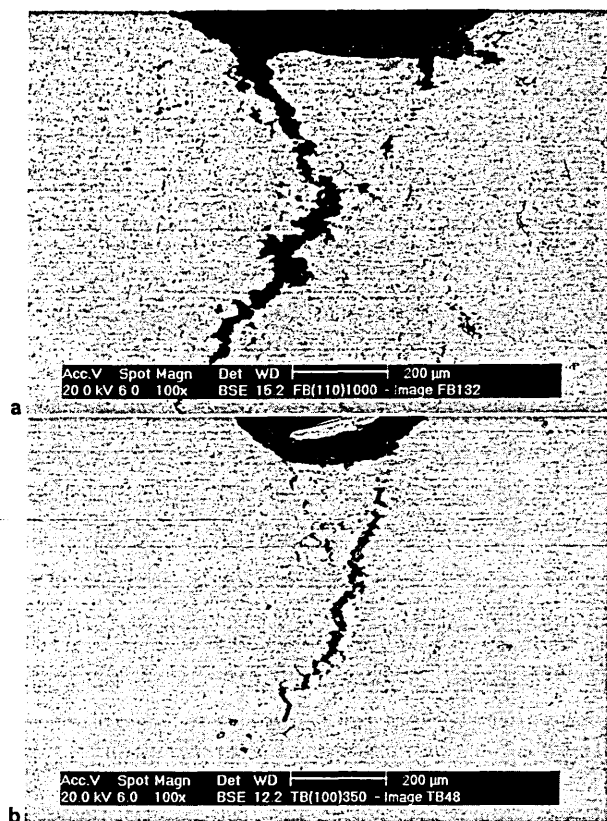
7 Variation of CTOD with crack extension

replicas produced from the original starting microstructures of the two materials (Fig. 12).

Discussion

The aim of the present study was to compare the mechanisms of creep damage accumulation ahead of a pre-existing defect in two microstructures of 2-25Cr-1Mo steel, with a view to appreciating how microstructural variables can affect creep life predictions.

Quantitative image analysis in the SEM enabled microstructures from creep tested, compact tension specimens to be studied in terms of creep damage accumulation ahead of a simulated defect tip in conjunction with microstructural examination.



a ferrite-bainite structure, 1000 h; b bainitic structure, 400 h

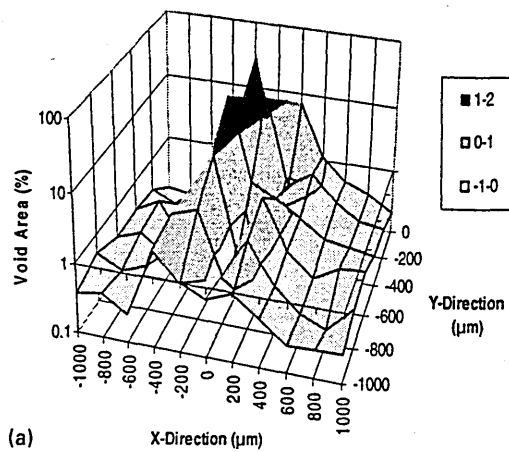
8 Low magnification images of voiding and microcracking around notch tip

In general, the results showed that during the initiation period $t_{i,mm}$ the ferrite-bainite material required a greater CTOD to extend the damage zone than did the fully bainitic structure. It was evident from Figs. 6b and 7b that a greater degree of strain, in the form of CTOD, could be accommodated at the notch tip of the ferrite-bainite specimen before the onset of damage by void accumulation and crack extension. This additional strain accommodation was considered partly to result from the ferrite phase regions acting as 'soft zones',¹¹ reducing the number of prior austenite grain boundaries, but also because the bainite in the mixed structure existed in a more 'mature' evolutionary state (Fig. 12).

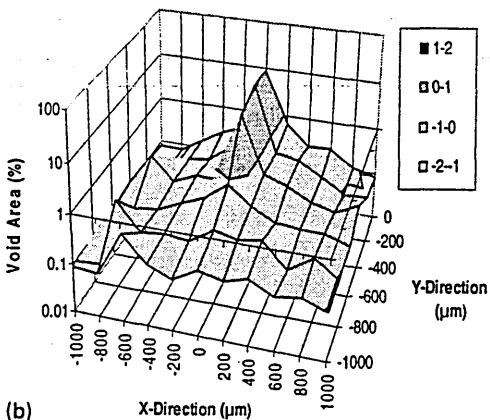
Creep crack initiation has been shown previously^{12,13} to occur on the attainment of a critical local crack tip strain, and this was also evident in the present study. Figure 7 demonstrated that, although the CTOD to generate a given Δa (damage) for the ferrite-bainite material during the incubation period was greater than that for the fully bainitic material, the critical value of CTOD $\delta_{i,mm}$ was similar for both microstructural variables and that, once the critical value had been exceeded, crack extension occurred at a similar rate for both materials with respect to CTOD.

The quantity and distribution of creep damage, in the form of grain boundary voids and microcracks, is depicted in Figs. 8 and 9 and shows the effect of variation in microstructure on the degree of constraint at the notch tip. In the incubation period it was evident that the higher ductility exhibited by the ferrite-bainite structure resulted in lower notch constraint and, hence, more extensive cavitation and microcracking before the onset of crack growth (crack extension > 1 mm).

To determine the mechanisms of creep cavity nucleation in the two microstructural variables, the orientation of the voids and microcracks was determined and studied in conjunction with microstructural evidence detected in the



(a)

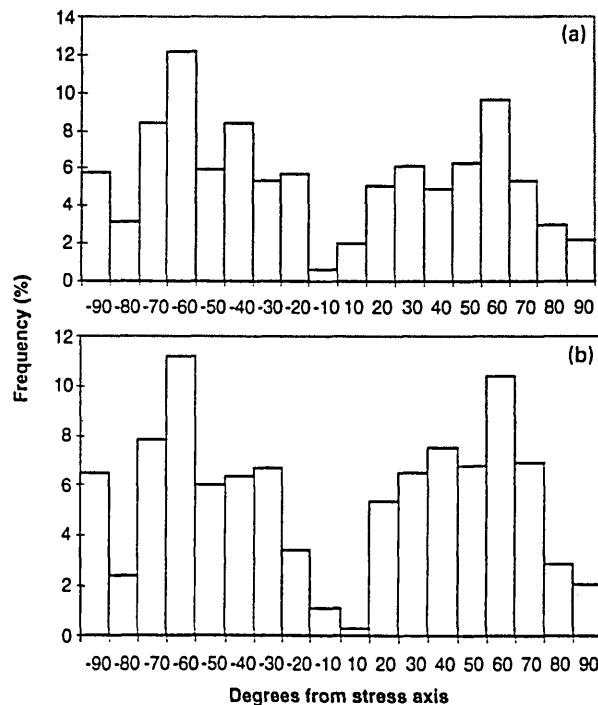


(b)

a ferrite-bainite structure, 1000 h; b bainitic structure, 400 h

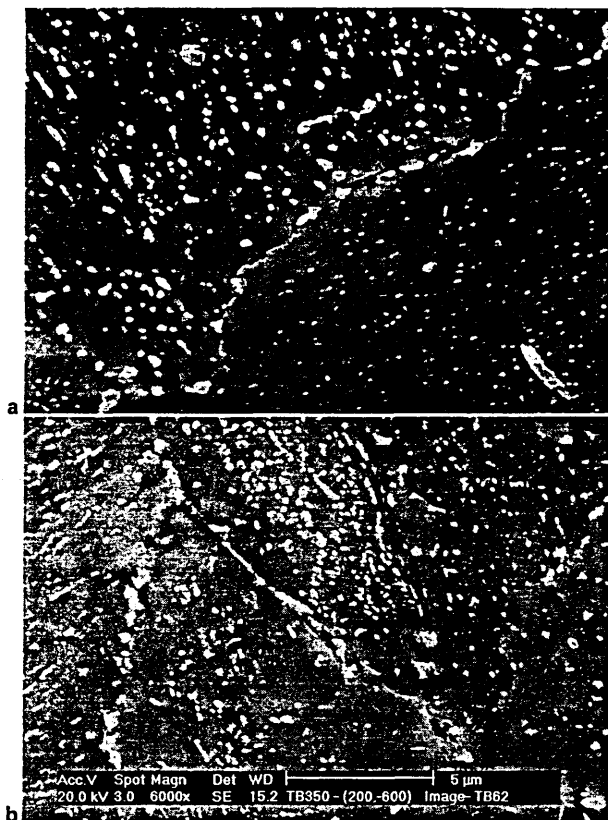
9 Quantitative void analysis data relative to notch tip position

SEM. Void orientation analysis showed that the cavities nucleated most frequently at angles of $\pm 60^\circ$ with respect to the notch tip (Fig. 10). Microstructural evidence, however,



a ferrite-bainite structure, 1000 h; b bainitic structure, 400 h

10 Frequency distribution charts for void orientation data



a ferrite-bainite structure, 1000 h; b bainitic structure, 400 h

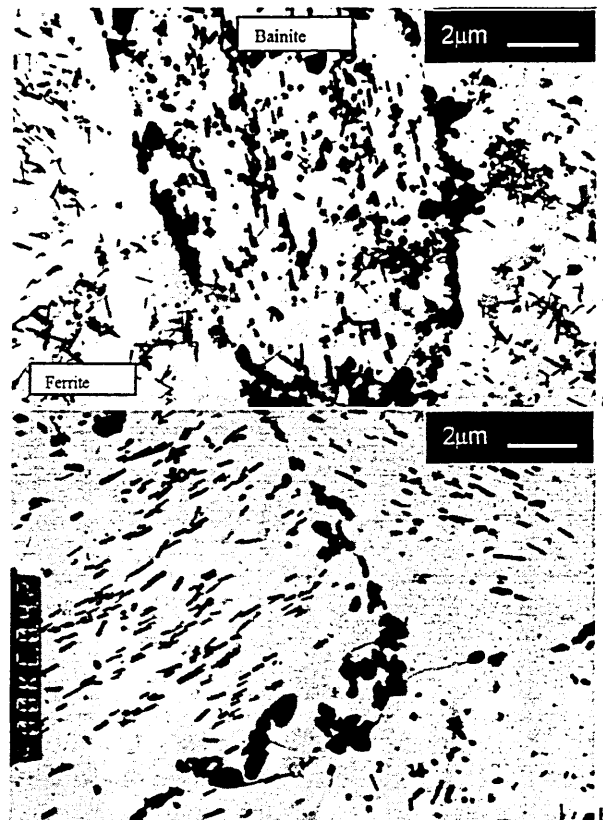
11 High magnification images of voiding at grain boundaries

showed that the boundaries, upon which the cavities nucleated and extended, were generally oriented at angles of $\pm 45^\circ$ with respect to the notch tip (Fig. 8). This combined evidence suggests that the mechanism of cavity nucleation and growth, in both the ferrite-bainite and fully bainitic structures, was not by grain boundary sliding alone, but by a combination of sliding and atom diffusion. High magnification imaging of the microstructure using secondary electrons in the SEM supported this theory (Fig. 11) in that diffusion of atoms appeared to be occurring away from the bainite phase regions, down substructure boundaries, towards the main grain boundaries. The large grain boundary carbides, predominantly $M_{23}C_6$ type, then appeared to grow and elongate along the boundary until they lost coherency with the matrix resulting in cavity nucleation.

Previous studies of the effect of transformation structure on the creep and rupture behaviour of 2-25Cr-1Mo steel¹¹ carried out on uniaxial creep test specimens showed that failure in high bainite content material occurred, as in the present study, by intergranular failure. However, in low bainite content material ($\sim 20\%$ bainite), failure was found to occur by intragranular cavitation and transgranular ductile fracture.¹¹ The difference observed in the present study may be caused by the triaxial state of stress ahead of the defect tip, encouraging diffusion and sliding on grain boundaries oriented at 45° to the principal stress axes.

Conclusions

1. Image analysis in the SEM can be used effectively to study creep damage accumulation in steel, providing that image stability can be maintained.



a mixed ferrite-bainite structure; b fully bainitic structure

12 Precipitate morphology of materials before testing

2. During the incubation period for creep crack extension ahead of a pre-existing defect in two structures of 2-25Cr-1Mo steel at 550°C :

- (i) the material, in both microstructural conditions, undergoes strain accumulation in the form of elastic-plastic deformation, grain boundary voiding, and microcracking
- (ii) voiding and microcracking occur predominantly at intergranular sites between the ferrite-bainite grains in the mixed structure and at the prior austenite boundaries in the fully bainitic material
- (iii) the ferrite-bainite structure is more creep ductile than the fully bainitic structure owing to the effective dispersal of the creep stress by the ferrite phase and mature bainite phase, leading to enhanced strain accommodation and reduced notch tip constraint
- (iv) grain boundary voiding appears to occur in both microstructural conditions because of the combined effects of atom diffusion down the bainitic substructure and grain boundary diffusion, precipitate growth, and sliding.

3. Upon the attainment of a critical notch tip strain, i.e. ϵ to give 1 mm of crack extension, the ferrite-bainite and fully bainitic structures appear to deform at a similar rate.

References

1. A. SAXENA: Proc. 57th Ann. Power Conf., Vol. 57, 1798-1821; 1995, Chicago, IL, Illinois Institute of Technology.
2. R. D. TOWNEND: in 'Microstructures and mechanical properties of aging materials', 1-17; 1993, Warrendale, PA, TMS.
3. E. G. ELLISON and M. P. HARPER: *J. Strain Anal. (Eng. Des.)*, 1978, 13, 35-51.
4. R. A. AINSWORTH and P. J. BUDDEN: *Mater. High Temp.*, 1998, 15, 291-297.
5. S. R. HOLDSWORTH: *Mater. High Temp.*, 1992, 10, 127-137.

6. S. M. BEECH, J. W. SELWAY, and A. D. BATTE: in 'Creep and fatigue of engineering materials and structures', (ed. B. Wilshire and D. R. J. Owen), Vol. 2, 925-936; 1984, Swansea, Pineridge Press.
7. K. H. KLOOS, J. GRANACHER, and R. TSCHESCHNER: *Z. Werkstofftech.*, 1987, 18, 390.
8. S. R. HOLDSWORTH and D. J. CUNNANE: 'Lifetime prediction of components containing defects', COST 501 WP5C Final Report, GEC Alstom Turbine Generators, Rugby, UK, 1993.
9. A. G. MILLER: *Pressure Vessels Piping*, 1988, 32, 197.
10. T. L. DA SILVA and I. LE MAY: *Mater. Charact.*, 1992, 28, 75-85.
11. B. J. CANE: 'The effect of transformation structure on the creep and rupture behaviour of 2.25%Cr-1%Mo steel', CEGB Report no. RD/L/N 236/75, Leatherhead, UK, March 1976.
12. R. A. AINSWORTH: *Int. J. Solid Struct.*, 1982, 18, 873.
13. R. A. AINSWORTH: Proc. Conf. Euromech 239: 'Mechanics of creep brittle materials', Leicester, UK, 13; 1988, Oxford, Elsevier.

BRITISH CERAMIC PROCEEDINGS 59

ENGINEERING WITH CERAMICS

Edited by

W. E. Lee and B. Derby

Contents: Recollections of Roger Davidge; Foreword; Characterization of Sub-Critical Crack Growth in Ceramics Using Indentation Cracks; Freeform Fabrication of Ceramics; Biaxial Disc Flexure - Modulus and Strength Testing; Hertzian Testing of Ceramics; The Flexure Strength of Multilayer Ceramic Capacitors; Indentation Damage Zone in Calcium and Lead Titanate Ceramics; *In Situ* Measurements of Residual Stresses in a Thermal Barrier Coating During Thermal Cycling; Towards More Predictable Deformation in Sanitaryware Products; Influence of Environment on Delayed Failure of Alumina Ceramics; An Experimental Study of the Fracture Behaviour of Magnesium Zinc Ferrites; Erosive Wear of Alumina/SiC Nanocomposite Ceramics; Sialon/TiB₂ Ceramic Composites: Synthesis, Properties and Tribology; Microstructural Requirements for Alumina/SiC Nanocomposites; Microstructure Characterisation and Superplasticity of an Alumina/Carbon Nanocomposite; The Evaluation of Novel Interphases for Oxide-Oxide Ceramic Matrix Composites; Multi-Phase Piezoelectric Structures Through Co-Extrusion; Optimisation of Ball Valve Processing Parameters; Influence of Additives to Ag Based Electrode Pastes on Bonding to PZT; The Fracture Behaviour of Dual Phase Composite Refractories; Dissolution of Dolomite and Doloma in a Model BOF Slag; Reactions of Silicon and Carbon in Reducing Atmospheres; Barium Hexaaluminate Refractories; *Author Index; Subject Index*

Book 713 ISBN 1 86125 087 8 Hbk

European Union £75/Members £60

Non-European Union \$150/Members \$120

p&p European Union £5.00/Non-EU \$10.00 per order

Orders to: IOM Communications Ltd, Shelton House, Stoke Road, Shelton,
Stoke-on-Trent, ST4 2DR Tel: +44 (0) 1782 202 116 Fax: +44 (0) 1782 202 421
Email: Orders@materials.org.uk Internet: www.materials.org.uk



IOM Communications

Reg. Charity No. 1059475 VAT Registration No. GB 649 1646 11

IOM Communications Ltd is a wholly-owned subsidiary of the Institute of Materials

Index to Table Nos.

Table No.	Title	Page
2.1	Nature Of carbides in normalised 2.25%Cr-1%Mo steel ^{[17] [28]} _[27]	15
2.2	Equilibrium compositions of $M_{23}C_6$ and M_7C_3 carbide - after Thomson ^[24] .	17
2.3	Creep damage categories, mechanisms and incorporation into continuum damage mechanics equations – after Dyson and McLean ^[113] .	51
2.4	Classification of damage process and exhausted creep life - after Dobrzanski and Hernas ^[103] .	52
3.1	Composition of as-received material.	65
3.2	Final commercial heat-treatment of as-received material.	65
3.3	Creep test loading conditions.	75
3.4	Elemental ratios determined by EDX spot analyses and used for carbide identification.	87
3.5	The compositional range of various metal carbides encountered in 2.25%Cr-1%Mo steel, as used in conjunction with EDX-Digiscan image analysis.	91
4.1	Hardness and tensile properties.	94
4.2	Grain size and phase proportions of starting materials.	96
4.3	Elemental ratios for the carbides observed in the ferrite / pearlite structure as indicated in plate 4.11.	106
4.4	Elemental ratios for the carbides observed in the ferrite / bainite structure as indicated in plate 4.13.	107
4.5	Elemental ratios for the carbides observed in the ferrite / bainite structure as indicated in plate 4.14.	108
4.6	Temper trial sample conditions	110
4.7	Hardness results for the tempered fully bainitic samples ($\pm 2\sigma$).	111
4.8	Carbide size distribution data for the fully bainitic sample tempered at 700°C for 0.5 hours.	121
4.9	Carbide size distribution data for the fully bainitic sample tempered at 700°C for 5 hours.	122
4.10	Carbide size distribution data for the fully bainitic sample tempered at 700°C for 50 hours.	123
4.11	Carbide size distribution data for the fully bainitic sample tempered at 700°C for 5000 hours.	124

Index to Table Nos. cont.

4.12	Change in carbide type with tempering time at 700°C for the fully bainitic samples.	125
4.13	Y-displacement values of hardness indentations for 100% tempered bainite starting material tested at a stress of 100MPa for times between 300 and 1000 hours.	131
4.14	Y-displacement values of hardness indentations for mixed ferrite / bainite starting material tested at a stress of 110MPa for times between 300 and 1500 hours.	131
4.15	Crack tip opening displacement results derived from CT specimens manufactured from the starting materials.	134
4.16	Void % analysis results for the 100% tempered bainite sample tested at 550°C and 100MPa For 300h.	139
4.17	Void % analysis results for the 100% tempered bainite sample tested at 550°C and 100MPa for 350h.	140
4.18	Void % analysis results for the 100% tempered bainite sample tested at 550°C and 100MPa for 400h.	141
4.19	Crack extension and void area % values for the tempered, fully bainitic, CT specimens.	143
4.20	Void % analysis results for the mixed ferrite / bainite sample tested at 550°C and 110MPa for 700h.	150
4.21	Void % analysis results for the mixed ferrite / bainite sample tested at 550°C and 110MPa for 850h.	151
4.22	Void % analysis results for the mixed ferrite / bainite sample tested at 550°C and 110MPa for 850h.	152
4.23	Crack extension and void area % values for the mixed ferrite / bainite CT specimens.	154
4.24	Void % analysis results for the mixed ferrite / pearlite sample tested at 550°C and 85MPa for 3680h.	161
4.25	Void % analysis results for the mixed ferrite / pearlite sample tested at 550°C and 85MPa for 6850h.	162
4.26	Crack extension and void area % values for the mixed ferrite / pearlite CT specimens.	164
4.27	Summary of creep testing investigation results.	170
5.1	Type and location of carbides detected in the three starting structures investigated in the current study.	193
5.2	Values of $\Delta a/\Delta CTOD$ and $\Delta a/\text{void area } \%$, determined from the ferrite / bainite and 100% bainite CT specimens at a crack extension of 0.5mm.	206

Index to Figure Nos.

Figure No.	Title	Page
1.1	Trend to higher steam conditions for steam power plant – after Scarlin ^[3] .	2
1.2	Flow diagram summarising the experimental process.	7
2.1	Continuous cooling diagrams for some Cr-Mo Steels – after Orr ^[20] .	11
2.2	Carbide evolution sequence for 2.25%Cr-1%Mo steel, where M indicates a mixture of metal atoms- after Baker and Nutting ^[17] .	14
2.3	Predicted evolution of precipitate volume fractions at 600°C in 2.25%Cr-1%Mo steel -after Robson and Bhadeshia ^[37] .	17
2.4	Typical deformation map – plot of normalised stress against homologous temperature - after Reidel ^[40] .	21
2.5	The climb force on a dislocation - after Ashby and Jones ^[46] . Where: τ =shear stress and b =Burgers vector.	22
2.6	Diffusion of atoms leading to dislocation climb - after Ashby and Jones ^[46] .	23
2.7	Diffusion along dislocation lines, core diffusion, at low T/T _m – after Ashby and Jones ^[46] .	24
2.8	The process of creep deformation by diffusion at high T/T _m – after Ashby and Jones ^[46] .	24
2.9	Creep rupture strength of carbon steels and Cr-Mo steels - after Abe and Yagi ^[62] .	26
2.10	Creep curves for various stress regimes at 565°C – after Kleuh ^[16] .	29
2.11	Creep rupture mechanism diagram for 2.25%Cr-1%Mo steel - after Yamauchi et al ^[66] .	29
2.12	Proposed creep deformation mechanism map of 2.25%Cr-1Mo steel – after Maruyama et al ^[67] .	30
2.13	Fracture Map – after Reidel ^[40] .	33
2.14	Wedge cracking at grain boundary triple point due to sliding – after Lagnebourg ^[74] .	34
2.15	Various mechanisms for grain boundary cavity nucleation due to grain boundary sliding – after Evans and Wiltshire ^[50] .	34
2.16	Stress concentration factor, σ_p/σ_∞ at particles versus applied stress – after Reidel ^[40] .	36

Index to Figure Nos. cont.

2.17	Model for grain boundary cavitation by surface and grain boundary diffusion – after Hull and Rimmer ^[83] . Adjoining grains are assumed to act as rigid bodies.	37
2.18	Schematic illustration of cavity growth by the combination of plastic creep flow and rapid surface diffusion – after Hancock ^[86] .	38
2.19	Comparison of creep curves from uniaxial creep data for 2.25%Cr-1%Mo steel compared with predictions for constrained and unconstrained cavity nucleation –after Reidel ^[40] .	39
2.20	The factors that affect ductile-brittle creep behaviour - after Gooch and King ^[95] .	42
2.21	The effect of specimen geometry on brittleness in plane strain –after Gooch and King ^[95] .	44
2.22	Influence of phase constitution and damage process on safe residual lifetime of 1Cr-0.5Mo steel - after Dobrzanski and Hernas ^[103] .	51
2.23	Variation of crack opening displacement and crack length in a fracture mechanics specimen indicating the importance of specifying crack initiation criteria – after Holdsworth ^[11] .	57
2.24	Derivation of δ_{ix} using hardness indentations – after Holdsworth ^[132] .	58
2.25	Influence of creep ductility on crack opening displacement and growth behaviour in a fracture mechanics test piece subject to steady load at high temperature, a) brittle 0.5%Cr-0.5%Mo-0.25%V HAZ, b) ductile 2.25%Cr-1%Mo weld metal – after Holdsworth ^[132] .	58
3.1	The continuous cooling transformation diagram for a 2.25%Cr-1.0%Mo steel – after M. Atkins ^[140] .	68
3.2	Plan for sectioning of bainite tempering samples.	69
3.3	Creep test rig design.	72
3.4	Schematic diagram of CT specimen and dimensions.	73
3.5	Crack opening displacement measurement. a) Schematic diagram of CT specimen notch and hardness indentations. b) Schematic diagram of crack opening displacement against indentation position.	76
3.6	Micro-specimen extraction from notch tip region.	80
3.7	Use of the SEM wave-form meter to ensure image consistency.	82
3.8	Selective preparation of notch tip and reference region extraction replicas.	86

Index to Figure Nos. cont.

3.9	STEM images of a) carbide precipitates and b) the corresponding digitised image.	90
3.10	EDX spectra of 2.25%Cr-1%Mo steel showing identification of elements of interest by formation of "windows".	91
4.1	Typical EDX spectra for the carbides in 2.25%Cr-1%Mo alloy.	109
4.2	Graph showing Vickers hardness values against tempering temperature and time. for the fully bainitic specimens.	112
4.3	Graph showing Vickers hardness values against the Larson-Miller parameter, $P = T \times (C + \log t)$, for the fully bainitic specimens. Where: T = temp. (K), C = a constant taken to be 20 and t = time (secs).	112
4.4	Size distribution curves for the various carbides identified in the fully bainitic sample tempered at 700°C for 0.5 hours.	121
4.5	Size distribution curves for the various carbides identified in the fully bainitic sample tempered at 700°C for 5 hours.	122
4.6	Size distribution curves for the various carbides identified in the fully bainitic sample tempered at 700°C for 50 hours.	123
4.7	Size distribution curves for the various carbides identified in the fully bainitic sample tempered at 700°C for 5000 hours.	124
4.8	Change in carbide type with tempering time at 700°C for the fully bainitic samples.	125
4.9	Graph showing M_3C type carbides as a percent of the total detected for each tempering duration plotted against mean diameter.	126
4.10	Graph showing M_2C type carbides as a percent of the total detected for each tempering duration plotted against mean diameter.	126
4.11	Graph showing M_7C_3 type carbides as a percent of the total detected for each tempering duration at 700°C plotted against mean diameter.	127
4.12	Graph showing $M_{23}C_6$ type carbides as a percent of the total detected for each tempering duration at 700°C plotted against mean diameter.	127
4.13	Graph showing M_6C type carbides as a percent of the total detected for each tempering duration at 700°C plotted against mean diameter.	128
4.14	Y-displacement values of hardness indentations for mixed ferrite / bainite starting material tested at a stress of 110MPa for times between 300 and 1500 hours.	132

Index to Figure Nos. cont.

4.15	Crack opening displacement values for the fully bainitic sample tested at a stress of 100MPa and 550°C for times between 300 – 600h.	132
4.16	Crack opening displacement values for the ferrite / bainite sample tested at a stress of 110MPa and 550°C for times between 300 – 1500h.	133
4.17	Crack opening displacement values for the ferrite / bainite sample tested at a stress of 110MPa and 550°C for times between 300 – 1000h.	133
4.18	Void % analysis distribution chart for the 100% tempered bainite sample tested at 550°C and 100MPa for 300h.	139
4.19	Void % analysis distribution chart for the 100% tempered bainite sample tested at 550°C and 100MPa For 350h.	140
4.20	Void % analysis distribution chart for the 100% tempered bainite sample tested at 550°C and 100MPa for 400h.	141
4.21	Frequency distribution analysis for void orientation in the fully bainitic sample tested at 550°C, 100MPa for 400h.	143
4.22	Void % analysis distribution chart for the ferrite / bainite sample tested at 550°C and 110MPa for 700h.	150
4.23	Void % analysis distribution chart for the mixed ferrite / bainite sample tested at 550°C and 110MPa for 850h.	151
4.24	Void % analysis distribution chart for the mixed ferrite / bainite sample tested at 550°C and 110MPa for 1000h.	152
4.25	Frequency distribution analysis for void orientation in the ferrite / bainite sample tested at 550°C and 110MPa for 850h.	154
4.26	Void % analysis distribution chart for the ferrite / pearlite sample tested at 550°C and 85MPa for 3680h.	161
4.27	Void % analysis distribution chart for the ferrite / pearlite sample tested at 550°C and 85MPa for 6850h.	162
4.28	Frequency distribution analysis for void orientation in the ferrite / pearlite sample tested @ 550°C, 85MPa and 3680h.	164
4.29	Variation of a) CTOD, b) Crack extension and c) Void area %, with test duration for 100% tempered bainite and mixed ferrite / bainite specimens.	171
4.30	Variation of a) CTOD and b) Crack extension with void area % for 100% tempered bainite and mixed ferrite / bainite specimens.	172
4.31	CTOD against crack extension for a) all samples, b) expanded scale delineating crack initiation region, i.e. <1mm of crack extension.	173

Index to Plate Nos.

Plate No.	Title	Page
4.1	Optical micrograph of the mixed pro-eutectoid ferrite / pearlite structure derived from pipe section fully annealed at 960°C.	101
4.2	Optical micrograph of the mixed pro-eutectoid ferrite / bainite structure derived from as-received bar normalised at 960°C, tempered at 705°C and stress relieved at 700°C .	101
4.3	Optical micrograph of the 100% bainite structure produced by normalising at 960°C and tempering at 700°C for 24h.	102
4.4	Low magnification SEM image of the ferrite / pearlite original microstructure.	102
4.5	High magnification SEM image of the ferrite / pearlite original microstructure.	103
4.6	Low magnification SEM image of the ferrite / bainite original microstructure.	103
4.7	High magnification SEM image of the ferrite / bainite original microstructure.	104
4.8	Low magnification SEM image of the fully bainitic original microstructure.	104
4.9	High SEM magnification image of the fully bainitic original microstructure.	105
4.10	TEM bright field Image of a thin foil specimen extracted from the as normalised material . Carbide precipitation observed between the ferrite laths identified the structure as upper bainite.	105
4.11	TEM micrograph of the carbide morphology in the ferrite / pearlite, as received, material .	106
4.12	TEM micrograph of the carbide morphology in the tempered mixed pro-eutectoid ferrite / bainite. Starting material.	107
4.13	TEM micrograph of the carbide morphology in the tempered, mixed pro-eutectoid ferrite / bainite starting material.	107
4.14	TEM micrograph of the carbide morphology in the tempered 100% bainite starting material.	108
4.15	SEM micrograph of the fully bainitic sample tempered at 700°C for 0.5h.	116
4.16	SEM micrograph of the fully bainitic sample tempered at 700°C for 5h.	116
4.17	SEM micrograph of the fully bainitic sample tempered at 700°C for 5h.	117

Index to Plate Nos. cont.

4.18	SEM micrograph of the fully bainitic sample tempered at 700°C For 100h.	117
4.19	SEM micrograph of the fully bainitic sample tempered at 700°C For 1000h.	118
4.20	High magnification SEM image of the area out-lined in plate 4.19 showing irregular growth of grain boundary carbides and associated precipitate free zones.	118
4.21	SEM micrograph of the fully bainitic sample tempered at 700°C For 5000h.	119
4.22	SEM micrograph of the fully bainitic sample tempered at 650°C for 50h.	119
4.23	SEM micrograph of fully bainitic sample tempered at 750°C for 50h.	120
4.24	Low magnification SEM image of the notch tip region in the fully bainitic sample tested at 550°C and 100MPa for 300 hours.	139
4.25	Low magnification SEM image of the notch tip region in the fully bainitic sample tested at 550°C and 100MPa for 350h.	140
4.26	Low magnification SEM image of the notch tip region in the fully bainitic sample tested at 550°C and 100MPa for 400h.	141
4.27	Montage of SEM images showing the microstructure in the area immediately adjacent to the notch tip in the 100% tempered bainite sample tested at 550°C and 100MPa For 400h.	142
4.28	High magnification SEM image of grain boundary voiding evident in the tempered, fully bainitic, material tested at 550°C and 100MPa for 400h. The red arrows indicate evidence of sub-structure boundaries adjacent to the cavitating regions.	144
4.29	High magnification SEM image of voiding at a grain boundary in the tempered, fully bainitic, material tested at 550°C and 100MPa for 400h. Elongated carbides, adjacent to PFZ's, are evident in the vicinity of the voids.	144
4.30	SEM micrograph showing a denuded zone adjacent to grain boundary voiding in the tempered, fully bainitic, material tested at 550°C and 100MPa for 400h.	145
4.31	SEM image showing voids opening up at triple points and evidence of atom migration down sub-structure boundaries in the tempered, fully bainitic, material tested at 550°C and 100MPa for 400h.	145
4.32	SEM micrograph showing the carbide morphology in a reference region remote from notch tip stress field in the tempered, fully bainitic, material tested at 550°C and 100MPa for 400h.	146

Index to Plate Nos. cont.

4.33	Low magnification SEM image of the notch tip region in the mixed ferrite / bainite sample tested at 550°C and 110MPa for 700h.	150
4.34	Low magnification SEM image of notch tip region in the ferrite / bainite sample tested at 550°C and 110MPa for 850h.	151
4.35	Low magnification SEM image of notch tip region in the mixed ferrite / bainite sample tested at 550°C and 110MPa for 1000h.	152
4.36	Montage of SEM images showing the microstructure in an area immediately adjacent to the notch tip in the ferrite / bainite sample tested @550°C and 110MPa for 1000h.	153
4.37	High magnification SEM image of voiding at a ferrite / bainite grain boundary .	155
4.38	High magnification SEM image of an area indicated in plate 4.37 above showing voiding at a grain boundaries and evidence of sub-structure boundaries in the bainite phase.	155
4.39	SEM micrograph showing large, irregular shaped, grain boundary carbide perpendicular to principal stress axis between two ferrite grains and adjacent to a denuded bainite grain.	156
4.40	SEM micrograph showing cavitation on a ferrite / bainite grain boundary and associated denuded region.	156
4.41	SEM image depicting cavitation on a ferrite / bainite grain boundary and growth of associated grain boundary carbides. PFZ evident in the ferrite grain adjacent to the grain boundary.	157
4.42	SEM image showing voiding in an intra-granular bainitic region of the mixed ferrite / bainite specimen tested for 1000 hours.	157
4.43	SEM micrograph showing carbide morphology in a reference region, remote from the notch tip stress field, of the ferrite / bainite specimen tested for 1000h.	158
4.44	High magnification SEM micrograph showing the carbide morphology in a reference region, remote from notch tip stress field, of the ferrite / bainite specimen tested for 1000h.	158
4.45	Low magnification SEM image of the notch tip region in the ferrite / pearlite sample tested at 550°C and 85MPa for 3680h.	161
4.46	Low magnification SEM image of the notch tip region in the ferrite / pearlite sample tested at 550°C and 85MPa for 6850h.	162
4.47	Montage of SEM micrographs showing the area adjacent to the notch tip in the ferrite / pearlite sample tested @550°C and 85MPa For 3680h.	163
4.48	SEM image showing voiding at a grain boundary between the ferrite and pearlite phase.	165

Index to Plate Nos. cont.

4.49	Voiding at a grain boundary between the ferrite and pearlite phase.	165
4.50	Voiding at a grain boundary between the ferrite and pearlite phase.	166
4.51	Voiding at a grain boundary between the ferrite and pearlite phase.	166
4.52	SEM micrograph showing the carbide morphology in a reference region, remote from notch tip stress field, of the ferrite / pearlite specimen tested for 3680h.	167
4.53	TEM micrograph showing the typical carbide morphology observed in a reference region of the tempered bainite CT specimen tested at a temperature 550°C and a stress of 100MPa for 350 hours.	178
4.54	TEM micrograph showing the typical carbide morphology observed in the notch tip region of the tempered bainite CT specimen tested at a temperature 550°C and a stress of 100MPa for 350 hours.	178
4.55	Typical boundary oriented at an angle with respect to the notch tip in the fully bainitic CT specimen tested at a temperature 550°C and a stress of 100MPa for 350 hours. Evolving carbides identified for EDX analysis in Plates 4.56 – 4.58.	179
4.56	Brightfield image of feature A in micrograph depicted in plate 4.55 and the corresponding elemental ratios for Fe:Cr, Mo:Cr and Mo:Fe determined by EDX analysis.	179
4.57	Dark field image of feature B in micrograph depicted in plate 4.55 and the corresponding elemental ratios for Fe:Cr, Mo:Cr and Mo:Fe from EDX analysis.	180
4.58	Bright field image of feature C in micrograph depicted in plate 4.55 and the corresponding elemental ratios for Fe:Cr, Mo:Cr and Mo:Fe from EDX analysis.	180
4.59	Growth of M_6C from $M_{23}C_6$ on a grain boundary almost parallel to the maximum principal stress in the notch tip region of the fully bainitic CT specimen tested at a temperature of 550°C and a stress of 100MPa for 350 hours and corresponding elemental ratios for Fe:Cr, Mo:Cr and Mo:Fe determined by EDX analysis.	181
4.60	M_6C type carbides at grain boundary triple points in the fully bainitic CT specimen tested at a temperature of 550°C and a stress of 100MPa for 350 hours.	181
4.61	High magnification TEM image of an elongated grain boundary carbide in the notch tip region of the fully bainitic CT specimen The elemental ratios of Fe:Cr, Mo:Cr and Mo:Fe, determined by EDX analysis, are indicated in this micrograph.	182

Index to Plate Nos. cont.

4.62	TEM micrograph showing the typical carbide morphology observed in a reference region of the ferrite / bainite CT specimen tested at a temperature 550°C and a stress of 110MPa for 850 hours.	183
4.63	TEM micrograph showing elongated carbides along a ferrite / bainite grain boundary oriented at an angle with respect to the notch tip and maximum principal stress.	183
4.64	High magnification TEM image of the elongated grain boundary carbide observed in plate 4.63 and corresponding elemental ratios for Fe:Cr, Mo:Cr and Mo:Fe determined by EDX analysis.	184
4.65	Evolution of $M_{23}C_6$ to M_6C by the gradual absorption of elements from adjacent carbides on a non-critically oriented ferrite / bainite grain boundary.	185
4.66	M_7C_3 type carbide at a typical ferrite / ferrite grain boundary in the ferrite / bainite CT specimen and corresponding elemental ratios for Fe:Cr, Mo:Cr and Mo:Fe.	185
4.67	Growth of M_7C_3 type carbide at a ferrite / ferrite grain boundary by absorption of adjacent M_2C carbides in the ferrite / bainite CT specimen.	186